Metal@carbon nitrogenated porous architectures as novel sustainable catalysts for electrocatalytic hydrogenation of biomass-derived organics

A thesis presented to

School of Chemistry, Trinity College Dublin, The University of Dublin

for the degree of

Doctor of Philosophy in Chemistry

by

Filippo Pota

Under the supervision of:

Prof. Paula E. Colavita

2025

Declaration

I declare that this thesis has not been submitted as an exercise for a degree at this or any other university and it is entirely my own work.

I agree to deposit this thesis in the University's open access institutional repository or allow the Library to do so on my behalf, subject to Irish Copyright Legislation and Trinity College Library conditions of use and acknowledgement.

I consent the examiner retaining a copy of the thesis beyond the examining period, should they so wish (EU GDPR May 2018).

Filippo Pota, February 2025

To all the people of Grafton Street

and to the happiness they unknowingly

gave me over these years,

making my journey special.

Acknowledgement

Among all the people who have been important during my PhD, I would first like to express my deepest gratitude to my supervisor, Prof. Paula E. Colavita. I first met Prof. Colavita in the summer of 2020, a time when uncertainty about the future was part of our everyday life. However, despite the circumstances, her enthusiasm and knowledge of the chemistry matter impressed me from the very beginning, strengthening my decision to move to Ireland during such an uncertain time. I am especially grateful to Prof. Colavita for being an inspiring teacher and mentor, for her patience and understanding, for giving me the opportunity to collaborate with her over these years, and for believing in my potential. The long scientific discussions and diverse opinions on the next steps, results, and data, have allowed me to deepen my understanding of how complex and beautiful the subject we study truly is. Finally, I want to thank Prof. Colavita for giving me the freedom to learn from my mistakes, for constantly pushing me beyond my limits, and for making me a better chemist.

I want to express my gratitude to the School of Chemistry of Trinity College Dublin, from the administrative staff to the technicians which have helped me over these years. In particular, I am grateful to Mr. Ben Power, Dr. Brendan Twamley, Dr. Manuel Ruether, and Dr. John O'Brien for their assistance and patience. A special mention goes to Dr. Aran Rafferty from the School of Chemistry, who conducted the BET and PSD measurements on my samples, and to Dr. Clara De Castro from the Geology Department, who assisted me with the XRF analysis.

I would like to thank Prof. Frédéric Barrière and Dr. James A. Behan, which I had the opportunity to meet during my one-month stay at Université de Rennes as part of the international “Ulysses” grant between Ireland and France. I am grateful to them, from whom I learned that sometimes stepping out of your comfort zone, even in science, can be beneficial. In particular, I would like to thank Dr. Behan for his valuable advice, for the inspiring conversations and for teaching me some electrochemical tricks. I would also like to thank Dr. Ludivine Rault from Université de Rennes for conducting TEM measurements on my samples, which significantly enhanced the level of my work.

A warm thank you goes to the Colavita Group which has been my foundation and family here in Ireland. I would especially like to thank my student, Nina Chen, who has allowed

me to see things from a different perspective and learn so much from that experience. Among all the people who have passed through the office these years, I want to express my deepest gratitude especially to Marc, Maida, Chris, Lua, Silvia, Sonsoles, Hugo, Federico, and Pietro - thank you for being my true friends even before being my colleagues.

A big thank you to my dear friends Mercedes, Justine, and Sandra for reminding me that there was life beyond the PhD and outside the laboratory. I am grateful for the happy and carefree moments we shared together over these years in Dublin. I would also like to thank Thomas McCluskey who has been my first friend here in Ireland, for helping me throughout these years in particular in my initial time in Dublin.

A heartfelt thank you to the busking community for making me feel welcomed and part of something wonderful. And to all the strangers who have stopped to listen to me over these years. Thank you for your smiles, your joy, and even the tears you've shared with me. You have given me moments that I will always carry with me as something truly precious.

Un ringraziamento speciale ai miei genitori per avermi supportato in questi anni, per avermi sempre incoraggiato a seguire la mia strada e per essere stati al mio fianco, anche mentre mi vedevano allontanare da casa. Ai miei fratelli, ai miei nipoti e a tutta la famiglia, per i momenti di gioia condivisi, che sono stati una ricarica periodica nei ritmi frenetici di questi anni. Un pensiero speciale a mia nonna, da cui mi sono dovuto allontanare negli ultimi anni della sua vita e che non ho potuto riabbracciare per un ultimo saluto. Grazie anche ai miei amici più lontani, in particolare a Saverio ed Andrea, per essere stati una fondamentale ancora di salvezza nei momenti di difficoltà.

Il mio ultimo pensiero va ad Ilaria, per l'amore incondizionato che mi ha donato in questi anni, e che mi ha spinto ad arrivare fino in fondo ai miei obiettivi. Per il legame che ci ha unito nonostante la distanza, le videochiamate, le sveglie all'alba, i piani per i voli organizzati mesi in anticipo, gli autobus, i treni, gli aerei, e per ogni altra difficoltà che insieme abbiamo superato. Grazie per avermi fatto scoprire la versione migliore di me. Grazie per i momenti di pura felicità. Grazie per esserci sempre stata.

Summary

The valorisation of biomass and waste feedstocks is a crucial strategy for reducing carbon emissions. Biomass stands out among renewables for its potential beyond energy production, serving as a sustainable source for high-value products such as fuels and chemicals. Biomass feedstock conversion often involves thermal catalytic hydrogenation (TCH), a common method for upgrading oxygenated compounds. However, TCH depends on costly precious metal catalysts, operates at high temperatures and pressures, and relies on fossil fuel-derived hydrogen.

Conversely, electrocatalytic hydrogenation (ECH) offers a more sustainable alternative, generating hydrogen in situ and avoiding the need of extreme conditions and fossil fuels, while also ensuring compatibility with renewable energy sources. However, its viability depends on developing efficient and selective electrocatalysts. As a result, research efforts are ongoing to explore new classes of abundant and cost-effective electrocatalyst materials. Metal@carbon:nitrogen (M@C:N) architectures have gained attention in electrocatalysis due to their versatility and ability to incorporate non-critical, low-cost metals. These materials are already widely studied for cathodic reactions like the hydrogen evolution reaction (HER), which also represents a key competitive process for ECH. Therefore, given the strong link between HER and ECH, M@C:N structures could be a viable, low-cost alternative for hydrogenating biomass-derived organics.

This thesis aims to position itself within this context exploring, for the first time, the use of low-cost and non-critical metals as active sites for the design, synthesis and characterisation of M@C:N architectures to be used for ECH applications. Three metals have been identified as potential candidates based on their activity towards HER: iron (Fe), molybdenum (Mo), and tungsten (W). Benzaldehyde (BZH) was instead selected as the model organic compound representative of biomass fraction for conducting ECH studies.

In the opening section of this thesis (Chapter 1), the state-of-the-art of the use of biomass as renewable resource is discussed, including the most widely employed methods for its valorisation. The electrochemical principles essential for understanding electrocatalyst design are explored, with a particular focus on the mechanisms of HER and ECH. A deeper insight into the design of porous carbon-based materials is provided, with

emphasis on M@C:N structures, along with an overview of the current findings on the ECH of benzaldehyde. Chapter 2 discusses the characterisation methods and their theoretical background used to study the prepared materials throughout this thesis.

The first results chapter (Chapter 3) assesses Fe@C:N as the initial material for BZH hydrogenation, based on its promising performance in other cathodic reactions. Special attention is given to optimising catalyst preparation by evaluating different annealing processes and carbon nanoscaffolds, providing at the same time a comprehensive material characterisation and preliminary electrochemical studies.

Chapter 4 explores the usability of these materials on larger conductive supports for quantitative studies, combining chronoamperometry with gas chromatography analysis. The development of a new stable electrode preparation is discussed, along with the evaluation of key ECH performance parameters, demonstrating the potential of Fe@C:N as a viable alternative to precious-metal-based electrocatalysts.

Chapter 5 expands the study to include Mo- and W-based materials, investigating different metal concentrations to assess their impact on structural and electrochemical properties. The results emphasise that the HER/ECH competition play a critical role in regulating the activity during BZH hydrogenation. High metal concentration in M@C:N leads to excessive HER activity, which appears to limit their potential application for ECH.

To clarify the role of the metal and its impact on ECH performance indicators, a more in-depth study is conducted in Chapter 6, where Mo@C:N and W@C:N materials are evaluated alongside a metal-free benchmark electrocatalyst. Both Mo- and W-based electrocatalysts exhibit superior ECH performance compared to the metal-free catalyst, highlighting the significant enhancement provided by metal encapsulation. Notably, W@C:N outperformed Fe- and Mo-based materials, positioning itself as a cost-effective alternative to precious-metal catalysts for ECH applications.

Table of Contents

List of Figures

CHAPTER 1

CHAPTER 2

CHAPTER 3

CHAPTER 4

coated with drop-cast ink (c). SEM-EDX mapping for C, F and O atomic species of the unmodified bare CC in (b); and SEM-EDX mapping for C, F and Fe atomic species of the Fe@C:N surface in (c). Figure adapted from Pota et al. reference 36.

Figure 4.5 (a) LSV collected for bare CC in 0.1 M H_2SO_4 (dashed line) and in 0.1 M H_2SO_4 + 30 mM BZH (solid line) at 10 mV s^{-1}. (b) LSV collected for Fe@C:N/CC in 0.1 M H_2SO_4 (dashed line) and in 0.1 M H_2SO_4 + 30 mM BZH (solid line) at 10 mV s^{-1}. (c) LSV collected for Fe@C:N/CC 0.1 M H_2SO_4 + 1.0, 10.0 and 30.0 mM BZH. (d), (e) and (f) CVs collected in the same conditions as (a), (b) and (c) but using 0.1 M Na_2SO_4 as supporting electrolyte instead of H_2SO_4. Figure adapted from Pota et al. reference 36.

Figure 4.6 (a) Schematic representation of H-cell setup. (b) Chronoamperometry recorded in 0.1 M H_2SO_4 + 30 mM BZH at -0.8 V vs RHE (red line), and 0.1 M Na_2SO_4 + 30 mM BZH at -1.0 V vs RHE (blue line). Carbon balance for 1, 10, and 30 mM BZH in (c) 0.1 M H_2SO_4 and (d) 0.1 M Na_2SO_4

Figure 4.7 Total faradaic efficiency (FE) given by the sum of BA and HBZ contributions in 0.1 M H_2SO_4 at -0.8 V applied potential (a) and 0.1 M Na_2SO_4 at -1.0 V applied potential (b), for 1.0,10.0 and 30.0 mM BZH. Contributions of benzyl alcohol (BA) and hydrobenzoin (HBZ) to the total FE in 0.1 M H_2SO_4 (c) and 0.1 M Na_2SO_4 (d). Figure adapted from Pota et al. reference 36.

Figure 4.8 (a) Total ECH Yield given by the sum of BA and HBZ contributions and (b) BA and HBZ Yield for 1, 10, 30 mM in 0.1 M H_2SO_4. Figure adapted from Pota et al. reference 36.

Figure 4.9 (a) Conversion of BZH as function of its concentration. (b) Geometry of the cell simulated from different plane view perspectives with key geometric parameters identified. (c) Cell cross-sections profile showing BZH concentration on the cell after 2 h reaction considering only diffusive mass transport. (d) On the left axis, evolution of the percentage of BZH moles remaining (from 30 mM BZH initial concentration) in the cell vs reaction time. On the right axis, evolution of current density vs reaction time. Figure adapted from Pota et al. reference 36.

Figure 4.10 (a) CV collected for Fe@C:N on CC-MPL in 0.1 M H_2SO_4/ 30 mM BZH at 10 mV/s. (b) Chronoamperometries collected for each potential for 2 h. Total ECH FE% (c) and total product rate with $TOF_{eff,bulk}$ values (d) for -0.26, -0.5, -0.8, -1 V vs RHE. Contribution of BA and HBZ to ECH FE% (e) and to product rate (f) for each potential. Figure adapted from Pota et al. reference 36.

CHAPTER 5

Figure 5.1 (a) XRD patterns, (b) nitrogen adsorption-desorption isotherm, (c) pore size distribution, and (d) TGA curves, collected for Mo@C:N and Mo@C:N-(L).

Figure 5.2 Survey XPS spectra of Mo-based electrocatalysts. Pecks associated to Mo are highlighted in yellow, while all other contributions are marked in grey.

Figure 5.3 XPS high resolution spectra of C 1s (a), N 1s (c) and Mo 3d (e) for Mo@C:N; and of C 1s (b), N 1s (d) and Mo 3d (f) for Mo@C:N-(L).

CHAPTER 6

W@C:N and Mo@C:N materials. (d) TGA curves for RPM/BP, W@C:N and Mo@C:N electrocatalyst.

Figure 6.4 (a) Survey XPS spectrum of RPM/BP with highlighted in yellow characteristic peaks and in grey In peaks. Corresponding high-resolution spectra in the (b) C1s and (c) N 1s regions.

Figure 6.5 LSV of W@C:N, Mo@C:N, RPM/BP and bare GC normalised by capacitance.

Figure 6.6 SEM images for (a) bare CC and (b) CC coated with RPM/BP, along with SEM images and EDX mapping of CC electrodes coated with (c) Mo@C:N and (d) W@C:N electrocatalyst inks. CV recorded at varying scan rates in 0.1 M Na_2SO_4 for (e) bare CC, (f) RPM/BP, (g) Mo@C:N and (h) W@C:N coated on CC supports.

Figure 6.7 (a) LSV measured in 0.1 M H_2SO_4 supporting electrolyte for all materials on CC current collectors at 10 mV s^{-1}. LSV measured in 0.1 M H_2SO_4 in absence and presence of 30 mM BZH for (b) RPM/BP, (c) Mo@C:N, (d) W@C:N coated on CC.

Figure 6.8 (a) LSV collected for W@C:N and Mo@C:N on CC support in 0.1 M H_2SO_4 + 30 mM BZH with highlighted potential at -0.26 V (♦), -0.5 V (●) and -0.8 V (■) vs RHE. (b) Representative chronoamperograms recorded for W@C:N and Mo@C:N, measured at -0.8 V. (c) Representative log-log plots of individual chronoamperograms at -0.26 V. (d) Summary of mass balance for electrolysis experiments carried out with all three investigated materials. (e) Conversion and (f) yield obtained from electrolysis experiments carried out with all three investigated materials.

Figure 6.9 Yield by product for all materials at (a) -0.26 V (b) -0.5 V and (c) -0.8 V. Selectivity by product for all materials at (d) -0.26 V (e) -0.5 V and (f) -0.8 V.

Figure 6.10 (a) Total FEECH calculated for all three investigated materials and potentials. Product rate normalised by geometric area (b), by capacitance (c), and by amount of metal in the bulk for both M@C:N (d).

Figure 6.11 $TOF_{eff,surface}$ calculated values for Mo@C:N and W@C:N samples normalised for surface atomic concentrations.

Figure 6.12 (a) $TOF_{eff,surface}$ normalised for surface atomic concentrations and (b) $TOF_{eff,bulk}$ normalised for bulk atomic concentrations, calculated for all sieved M@C:N samples.

List of Tables

CHAPTER 1

CHAPTER 2

CHAPTER 3

CHAPTER 5

CHAPTER 6

List of Abbreviations

ACP	Acetophenone
BA	Benzyl alcohol
BE	Binding energy
BET	Brunauer-Emmett-Teller
BJH	Barrett-Joyner-Halenda
BP	Black Pearl 2000®
BSE	Backscattered electrons
BZH	Benzaldehyde
CC	Carbon cloth
CE	Counter electrode
CV	Cyclic voltammetry
DFT	Density Functional Theory
ECH	Electrocatalytic hydrogenation
ECSA	Electrochemically active surface area
EDX	Energy Dispersive X-ray Spectroscopy
FA	Furfuryl alcohol
FE	Faradaic efficiency
FID	Flame Ionization Detector
GC	Gas chromatography
GC disk	Glassy carbon disk
GC plate	Glassy carbon plate
G	Guaiacyl
H	p-Hydroxyphenyl
H_{ads}	Chemisorbed hydrogen
HBZ	Hydrobenzoin
HDO	Hydrodeoxygenation
HER	Hydrogen evolution reaction
HMF	Hydroxymethylfurfural
ICP-OES	Inductively coupled plasma optical emission spectroscopy
IPA	Isopropyl alcohol
LCB	Lignocellulosic biomass
LSV	Linear sweep voltammetry
M@C:N	Metal@Carbon:Nitrogen
MF	Methylfuran
MPL	Microporous layer
ORR	Oxygen reduction reaction
PCMs	Porous carbon-based materials
PDS	Pore size distribution
PES	Photoelectron spectroscopies
RHE	Relative hydrogen electrode

RE	Reference electrode
RF	Resorcinol-formaldehyde
r.d.s	Rate determining step
RSFs	Relative sensitivity factors
S	Syringyl
SE	Secondary electrons
SEM	Scanning electron microscopy
TEM	Transmission electron microscopy
TCH	Thermocatalytic hydrogenation
TGA	Thermogravimetric analysis
TOF	Turn over frequency
UPS	Ultraviolet photoelectron spectroscopy
VUL	Vulcan XC72R®
WE	Working electrode
XPS	X-ray photoelectron spectroscopy
XRD	X-ray diffraction
XRF	X-ray fluorescence

CHAPTER 1

Introduction

1.1 The evolving energy scenario

The energy supply represents today one of the biggest challenges for modern society as it seeks to balance the needs of populations with the urgent issues of climate change. The latest Copernicus Global Climate Highlights Report has confirmed that 2024 was the warmest year on record and the first to exceed the 1.5 °C target set by the Paris Agreement to prevent the most severe impacts of climate change.[1-3] Emissions from fossil fuels are one of the primary drivers of global warming, with CO_2 accounting for nearly 80% of all greenhouse gas emissions.[4] The transition to more sustainable energy sources is therefore essential to reverse this tendency and adopt a more environmentally friendly approach. Although fossil fuels have historically been the primary source of global energy production, the last years have seen a decline in their use in favour of renewable energy sources, along with an almost complete abandonment of nuclear energy. This trend is highlighted in the 2024 annual Statistical Review of World Energy and presented in **Figure 1.1a** as percentage of electricity production.[5] In 2023 for the first time in 40 years, fossil fuels and nuclear energy have hit record lows in global electricity production, accounting for 60% and 9%, respectively. Conversely, over the past 15 years, renewables have nearly doubled their contribution to global electricity generation, reaching 30% in 2023. **Figure 1.1b** compares the production and consumption of electricity sources for the year 2023.[5] The higher consumption of fossil fuels compared to production highlights the continued dependence on these energy sources, while the differing trends in the production-to-consumption ratio for renewables underscore the necessity for strategic investments to close this gap. As indicated in the 2023 World Energy Investment Report and shown in **Figure 1.1c**, global investment in clean energy has from several years surpassed that in fossil fuels, reaching a record amount of 1,740 billion USD in 2023.[6] This reflects a dedicated effort to advance the technology associated with renewable energy solutions, whose market is diverse and dominated by four main categories: wind power, solar energy, hydropower, bioenergy and other renewables (which include wave and tidal energy).[5] **Figure 1.1d** shows the energy generation contribution % for each of these categories over the last 40 years. The hydropower has become slowly less popular to leave room for wind power and solar energy. This trend is largely due to the evolving costs of each technology and advancements in strategies to improve performance and efficiency. Notably, as detailed in the 2023 Renewable Power Generation Costs Report, the average costs for solar and wind energy dropped by 90% and 70%, respectively,

between 2010 and 2023, whereas hydropower costs increased by 33% over the same period.[7] Bioenergy – renewable energy sourced from organic materials known as biomass, including plant and animal matter, agricultural and forestry residues, and organic waste[8] – did not experience the surge in popularity seen with solar and wind energy for electricity production, and instead faced a worldwide decline over the last years (**Figure 1.1d**). This decline is due to several factors related to the unique economics of biomass power generation compared to wind, solar, or hydropower. Bioenergy costs depend on the availability of feedstock supplies (such as wood and organic waste), as well as the expenses associated with their collection, transportation, and the volatility in biomass pricing.

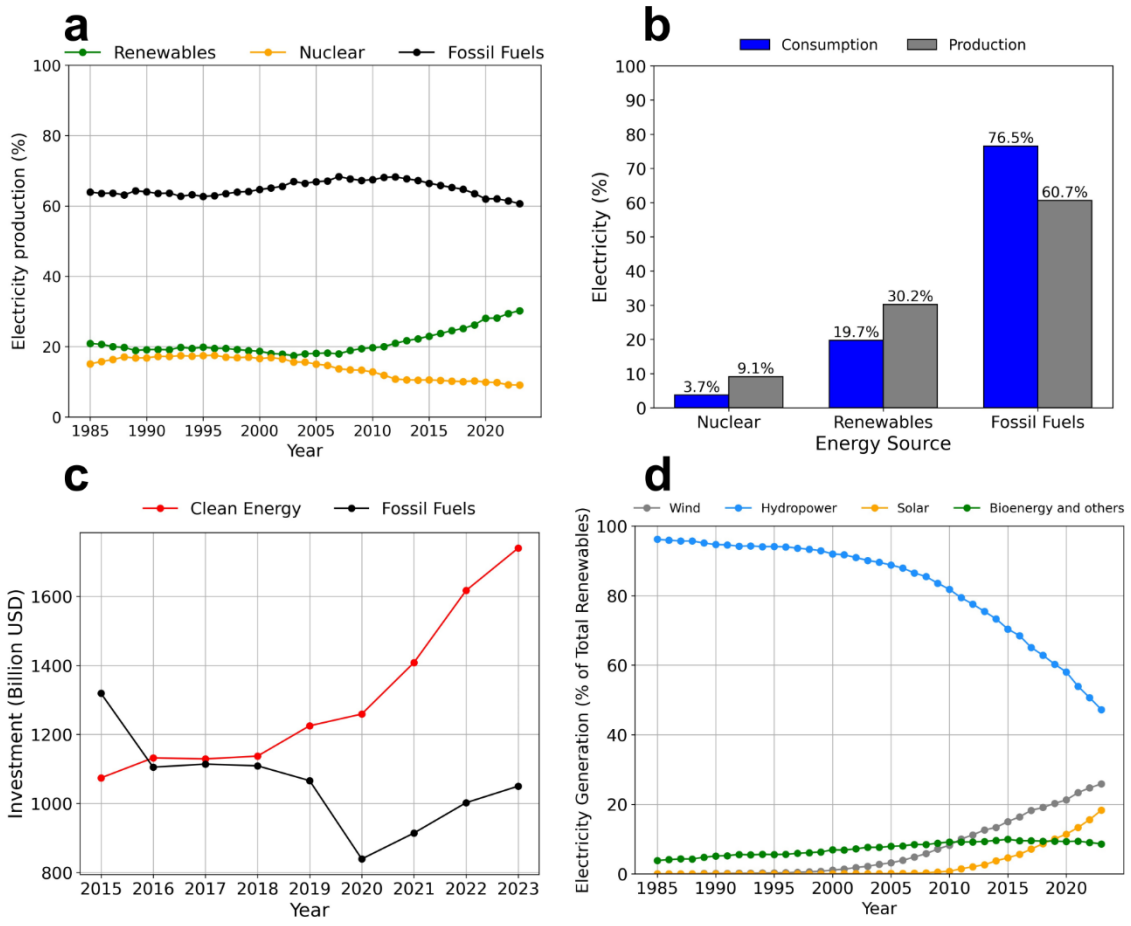

Figure 1.1 (a) Electricity production over the years for renewables, nuclear and fossil fuels; dataset from reference 5. (b) Electricity production and consumption in 2023 for energy sources.[5] (c) Investment in billion USD over the years for clean energy and fossil fuels (Licence: CC BY 4.0).[6] Clean energy includes renewable power, electric vehicle, battery storage, nuclear and low emission fuels. (d) Electricity generation from renewables sources over the years; dataset from reference 5.

Despite these challenges, bioenergy remains highly competitive in the renewable energy market, particularly when considering its potential beyond electricity and heat production. According to the 2024 Union Bioenergy Sustainability Report, bioenergy accounted for 58.9% of the total renewable energy consumed in EU-27 member states in 2021, compared to 7.2% for solar energy, 11.9% for hydropower, and 13.2% for wind energy, with minor contributions attributed to ambient heat (6.1%) and geothermal energy (2.7%).[9] More importantly, biomass as a feedstock is essential for effectively utilising low-cost agricultural and forestry products, along with organic waste from industrial activities that would otherwise go unused, supporting circular economy practices. The potential of biomass extends far beyond energy production; biomass valorisation plays a crucial role not only in reducing emissions but also as a renewable and abundant hydrocarbon resource with wide-ranging applications. It supports the production of electricity and heat, liquid and gaseous biofuels, as well as biochemicals and materials.

This introduction chapter presents an overview of biomass uses as a valuable feedstock for circular economy and valorisation purposes, employing electrocatalysts materials as a sustainable approach. Section 1.2 describes biomass categories and sources, along with their composition and properties, with a focus on valorisation processes in biorefineries. Electrochemical and electrocatalysis concepts, are introduced in Section 1.3, with attention to processes related to biomass valorisation. Section 1.4 examines the preparation of porous-carbon materials, while Section 1.5 discusses the use of Metal@Carbon:Nitrogen (M@C:N) architectures as candidates for biomass valorisation catalysts. Section 1.6 addresses the use of benzaldehyde (BZH) as a model organic compound, while Section 1.7 and Section 1.8 outline the aim and objectives of the thesis, respectively.

1.2 Biomass valorisation and biorefinery

1.2.1 Lignocellulose biomass

Biomass is a crucial renewable feedstock, produced directly or indirectly through photosynthesis, its valorisation processes offer a sustainable solution for generating chemicals and energy, while also helping to manage waste production.[10,11] Biomass can be classified into three categories: primary, secondary, and tertiary. Primary biomass is

produced directly through photosynthesis and is sourced from the land. Secondary biomass consists of materials derived from the processing of primary biomass, while tertiary biomass includes by-products generated after consumer use. This classification can also encompass various biomass sources, which include forest, agricultural, and organic waste biomass (**Figure 1.2**).[9,12] Forest biomass includes tree branches and tops, stumps, and roundwood, as well as by-products from the forestry industry such as bark, wood chips, sawdust, and other wood particles, along with black liquor and tall oil. Agricultural biomass comprises food and agricultural waste, along with crops like corn and sugarcane, as well as residues such as straw, rice husks, and nutshells.

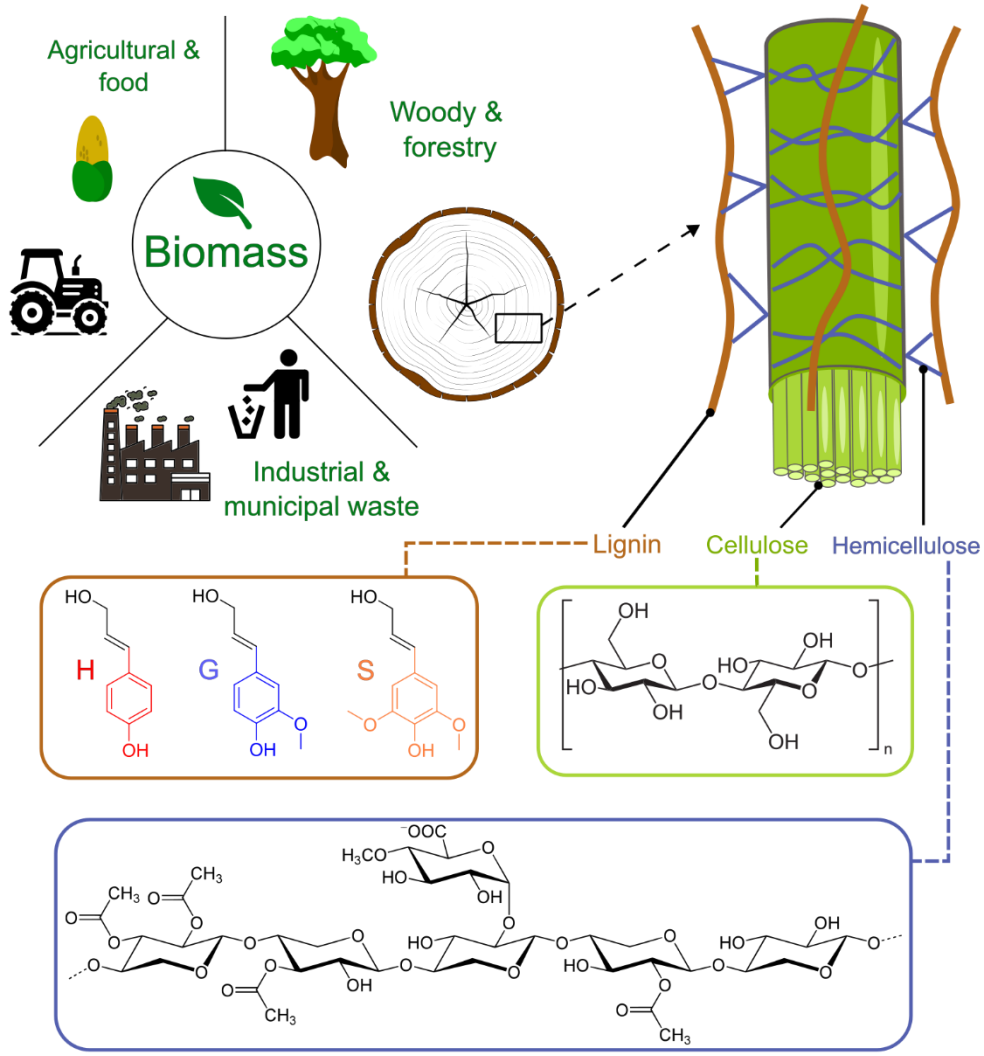

Figure 1.2 Main sources of biomass and a schematic representation of lignocellulose, including the molecular structures of cellulose[13], hemicellulose (Xylan polysaccharide)[14] and lignin monomers p-coumaryl alcohol, coniferyl alcohol and sinapyl alcohol [15] with highlighted the p-hydroxyphenyl (H), guaiacyl (G) and syringyl (S) units, respectively.[16]

Forest biomass can be considered as primary and secondary biomass source, while agricultural as primary and tertiary biomass. Organic waste biomass, which includes the organic components of industrial and municipal waste as well as sewage sludge, forms the majority of tertiary biomass. Additional biomass sources include various plant materials, glycerin, black liquor, bagasse, and winemaking residues, all of which constitute secondary biomass. Forest biomass is the main source of biomass by volume in the EU (66%) followed by biomass from organic waste (26%) and agricultural biomass (8%).[9] Woody and forestry biomass is highly valued for its capacity to capture CO_2 from the atmosphere, its abundant and affordable supply, its sustainability, and especially for its versatility and rich organic molecular composition.[12,17] Plant-based biomass consists of lignocellulosic biomass (LCB), a complex material that can be divided into three primary biopolymers: cellulose (30-45%), hemicellulose (20-40%), and lignin (10-25%), as schematically shown in **Figure 1.2**.[13,18] These percentage contents can vary depending on the different biomass sources considered.[12] Cellulose is a linear polymer of glucose units linked by β(1−4) glycosidic bonds, and it is characterised by sheet-like structures that stack into crystalline fibrils making it resistant to hydrolysis. Hemicellulose is a branched polymer comprising short chains of various polysaccharides, such as xylan (which structure's is presented in **Figure 1.2**), galactomannan, glucomannan, and xyloglucan.[14] Hemicellulose's amorphous structure makes it easier to hydrolyse than cellulose, and it also functions as a binding agent between cellulose microfibrils and lignin. Lignin is an aromatic polymer and considered the most abundant source of aromatic compounds in nature.[15] It is made up of three building blocks phenylpropane monomers: p-coumaryl alcohol, coniferyl alcohol and sinapyl alcohol, which are commonly referred to as p-hydroxyphenyl (H), guaiacyl (G), and syringyl (S) units, respectively (**Figure 1.2**).[16] It provides strength to plant cell walls and plays a role in protecting plants from pests and diseases.[19] In addition to these three main components, lignocellulose also contains small amounts of pectin, glycosylated proteins, extractives (such as chlorophyll, waxes, and non-structural sugars), and inorganic materials like silica. The complexity and variety of organic molecules in LCB, along with the tightly interwoven connections among its components, contribute to its recalcitrant nature– i.e. the resistance of a material to degradation or decomposition.[13] Indeed, the recalcitrance refers to the difficulty in separating LCB main components (cellulose, hemicellulose, and lignin) and converting them into useful products. The crystalline structure of cellulose resistant to hydrolysis, and the complex nature of lignin that acts as both a physical and

chemical barrier, present significant obstacles to the degradation of lignocellulose. Therefore, pretreatment methods are essential for facilitate this degradation, together with valorisation steps for converting LCB into higher-value products.

1.2.2 Biorefinery

Biomass valorisation takes place in biorefineries, where LCB is transformed into a variety of valuable products, such as biofuels, biomaterials, chemicals, and energy. The biorefinery process consists of two main steps: pretreatment and valorisation (**Figure 1.3**). The aim of the pretreatment step is to depolymerise and fractionate the interlinking of cellulose, hemicellulose and lignin. There are several pretreatment methods, including physical, chemical and biological, or combinations of these approaches. Chemical pretreatments, which include acid, alkaline, oxidative and organo-solvent methods, are among the most studied and widely applied. They are generally more effective at increasing cellulose accessibility but can present high costs. Physical pretreatments such as milling and grinding are often considered more economic than chemical pretreatments, though they may be less effective. Finally, biological pretreatments offer a promising alternative due to their superior environmental sustainability compared to chemical and physical methods, but large-scale application remains limited to date.[12] The second key step, valorisation, involves transforming the three isolated biopolymers that constitute LCB into intermediate products (known as platform molecules) before further refining them into high-value final products through reductive upgrading processes (**Figure 1.3**).[10,15,20]

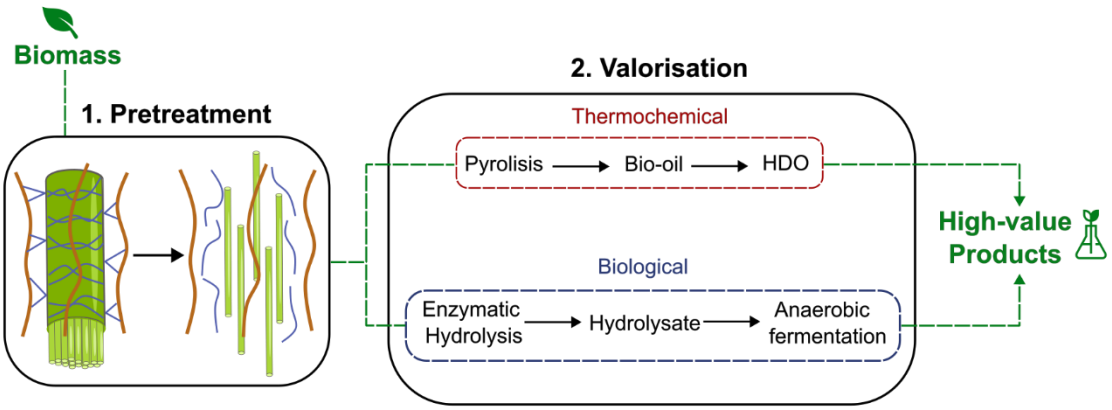

Figure 1.3 Schematic representation of the two main steps of biorefinery: pretreatment and valorisation.

These valorisation processes are divided into thermochemical ones, such as pyrolysis, and biological ones, such as enzymatic hydrolysis or saccharification.[15] An overview of the most common thermochemical methods, including operating conditions and resulting products, is provided in **Table 1.1**. Most thermochemical processes primarily produce bio-oil a highly oxygenated, multi-component liquid mixture containing acids, alcohols, sugars, aldehydes, esters, ketones, phenolics, aromatics, and oligomers.[21-23]

Table 1.1 Most common thermochemical conversion methods for LCB biomass together with operative conditions and final products.

Method	Conditions	Product	Reference
Pyrolysis	T= 350 – 550 °C (in O_2) T= 700 – 800 °C (absence of O_2)	Bio-oil	11
Combustion	T > 800 °C (in O_2)	Heat	
Gasification	T = 500 – 800 °C (in O_2)	Syngas (mix of CO and H_2)	10
Torrefaction	225 – 300 °C (absence of O_2)	Bio-oil	11
Hydrothermal liquefaction (HTL)	H_2O at 280 – 340 °C P = 10-25 Mpa	Bio-oil	

Biological valorisation processes yield a carbohydrate-rich stream known as hydrolysate, a solution of fermentable sugars that also contains various other components derived from the biomass.[20] Both thermochemical and biological processes produce platform molecules, or a mix of them, that are rich in oxygen but poor in hydrogen content, making these products unsuitable for direct use as fuels (which are oxygen poor and hydrogen rich). Hence, additional reductive steps are necessary to obtain final value-added products.

In biological methods, anaerobic fermentation of sugars by microorganisms is used to produce a variety of bioproducts, including biofuels (e.g., ethanol, butanol), biochemical products (e.g., lactic acid, succinic acid), and biomaterials.[20] In thermochemical processes, the bio-oil produced along with a high oxygen content (35–40 wt%) and water content (15–30 wt%), has also high viscosity and acidity. To address this, catalytic processes are employed to optimise the bio-oil's energy density (C–H bonds) and molecular weight (C–C bonds), while reducing its oxygen content (C–O bonds) in the final products. One of the standard catalytic methods for this purpose is the

hydrodeoxygenation (HDO), which uses a variety of heterogeneous catalysts, including noble metals (supported on carbon or metal oxides) and transition metal carbides, nitrides, and phosphides.[22,24,25] This and other similar thermochemical processes for bio-oil upgrading are referred to under the name of thermocatalytic hydrogenation (TCH), and generally require high temperatures (200–400 °C) and high hydrogen pressures (100–200 bar) to achieve efficient production rates. A more detailed discussion on the catalyst materials required for TCH to enhance selectivity and reduce operating conditions is provided in Section 1.2.3. The choice of the most suitable and efficient pretreatment and valorisation method in biorefinery processes depends on several factors, which include the desired final product, cost, and environmental impact.[12,26] Notably nowadays, the biorefinery industry focus primary on valorising cellulose and hemicellulose, while lignin is often considered a byproduct.[27] Compared to lignin, cellulose and hemicellulose have simpler chemical structures and are easier to break down and convert into useful products. For instance, cellulose is already widely used in the production of paper, textiles, and other materials; hemicellulose can be used to produce fermentable sugars for biofuels and bioproducts; while lignin is frequently burned to generate energy and heat. Although significant progress has been made in recent years in developing new technologies for lignin valorisation, and even if its potential for producing high-value-added products is increasingly recognised;[10,12] there are still significant obstacles in terms of cost, sustainability and applicability to be faced. Due to the complexity of lignin structure there exists no effective way to biochemically cleave its ether bonds via enzymes and microorganisms for producing value-added materials and chemicals.[19,28] Therefore, thermochemical methods and TCH processes for platform molecules valorisation are generally preferred over biological methods, for their higher yields in the conversion of all three main component of LCB, i.e lignin, hemicellulose and cellulose.

1.2.3 Benefits and limitations of thermocatalytic hydrogenation

The HDO enable the convert biomass feedstocks and platform molecules to high-value products, enabling them to perform the properties of petroleum-based products.[29,30] TCH using heterogeneous catalysts is a conventional method for upgrading oxygenated biomass derived chemicals through HDO. Due to the complex composition of LCB, research on catalytic hydrogenation is based on model organic compounds that are representative of biomass fractions. This approach is adopted for a deeper understanding

of reaction mechanisms and the synthesis of selective chemical products, as well as to provide a solid theoretical foundation for the industrialization of biomass hydrogenation processes.[29,31] **Figure 1.4** illustrates main organic molecules that can be derived from each LCB biopolymer. Cellulose can yield hexoses, furans, and organic acids as platform molecules which can be converted into valuable products such as hydroxymethylfurfural (HMF) and levulinic acid. From hemicellulose, furfural can be obtained, which can be further converted into industrial chemicals and fuels such as furfuryl alcohol (FA), and 2-methylfuran (MF).[30] Lignin, on the other hand, can be used to extract aromatics and olefins, including phenols, benzene, toluene and light olefins. The TCH reaction generally involves the activation of biomass compounds and H_2 upon adsorption onto the catalyst surface; then reactions between these activated intermediates lead to the formation of the desired products. Thus, beyond factors such as reaction temperature, hydrogen pressure, and solvent choice, designing targeted catalysts is essential for enhancing the activity and selectivity of the TCH reaction.[29]

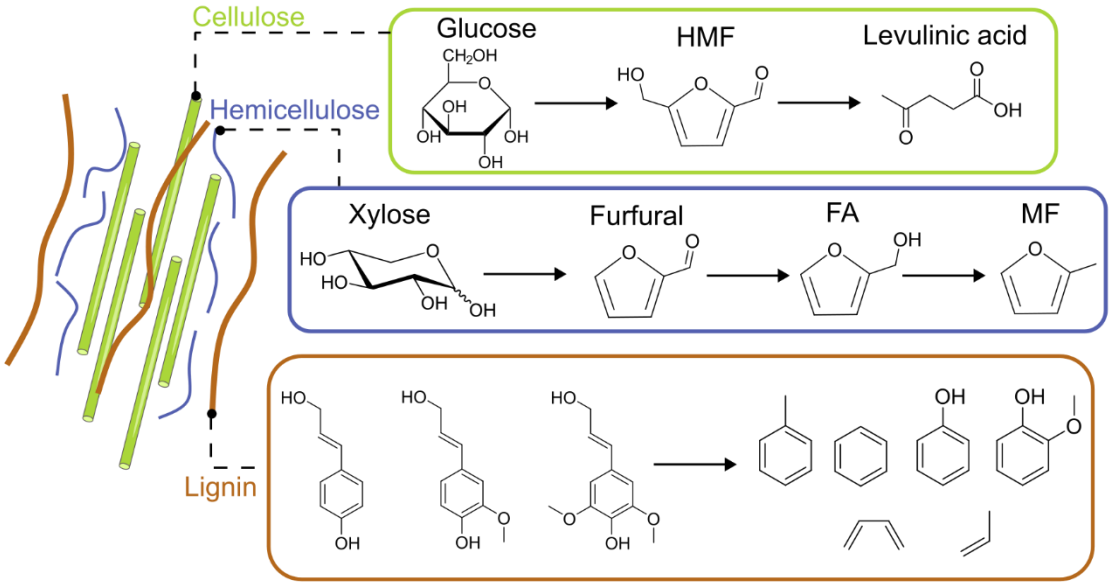

Figure 1.4 Examples of organic molecules derived from LCB.

Precious metals are the most popular catalysts for the HDO of model organic compounds for biomass-derivatives. For instance, the use of Ru/C and Pd/C for converting glucose in ethylene glycol and 2-propanediol, respectively, has been reported.[32,33] Pt, Ir, Pd and Ru were proposed as catalysts for the HDO of HMF,[34] while Cu, Ni and Pd have been reported for the reduction of furfural.[35]

Table 1.2 provides an overview of the heterogeneous catalysts used in HDO of lignin model aromatic compounds, including operating conditions and resulting products. The widespread use of precious metal catalysts is made problematic by high demand and elevated costs of such materials, which substantially increase the overall costs associated with TCH. This expense is further increased by the use of H_2, 95 % of which is produced from fossil fuels resources, through methane steam reforming or coal gasification.[36] Moreover, high temperatures can promote side reactions that hinder the ability to selectively produce a specific product.[15,37]

Table 1.2 Overview of catalysts studied for HDO of lignin organic model compounds and operational conditions.

Catalyst	Model compound	Main product(s)	Conditions	Ref.
Pd/C	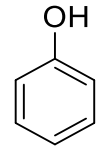	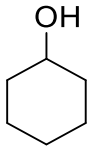	H_2O, 200°C, 5 MPa H_2	43
	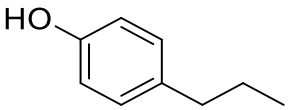	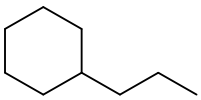	H_3PO_4- H_2O, 250 °C, 5 Mpa H_2	
	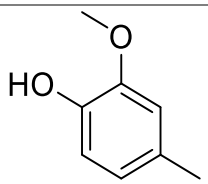	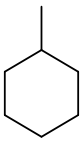	H_3PO_4-H_2°, 250 °C, 5 Mpa H_2	
Ru/C	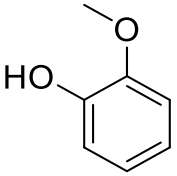	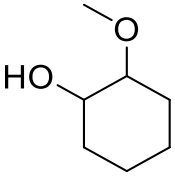	H_2O, 200 °C, 13.8 Mpa H_2	44
Rh/C	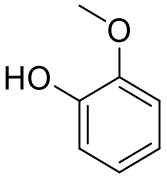	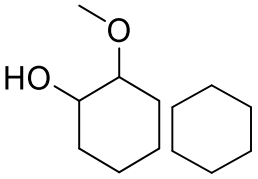	n-Decane, 250 °C, 4 Mpa H_2	45
Ru/C	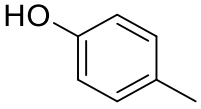	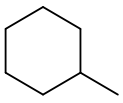	Acetic acid, 300 °C, 4.8 Mpa H_2	46
Pt/Al_2O_3	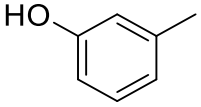	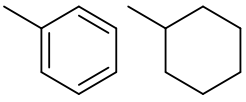	260 °C, 50.5 kPa H_2	47

Considering these limitations, the past 25 years have seen significant efforts to explore alternative pathways for biomass valorisation using more sustainable and cost-effective methods. Among the possible alternatives the use of electrochemistry and electrocatalysis has been the most popular and explored route.[38-42] In particular, a potentially sustainable strategy is the use of electrocatalytic hydrogenation (ECH)[48] for the valorisation of oxygenated organic molecules derived from biomass. ECH involves the generation of chemisorbed hydrogen (H_{ads}) via electroreduction of H_3O^+ or water, followed by reaction of H_{ads} with the adsorbed unsaturated compound and desorption of products. ECH can bypass the problem of activating H_2, thanks to in situ generation of H_{ads} from protons/water. Furthermore, it eliminates the need for using H_2 with high purity and at high pressure and temperature conditions, thus lowering operational costs. This means that electrocatalytic hydrogenation could enable the valorisation of biomass and waste streams that cannot be processed in an economically feasible manner via TCH.[41,49,50] Moreover, the coupling of ECH with renewable sources can improve the sustainability of the processes and reduce their carbon footprint. ECH could be used as a way of electrifying the hydrogenation processes, thus substituting fossil fuel-based technologies with technologies that use electricity. This is known as electrification, and it is envisioned as a strategy to decouple economic activities from carbon emissions. The integration of thermochemical pre-treatment processes with ECH for bio-oil production, coupled with upgrading powered by renewable energy from solar or wind, has been proposed as valuable alternative to TCH to produce sustainable, carbon-neutral fuels and chemicals (**Figure 1.5**).[51,52]

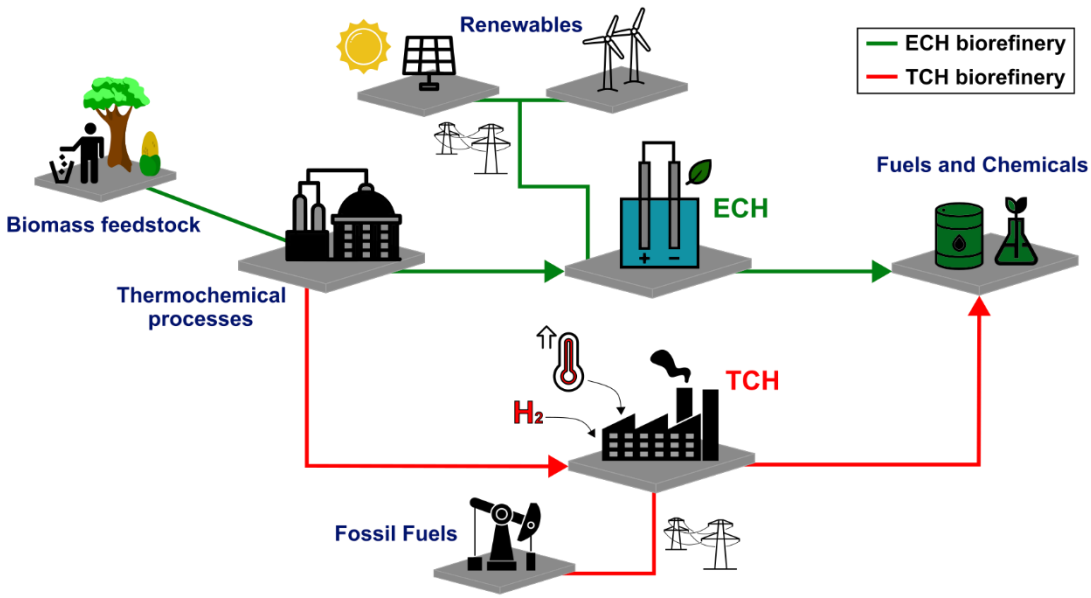

Figure 1.5 Scheme of TCH- and ECH-based biorefinery alternatives, adapted from reference 51.

However, ECH cannot fully replace standard technologies without the development of high-performance electrocatalysts that offer both high efficiency and selectivity. Even though H_2 can be produced in situ and high temperatures are unnecessary, the catalysts currently used for this process predominantly rely on precious metals, which greatly impact the economic viability of ECH. Additionally, ECH faces competition from other electrochemical processes, such as the hydrogen evolution reaction (HER), that occur simultaneously under similar conditions. To overcome these challenges, there is an ongoing research effort to develop new electrocatalysts made from abundant and low-cost materials that can minimise competing reactions and enhance efficiency. In this context, utilising non-critical raw metals or those with a low criticality index is particularly relevant. A material's criticality is determined by its abundance in the Earth's crust and the risk of supply disruption. According to the latest EU criticality assessment, metals such as Fe, Mo, and W are classified as non-critical or relatively low supply risk, making them promising candidates for preparing new electrocatalyst materials.[53]

The following section will cover the electrochemical principles essential for understanding the design of electrocatalysts, with a particular focus on the mechanisms of HER and ECH. It will also explore various approaches for evaluating catalytic performance and provide an overview of the current state-of-the-art for these processes.

1.3 Electrocatalysis: main concepts and general background

1.3.1 Introduction to electrochemical principles

Electrochemistry is the study of chemical processes driven by the movement of electrons at the interface between a solid electron conductor phase (electrode) and a liquid ionic conductor phase (electrolyte). Redox species in the electrolyte can donate or accept electrons from the electrode material, which acts as either a donor or acceptor of charge. The mutual exchange of electrons at the interface constitutes the electrochemical reactions, commonly referred to as Faradaic processes. Electrochemical systems, however, can promote other processes that do not involve electron transfer but result in current flows, these are referred to as non-Faradaic processes. An example of such processes is the capacitive current which arises from the charging and discharging of the electrical double layer at the electrode/electrolyte interface. Electrochemical processes are governed by both thermodynamics and kinetics effects. Thermodynamics determines the feasibility of an electrochemical processes and is influenced by the electrode potential, which quantifies the driving force for a given redox reaction, i.e., the tendency of the electrode to gain or lose electrons. The Nernst equation (Eq 1.1) enables calculation of the electrode potential under non-standard conditions, taking into account concentrations and temperature, and provides a relationship between the standard electrode potential (E^0) and the electrode potential E for a given set of product/reactant activities.

$$E = E^0 - \frac{RT}{nF} \ln \frac{a_{Red}}{a_{Ox}} \qquad \text{(Eq 1.1)}$$

Where R is the ideal gas constant, T is the absolute temperature, n is the number of moles of electrons transferred in the redox reaction, F is the Faraday constant, a_{Red} is the activity of the reduced species and a_{Ox} is the activity of the oxidised species.

Charge transfer processes can be controlled by applying an external potential, which shifts the electrode potential and alters the thermodynamic balance between oxidised and reduced species at the surface.[54] However, reaction kinetics plays a crucial role in electrochemical processes by determining the rate with which redox reactions take place upon a change in applied potential. Further, the kinetics of mass transport is also important

and refers to the movement of reactants to the electrode and the removal of products from it. Mass transport occurs via three primary mechanisms:

- Diffusion: The movement of species from regions of high concentration to low concentration, typically driven by concentration gradients near the electrode surface.
- Convection: The bulk movement of solution, usually induced by stirring or external forces, which helps to refresh the concentration of reactants and products at the electrode surface. Convection can also occur naturally, driven by density gradients and leading to spontaneous fluid motion near the electrode.
- Migration: The movement of ions due to an electric field, though this is typically less influential than diffusion and convection in most electrochemical systems.

A slow transport of redox species at the electrode surface can result in mass transport-limited reactions. Indeed, electrochemical systems often operate under conditions where kinetic limitations lead to deviations from ideal behaviour. These deviations manifest as overpotential (Eq 1.2), which is defined as the potential of an electrode above its equilibrium value that is required to cause a given current to flow through the electrode.[54]

$$\eta = E - E^0 \qquad \text{(Eq 1.2)}$$

The electrical current (j) that is passing through the electrode during a kinetically controlled electrochemical process, even in the absence of any mass transport limitations, is affected by the overpotential. The Butler-Volmer electron transfer kinetics model describes the kinetic current dependence on overpotential as shown by (Eq 1.3).[55,56]

$$j = j_0 \times \left[e^{-\frac{\alpha_A n F \eta}{RT}} - e^{-\frac{\alpha_C n F \eta}{RT}} \right] \qquad \text{(Eq 1.3)}$$

Where j_0 is the exchange current density, α_A is the anodic charge transfer coefficient, α_C is the cathodic charge transfer coefficient, n is the number of electrons involved in the electrode reaction. The left addendum of the equation represents the anodic current density, while the right term corresponds to the cathodic current density. When the potential is highly negative, as is the case of cathodic reactions, the anodic contribution becomes negligible.[55] Therefore, (Eq 1.3) can be rewritten to obtain the cathodic Tafel equation (Eq 1.4).

$$j = j_0 \times \left[e^{-\frac{\alpha_C n F \eta}{RT}} \right] \quad \text{(Eq 1.4)}$$

The Tafel equation indicates that for small overpotentials the current density increases exponentially, therefore a logarithmic plot of current versus potential is expected to exhibit a linear region, allowing the so called Tafel slope to be determined. The Tafel slope value can be used to understand the rate determining step (r.d.s) which is the step that kinetically limits a given electrochemical reaction.

Overall, processes such as adsorption, desorption, and transport of reactants/products within the electrolyte, influence the performance of an electrochemical system. These effects highlight the role of electrode materials, which serve as catalysts to lower energy barriers and enhance reaction rates. The ideal catalyst balances efficient electron transfer with optimal interaction between the surface and reactive species. Indeed, according to the Sabatier principle,[57] a heterogeneous catalyst should bind reactants with just the right strength; strong enough to enable effective interaction with the active site, yet not so strong to allow desorption of the products. The design of electrocatalysts, therefore, requires a deep understanding of the relationship between the material properties and reaction dynamics enables the development of systems with improved efficiency, selectivity, and stability.

1.3.2 Hydrogen evolution reaction

For a clear understanding of the electrocatalytic hydrogenation mechanism, it is essential to first introduce the main electrochemical process that competes with it, i.e. the hydrogen evolution reaction. HER stands out as a key reaction for sustainable energy production and green chemical synthesis and involves the electrochemical generation of molecular hydrogen (H_2) through the reduction of protons or water, depending on the pH of the electrolyte.[58] Although the overall reaction in acid can be written as shown in (Eq 1.5) and consists of a two-electron transfer, the HER mechanism is a two-step process. The first step is the formation of H_{ads} on the surface-active site of the catalyst (*) via proton reduction, also called the Volmer step (Eq 1.6). Then the reaction can proceed to the desorption of the H_2 product through two possible pathways. A first pathway involves electrochemical desorption, where an H_{ads} reacts with a proton and an electron to form the product, processes referred to as the Heyrovsky step (Eq 1.7). The second pathway is

chemical desorption, which occurs through the reaction between two H_{ads} and referred to as the Tafel step (Eq 1.8).

$$HER \qquad 2\,H^+ + 2\,e^- \rightarrow H_2 \qquad \text{(Eq 1.5)}$$

$$Volmer\ step \qquad * + H^+ + e^- \rightarrow H_{ads} \qquad \text{(Eq 1.6)}$$

$$Heyrovsky\ step \qquad H_{ads} + H^+ + e^- \rightarrow H_2 \qquad \text{(Eq 1.7)}$$

$$Tafel\ step \qquad H_{ads} + H_{ads} \rightarrow H_2 \qquad \text{(Eq 1.8)}$$

Any of the three steps described above might be the r.d.s for the HER, and the Tafel slope provides valuable insights into the reaction mechanism, helping to identify which step controls the overall reaction rate. The theoretical Tafel slopes for the Volmer, Heyrovsky and the Tafel step are 120,40, and 30 mV/dec, respectively.[59,60] For instance, the Tafel slope for the best reported HER electrocatalysts based on Pt-group metals in acidic conditions is 37 mV/dec.[61] This indicates that the reaction proceeds via the Volmer–Tafel process and the r.d.s for the reaction is the Tafel step.[62]

Tafel slope is just one of the possible approaches for evaluating the HER catalytic performance of a given material. Ideally, a good HER electrocatalyst should yield high current densities (rate of H_2 evolution) at low values of overpotential, so as to facilitate the processes more efficiently and reducing energy losses. Low overpotential also indicates that the catalyst reduces the activation energy of the HER limiting step enabling faster reaction kinetics. Notably, the overpotential to run HER with Pt electrodes is ≈ 0 V.[63] High exchange currents – i.e. current density at the equilibrium potential where the cathodic current equals the anodic current[54] – are also desirable for an efficient HER electrocatalyst. In fact, the exchange current density reflects the intrinsic charge transfer activity between the electrode and electrolyte, and it tends to be higher on the surface of catalysts with greater catalytic activity.[64] Finally, the stability and durability of the electrocatalyst are crucial parameters in evaluating its practical application. Indeed, the ability of the material to maintain its original catalytic activity over a long period of time under operating conditions reflects its reliability and resilience. Precious metals are the most studied and efficient electrocatalysts for the HER since they combine low overpotential with high exchange current and stability. Such behaviour is a consequence

of the Sabatier principle and the strength of the M-H bond. **Figure 1.6** shows the Volcano plot between the current density versus the strength of the M-H bond.[65]

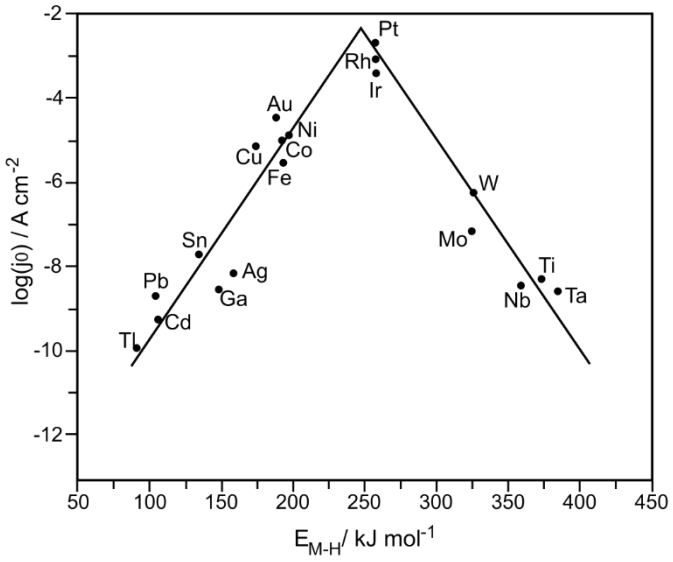

Figure 1.6 Volcano-type dependence between the exchange current density and M–H bond strength. Data replotted from reference 65.

The elements on the left side of the graph exhibit weaker M–H bonds, while those on the right have a strong M–H bond. The metals that are positioned at the peak possess hydrogen binding energy close to optimum value, allowing the thermodynamically easiest transition from reactants through intermediates to product. However, the Sabatier principle does not always accurately describe the real dependence of HER current density on M–H bond strength.[66] In particular this is true for elements like W, Mo or, Ti, as under conditions corresponding to the studied reaction, they are typically covered by an oxide layer. In fact, oxide films are present on them so that hydrogen atoms are not in contact with the metal surface, thus reducing the reaction rate and shifting the materials to stronger M-H.

Table 1.3 Summary of HER catalysts with overpotentials measured at current density of 10 mA/cm^2 against RHE for different pH conditions.

Catalyst	pH	η_{10} mA/cm^2 (mV, vs. RHE)	Reference
Pt	7	0	67
Pt/C	1	16	68
Pd/C	10	43	69
N-doped C	1	239	70
Co	7	350	67
Mo	7	240	67
Mo_2C	1	134	71
W_2C	1	173	71
Fe_3C	1	200	72

Taking into account the high cost and scarce reserves of Pt and similar precious metals, in the last years there has been increasing interest in discovering new HER catalysts based on more abundant and low-cost materials. For instance, molybdenum sulphide, MoS_2 has been shown to have high activity and stability for the HER in acid.[73,74] Carbon materials have also been used as conductive supports for metals, yielding materials capable to electrocatalyse the HER and facilitating the formation of active H_{ads} species. Pure carbon electrodes typically exhibit high overpotentials for H_{ads} formation[75,76] and are therefore intrinsically poor electrocatalysts; however, this limitation can be mitigated and controlled through doping of the carbon framework with heteroatoms or metals, as well as through defect engineering.[77] Notably, nitrogen incorporation in the form of pyridinic, pyrrolic, and graphitic functionalities has been shown to produce synergistic effects with structural defects, regulating interfacial interactions of intermediates for catalysis.[76] This approach has demonstrated significant experimental improvements in HER performance by enhancing the chemisorption strength H_{ads} and activity.[75,78] **Table 1.3** presents a summary of examples of HER electrocatalysts reported in the literature, including Pt-group metals, N-doped metal-free carbon materials, transition metals, and non-precious metal carbides, along with their respective overpotential as performance indicator. Pt/C shows the best overpotential, close to zero;[68] N-doped carbon and pure transitions metals such us Co and Mo show higher overpotentials that make them less suitable as

electrocatalysts for HER purposes.[67] Carbides of transition metals such us Mo, W and Fe show higher HER performance compared to their corresponding metals, with overpotential of 134, 173 and 200 mV, respectively in acid conditions.[71,72]

1.3.3 Electrocatalytic hydrogenation

The importance of electrocatalytic hydrogenation (ECH) as alternative electrochemical process for biomass-valorisation it was introduced in previous paragraph. This section will focus on the mechanisms of ECH, as well as the current state-of-the-art electrocatalysts and the model organic molecules commonly studied.

The ECH consists in the hydrogenation of unsaturated organics using H_{ads} as the hydrogen source.[48] The overall reaction can be written as shown in (Eq 1.9) but it consists of different steps. The first is the generation of H_{ads} on the surface-active site of the catalyst trough the Volmer step (Eq 1.6). This is followed by the adsorption of the target organic molecule (Y=Z, reagent) and generation of $YH{=}ZH_{ads}$ specie (Eq 1.10). The adsorbed species H_{ads} and $YH{=}ZH_{ads}$ can then reacts together to generate the adsorbed hydrogenated product $YH–ZH_{ads}$ (Eq 1.11). Finally, product is desorbed as shown in (Eq 1.12). Poisoning and/or side products can also be generated via hydrogenolysis (Eq 1.13).

$$ECH \qquad Y = Z + 2\,H^+ + 2\,e^- \rightarrow YH - ZH \qquad \text{(Eq 1.9)}$$

$$Reagent\ adsorbiton \qquad * + Y = Z \rightarrow Y = Z_{ads} \qquad \text{(Eq 1.10)}$$

$$Hydrogenation \qquad Y = Z_{ads} + 2H_{ads} \rightarrow YH - ZH_{ads} \qquad \text{(Eq 1.11)}$$

$$Product\ desorption \qquad YH - ZH_{ads} \rightarrow YH - ZH \qquad \text{(Eq 1.12)}$$

$$Hydrogenolysis \qquad YH - ZH_{ads} + 2H_{ads} \rightarrow YH_2 + ZH_2 \qquad \text{(Eq 1.13)}$$

The ECH mechanism may also involve a direct reduction pathway, based on a two-proton–two-electron reductive transformation of the organic molecule, at high overpotential and without involving H_{ads}.[79]

The difference between HER and ECH reactions then lies in how chemisorbed hydrogen is utilised **(Figure 1.7**). In the HER H_{ads} is employed for the production of molecular hydrogen, while in the ECH the H_{ads} is used to reduce other organic species adsorbed on the catalyst surface. Then, Heyrovsky (Eq 1.7) and Tafel (Eq 1.8) steps are competing reactions for ECH. The HER reaction consumes electrons, which cannot be used for ECH, and may drastically lower the current efficiency of the hydrogenation, and even prevent it entirely.[80]

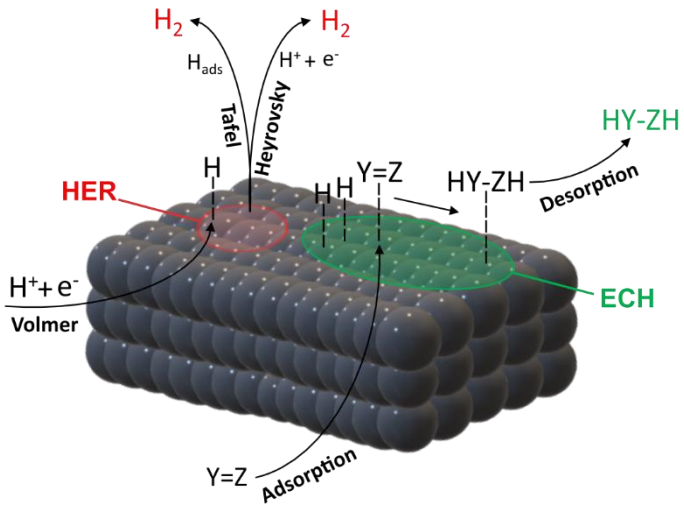

Figure 1.7 Schematic representation of the main steps for HER (highlighted in red) and ECH (highlighted in green) mechanisms. Scheme adapted from Pota et al. reference 81.

The strong interconnection between the HER and ECH makes it challenging to decouple them effectively. As a result, methods for evaluating ECH electrocatalysts and overall ECH efficiency must account for this close relationship. Among criteria already mentioned for HER catalysts such as Tafel slope or overpotential, for ECH it is important to introduce other performance parameters. Conversion (Eq 1.14) and selectivity (Eq 1.15) are useful for comparing the activity of ECH to HER for a given catalyst, but they may be limited in providing a comprehensive assessment of efficiency. Yield offers a more direct measure of practical efficiency by indicating how much of the reactant is actually converted into the target product (Eq 1.16). However, yield does not account for electron efficiency. In contrast, Faradaic efficiency (FE, (Eq 1.17) describes the prevalent use of electrons for ECH over HER and can be used as reaction efficiency parameter at a given potential.[31] Also, product rate (Eq 1.18) and turn over frequency (TOF) (Eq 1.19) can be used to calculate the specific rate and catalyst efficiency per unit time at a given potential, respectively. Normalisation to the electrochemically active surface area

(ECSA) or number of active sites can be used for cross-comparison among different catalyst. Notably, product rate and TOF parameters are generally preferred to report efficiency even if they can be affected by the operative conditions such as pH, electrolyte solution and concentration.

$$Coversion\ (\%) = \frac{mol_{reagent}}{mol_{reagent\ (t=0)}} \cdot 100 \qquad \text{(Eq 1.14)}$$

$$Selectivity\ (\%) = \frac{mol_{product}}{mol_{reagent}} \cdot 100 \qquad \text{(Eq 1.15)}$$

$$Yield\ (\%) = \frac{mol_{product}}{mol_{reagent\ (t=0)}} \cdot 100 \qquad \text{(Eq 1.16)}$$

$$FE\ (\%) = \frac{n_e \cdot mol_{product}}{mol_{e-}} \cdot 100 \qquad \text{(Eq 1.17)}$$

$$Product\ Rate\ (mol\ g_{metal}^{-1}\ s^{-1}) = \frac{mol_{product}}{M \cdot time} \qquad \text{(Eq 1.18)}$$

$$TOF\ (h^{-1}) = Product\ Rate \cdot MW_{metal} \qquad \text{(Eq 1.19)}$$

Where $mol_{reagent}$ are the moles of reagent consumed, $mol_{reagent(t=0)}$ are the moles of reagent at time zero, $mol_{product}$ are the moles of desired product, mol_{e-} are the moles of electrons, n_e is the number of electrodes consumed by ECH processes and M is the metal loading.

As mentioned in the earlier section, the most studied electrocatalysts for ECH are based on precious metals, including Pt, Pd, and Rh, with some reports highlighting the use of Ni and Cu as well. These metals can drive the electrocatalytic reduction of oxygenated compounds, e.g. saturation of aromatic rings, hydrogenation of C=C double bonds, hydrogenation of carbonyl groups, and C−O cleavage in ether bonds and alcohols. Due to its extensive use in fuel cell and electrolysis technologies, Pt has become the most widely studied metal for reduction reactions.[82-84] Pt typically results in low FE compared to other noble metals, but it is active for the reduction of a large variety of organic compounds for complete hydrogenation. The use of Pt as ECH electrocatalyst can be traced back to 1914 when Fichter and Stocker reported the electrocatalytic oxidation and reduction of phenol, obtaining cyclohexanone and cyclohexanol as products.[85] These had open the way to a series of studies on the use of Pt for the hydrogenation of phenol and

related molecules all the way to aliphatic cyclic alcohols, or benzene to cyclohexane.[86-88] Pd has been shown to catalyse both the hydrogenation of aromatic rings to ketones and their subsequent conversion to alcohols in phenolic compounds.[89] Additionally, it exhibits strong catalytic activity in the hydrogenation of aromatic carbonyl compounds, though without affecting the aromatic ring – an outcome that may be desirable in certain cases. For instance, Pd/C has been reported as an efficient electrocatalyst for the hydrogenation of benzaldehyde to benzyl alcohol, achieving both high TOF and FE,[90] as well as for the conversion of acetophenone to 1-phenylethanol.[91] Base metals like Raney Ni have been investigated as alternatives to precious metals, showing promising results for the hydrogenation of aromatic rings and the conversion of carbonyl or nitro groups into hydroxyl or amine groups.[92-94] Cu has also been investigated for similar reactions but exhibits lower reactivity compared to Ni. Cu can reduce substituent nitro groups to amines, C=C bonds, and aromatic rings.[95,96] However, the hydrogenation of cyclohexanones to the corresponding alcohols appears to be challenging with Cu and Ni.[97] Other base metals, like Co, Fe, and Zn, have demonstrated inferior performance compared to Cu and Ni for the same reactions under similar conditions.[98,99] Notably, these low-cost metals, despite achieving a conversion similar to Pt-group catalysts, exhibit ECH activity at more cathodic potentials, promoting a radical mechanism and side reaction pathways.[98,99] Indeed, selectivity toward a specific product is a parameter to take into account when comparing performances of different electrocatalysts. The reactivity of organic compounds and the reaction routes available for their reduction strongly depend on the metal itself. For instance, in case of conversion of benzaldehyde, the alcohol is the prevalent product for Pd and Cu, while the dimer side-product is preferred on Co, Ni and Zn.[98] Moreover Fe, Co, Cu and Ni studied for ECH of HMF and glucose have showed high preference for the dimer product rather than the alcohol.[100,101] A natural progression in catalyst design has been the dispersion of metals on carbon[37,42] or conductive polymers[102,103] allowing for a lower current density and therefore high FE.[104] Apart for the choice of the metal, the modification of the carbon support has been suggested as an effective strategy for improving ECH performances. As in the case of the HER discussed in the previous section, nitrogen functionalisation has also been reported as an effective method for enhancing ECH rates of carbonyl groups in aqueous phase.[105]

Table 1.4 Overview of catalysts employed for the ECH of some of the most common lignin model organic compounds.

Electrocatalysts	Model compound	Main product(s)	Ref.
Pt	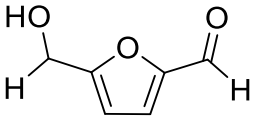	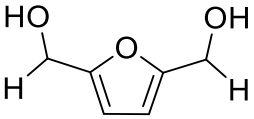	106
Pt, **Ni,** **Cu**	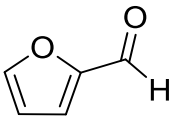	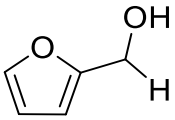	80
Pd/C	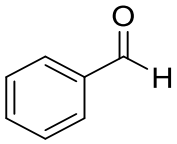	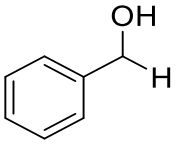	90
	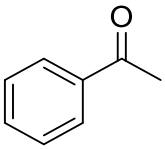	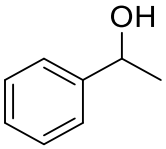	91
Pt/C, **Raney Ni**	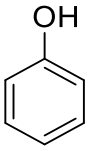	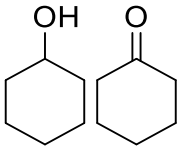	107,108
Ru/C	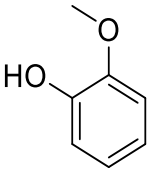	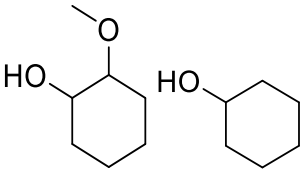	49
Rh/C	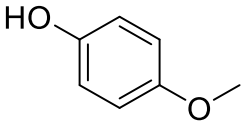	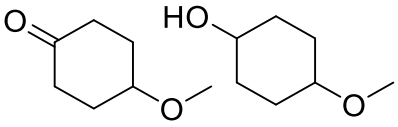	109

Table 1.4 provides an overview of electrocatalysts employed for the reduction of some of the most widely studied lignin model organic molecules. As for the HER, the heavy reliance on precious metals significantly increases the costs associated with ECH. Therefore, the development of cost-effective electrocatalysts is crucial for advancing the practical applications of electrochemical hydrogenation. The next two sections of this chapter introduce a class of materials based on porous carbon, proposed as a viable alternative to precious metals for use as electrocatalysts in ECH.

1.4 Porous carbon-based materials

Porous carbon-based materials (PCMs) are significant in catalysis due to their unique structural and chemical properties, which make them versatile as effective supports, or active catalysts for various reactions. PCMs have generated attention in different applications because of their advantages over conventional materials.[110] Their high surface area provides more active sites for reactions to occur and enhance catalytic efficiency, while their inherent chemical stability ensures they remain effective under challenging reaction conditions. PCMs possess other remarkable features, including low production costs, high thermal stability, and eco-friendliness.[111] Moreover, they exhibit excellent electrical conductivity, which makes them ideal for electrocatalysis, and good mechanical strength combined with a lightweight structure, which improves their usability in industrial applications.[112] The possibility to functionalise the surface of porous carbon with heteroatoms and/or metals is another important feature of such materials that allows for enhanced catalytic activity by introducing active sites at the material interface.[113] PCMs, like porous materials in general, are classified according to their pore sizes. The International Union of Pure and Applied Chemistry (IUPAC) defines three primary categories of pore structures: micropores (<2 nm), mesopores (2–50 nm), and macropores (>50 nm) (**Figure 1.8**).[114]

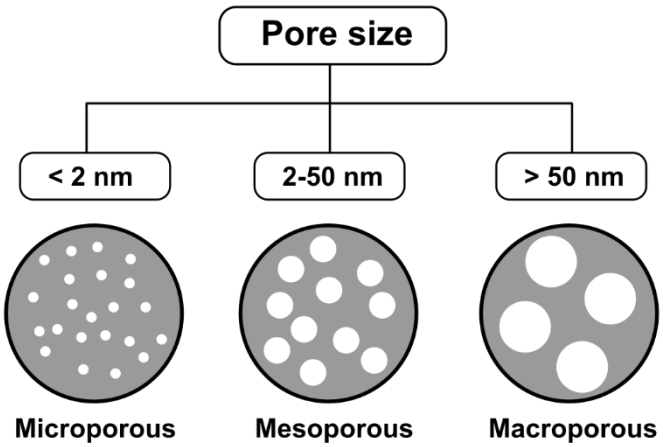

Figure 1.8 Classification of microporous, mesoporous, and macroporous structures based on pore size as defined by IUPAC.[114]

Microporous carbon materials, commonly referred to as activated carbon, are highly effective for adsorption and catalytic applications; their structure allows for selective

interactions based on molecular size, shape, or confinement effects, with wide range of applications in industrial and environmental processes.[115] Mesoporous carbon materials feature intermediate-sized pores that offer a balance between accessibility and surface area; they have received significant attention for their advantages in heterogeneous catalysis applications where larger molecules need to be processed.[116]

Finally, macroporous materials have large pores that facilitate fluid flow and mass transfer; these properties are beneficial in applications requiring minimal flow resistance, such as wastewater treatment, catalytic supports for bulk-phase reactions and in oxygen reduction reaction (ORR) applications.[117] Each type of porosity contributes uniquely to material performance, and their combination in PCMs can further optimise processes like catalysis, adsorption, and separation.

The most common approach for the synthesis of PCMs and pore generation is based on templating techniques.[118] This method allows to control the porous structure, typically in the meso- and/or microporous range, and can be divided into soft and hard templating methods. Soft templating involves use of self-assembling molecules, such as surfactants or block copolymers, which form micelles or organised mesophases in solution. These micelles serve as anchors, providing sites where the carbon precursor (typically an organic carbon source) can develop through hydrogen bonding or other interactions. Then the amphiphilic molecules can be removed through heating treatment (calcination) or solvent extraction to generate porous structures. A final step known as carbonization is necessary to convert the carbon precursor into the final porous carbon structure. This step is typically carried out by annealing the material at high temperatures under an inert atmosphere, such as nitrogen or argon, to prevent oxidation and combustion of the carbon (**Figure 1.9a**), while also serving as a method to remove the soft template.[119,120] Hard templating uses a distinct approach, involving pre-formed, rigid porous templates such as silica nanoparticles or colloidal crystals. In this method, the carbon precursor infiltrates the pores of the template, which serves to shape and define the final porous structure. Upon infiltration, the precursor undergoes carbonization, solidifying the structure into carbon, and the template is subsequently removed through chemical etching (e.g., with HF or NaOH), leaving behind the meso- and/or macroporous carbon material (**Figure 1.9b**).[121,122] Hard templating method requires the pre-synthesis of the template, which is time-consuming and costly, making it unsuitable for large-scale production.[123] In contrast, soft templating is simpler and more cost-effective, which has made it particularly popular

in the research and development of carbon-based materials, especially for electrocatalysis applications. Soft templating allows for the creation of mesoporous carbons with high surface area and tunable porosity, properties that are essential for enhancing electrocatalytic performance in reactions such as HER and ORR. Moreover, in soft templating it is more common to introduce heteroatom doping because of the flexibility in the synthesis process. For instance nitrogen can be incorporated by using dopant-containing precursors or by adding heteroatom-containing compounds such as melamine during the synthesis,[124] or ether by using NH_3 during the annealing process.[125] These approaches further enhance the catalytic efficiency of the resulting materials.[123]

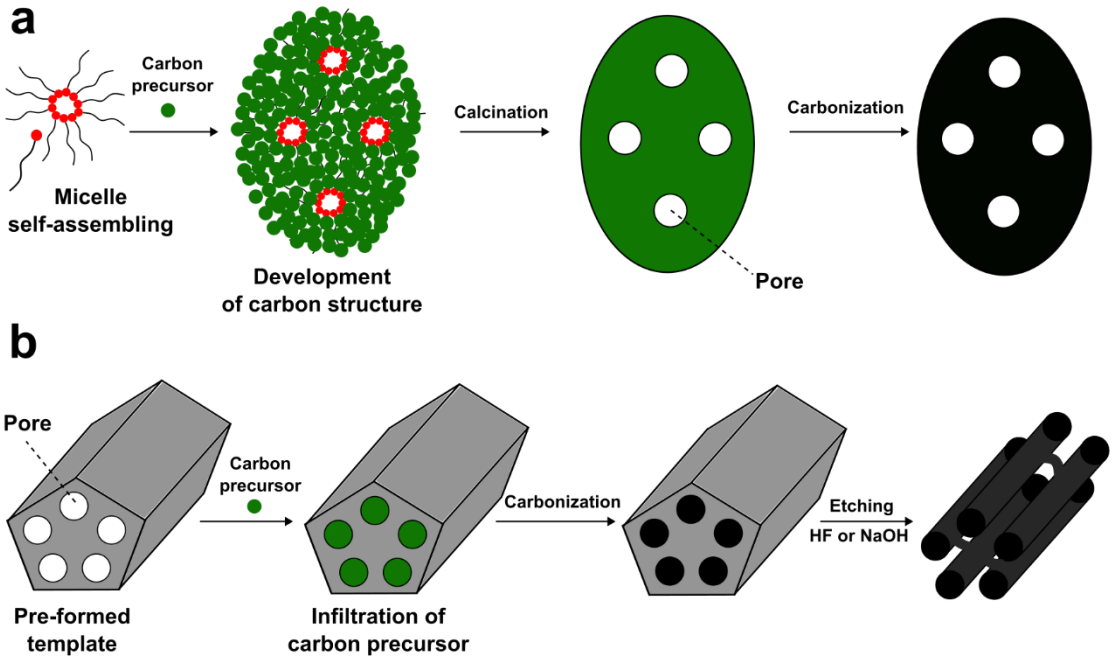

Figure 1.9 (a) Soft templating method and (b) hard templating method with key steps highlighted.

One of the most widely used organic carbon precursors in the soft templating method is resorcinol-formaldehyde (RF) resin, which belongs to the broader category of sol-gel resins. These resins are formed through a sol-gel process, a versatile technique that transitions materials from a liquid solution (sol) into a solid gel phase.[126] In the case of the RF resin, the polycondesation between resorcinol and formaldehyde, that can be catalysed by both acid and base in an aqueous medium, leads to the formation of a cross-linked polymeric gel held together by methylene and methylene-ether bridges. The

condensation reaction was proposed for the first time by Pekala and is showed in **Figure 1.10** for acid conditions.[127,128] The reaction can then progress by incorporating melamine into the resin, resulting in nitrogen doping of the final carbon network.[129] Pluronic-127® can be used as block copolymer in the preparation of these materials. Its amphiphilic nature creates self-assembled micellar structures which serve as templates for the formation of ordered porous structures held together by H-bond interaction between Pluronic F-127 and the resin. The subsequent annealing process has the double effect of removing the soft template while graphitising the resin.

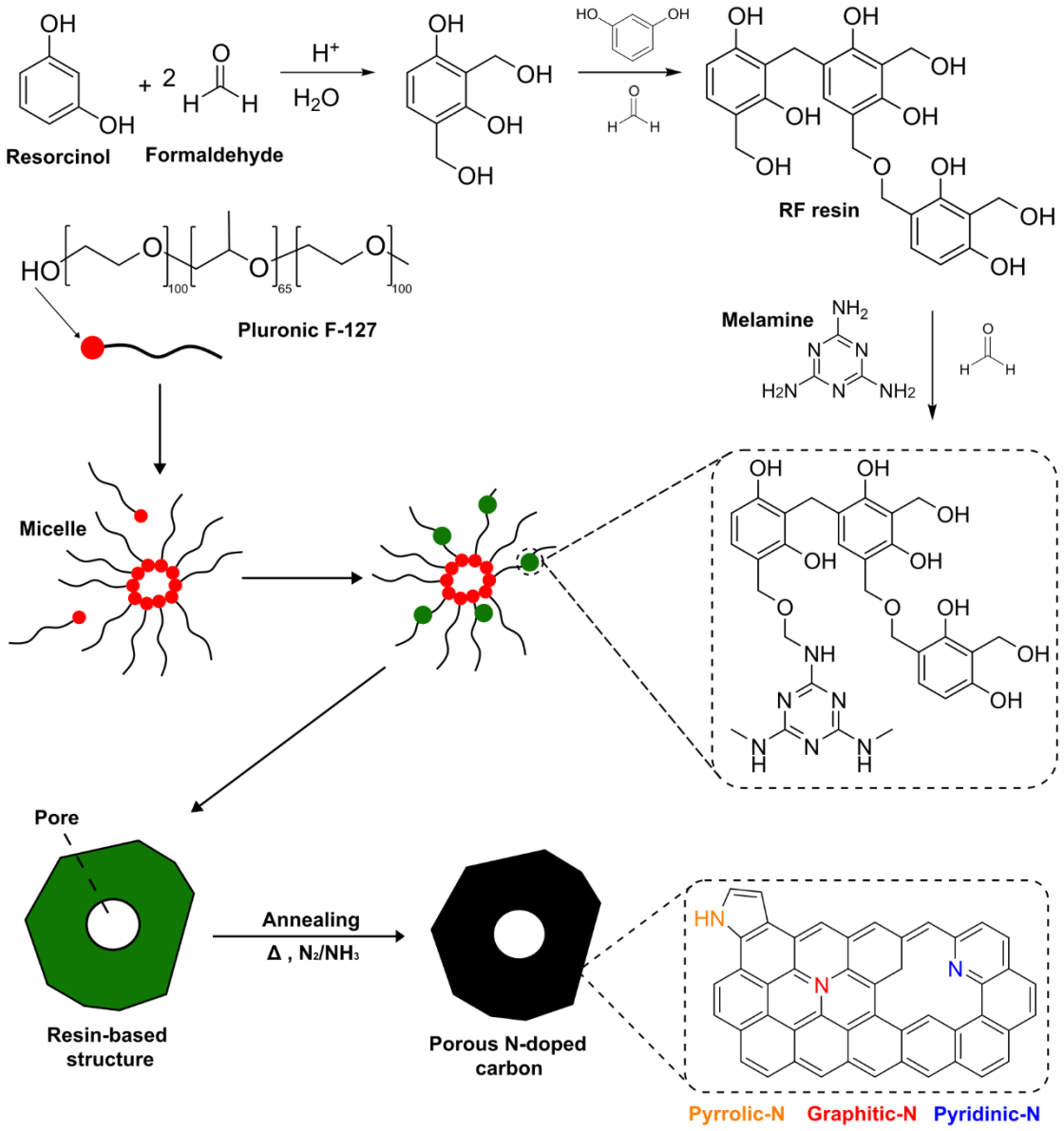

Figure 1.10 Polycondensation reaction of resorcinol, formaldehyde, and melamine under acidic conditions, alongside a schematic representation of the self-assembling micelles of Pluronic F-127 and the annealing process. The resulting porous N-doped carbon structure highlights pyrrolic-N (yellow), graphitic-N (red), and pyridinic-N (blue) sites.

Indeed, the presence of aromatic rings in the structure creates a framework for the formation of polycyclic aromatic hydrocarbons during carbonization which can evolve into graphene-like layers. The methylene and methylene-ether bonds, together with a highly cross-linked structure allow the material to conserve integrity while undergoing dehydrogenation during annealing. As hydrogen and oxygen are removed from the polymer, carbon atoms are left behind. The tight cross-linked network consents these carbon atoms to organise themselves into graphene-like sheets aligning into sp^2 hybridised structures. Nitrogen is incorporated into the final porous N-doped carbon structure in the form of graphitic-N, pyridinic-N and pyrrolic-N based on the position of the heteroatom in the graphene-like layer as show in **Figure 1.10**.

1.5 Metal@Carbon:Nitrogen (M@C:N) architectures

Materials based on N-doped carbon structure have received significant attentions for different applications in electrocatalysis and energy storage.[70,75,77,130] These structures can be further implemented including metal cores as active site into the carbon framework, resulting in metal@carbon:nitrogen composites (M@C:N) with optimised electronic structure due to close interactions between the metal core and carbon shell.[131] The encapsulation of the metal within the N-doped carbon framework protects the metal sites from air oxidation and decreases the probability of corrosion and aggregation (**Figure 1.11**), at the same time heteroatom doping is suggested to enhance the H_{ads} chemisorption strength.[78]

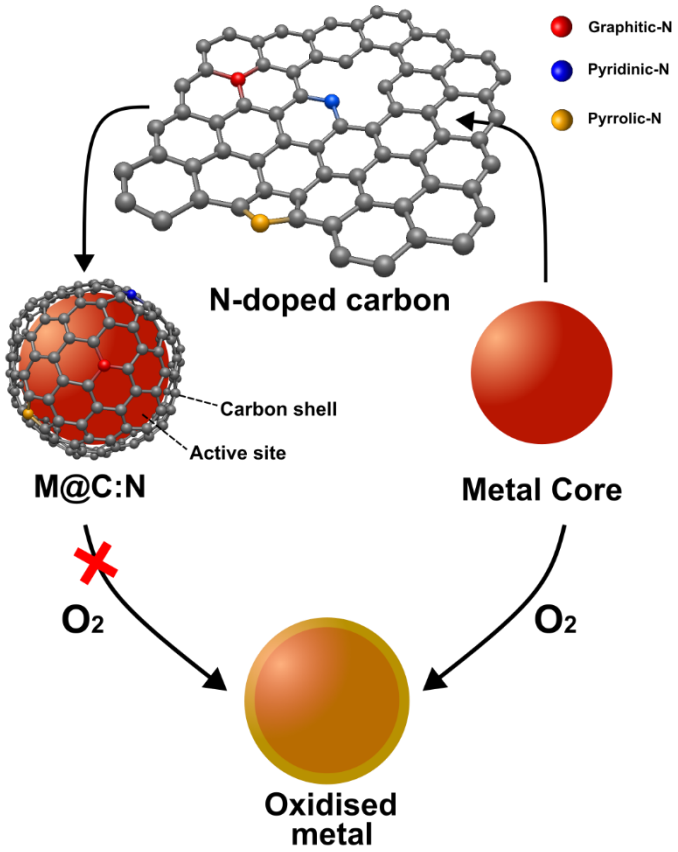

Figure 1.11 Schematic representation of the encapsulation of metal cores into N-doped carbon frameworks forming M@C:N architectures.

Integrating these two approaches, metal@carbon and N-doping, into a single electrocatalyst provides significant advantages, allowing for the use of non-precious metal electrocatalysts at low pH with good stability.[78] In this way, metals such as Co, Ni,

Fe, Mo, and W, typically considered unsuitable for cathodic reactions like HER according to the Sabatier principle, can perform effectively in M@C:N architectures with good activity. As shown in **Table 1.5** a general improvement of HER performances is observed for electrocatalysts when the metal cores are inserted in a carbon framework doped with heteroatoms. For instance, Co@C:N has been reported as good electrocatalyst for HER in acid conditions, displaying lower overpotentials than that of the pure Cobalt metal.[132] A combination of Co with Ni in the same N-doped architecture was reported as a way to increase this activity.[78] Also for Ni the encapsulation in the carbon shell improves the HER performances compared to pure Nikel metal.[133,134] Carbides of Fe, Mo and W shows higher overpotentials compared to M@C:N doped architectures in acid conditions as showed in **Table 1.5**. In particular, Wei et al. have reported the preparation of Mo_2C@C:N doped electrocatalysts with low overpotential of 82 mV.[135] Although the literature lacks a detailed explanation for this specific trend, it is likely attributed to the encapsulation of the metal within the N-doped carbon framework.[131, 78]

Table 1.5 Comparison of HER performances based on overpotentials at 10 mA/cm^2 for metal electrocatalysts and M@C:N architectures.

Metal core	η_{10} mA/cm^2 (mV, vs RHE) M/M_xC_x	η_{10} mA/cm^2 (mV, vs RHE) M@C:N	Ref.
Co	350	191	132
Ni	140	85	133,134
Fe	200	135	72,136
Mo	134	82	71,135
W	173	113	71,137

The interfacial charge transfer from the metal core to the carbon shell is suggested to be the primary mechanism driving the electrocatalytic performance, emphasising the critical role of the metal in designing such structures.[138] The presence of the metal has also been suggested to catalytically influence the graphitisation process, enhancing electrical conductivity and stability while reducing the Brunauer-Emmett-Teller (BET) surface area.[139-141] The properties of the carbon shell are important as well since reactions occur at its surface. Its role is to acts as a physical barrier, preventing the metal core from oxidation, corrosion, or aggregation under challenging conditions such as high

temperatures or acidic/alkaline environments; while the doping with heteroatoms can manipulate the effective activity towards specific reactions. The carbon shell has also been proposed to allow controlled permeation of reactants to the metal core, and this can optimise catalytic activity and selectivity by restricting access to specific molecules or intermediates, acting as a molecular sieve.[131,142,143] Notably, the precise identification of the active site in M@C:N structures continues to be a subject of debate in the literature for HER processes. As explored in detail by Yoo et al.,[131] two plausible and experimentally supported explanations for H_{ads} activation in carbon-encapsulated architectures have been proposed. One suggests that M-sites directly exposed to the electrolyte exhibit reactivity influenced by the surrounding carbon matrix, while the other considers C/N-sites whose reactivity is modulated by subsurface metals.

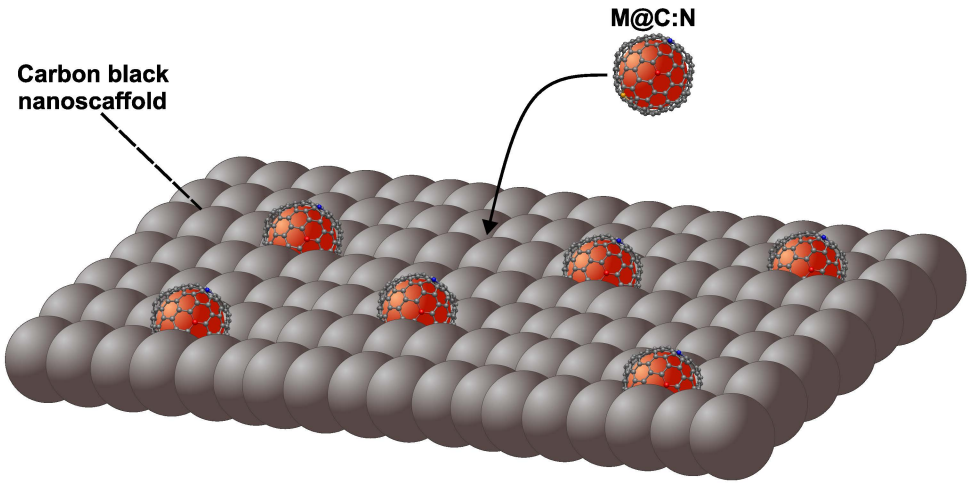

Figure 1.12 M@C:N architectures dispersed onto carbon black substrate.

In addition to carbon shells generated from the pyrolysis of a resin structure, commercial carbon nanoscaffolds like Vulcan® and Black Pearls® are usually used for preparing M@C:N materials. These carbon black materials have high surface area and conductivity and serve to provide structural and electrical support to catalytic systems. They act as a stable substrate onto which active encapsulated architectures are dispersed (**Figure 1.12**).[142] The availability and advantageous properties of carbon black make them suitable for large-scale applications compared to alternatives like carbon nanotubes or nanofibers, highlighting them as ideal candidates for electrocatalyst development.

Despite the promising results achieved with M@C:N architecture as HER electrocatalysts, their potential in other cathodic reactions remains largely unexplored. Due to the mechanistic similarity in the Volmer step, this design approach could be adapted for materials that are ECH active by using the optimal combination of carbon nanoscaffolds and metal cores to enhance catalyst performance through balancing HER and ECH competition. Furthermore, the possibility of relying on abundant and base metals in the preparation of M@C:N architectures represents an important advantage in terms of operative costs. **Figure 1.13** shows the market prices for the most studied precious electrocatalysts compared to those of base metals, revealing a price difference of 3 to 4 orders of magnitude, which can reach up to 5 orders of magnitude for metals like Ir or Rh.[144] The use of base metals in M@C:N architecture is therefore crucial for achieving cost-effective ECH processes.

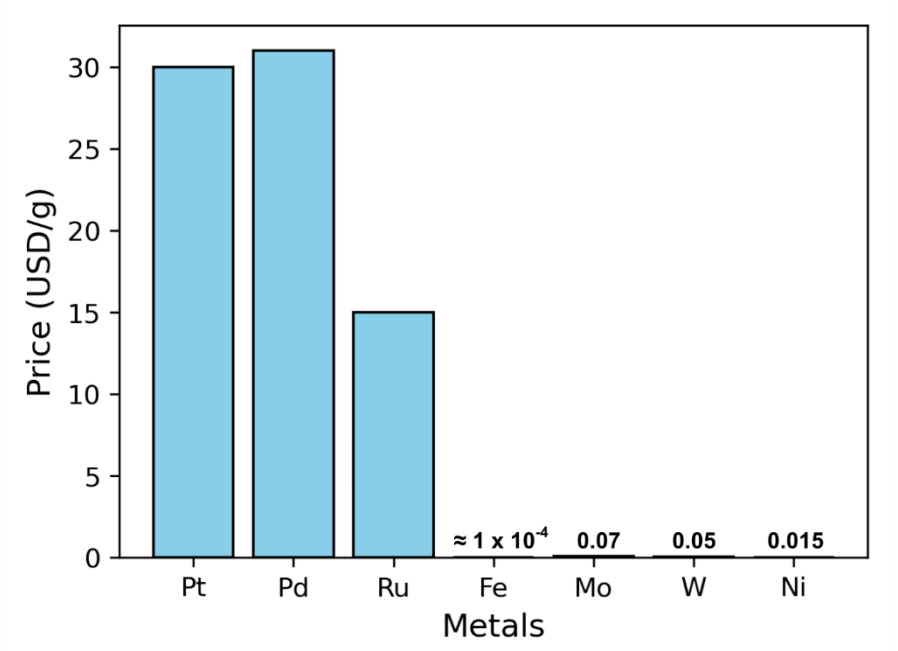

Figure 1.13 Market prices of precious and base metals in USD/g. Data sourced from reference 144.

1.6 Benzaldehyde as model organic molecule for ECH studies

As discussed in the previous section, electrocatalytic hydrogenation studies are usually performed on model organic compounds that are representative of biomass fractions. Notably, lignin-derived organics are particularly important, as this fraction of LCB is often treated as waste, and its valorisation remains limited. Among the different possible diagnostic compounds for lignin-derivatives, benzaldehyde (BZH) emerges as one of the most studied. Benzaldehyde and substituted BZH are commonly found in the pyrolysis of lignin,[145-148] and are key examples of biomass-derived aromatic aldehydes.[149] The widespread popularity of BZH lies in its high water solubility,[150] moderate reactivity,[151] and low toxicity[152] compared to other organic compounds, making it the focus of numerous studies recently published yielding promising results.[153-155] The high reactivity of the carbonyl group in BZH, compared to other analogous compounds like aliphatic aldehydes, arises from the molecule's aromaticity,[151] while the substituent group also influences the adsorption strength on the catalyst surface. This explains why BZH exhibits different reactivity from that of other aromatic diagnostic compounds such as phenol or benzene.[15] Although benzaldehyde is planar in its equilibrium geometry,[156] its adsorption on an electrocatalyst surface can occur in either a coplanar or distorted mode, depending on factors such as the metal type, surface charge, and the presence of a solvent. As suggested by Yuk et al., coplanar adsorption is typical on Pt and charged Pd, whereas distorted adsorption occurs on neutral Pd.[157] This difference in adsorption plays a crucial role in determining the effectiveness of the hydrogenation reaction. Rasmussen et al. also proposed that BZH can adsorb via the aromatic ring when arranged in dimer-packed structures facilitated by interactions between carbonyl groups.[158] Despite the nature of BZH adsorption remains debated in the literature, the prevailing hypothesis is that the interaction with the carbonyl group is stronger than with the aromatic ring for most metals, leading to adsorption that positions the carbonyl closer to the surface. As a result, the hydrogenation of BZH does not lead to ring saturation, unlike what occurs with phenol.[159] The electrocatalytic hydrogenation of benzaldehyde to benzyl alcohol (BA) proceeds via a two-step hydrogenation process, through α-hydroxybenzyl radical (ketyl intermediate). This intermediate may also undergo dimerization via pinacolic reaction, producing hydrobenzoin (HBZ) as side product. The two reactions are always in competition and the proposed concerted mechanism is illustrated in **Figure 1.14**.[98,160] Both products are of significant interest: benzyl alcohol is the most important aromatic

alcohol from a commercial perspective and a high value commodity for its applications across industries such as petrochemicals, coatings, plastics, cosmetics, and food;[161,162] while hydrobenzoin is a high-value compound with applications in the pharmaceutical industry.[149,163]

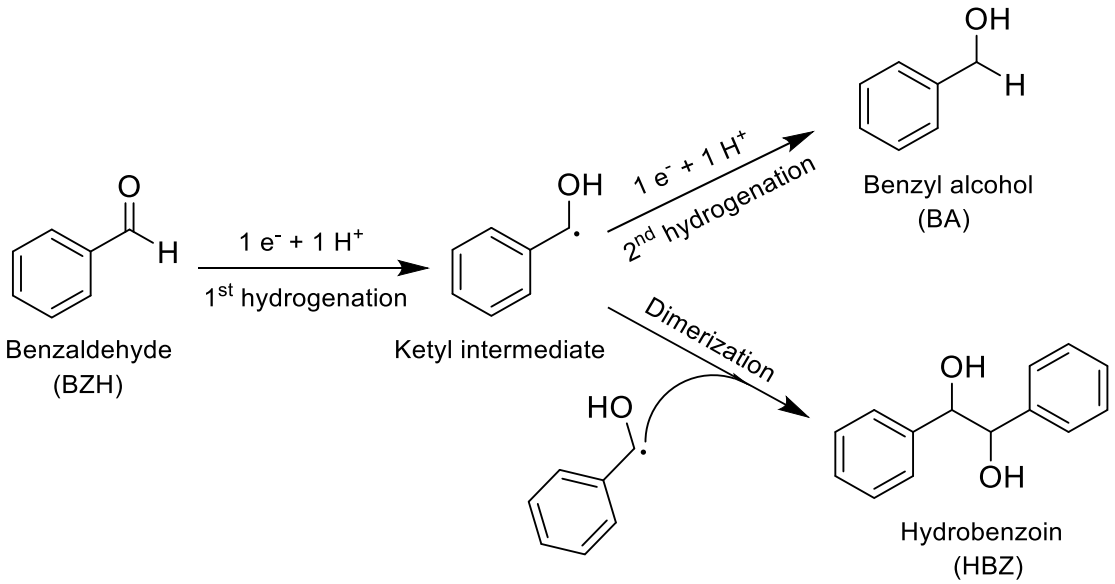

Figure 1.14 Proposed concerted mechanism of benzaldehyde hydrogenation from reference 98,160.

Mechanistically, when BZH is near to the electrode surface it may undergo either reduction or protonation. Then, although the overall ECH is a two-proton–two-electron process, it can also proceed through subsequential multi-step proton/electron competing additions, as proposed by Cantu et al.[79]. At high cathodic overpotentials where HER competition is more significant, proton-coupled reduction without H_{ads} formation (as in an Eley-Rideal type mechanism) could become an energetically favourable pathway.

Indeed, when evaluating the performance of electrocatalysts for BZH hydrogenation, it is essential to account for the competition between the HER and ECH. A variety of base metals (i.e. Cu, Ni, Zn, Co), and platinum group metals (i.e. Pd, Rh, Cu) have been investigated in this sense, combining theoretical and experimental methods.[99] **Figure 1.15** provides volcano plots generated by combination of density functional theory (DFT) calculations used to estimate the binding energies of BZH and H_2 on the metals, and experimentally measured TOF. Pd shows an optimal binding energy for BZH, which in line with the Sabatier principle places it at the peak of the volcano plot, indicating high activity and selectivity for ECH over HER (**Figure 1.15a**).[99] On the other hand, BZH

binds weakly on Cu but strongly on Ru and as a result, they showed the same ECH activity despite being at the opposite sides of the ECH volcano plot; other metals such as Zn, Rh and Co exhibit negligible ECH rates. Notably, Pt-based electrocatalysts displays higher selectivity for BA, while low-cost metals favoured dimerization process.[98,99] For HER, precious metals are more active while base metals displays poorer activity due to relatively weak or strong interactions with H_2 (**Figure 1.15b**).[99]

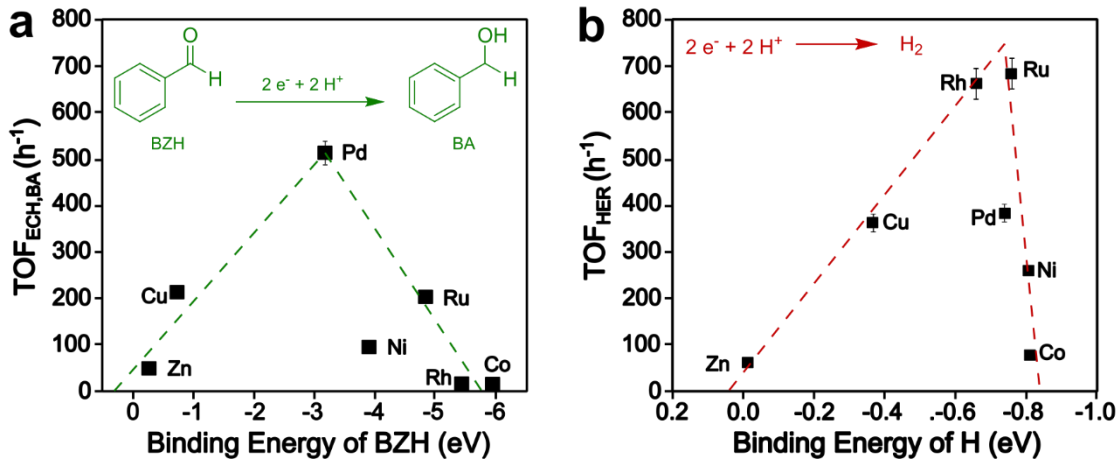

Figure 1.15 (a) Volcano plot generated for (a) ECH of benzaldehyde to benzyl alcohol, and for (b) HER in the presence of benzaldehyde. Data adapted from reference 99.

As reported by Song et al. the hydrogenation of BZH has been tested on carbon-supported metals with results aligned to those coming from computational studies discussed above.[90] In particular selectivity towards ECH increases in the order Ni/C < Pt/C < Rh/C < Pd/C, with Pd/C reaching TOF values of 3899 h^{-1} and FE above 90% at *ca.* -0.6 V vs RHE. Conversely, Rh/C and Pt/C show lower TOF of *ca.*2000 h^{-1} at the same tested potential. For Rh/C, FE remained constant at around 65%, while for Pt/C it decreased from 68% to 39% as the potential became more cathodic suggesting a higher HER contribution compared to ECH. Other studies have also reported Cu/C as an effective electrocatalyst for the ECH of benzaldehyde under conditions similar to those identified by Song. For Cu/C, TOF values of *ca.*3000 h^{-1} were observed for BZH in the presence of phenol, while FE exceeded 90% at -0.5 V vs. RHE in only BZH solution.[164,165]

The choice of metal to be used as ECH electrocatalyst is then critical. The ideal metal should exhibit activity for the HER, but not to the extent that it entirely suppresses the ECH. The balancing between these two competitive reactions is the key for the design of new innovative, low-cost and efficient ECH electrocatalysts.

1.7 Aim of this thesis

The electrocatalytic hydrogenation of oxygenated organic molecules obtained from biomass represent nowadays a promising sustainable approach for circular economy purposes. Its cost-effectiveness, combined with the use of renewable energy sources, offers an attractive alternative to conventional carbon-intensive methods for producing high-value products like fuels and chemicals. However, widespread adoption of ECH will require the development of innovative electrocatalysts based on non-critical metals, offering performances levels comparable to those of precious of Pt-group electrode materials.

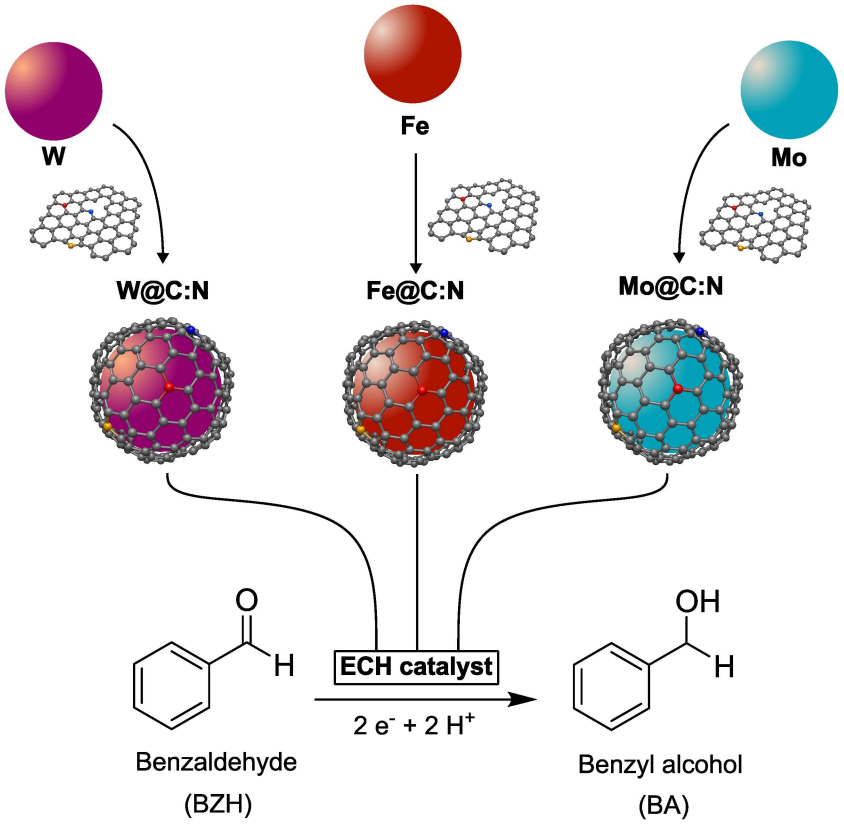

Figure 1.16 Graphical representation of the aims of this thesis.

The aim of this thesis is to explore the synthesis and performance of M@C:N architectures as viable alternative catalyst materials for the electrocatalytic hydrogenation, using benzaldehyde as diagnostic unsaturated substrate representative of oxygenated organics commonly found in bio-oil. Three low-cost metals, i.e. molybdenum (Mo), iron (Fe), and tungsten (W) were selected, based on their good activity toward

HER, as core metals to be encapsulated into M@C:N structures (**Figure 1.16**). This thesis also aims to contribute to the development and optimisation of methods for the fabrication of stable porous based electrocatalyst on different conductive supports tailored for different operational conditions.

Chapter 2 introduces the characterisation methods and their theoretical background employed for study of the prepared materials. Chapter 3 focuses on optimising catalyst preparation using Fe as the metal core in the M@C:N architecture, providing comprehensive material characterisation along with preliminary electrochemical studies. Chapter 4 examines the stabilisation of ink dispersion on a large conductive support, along by quantitative analysis and performance evaluation. Chapter 5 explores the role of metal core concentration in M@C:N structures, specifically considering Mo and W, and presents their structural and electrochemical analysis. Chapter 6 investigates the effect of different metal cores at equal concentrations on the composition and ECH performance of electrocatalysts based on W and Mo. A comprehensive comparison of Fe, Mo, and W, based primarily on TOF values, is also presented. Finally, Chapter 7 outlines the conclusions and future research directions arising from this thesis.

The results of this research have been communicated to the scientific community through peer-review articles in well-recognised journals and through international conference presentations.

1.8 Objectives of the thesis

This thesis seeks to address the challenges associated with the development of non-precious metal electrocatalysts for electrocatalytic hydrogenation (ECH) by pursuing the following specific objectives:

- To synthesise M@C:N electrocatalyst structures incorporating three non-critical metals Fe, Mo, and W, and to evaluate their suitability for the ECH of oxygenated organic substrates such as benzaldehyde.
- To optimise the preparation and structural tuning of Fe-based M@C:N materials and investigate their physicochemical and electrochemical properties.

- To investigate the dispersion and stabilisation of catalyst inks on large-area conductive supports, with a focus on practical deployment.
- To assess the influence of core metal concentration (particularly for Mo and W) on the structure–performance relationship of the catalysts.
- To compare the electrocatalytic performance of Fe-, Mo-, and W-based catalysts, including activity benchmarks such as turnover frequency (TOF), under comparable operating conditions.
- To develop and refine characterisation methodologies aimed at understanding the composition–function relationship within M@C:N structures.

1.9 References

1. Copernicus. *Copernicus Global Climate Highlights Report 2024*;**2025**.

2. Budget, G. C. *Global Carbon Budget 2023*;**2023**.

3. Agreement, P. Paris agreement. In *report of the conference of the parties to the United Nations framework convention on climate change (21st session,2015: Paris). Retrived December*,2015; HeinOnline: Vol.4, p 2.

4. EPA. *Inventory of U.S. Greenhouse Gas Emissions and Sinks:1990-2022 U.S. Environmental Protection Agency, EPA 430R-24004.*;**2024**.

5. EI. *Statistical Review of World Energy 2024*;**2024**.

6. IEA. *World Energy Investment 2023*;**2023**.

7. IRENA. *Renewable power generation costs in 2023*;**2024**.

8. Bioenergy, I. *IEA Bioenergy Annual Report 2023*;**2023**.

9. commision, E. *Union Bioenergy Sustainability Report*;**2024**.

10. Takkellapati, S.; Li, T.; Gonzalez, M. A. An overview of biorefinery-derived platform chemicals from a cellulose and hemicellulose biorefinery. *Clean Technologies and Environmental Policy* **2018**,*20* (7),1615-1630.

11. Joshi, N. C.; Sinha, S.; Bhatnagar, P.; Nath, Y.; Negi, B.; Kumar, V.; Gururani, P. A concise review on waste biomass valorization through thermochemical conversion. *Current Research in Microbial Sciences* **2024**,*6*,100237.

12. Joshi, M.; Manjare, S. Chemical approaches for the biomass valorisation: a comprehensive review of pretreatment strategies. *Environmental Science and Pollution Research* **2024**,*31* (36),48928-48954.

13. Brethauer, S.; Shahab, R. L.; Studer, M. H. Impacts of biofilms on the conversion of cellulose. *Applied Microbiology and Biotechnology* **2020**,*104* (12),5201-5212.

14. Schmitt, U.; Koch, G.; Lehnen, R. Wood. In *Ullmann's Encyclopedia of Industrial Chemistry*, pp 1-18.

15. Wijaya, Y. P.; Smith, K. J.; Kim, C. S.; Gyenge, E. L. Electrocatalytic hydrogenation and depolymerization pathways for lignin valorization: toward mild synthesis of chemicals and fuels from biomass. *Green Chemistry* **2020**,*22* (21),7233-7264,10.1039/D0GC02782K.

16. Taverna, M. E.; Felissia, F.; Area, M. C.; Estenoz, D. A.; Nicolau, V. V. Hydroxymethylation of technical lignins from South American sources with potential use in phenolic resins. *Journal of Applied Polymer Science* **2019**,*136* (26),47712.

17. Commision, E. T. *Mind the Gap: How Carbon Dioxide Removals Must Complement Deep Decarbonisation to Keep 1.5°C Alive*;**2022**.

18. Hu, M.; Chen, J.; Yu, Y.; Liu, Y. Peroxyacetic Acid Pretreatment: A Potentially Promising Strategy towards Lignocellulose Biorefinery. *Molecules* **2022**,*27* (19),6359.

19. Erfani Jazi, M.; Narayanan, G.; Aghabozorgi, F.; Farajidizaji, B.; Aghaei, A.; Kamyabi, M. A.; Navarathna, C. M.; Mlsna, T. E. Structure, chemistry and physicochemistry of lignin for material functionalization. *SN Applied Sciences* **2019**,*1* (9),1094.

20. Wang, Y.; Zhang, Y.; Cui, Q.; Feng, Y.; Xuan, J. Composition of Lignocellulose Hydrolysate in Different Biorefinery Strategies: Nutrients and Inhibitors. *Molecules* **2024**,*29* (10),2275.

21. Zhang, Q.; Chang, J.; Wang, T.; Xu, Y. Review of biomass pyrolysis oil properties and upgrading research. *Energy Conversion and Management* **2007**,*48* (1),87-92.

22. Xiu, S.; Shahbazi, A. Bio-oil production and upgrading research: A review. *Renewable and Sustainable Energy Reviews* **2012**,*16* (7),4406-4414.

23. Basu, P. Chapter 9 - Production of Synthetic Fuels and Chemicals from Biomass. In *Biomass Gasification and Pyrolysis*, Basu, P. Ed.; Academic Press,2010; pp 301-323.

24. Mortensen, P. M.; Grunwaldt, J.-D.; Jensen, P. A.; Knudsen, K.; Jensen, A. D. A review of catalytic upgrading of bio-oil to engine fuels. *Applied Catalysis A: General* **2011**,*407* (1-2),1-19.

25. Ruddy, D. A.; Schaidle, J. A.; Ferrell III, J. R.; Wang, J.; Moens, L.; Hensley, J. E. Recent advances in heterogeneous catalysts for bio-oil upgrading via “ex situ catalytic fast pyrolysis”: catalyst development through the study of model compounds. *Green Chemistry* **2014**,*16* (2),454-490.

26. Seidl, P. R.; Goulart, A. K. Pretreatment processes for lignocellulosic biomass conversion to biofuels and bioproducts. *Current Opinion in Green and Sustainable Chemistry* **2016**,*2*,48-53.

27. Li, C.; Zhao, X.; Wang, A.; Huber, G. W.; Zhang, T. Catalytic Transformation of Lignin for the Production of Chemicals and Fuels. *Chemical Reviews* **2015**,*115* (21),11559-11624.

28. Sergeev, A. G.; Hartwig, J. F. Selective, nickel-catalyzed hydrogenolysis of aryl ethers. *Science* **2011**,*332* (6028),439-443.

29. Zhang, L.; Rao, T. U.; Wang, J.; Ren, D.; Sirisommboonchai, S.; Choi, C.; Machida, H.; Huo, Z.; Norinaga, K. A review of thermal catalytic and electrochemical hydrogenation approaches for converting biomass-derived compounds to high-value chemicals and fuels. *Fuel Processing Technology* **2022**,*226*,107097.

30. Tuan Hoang, A.; Viet Pham, V.2-Methylfuran (MF) as a potential biofuel: A thorough review on the production pathway from biomass, combustion progress, and application in engines. *Renewable and Sustainable Energy Reviews* **2021**,*148*,111265.

31. Akhade, S. A.; Singh, N.; Gutiérrez, O. Y.; Lopez-Ruiz, J.; Wang, H.; Holladay, J. D.; Liu, Y.; Karkamkar, A.; Weber, R. S.; Padmaperuma, A. B.; et al. Electrocatalytic Hydrogenation of Biomass-Derived Organics: A Review. *Chemical Reviews* **2020**,*120* (20),11370-11419.

32. Liu, Y.; Luo, C.; Liu, H. Tungsten Trioxide Promoted Selective Conversion of Cellulose into Propylene Glycol and Ethylene Glycol on a Ruthenium Catalyst. *Angewandte Chemie International Edition* **2012**,*51* (13),3249-3253.

33. Wang, J.; Yao, G.; Wang, Y.; Zhang, H.; Huo, Z.; Jin, F. A novel Pd/C-catalyzed conversion of glucose to 1,2-propanediol by water splitting with Zn. *RSC Advances* **2015**,*5* (63),51435-51439,10.1039/C5RA08482B.

34. Luo, J.; Arroyo-Ramírez, L.; Wei, J.; Yun, H.; Murray, C. B.; Gorte, R. J. Comparison of HMF hydrodeoxygenation over different metal catalysts in a continuous flow reactor. *Applied Catalysis A: General* **2015**,*508*,86-93.

35. Sitthisa, S.; Resasco, D. E. Hydrodeoxygenation of Furfural Over Supported Metal Catalysts: A Comparative Study of Cu, Pd and Ni. *Catalysis Letters* **2011**,*141* (6),784-791.

36. Ogden, J. M. Prospects for building a hydrogen energy infrastructure. *Annual review of energy and the environment* **1999**,*24* (1),227-279.

37. Amouzegar, K.; Savadogo, O. Electrocatalytic hydrogenation of phenol on dispersed Pt: reaction mechanism and support effect. *Electrochimica Acta* **1998**,*43* (5),503-508.

38. Chen, G. Electrochemical technologies in wastewater treatment. *Separation and Purification Technology* **2004**,*38* (1),11-41.

39. Jüttner, K.; Galla, U.; Schmieder, H. Electrochemical approaches to environmental problems in the process industry. *Electrochimica Acta* **2000**,*45* (15),2575-2594.

40. Upton, B. M.; Kasko, A. M. Strategies for the Conversion of Lignin to High-Value Polymeric Materials: Review and Perspective. *Chemical Reviews* **2016**,*116* (4),2275-2306.

41. Lam, C. H.; Lowe, C. B.; Li, Z.; Longe, K. N.; Rayburn, J. T.; Caldwell, M. A.; Houdek, C. E.; Maguire, J. B.; Saffron, C. M.; Miller, D. J.; et al. Electrocatalytic upgrading of model lignin monomers with earth abundant metal electrodes. *Green Chemistry* **2015**,*17* (1),601-609,10.1039/C4GC01632G.

42. Zhao, B.; Guo, Q.; Fu, Y. Electrocatalytic Hydrogenation of Lignin-Derived Phenol into Alkanes by Using Platinum Supported on Graphite. *Electrochemistry* **2014**,*82* (11),954-959.

43. Zhao, C.; He, J.; Lemonidou, A. A.; Li, X.; Lercher, J. A. Aqueous-phase hydrodeoxygenation of bio-derived phenols to cycloalkanes. *Journal of Catalysis* **2011**,*280* (1),8-16.

44. Elliott, D. C.; Hart, T. R. Catalytic Hydroprocessing of Chemical Models for Bio-oil. *Energy & Fuels* **2009**,*23* (2),631-637.

45. Lee, C. R.; Yoon, J. S.; Suh, Y.-W.; Choi, J.-W.; Ha, J.-M.; Suh, D. J.; Park, Y.-K. Catalytic roles of metals and supports on hydrodeoxygenation of lignin monomer guaiacol. *Catalysis Communications* **2012**,*17*,54-58.

46. Wan, H.; Chaudhari, R. V.; Subramaniam, B. Aqueous Phase Hydrogenation of Acetic Acid and Its Promotional Effect on p-Cresol Hydrodeoxygenation. *Energy & Fuels* **2013**,*27* (1),487-493.

47. Do, P. T. M.; Foster, A. J.; Chen, J.; Lobo, R. F. Bimetallic effects in the hydrodeoxygenation of meta-cresol on γ-Al2O3 supported Pt–Ni and Pt–Co catalysts. *Green Chemistry* **2012**,*14* (5),1388-1397,10.1039/C2GC16544A.

48. Lessard, J. Electrocatalytic Hydrogenation. In *Encyclopedia of Applied Electrochemistry*, Kreysa, G., Ota, K.-i., Savinell, R. F. Eds.; Springer New York,2014; pp 443-448.

49. Li, Z.; Garedew, M.; Lam, C. H.; Jackson, J. E.; Miller, D. J.; Saffron, C. M. Mild electrocatalytic hydrogenation and hydrodeoxygenation of bio-oil derived phenolic compounds using ruthenium supported on activated carbon cloth. *Green Chemistry* **2012**,*14* (9),2540-2549,10.1039/C2GC35552C.

50. Weber, R. S. Effective Use of Renewable Electricity for Making Renewable Fuels and Chemicals. *ACS Catalysis* **2019**,*9* (2),946-950.

51. Deng, W.; Xu, K.; Xiong, Z.; Chaiwat, W.; Wang, X.; Su, S.; Hu, S.; Qiu, J.; Wang, Y.; Xiang, J. Evolution of Aromatic Structures during the Low-Temperature Electrochemical Upgrading of Bio-oil. *Energy & Fuels* **2019**,*33* (11),11292-11301.

52. Lam, C. H.; Deng, W.; Lang, L.; Jin, X.; Hu, X.; Wang, Y. Minireview on Bio-Oil Upgrading via Electrocatalytic Hydrogenation: Connecting Biofuel Production with Renewable Power. *Energy & Fuels* **2020**,*34* (7),7915-7928.

53. Commission, E.; Directorate-General for Internal Market, I., Entrepreneurship; SMEs; Grohol, M.; Veeh, C. *Study on the critical raw materials for the EU 2023 – Final report*; Publications Office of the European Union,**2023**.

54. Bard, A. J.; Faulkner, L. R.; White, H. S. *Electrochemical methods: fundamentals and applications*; John Wiley & Sons,**2022**.

55. Compton, R. G.; Banks, C. E. *Understanding voltammetry*; World Scientific,**2018**.

56. Kendall, K.; Kendall, M. *High-temperature solid oxide fuel cells for the 21st century: fundamentals, design and applications*; Elsevier,**2015**.

57. Ooka, H.; Huang, J.; Exner, K. S. The Sabatier Principle in Electrocatalysis: Basics, Limitations, and Extensions. *Frontiers in Energy Research* **2021**,*9*, Review.

58. Zhao, G.; Rui, K.; Dou, S. X.; Sun, W. Heterostructures for Electrochemical Hydrogen Evolution Reaction: A Review. *Advanced Functional Materials* **2018**,*28* (43),1803291.

59. Conway, B.; Tilak, B. Interfacial processes involving electrocatalytic evolution and oxidation of H2, and the role of chemisorbed H. *Electrochimica acta* **2002**,*47* (22-23),3571-3594.

60. Kucernak, A. R.; Zalitis, C. General models for the electrochemical hydrogen oxidation and hydrogen evolution reactions: theoretical derivation and experimental results under near mass-transport free conditions. *The Journal of Physical Chemistry C* **2016**,*120* (20),10721-10745.

61. Marković, N. M.; Grgur, B. N.; Ross, P. N. Temperature-Dependent Hydrogen Electrochemistry on Platinum Low-Index Single-Crystal Surfaces in Acid Solutions. *The Journal of Physical Chemistry B* **1997**,*101* (27),5405-5413.

62. Li, Y.; Wang, H.; Xie, L.; Liang, Y.; Hong, G.; Dai, H. MoS2 nanoparticles grown on graphene: an advanced catalyst for the hydrogen evolution reaction. *Journal of the American Chemical Society* **2011**,*133* (19),7296-7299.

63. Xue, S.; Haid, R. W.; Kluge, R. M.; Ding, X.; Garlyyev, B.; Fichtner, J.; Watzele, S.; Hou, S.; Bandarenka, A. S. Enhancing the hydrogen evolution reaction activity of platinum electrodes in alkaline media using nickel–iron clusters. *Angewandte Chemie International Edition* **2020**,*59* (27),10934-10938.

64. Hamann, C.; Vielstich, W. Electrochemistry 2.[Book in German]. Elektrochemie 2. Elektrodenprozesse, Angewandte Elektrochemie.**1981**.

65. Ďurovič, M.; Hnát, J.; Bouzek, K. Electrocatalysts for the hydrogen evolution reaction in alkaline and neutral media. A comparative review. *Journal of Power Sources* **2021**,*493*,229708.

66. Quaino, P.; Juarez, F.; Santos, E.; Schmickler, W. Volcano plots in hydrogen electrocatalysis–uses and abuses. *Beilstein journal of nanotechnology* **2014**,*5* (1),846-854.

67. Short, G. D.; Bishop, E. Concentration Overpotentials on Antimony Electrodes in Differential Electrolytic Potentiometry. *Analytical Chemistry* **1965**,*37* (8),962-967.

68. Li, C.; Baek, J.-B. Recent Advances in Noble Metal (Pt, Ru, and Ir)-Based Electrocatalysts for Efficient Hydrogen Evolution Reaction. *ACS Omega* **2020**,*5* (1),31-40.

69. Jiang, B.; Liu, S.; Cheng, L.; Zhou, L.; Cui, H.; Liu, M.; Wen, M.; Wang, C.; Wang, W.; Li, S.; et al. Mass synthesis of Pt/C catalysts with high Pt loading for low-overpotential hydrogen evolution. *International Journal of Hydrogen Energy* **2024**,*58*,268-278.

70. Huang, X.; Zhao, Y.; Ao, Z.; Wang, G. Micelle-Template Synthesis of Nitrogen-Doped Mesoporous Graphene as an Efficient Metal-Free Electrocatalyst for Hydrogen Production. *Scientific Reports* **2014**,*4* (1),7557.

71. Hussain, S.; Vikraman, D.; Feroze, A.; Song, W.; An, K.-S.; Kim, H.-S.; Chun, S.-H.; Jung, J. Synthesis of Mo2C and W2C Nanoparticle Electrocatalysts for the Efficient

Hydrogen Evolution Reaction in Alkali and Acid Electrolytes. *Frontiers in Chemistry* **2019**,*7*, Original Research.

72. Fan, X.; Peng, Z.; Ye, R.; Zhou, H.; Guo, X. M3C (M: Fe, Co, Ni) Nanocrystals Encased in Graphene Nanoribbons: An Active and Stable Bifunctional Electrocatalyst for Oxygen Reduction and Hydrogen Evolution Reactions. *ACS Nano* **2015**,*9* (7),7407-7418.

73. Kibsgaard, J.; Jaramillo, T. F. Molybdenum phosphosulfide: an active, acid-stable, earth-abundant catalyst for the hydrogen evolution reaction. *Angewandte Chemie International Edition* **2014**,*53* (52),14433-14437.

74. Hua, W.; Sun, H.-H.; Xu, F.; Wang, J.-G. A review and perspective on molybdenum-based electrocatalysts for hydrogen evolution reaction. *Rare Metals* **2020**,*39*,335-351.

75. Zheng, Y.; Jiao, Y.; Li, L. H.; Xing, T.; Chen, Y.; Jaroniec, M.; Qiao, S. Z. Toward Design of Synergistically Active Carbon-Based Catalysts for Electrocatalytic Hydrogen Evolution. *ACS Nano* **2014**,*8* (5),5290-5296.

76. Zhou, W.; Jia, J.; Lu, J.; Yang, L.; Hou, D.; Li, G.; Chen, S. Recent developments of carbon-based electrocatalysts for hydrogen evolution reaction. *Nano Energy* **2016**,*28*,29-43.

77. Jiang, H.; Gu, J.; Zheng, X.; Liu, M.; Qiu, X.; Wang, L.; Li, W.; Chen, Z.; Ji, X.; Li, J. Defect-rich and ultrathin N doped carbon nanosheets as advanced trifunctional metal-free electrocatalysts for the ORR, OER and HER. *Energy & Environmental Science* **2019**,*12* (1),322-333,10.1039/C8EE03276A.

78. Deng, J.; Ren, P.; Deng, D.; Bao, X. Enhanced Electron Penetration through an Ultrathin Graphene Layer for Highly Efficient Catalysis of the Hydrogen Evolution Reaction. *Angewandte Chemie International Edition* **2015**,*54* (7),2100-2104.

79. Cantu, D. C.; Padmaperuma, A. B.; Nguyen, M.-T.; Akhade, S. A.; Yoon, Y.; Wang, Y.-G.; Lee, M.-S.; Glezakou, V.-A.; Rousseau, R.; Lilga, M. A. A Combined Experimental and Theoretical Study on the Activity and Selectivity of the Electrocatalytic Hydrogenation of Aldehydes. *ACS Catalysis* **2018**,*8* (8),7645-7658.

80. zhao, B.; Chen, M.; Guo, Q.; Fu, Y. Electrocatalytic hydrogenation of furfural to furfuryl alcohol using platinum supported on activated carbon fibers. *Electrochimica Acta* **2014**,*135*,139-146.

81. Pota, F.; Costa de Oliveira, M. A.; Schröder, C.; Brunet Cabré, M.; Nolan, H.; Rafferty, A.; Jeannin, O.; Camerel, F.; Behan, J. A.; Barrière, F.; et al. Porous N-Doped Carbon-encapsulated Iron as Novel Catalyst Architecture for the Electrocatalytic Hydrogenation of Benzaldehyde. *ChemSusChem* **2025**,*18* (1), e202400546.

82. Wakisaka, M.; Kunitake, M. Direct electrochemical hydrogenation of toluene at Pt electrodes in a microemulsion electrolyte solution. *Electrochemistry Communications* **2016**,*64*,5-8.

83. Huang, H.; Yu, Y.; Chung, K. H. Performance of Au/Nafion/Pt electrodes in benzene–water electrochemical hydrogenation. *International journal of hydrogen energy* **2014**,*39* (25),13832-13837.

84. Huang, S.; Wu, X.; Chen, W.; Wang, T.; Wu, Y.; He, G. A bilateral electrochemical hydrogen pump reactor for 2-propanol dehydrogenation and phenol hydrogenation. *Green Chemistry* **2016**,*18* (8),2353-2362.

85. Fichter, F.; Stocker, R. Die elektrochemische Oxydation aromatischer Kohlenwasserstoffe und Phenole. *Berichte der deutschen chemischen Gesellschaft* **1914**,*47* (2),2003-2019.

86. Miller, L. L.; Christensen, L. Electrocatalytic hydrogenation of aromatic compounds. *The Journal of Organic Chemistry* **1978**,*43* (10),2059-2061.

87. Sasaki, K.; Kunai, A.; Harada, J.; Nakabori, S. Electrolytic hydrogenation of phenols in aqueous acid solutions. *Electrochimica Acta* **1983**,*28* (5),671-674.

88. Coche, L.; Moutet, J. C. Electrocatalytic hydrogenation of organic compounds on carbon electrodes modified by precious metal microparticles in redox active polymer films. *Journal of the American Chemical Society* **1987**,*109* (22),6887-6889.

89. Cirtiu, C. M.; Hassani, H. O.; Bouchard, N.-A.; Rowntree, P. A.; Ménard, H. Modification of the surface adsorption properties of alumina-supported Pd catalysts for the electrocatalytic hydrogenation of phenol. *Langmuir* **2006**,*22* (14),6414-6421.

90. Song, Y.; Sanyal, U.; Pangotra, D.; Holladay, J. D.; Camaioni, D. M.; Gutiérrez, O. Y.; Lercher, J. A. Hydrogenation of benzaldehyde via electrocatalysis and thermal catalysis on carbon-supported metals. *Journal of Catalysis* **2018**,*359*,68-75.

91. Sáez, A.; García-García, V.; Solla-Gullón, J.; Aldaz, A.; Montiel, V. Electrocatalytic hydrogenation of acetophenone using a Polymer Electrolyte Membrane Electrochemical Reactor. *Electrochimica Acta* **2013**,*91*,69-74.

92. Chiba, T.; Okimoto, M.; Nagai, H.; Takata, Y. Electrocatalytic reduction using Raney nickel. *Bulletin of the Chemical Society of Japan* **1983**,*56* (3),719-723.

93. Yamada, T.; Osa, T.; Matsue, T. Hydrogenation of benzene ring by paired electrosynthesis with Raney-nickel cathode. *Chemistry Letters* **1987**,*16* (10),1989-1992.

94. Matsue, T.; Yamada, T.; Takahashi, H.; Osa, T. Catalytic and electrocatalytic hydrogenation of benzylideneazlactone and benzylidenehydantoin. *Bulletin of the Chemical Society of Japan* **1986**,*59* (11),3690-3692.

95. Ivanova, N. M.; Soboleva, E. A.; Kulakova, E. V.; Malyshev, V. P.; Kirilyus, I. V. Reduction of nitrophenols in an electrocatalytic system. *Russian Journal of Applied Chemistry* **2009**,*82* (3),421-428.

96. Belot, G.; Desjardins, S.; Lessard, J. Electrocatalytic hydrogenation of organic compounds on Devarda copper and Raney nickel electrodes in basic media. *Tetrahedron Letters* **1984**,*25* (47),5347-5350.

97. Dabo, P.; Mahdavi, B.; Ménard, H.; Lessard, J. Selective electrocatalytic hydrogenation of 2-cyclohexen-1-one to cyclohexanone. *Electrochimica Acta* **1997**,*42* (9),1457-1459.

98. Andrews, E.; Lopez-Ruiz, J. A.; Egbert, J. D.; Koh, K.; Sanyal, U.; Song, M.; Li, D.; Karkamkar, A. J.; Derewinski, M. A.; Holladay, J.; et al. Performance of Base and Noble Metals for Electrocatalytic Hydrogenation of Bio-Oil-Derived Oxygenated Compounds. *ACS Sustainable Chemistry & Engineering* **2020**,*8* (11),4407-4418.

99. Lopez-Ruiz, J. A.; Andrews, E.; Akhade, S. A.; Lee, M.-S.; Koh, K.; Sanyal, U.; Yuk, S. F.; Karkamkar, A. J.; Derewinski, M. A.; Holladay, J.; et al. Understanding the Role of Metal and Molecular Structure on the Electrocatalytic Hydrogenation of Oxygenated Organic Compounds. *ACS Catalysis* **2019**,*9* (11),9964-9972.

100. Kwon, Y.; Koper, M. T. M. Electrocatalytic Hydrogenation and Deoxygenation of Glucose on Solid Metal Electrodes. *ChemSusChem* **2013**,*6* (3),455-462.

101. Nilges, P.; Schröder, U. Electrochemistry for biofuel generation: production of furans by electrocatalytic hydrogenation of furfurals. *Energy & Environmental Science* **2013**,*6* (10),2925-2931,10.1039/C3EE41857J.

102. Lofrano, R. C. Z.; Madurro, J. M.; Abrantes, L. M.; Romero, J. R. Electrocatalytic hydrogenation of carbonylic compounds using an electrode with platinum particles dispersed in films of poly-[allyl ether p-(2-aminoethyl) phenol] co-polymerized with allyl phenyl ether. *Journal of Molecular Catalysis A: Chemical* **2004**,*218* (1),73-79.

103. Moutet, J.-C.; Ouennoughi, Y.; Ourari, A.; Hamar-Thibault, S. Electrocatalytic hydrogenation on noble metal particles dispersed in polymer films. Enhanced catalytic activity induced by the incorporation of bimetallic catalysts. *Electrochimica Acta* **1995**,*40* (12),1827-1833.

104. Amouzegar, K.; Savadogo, O. Electrocatalytic hydrogenation of phenol on highly dispersed Pt electrodes. *Electrochimica Acta* **1994**,*39* (4),557-559.

105. Koh, K.; Sanyal, U.; Lee, M.-S.; Cheng, G.; Song, M.; Glezakou, V.-A.; Liu, Y.; Li, D.; Rousseau, R.; Gutiérrez, O. Y.; et al. Electrochemically Tunable Proton-Coupled Electron Transfer in Pd-Catalyzed Benzaldehyde Hydrogenation. *Angewandte Chemie International Edition* **2020**,*59* (4),1501-1505.

106. Roylance, J. J.; Choi, K.-S. Electrochemical reductive biomass conversion: direct conversion of 5-hydroxymethylfurfural (HMF) to 2,5-hexanedione (HD) via reductive ring-opening. *Green Chemistry* **2016**,*18* (10),2956-2960,10.1039/C6GC00533K.

107. Dabo, P.; Cyr, A.; Lessard, J.; Brossard, L.; Ménard, H. Electrocatalytic hydrogenation of 4-phenoxyphenol on active powders highly dispersed in a reticulated vitreous carbon electrode. *Canadian Journal of Chemistry* **1999**,*77* (7),1225-1229.

108. Martel, A.; Mahdavi, B.; Lessard, J.; Ménard, H.; Brossard, L. Electrocatalytic hydrogenation of phenol on various electrode materials. *Canadian Journal of Chemistry* **1997**,*75* (12),1862-1867.

109. Song, Y.; Chia, S. H.; Sanyal, U.; Gutiérrez, O. Y.; Lercher, J. A. Integrated catalytic and electrocatalytic conversion of substituted phenols and diaryl ethers. *Journal of Catalysis* **2016**,*344*,263-272.

110. Sam, D. K.; Li, H.; Xu, Y.-T.; Cao, Y. Advances in porous carbon materials for a sustainable future: A review. *Advances in Colloid and Interface Science* **2024**,*333*,103279.

111. Sun, L.; Gong, Y.; Li, D.; Pan, C. Biomass-derived porous carbon materials: synthesis, designing, and applications for supercapacitors. *Green Chemistry* **2022**,*24* (10),3864-3894,10.1039/D2GC00099G.

112. Pal, N.; Bhaumik, A. Mesoporous materials: versatile supports in heterogeneous catalysis for liquid phase catalytic transformations. *RSC Advances* **2015**,*5* (31),24363-24391,10.1039/C4RA13077D.

113. Figueiredo, J. L. Functionalization of porous carbons for catalytic applications. *Journal of Materials Chemistry A* **2013**,*1* (33),9351-9364,10.1039/C3TA10876G.

114. Thommes, M.; Kaneko, K.; Neimark, A. V.; Olivier, J. P.; Rodriguez-Reinoso, F.; Rouquerol, J.; Sing, K. S. W. Physisorption of gases, with special reference to the evaluation of surface area and pore size distribution (IUPAC Technical Report). *Pure and Applied Chemistry* **2015**,*87* (9-10),1051-1069.

115. Benzigar, M. R.; Talapaneni, S. N.; Joseph, S.; Ramadass, K.; Singh, G.; Scaranto, J.; Ravon, U.; Al-Bahily, K.; Vinu, A. Recent advances in functionalized micro and mesoporous carbon materials: synthesis and applications. *Chemical Society Reviews* **2018**,*47* (8),2680-2721,10.1039/C7CS00787F.

116. Mehdipour-Ataei, S.; Aram, E. Mesoporous Carbon-Based Materials: A Review of Synthesis, Modification, and Applications. *Catalysts* **2023**,*13* (1),2.

117. Li, X.; Zhao, Y.; Yang, Y.; Gao, S. A universal strategy for carbon–based ORR–active electrocatalyst: One porogen, two pore–creating mechanisms, three pore types. *Nano Energy* **2019**,*62*,628-637.

118. Zhao, X. S.; Su, F.; Yan, Q.; Guo, W.; Bao, X. Y.; Lv, L.; Zhou, Z. Templating methods for preparation of porous structures. *Journal of Materials Chemistry* **2006**,*16* (7),637-648,10.1039/B513060C.

119. Javed, H.; Pani, S.; Antony, J.; Sakthivel, M.; Drillet, J.-F. Synthesis of mesoporous carbon spheres via a soft-template route for catalyst supports in PEMFC cathodes. *Soft Matter* **2021**,*17* (33),7743-7754,10.1039/D1SM00450F.

120. Chuenchom, L.; Kraehnert, R.; Smarsly, B. M. Recent progress in soft-templating of porous carbon materials. *Soft Matter* **2012**,*8* (42),10801-10812,10.1039/C2SM07448F.

121. Xin, W.; Song, Y. Mesoporous carbons: recent advances in synthesis and typical applications. *RSC Advances* **2015**,*5* (101),83239-83285,10.1039/C5RA16864C.

122. Li, J.; Jiang, Q.; Wei, L.; Zhong, L.; Wang, X. Simple and scalable synthesis of hierarchical porous carbon derived from cornstalk without pith for high capacitance and energy density. *Journal of Materials Chemistry A* **2020**,*8* (3),1469-1479,10.1039/C9TA07864A.

123. Liang, K.; Wang, W.; Yu, Y.; Liu, L.; Lv, H.; Zhang, Y.; Chen, A. Synthesis of nitrogen-doped mesoporous carbon for high-performance supercapacitors. *New Journal of Chemistry* **2019**,*43* (6),2776-2782,10.1039/C8NJ05938A.

124. Yu, J.; Guo, M.; Muhammad, F.; Wang, A.; Yu, G.; Ma, H.; Zhu, G. Simple fabrication of an ordered nitrogen-doped mesoporous carbon with resorcinol–melamine–formaldehyde resin. *Microporous and Mesoporous Materials* **2014**,*190*,117-127.

125. Wang, X.; Lee, J. S.; Zhu, Q.; Liu, J.; Wang, Y.; Dai, S. Ammonia-Treated Ordered Mesoporous Carbons as Catalytic Materials for Oxygen Reduction Reaction. *Chemistry of Materials* **2010**,*22* (7),2178-2180.

126. Hench, L. L.; West, J. K. The sol-gel process. *Chemical reviews* **1990**,*90* (1),33-72.

127. Pekala, R. W. Organic aerogels from the polycondensation of resorcinol with formaldehyde. *Journal of Materials Science* **1989**,*24* (9),3221-3227.

128. Alonso-Buenaposada, I. D.; Rey-Raap, N.; Calvo, E. G.; Menéndez, J. A.; Arenillas, A. Acid-based resorcinol-formaldehyde xerogels synthesized by microwave heating. *Journal of Sol-Gel Science and Technology* **2017**,*84* (1),60-69.

129. Merline, D. J.; Vukusic, S.; Abdala, A. A. Melamine formaldehyde: curing studies and reaction mechanism. *Polymer Journal* **2013**,*45* (4),413-419.

130. Li, J.; Han, K.; Wang, D.; Teng, Z.; Cao, Y.; Qi, J.; Li, M.; Wang, M. Fabrication of high performance structural N-doped hierarchical porous carbon for supercapacitors. *Carbon* **2020**,*164*,42-50.

131. Yoo, J. M.; Shin, H.; Chung, D. Y.; Sung, Y.-E. Carbon Shell on Active Nanocatalyst for Stable Electrocatalysis. *Accounts of Chemical Research* **2022**,*55* (9),1278-1289.

132. Zhang, H.; Ma, Z.; Duan, J.; Liu, H.; Liu, G.; Wang, T.; Chang, K.; Li, M.; Shi, L.; Meng, X.; et al. Active Sites Implanted Carbon Cages in Core–Shell Architecture: Highly Active and Durable Electrocatalyst for Hydrogen Evolution Reaction. *ACS Nano* **2016**,*10* (1),684-694.

133. Eiler, K.; Suriñach, S.; Sort, J.; Pellicer, E. Mesoporous Ni-rich Ni–Pt thin films: Electrodeposition, characterization and performance toward hydrogen evolution reaction in acidic media. *Applied Catalysis B: Environmental* **2020**,*265*,118597.

134. Nguyen, V.-T.; Lee, G.-J.; Ngo, Q.-T.; Omelianovych, O.; Nguyen, N.-A.; Trinh, V.-H.; Choi, H.-S.; Mnoyan, A.; Lee, K.; Larina, L. L.; et al. Robust carbon-encapsulated Ni nanoparticles as high-performance electrocatalysts for the hydrogen evolution reaction in highly acidic media. *Electrochimica Acta* **2021**,*398*,139332.

135. Wei, H.; Wang, J.; Lin, Q.; Zou, Y.; Chen, X. a.; Zhao, H.; Li, J.; Jin, H.; Lei, Y.; Wang, S. Incorporating ultra-small N-doped Mo2C nanoparticles onto 3D N-doped flower-like carbon nanospheres for robust electrocatalytic hydrogen evolution. *Nano Energy* **2021**,*86*,106047.

136. Tavakkoli, M.; Kallio, T.; Reynaud, O.; Nasibulin, A. G.; Johans, C.; Sainio, J.; Jiang, H.; Kauppinen, E. I.; Laasonen, K. Single-Shell Carbon-Encapsulated Iron

Nanoparticles: Synthesis and High Electrocatalytic Activity for Hydrogen Evolution Reaction. *Angewandte Chemie International Edition* **2015**,*54* (15),4535-4538.

137. Han, N.; Yang, K. R.; Lu, Z.; Li, Y.; Xu, W.; Gao, T.; Cai, Z.; Zhang, Y.; Batista, V. S.; Liu, W.; et al. Nitrogen-doped tungsten carbide nanoarray as an efficient bifunctional electrocatalyst for water splitting in acid. *Nature Communications* **2018**,*9* (1),924.

138. Peng, Y.; Chen, S. Electrocatalysts based on metal@carbon core@shell nanocomposites: An overview. *Green Energy & Environment* **2018**,*3* (4),335-351.

139. Hunter, R. D.; Ramírez-Rico, J.; Schnepp, Z. Iron-catalyzed graphitization for the synthesis of nanostructured graphitic carbons. *Journal of Materials Chemistry A* **2022**,*10* (9),4489-4516,10.1039/D1TA09654K.

140. Baker, R. T. K.; Chludzinski, J. J.; Dispenziere, N. C.; Murrell, L. L. Catalytic gasification of graphite by: Tungsten, rhenium, and tungsten-rhenium. *Carbon* **1983**,*21* (6),579-588.

141. Guo, H.; Song, Y.; Chen, P.; Lou, H.; Zheng, X. Effects of graphitization of carbon nanospheres on hydrodeoxygenation activity of molybdenum carbide. *Catalysis Science & Technology* **2018**,*8* (16),4199-4208,10.1039/C8CY01136B.

142. Choi, H.; Choi, Y.; Min, J.; Ko, K.; Kim, Y.; Chougule, S. S.; Khikmatulla, D.; Jung, N. Origin and Formation Mechanism of Carbon Shell-Encapsulated Metal Nanoparticles for Powerful Fuel Cell Durability. *Nanomaterials* **2023**,*13* (21),2862.

143. Min, J.; Kim, S.; Jeffery, A. A.; Shin, H.; Kang, Y. S.; Kim, Y.; Jang, J.; Lee, S.; Park, S.-H.; Park, G.-G.; et al. A paradigm shift in CO tolerant catalyst design for fuel cells via introducing defect-controlled carbon molecular sieve layers. *Materials Today Energy* **2022**,*29*,101124.

144. *Price of metals*.2024. https://www.dailymetalprice.com/ (accessed 2024 11/12/2024).

145. Vasiliou, A. K.; Kim, J. H.; Ormond, T. K.; Piech, K. M.; Urness, K. N.; Scheer, A. M.; Robichaud, D. J.; Mukarakate, C.; Nimlos, M. R.; Daily, J. W.; et al. Biomass pyrolysis: Thermal decomposition mechanisms of furfural and benzaldehyde. *The Journal of Chemical Physics* **2013**,*139* (10).

146. Evans, R. J.; Milne, T. A. Molecular characterization of the pyrolysis of biomass. *Energy & Fuels* **1987**,*1* (2),123-137.

147. Nowakowski, D. J.; Bridgwater, A. V.; Elliott, D. C.; Meier, D.; de Wild, P. Lignin fast pyrolysis: Results from an international collaboration. *Journal of Analytical and Applied Pyrolysis* **2010**,*88* (1),53-72.

148. Bährle, C.; Custodis, V.; Jeschke, G.; van Bokhoven, J. A.; Vogel, F. In situ Observation of Radicals and Molecular Products During Lignin Pyrolysis. *ChemSusChem* **2014**,*7* (7),2022-2029.

149. Yu, J.; Zhang, P.; Li, L.; Li, K.; Zhang, G.; Liu, J.; Wang, T.; Zhao, Z.-J.; Gong, J. Electroreductive coupling of benzaldehyde by balancing the formation and dimerization of the ketyl intermediate. *Nature Communications* **2022**,*13* (1),7909.

150. Mitchell, A. G.; Wan, L. S. C. Oxidation of Aldehydes Solubilized in Nonionic Surfactants I: Solubility of Benzaldehyde and Methylbenzaldehyde in Aqueous Solutions of Polyoxyethylene Glycol Ethers. *Journal of Pharmaceutical Sciences* **1964**,*53* (12),1467-1470.

151. Hammerich, O.; Speiser, B. *Organic electrochemistry*; CRC press Boca Raton,**2016**.

152. Final Report on the Safety Assessment of Benzaldehyde1. *International Journal of Toxicology* **2006**,*25* (1_suppl),11-27.

153. Ran, Y.; Li, J.; Sun, J.; Yu, B.; Tan, F.; Cheng, G.; Zhang, Z. Impact of alloying on electrocatalytic hydrogenation of benzaldehyde over sputtered NiCu film catalysts. *Applied Catalysis A: General* **2024**,*678*,119725.

154. Gong, L.; Zhang, C. Y.; Li, J.; Montaña-Mora, G.; Botifoll, M.; Guo, T.; Arbiol, J.; Zhou, J. Y.; Kallio, T.; Martínez-Alanis, P. R.; et al. Enhanced Electrochemical Hydrogenation of Benzaldehyde to Benzyl Alcohol on Pd@Ni-MOF by Modifying the Adsorption Configuration. *ACS Applied Materials & Interfaces* **2024**,*16* (6),6948-6957.

155. Cheng, G.; Sun, J.; Ran, Y.; Tan, F.; Ma, W.; Zhang, Z. Effective free-standing electrodes with refined structure via sputtering Ti sublayer and altering working pressure for electrocatalytic benzaldehyde hydrogenation. *Chemical Engineering Journal* **2024**,*481*,148735.

156. Borisenko, K. B.; Bock, C. W.; Hargittai, I. Molecular Geometry of Benzaldehyde and Salicylaldehyde: A Gas-Phase Electron Diffraction and ab Initio Molecular Orbital Investigation. *The Journal of Physical Chemistry* **1996**,*100* (18),7426-7434.

157. Yuk, S. F.; Lee, M.-S.; Akhade, S. A.; Nguyen, M.-T.; Glezakou, V.-A.; Rousseau, R. First-principle investigation on catalytic hydrogenation of benzaldehyde over Pt-group metals. *Catalysis Today* **2022**,*388-389*,208-215.

158. Rasmussen, A. M. H.; Hammer, B. Adsorption, mobility, and dimerization of benzaldehyde on Pt(111). *The Journal of Chemical Physics* **2012**,*136* (17).

159. Singh, N.; Sanyal, U.; Ruehl, G.; Stoerzinger, K. A.; Gutiérrez, O. Y.; Camaioni, D. M.; Fulton, J. L.; Lercher, J. A.; Campbell, C. T. Aqueous phase catalytic and electrocatalytic hydrogenation of phenol and benzaldehyde over platinum group metals. *Journal of Catalysis* **2020**,*382*,372-384.

160. Anibal, J.; Malkani, A.; Xu, B. Stability of the ketyl radical as a descriptor in the electrochemical coupling of benzaldehyde. *Catalysis Science & Technology* **2020**,*10* (10),3181-3194,10.1039/D0CY00282H.

161. Bhanushali, J. T.; Kainthla, I.; Keri, R. S.; Nagaraja, B. M. Catalytic Hydrogenation of Benzaldehyde for Selective Synthesis of Benzyl Alcohol: A Review. *ChemistrySelect* **2016**,*1* (13),3839-3853.

162. *Benzyl Alcohol Price Outlook*. https://medium.com/intratec-products-blog/benzyl-alcohol-prices-latest-historical-data-in-several-countries-6203daaecd3b (accessed 12/12/2024).

163. Okano, K. Synthesis and application of chiral hydrobenzoin. *Tetrahedron* **2011**,*67* (14),2483-2512.

164. Sanyal, U.; Yuk, S. F.; Koh, K.; Lee, M. S.; Stoerzinger, K.; Zhang, D.; Meyer, L. C.; Lopez-Ruiz, J. A.; Karkamkar, A.; Holladay, J. D. Hydrogen bonding enhances the electrochemical hydrogenation of benzaldehyde in the aqueous phase. *Angewandte Chemie* **2021**,*133* (1),294-300.

165. Chen, H.; Iyer, J.; Liu, Y.; Krebs, S.; Deng, F.; Jentys, A.; Searles, D. J.; Haider, M. A.; Khare, R.; Lercher, J. A. Mechanism of Electrocatalytic H2 Evolution, Carbonyl Hydrogenation, and Carbon–Carbon Coupling on Cu. *Journal of the American Chemical Society* **2024**,*146* (20),13949-13961.

CHAPTER 2

Characterisation techniques and methods

2.1 Introduction

In this chapter the characterisation methods employed throughout this thesis are discussed along with their theoretical background. A comprehensive overview of the instrumentation techniques and conditions used to analyse the materials in the following chapters is also provided. Detailed information on materials, catalyst synthesis and electrochemical characterisation of each material can be found in the experimental section of the respective chapters.

The chapter is organised into sections based on the type of characterization technique discussed, including surface analysis, bulk analysis, electrochemical techniques, and quantitative analysis. The surface analysis section covers X-ray photoelectron spectroscopy (XPS), Brunauer-Emmett-Teller (BET) theory and the complementary pore size distribution (PDS) method, scanning electron microscopy (SEM) and SEM-EDX analysis. The bulk analysis section includes X-ray diffraction (XRD), thermogravimetric analysis (TGA), X-ray fluorescence (XRF), and inductively coupled plasma optical emission spectroscopy (ICP-OES). The electrochemical section provides an overview of the main electrochemical techniques used in this thesis such as chronoamperometry, linear sweep voltammetry (LSV) and cyclic voltammetry (CV). Finally, the quantitative analysis section emphasises gas chromatography (GC) as the primary quantification method.

2.2 Surface analysis

2.2.1 X-Ray Photoelectron Spectroscopy (XPS)

Photoelectron spectroscopies (PES) are spectroscopic methods that relay on photoelectric effect.[1,2] This effect involves the ejection of electrons from a material upon irradiation by photons with sufficient energy. The kinetic energy (K_E) of the emitted photoelectrons is analysed to extract their binding energy (BE), which is characteristic of specific elements. The relationship is described by the equation:[3,4]

$$K_E = hv - BE - \varphi_{spec} \qquad \text{(Eq 2.1)}$$

Where hv is the energy of the incident photon, BE the binding energy of the core electron state, and φ_{spec} the spectrometer work function which is typically between 2-5 eV and is defined as the energy required to remove an electron from the spectrometer material (analyser/detector) into vacuum. This work function has to be calibrated and ensures that the instrument correctly measures the kinetic energy of electrons. The sample work function (φ_{sample}) is instead defined as the energetic input required to transfer an electron from the Fermi level to the vacuum, and is characteristic of the material analysed (**Figure 2.1**, (Eq 2.2).

$$\varphi_{sample} = E_{vacuum} - E_{Fermi} \qquad \text{(Eq 2.2)}$$

PES techniques are crucial for surface and material science because are highly sensitive to the outermost layers of a material. They provide both qualitative and quantitative information about a sample's surface composition and chemical states.[2]

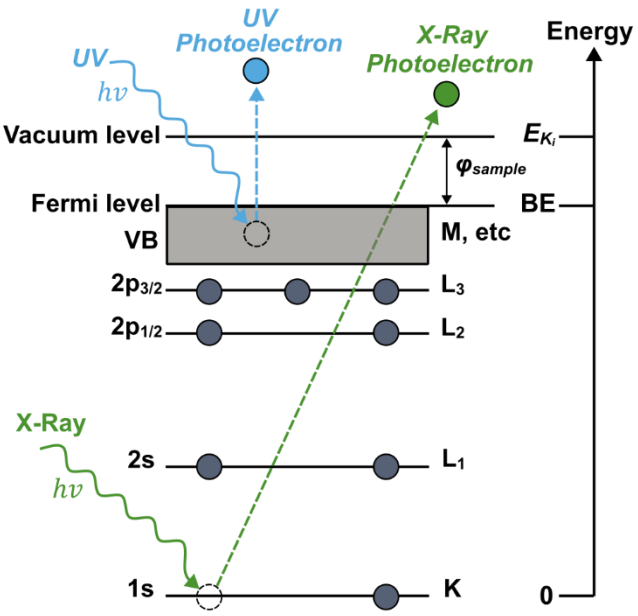

Figure 2.1 Photoelectric effect using UV light and X-ray radiation, along with emission of UV and X-ray photoelectrons. Where E_{Ki} is the initial kinetic energy of the emitted photoelectron and VB is the valence band.

Depending on the type of radiation used to irradiate the sample, PES techniques are classified into X-ray photoelectron spectroscopy (XPS),[5] and ultraviolet photoelectron spectroscopy (UPS).[6] Due to the lower energy of UV radiation (~10–40 eV), UPS is strictly limited on valence electrons, which are those located in valence band, the

outermost electrons. For this reason, UPS is particularly relevant for studies in semiconductor physics, organic electronics, and materials with interesting surface properties.[6] Conversely in XPS, the use of high-energy X-rays radiation, often generated from sources like Al K_α 1486.6 eV, allow the ejection of core-level electrons, which are tightly bound and highly characteristic of the specific element and chemical state (e.g., oxidation state, coordination environment). This makes XPS highly effective for detailed elemental and chemical analysis. The surface-sensitive nature of XPS is based on the inelastic mean free path (IMFP) of electrons, i.e. the average distance that an electron with a given kinetic energy can travel through a solid before losing energy due to inelastic scattering; typically is limited to about 10–20 Å. Depending on the material and photon energy the XPS probing depth is *ca.*5-10 nm allowing it to analyse not just the extreme surface but also a small subsurface region.[3]

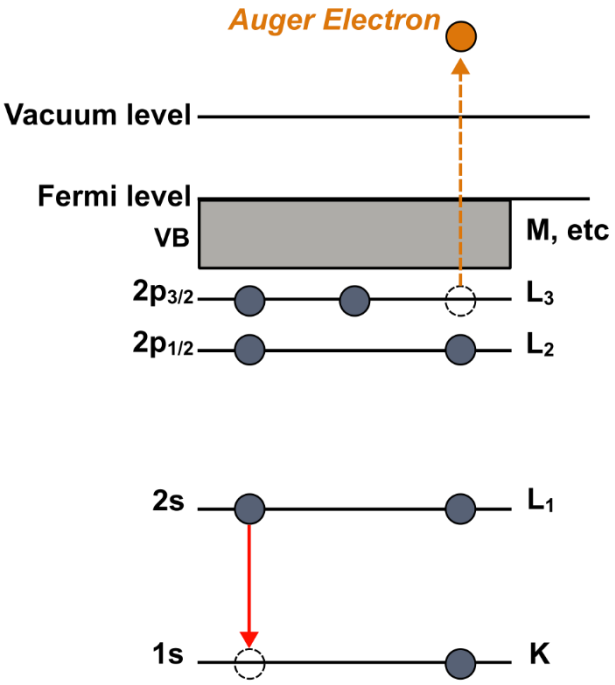

Figure 2.2 Relaxation and emission of an Auger electron.

XPS spectra are a summation of contributions from all elements present in the sample, necessitating careful peak deconvolution to isolate individual signals. Relative sensitivity factors (RSFs), which account for factors like the IMFP, photoemission cross-section, and spectrometer transmission, are used for quantitative analysis.[7] A significant feature of XPS is its ability to reveal chemical shifts - variations in binding energy caused by differences in the chemical environment. For instance, binding to atoms with higher

electronegativity shifts the BE to higher values, providing insights into oxidation states and chemical bonding. As a result, XPS can determine not only the presence of specific elements but also their chemical states, such as distinguishing between sp^2 and sp^3 hybridised carbon in amorphous carbon materials.[3] XPS spectra include core-level peaks and background signals caused by inelastically scattered electrons. Accurate fitting of these peaks requires careful consideration of line shapes, background subtraction, and spin-orbit splitting, which occurs in higher core levels.[3] Auger electron peaks are another essential feature of XPS spectra. Following the ejection of a core electron, an electron from a higher energy orbital may fill the vacancy, releasing energy. This energy can either be emitted as a photon or transferred to another electron, which is subsequently ejected (**Figure 2.2**). The Auger electron's energy is independent of the incident photon energy, making it distinguishable from primary photoelectron peaks when the X-ray source energy is varied.[3]

Although XPS is primarily used for thin film analysis, it also plays a crucial role in studying powder samples, offering detailed insights into their surface composition and the chemical states of the particles. Unlike thin films, powders are often heterogeneous, with surfaces that can differ significantly from their bulk composition due to factors like oxidation, contamination, or environmental adsorption. XPS is a valuable tool in detecting and quantifying the surface elements of powders containing metals, distinguishing between different oxidation states (e.g., metallic vs. oxidised forms) and identifying any contaminants or adsorbed species, such as hydrocarbons or oxygenated compounds. This is particularly important for understanding the reactivity, stability, or catalytic behaviour of metal-containing powders. Despite its strengths, XPS has several limitations when applied to these samples. As a surface-sensitive technique, it only probes the top few nanometres of the material, making it unsuitable for bulk composition analysis without combining it with complementary methods. The preparation of powder samples can also be challenging, as powders need to be securely mounted to avoid charging,[3] particle movement, or inconsistent results during measurement. Additionally, the inherent heterogeneity of powders means that individual measurements may vary, and multiple spots or averages are often required for reliable data.

2.2.2 Brunauer-Emmett-Teller (BET) theory and pore size distribution (PSD)

The Brunauer-Emmett-Teller (BET) method is a technique used to determine the specific surface area of materials, particularly porous solids like powders, catalysts, and activated carbon.[8] The method is based on the physical adsorption of gas molecules (usually nitrogen) onto the surface of a material and extends the Langmuir adsorption theory.[8,9] A gas is adsorbed onto the surface of a solid material at various relative pressures (P/P_0), where P is the actual pressure and P_0 is the vapor pressure of the gas at a given temperature. As the gas adsorbs, it forms layers, with the first layer being adsorbed directly onto the surface (referred to as the monolayer) and subsequent layers adsorbing above it (**Figure 2.3**).

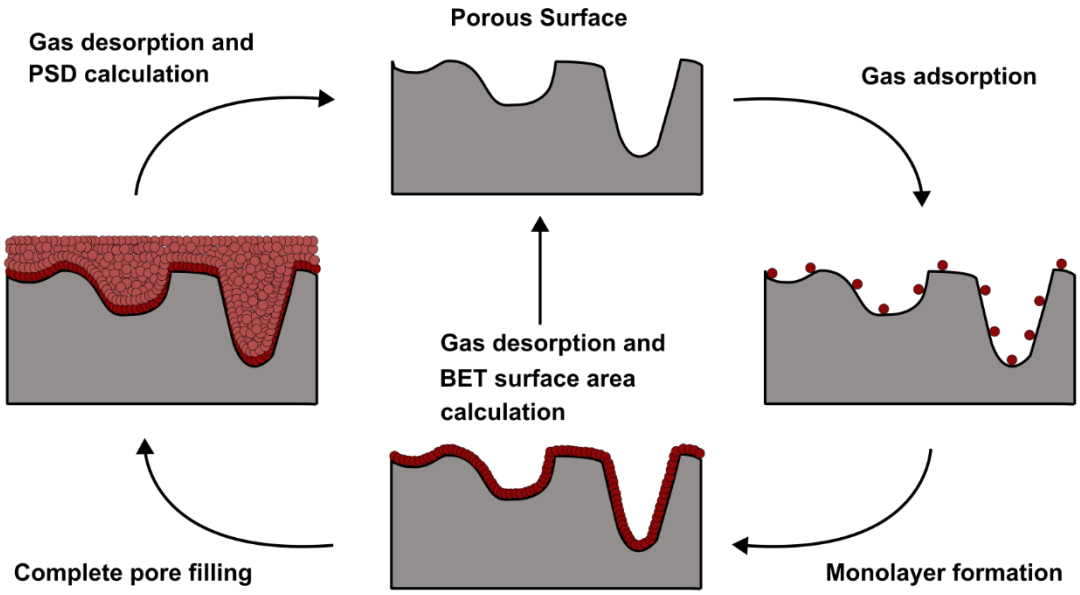

Figure 2.3 Scheme of BET and PSD measures with highlighted the main steps.

The BET theory assumes these adsorbed layers interact differently, with stronger forces between the gas molecules and the solid surface than between the gas molecules in the higher layers. To describe this process, the BET equation is used (Eq 2.3), which relates the amount of gas adsorbed to the relative pressure.[8]

$$\frac{P}{v\,(P_0 - P)} = \frac{1}{v_m\,c} + \frac{c-1}{v_m\,c}\left(\frac{P}{P_0}\right) \qquad \text{(Eq 2.3)}$$

Where v is the volume of gas adsorbed at a particular pressure, v_m is the volume of gas adsorbed when the entire surface is covered by the monolayer, and c is a constant. From the equation, it is possible to calculate the monolayer volume, i.e. the volume of gas required to form the monolayer, and this value is directly tied to the total surface area (S_{tot}) and the specific surface area (S_{BET}) of the material, as described in (Eq 2.4) and (Eq 2.5).[10]

$$S_{tot} = \frac{v_m N A}{V} \quad \text{(Eq 2.4)}$$

$$S_{BET} = \frac{S_{tot}}{a} \quad \text{(Eq 2.5)}$$

Where N is Avogadro's number, A is the cross-sectional area of a single gas molecule, V the molar volume of the adsorbate gas, and a is the mass of the sample.

The determination of pore size distribution (PSD) is a crucial complement to the BET method, as it provides deeper insights into the structure and functionality of porous materials. While the BET method calculates the overall specific surface area, PSD analysis reveals how the material's pores are distributed in size, offering critical information for applications like catalysis, gas storage, and filtration. Two common methods for PSD determination are the Barrett-Joyner-Halenda (BJH)[11] method and Density Functional Theory (DFT).[12,13] The BJH method analyses the desorption branch of an adsorption isotherm using the Kelvin equation, which relates the relative pressure to pore size based on capillary condensation. It is effective for mesopores (2–50 nm), but its reliance on assumptions of cylindrical pores and bulk properties of the adsorbed gas makes it less accurate for micropores (< 2 nm). In contrast, DFT models adsorption at the molecular level, accounting for interactions between gas molecules and pore walls and accommodating various pore geometries (e.g., slit, cylindrical). DFT is highly accurate for micropores and mesopores and offers a high-resolution PSD, but it is computationally intensive and heavily dependent on the choice of pore models. While BJH is useful for rapid analysis of mesopores, DFT provides a more precise and detailed understanding of complex porous structures, making it indispensable for advanced materials with diverse pore sizes. Combining PSD methods with BET surface area measurements enables a comprehensive characterization of porous materials, ensuring their optimal design and use in targeted applications.

2.2.3 Scanning electron microscopy (SEM)

Scanning electron microscopy (SEM) is a powerful imaging technique that uses focused beams of electrons to scan the surface of a sample, creating highly detailed, high-resolution images. Unlike traditional light microscopes, which use light to visualise samples, SEM relies on electron interactions to provide a much greater depth of field and magnification and is mainly used to examine the surface structure and morphology of materials.[14] There are also other types of electron microscopy, including transmission electron microscopy (TEM), which examines the internal structure of ultra-thin sample slices, and scanning transmission electron microscopy (STEM), which combines aspects of both SEM and TEM to analyse both surface and internal features.[15]

The electron gun is the main part of an SEM instrument and is where high-energy electrons, known as primary electron (PE), are generated. The energy of the PE is typically between 0.5 – 30 KeV and determines the depth of penetration into the sample and the types of signals generated. This beam is directed toward the sample through an electron column that includes a series of lenses (magnetic or electrostatic) used to focus and control the beam's size and shape. Various types of electron and photon interactions occur when the PE electrons beam interacts with the sample generating different signals.[14] One such signal is secondary electrons (SE), which are low-energy electrons (less than 50 eV) emitted from the outer shells of the sample's atoms as a result of inelastic collisions with the primary electrons (**Figure 2.4**). Secondary electrons can be categorised into two main types based on their origin and detection. SE1 electrons are emitted directly from the surface of the sample beneath the focused primary beam and provide high-resolution, topographic information. These SE1 electrons are detected by the In-lens detector, which is located within the SEM column, near the objective lens (**Figure 2.4**). The In-lens detector is optimized to capture the SE1 signal due to its position along the primary beam path, ensuring superior resolution. In contrast, SE2 electrons originate from regions slightly farther from the primary beam impact area and are typically the result of scattering events. These electrons are detected by the Everhart-Thornley Detector (ETD), which is mounted off-axis inside the SEM chamber (**Figure 2.4**). The ETD is positioned to collect SE2 electrons that are deflected toward it by a combination of the sample's geometry and an applied bias near the detector. While SE2 signals contribute to the image, they generally provide less spatial resolution than SE1 signals. Because of this, the two SE signals and detectors are usually used in conjunction to provide complementary data.

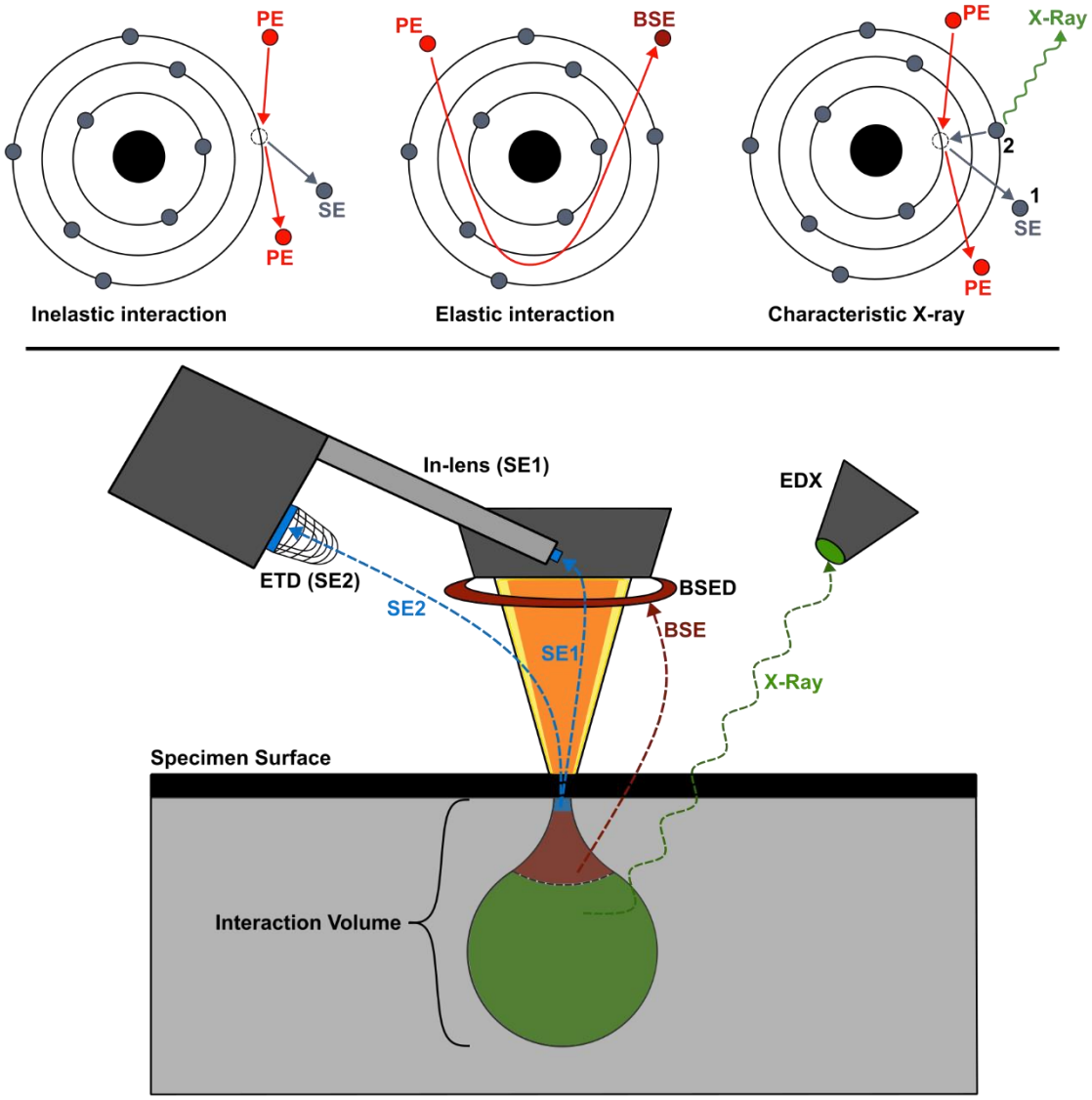

Figure 2.4 Types of electron interactions: inelastic, elastic, and characteristic X-ray (top). Schematic representation of an SEM chamber, highlighting the main detectors and electron signals (bottom).

In addition to secondary electrons, backscattered electrons (BSE) are another important signal, consisting of high-energy electrons that are elastically scattered back out of the sample after interacting with atomic nucleus. BSEs are detected by dedicated BSE detectors (BSED), often positioned above the sample or integrated within the SEM column, and provide compositional contrast based on the atomic number of the sample's elements, with heavier elements appearing brighter in BSE images (**Figure 2.4**). Additionally, the interaction of primary electrons with inner-shell electrons in the sample generates characteristic X-rays, emitted when an outer-shell electron fills the vacancy and

releases energy as X-rays. These X-rays, which originate from deeper regions of the sample (up to a few microns depending on the beam energy), are used for elemental analysis through techniques like Energy Dispersive X-ray Spectroscopy (EDX). SEM can also be paired with Auger Electron Spectroscopy (AES), which detects Auger electrons emitted when an inner-shell electron is ejected and replaced by a higher-energy electron (see paragraph 2.2.1). However, SEM does not provide detailed information from deeper within the material, which would require techniques like X-ray diffraction (XRD) or TEM. A comprehensive summary of all the characteristic signals in SEM is provided in **Table 2.1**.

Table 2.1 Summary of characteristic signals in SEM**,** including type of source, energy, depth of origin and information provided.[14]

Signal	Source	Energy	Depth of Origin	Information Provided
Primary Electrons	Electron gun	~0.5–30 keV	N/A	Initiates interactions
Secondary Electrons	Outer-shell electrons	<50 eV	Surface (~1–10 nm)	Topographic details
Backscattered Electrons	Elastic scattering with nucleus	~Beam energy	Deeper (~0.1–5 µm)	Atomic number (Z) contrast
Characteristic X-rays	Inner-shell ionization	Element-specific	~1–3 µm	Elemental composition
Auger Electrons	Surface electron relaxation	<1 keV	Surface (<1 nm)	Surface chemistry

It is important to note that high vacuum conditions are required in the SEM chamber to prevent scattering of PE by air molecules. This vacuum also ensures that the electron interactions with the sample remain undisturbed, providing high-quality images and accurate data. Another important aspect is sample preparation; if the sample is not conductive, it may require pretreatment with a thin coating of conductive material, such as gold, platinum, or carbon, to prevent charging and improve image quality.[14] Finally, SEM is a powerful imaging technique that provides valuable insights into the morphology and composition of a material, especially when combined with other analytical methods.

2.3 Bulk analysis

2.3.1 X-Ray Diffraction (XRD)

X-ray diffraction is a non-destructive analytical technique used to identify the crystalline phases of a sample and determine structural parameters such as lattice spacing and crystal orientation. When an X-ray beam interacts with a crystal lattice, the incident rays are scattered by the atoms within the lattice planes. Depending on the diffraction angle and the atomic arrangement, these scattered rays interfere either constructively or destructively (**Figure 2.5**). Constructive interference occurs when the path difference between rays satisfies Bragg's law, expressed as:[16]

$$n\lambda = 2d \sin\theta \qquad \text{(Eq 2.6)}$$

Where n is the order of diffraction (an integer corresponding to the number of wavelengths in the path difference), λ is the wavelength of the incident X-ray beam, d is the interplanar spacing between the lattice planes, and θ is the angle of incidence (or diffraction angle).

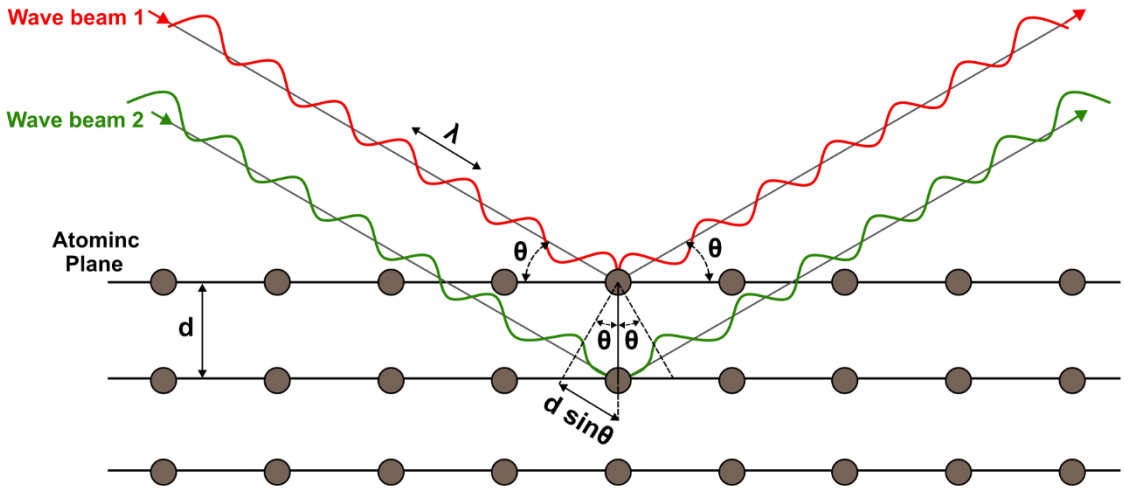

Figure 2.5 Bragg diffraction illustrated: Two beams with the same wavelength and phase (red and green) approach a crystalline solid and scatter off two distinct atoms within it. The lower beam travels an additional path length of 2dsinθ.

X-rays used in diffraction are typically generated by heating a filament to produce electrons, which are accelerated toward a target material (anode) by applying a high

voltage. When the accelerated electrons possess sufficient energy to dislodge inner-shell electrons in the anode material, characteristic X-ray emissions are produced.[17] The emitted X-ray spectrum includes distinct components such as K_α and K_β radiation, with the specific wavelengths depending on the target material. For instance, copper is commonly used in XRD with a wavelength of $\lambda = 1.5418$ Å characteristic of CuK_α radiation. The generated X-rays are collimated and directed onto the sample. As the sample and detector are rotated, the intensity of the diffracted X-rays is measured. When the geometry of the incident X-rays and the sample satisfies Bragg's law, constructive interference produces an intensity peak in the diffraction pattern. An X-ray diffractometer is designed to measure diffraction patterns with high precision. The sample rotates at an angle θ in the path of the incident X-ray beam, while the detector, mounted on a rotating arm, records the diffracted X-rays at an angle of 2θ. This configuration ensures that Bragg's condition is satisfied for a wide range of lattice spacings. The instrument's goniometer maintains precise angular alignment of the sample and detector during data collection.

XRD techniques are classified in single-crystal X-ray diffraction (SCXRD) and powder X-ray diffraction (PXRD). SCXRD focuses on a single, well-formed crystal to provide detailed atomic-level structural information, such as bond lengths, angles, and symmetry. It requires high-quality crystals and is ideal for determining complex structures or unknown phases. In contrast, PXRD analyses polycrystalline samples composed of numerous tiny, randomly oriented crystallites. While PXRD may appear less precise due to the disordered nature of these samples, it leverages the collective behaviour of the crystallites, ensuring that all possible orientations are represented in the diffraction pattern. This is a fingerprint of the material's crystalline structure, enables to extract averaged structural information, such as lattice parameters and interplanar spacings, and makes it particularly suited for phase identification and bulk material analysis. PXRD also has limitations, such as lower resolution compared to single-crystal XRD, which makes it challenging to resolve complex structures or subtle structural details. Additionally, overlapping diffraction peaks in multiphase samples can complicate phase identification and quantitative analysis. For powder diffraction experiments, data is typically collected over a 2θ range from 5° to 90°, depending on the experimental requirements.[17]

2.3.2 Thermogravimetric analysis (TGA)

Thermogravimetric analysis (TGA) is a qualitative and quantitative analytical technique used to measure changes in the mass of a sample as a function of temperature or time. It is a valuable method for determining the composition of materials since provides information about the thermal stability, composition, and decomposition.[18]

The sample is typically heated at a constant rate or held at a constant temperature, while the atmosphere surrounding it can be inert, oxidizing, or reactive, and may be changed during the measurement. TGA instruments consist of a high-precision balance, a furnace, a temperature programmer, and a gas delivery system (**Figure 2.6**). The sample is placed in a crucible that is connected to the balance, which measures any change in mass while the furnace heats the sample. The results are displayed as a TGA curve, plotting mass against temperature and/or time. Mass changes occur when a sample loses material through various processes such as decomposition or reaction with the atmosphere. Thermal decomposition produces a downward step in the TGA curve due to the formation of volatile products, while oxidation leads to an increase in mass.

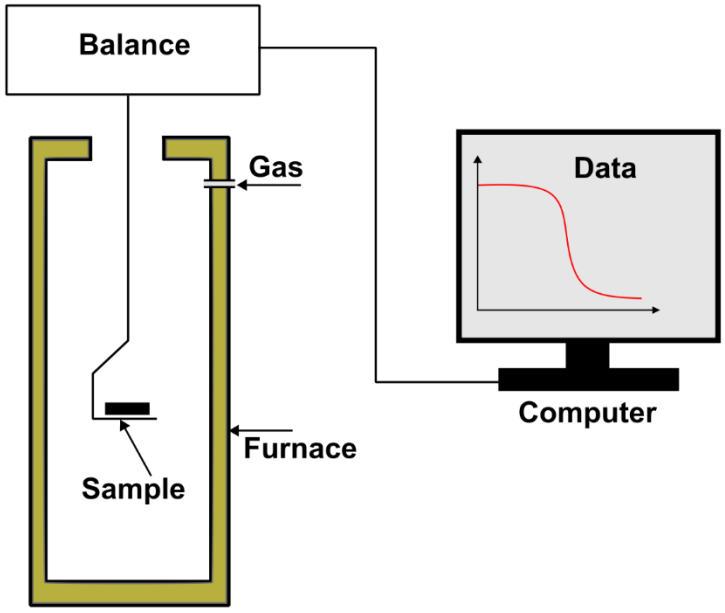

Figure 2.6 Scheme of a TGA instrument.

For inorganic samples, TGA results particularly useful in the determination of the weight percentage (wt%) of a metal within the sample, although this is usually done indirectly

by analysing the mass changes associated with the formation of metal oxides or other compounds.[19] In cases where the metal does not react with the atmosphere, it remains as a stable residue at the end of the TGA experiment. The mass of this residue can then be used to determine the amount of metal present, especially if other components in the sample decompose and volatilise. However, this method assumes that the metal does not undergo significant changes during heating and remains as a stable residue. If a metal-containing compound undergoes a stoichiometric reaction, the mass change observed in the TGA curve can be used to calculate the amount of metal present using the known molar mass of the eliminated molecule. For example, if a metal carbonate decomposes into metal oxide and carbon dioxide, the mass loss can be used to determine the amount of the original metal carbonate, and thus the metal content. It's important to note that TGA is more effective in quantifying the total amount of inorganic material in a sample, including metals, rather than identifying specific metal compounds. TGA cannot distinguish between different metal species; other techniques like X-ray fluorescence (XRF) and infrared spectroscopy may be required for further identification. Also, if a sample contains multiple metals that oxidise or decompose at similar temperatures, the TGA curve might be complex, and isolating the mass change associated with a specific metal might not be straightforward.

2.3.3 X-ray fluorescence analysis (XRF)

X-ray fluorescence analysis (XRF) is a non-destructive technique used to determine the elemental composition of solid and liquid samples. It is based on the photoelectric effect, as described in paragraph 2.2.1, which serves as the initiating process. When an inner-shell electron is ejected, a vacancy is created in that shell (e.g., K-shell or L-shell). Electrons from higher energy levels (e.g., L or M shells) subsequently transition to fill this vacancy, releasing energy in the form of characteristic X-ray fluorescence (**Figure 2.7**).[20] The unique energy of these fluorescent X-rays for each element provides the foundation for elemental analysis in XRF. Unlike other techniques based on the photoelectric effect previously discussed, such as XPS, XRF is mainly used for bulk analysis because the emitted characteristic X-rays have relatively high penetration depths. This allows XRF to probe and provide information about the elemental composition of a larger volume of material beneath the surface.

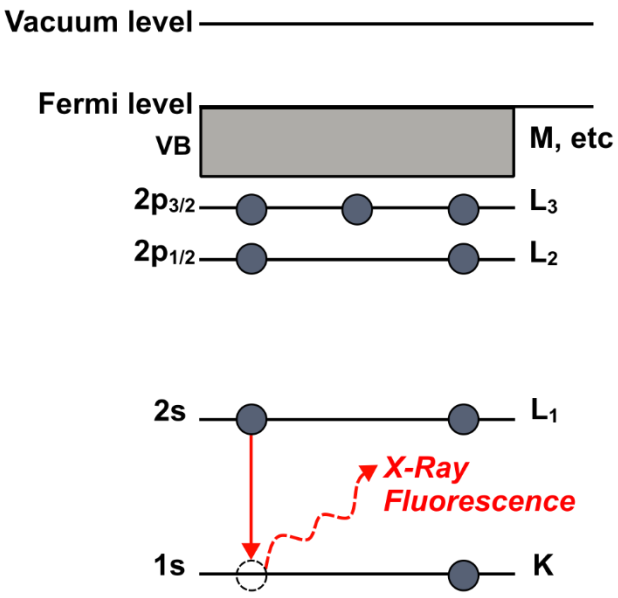

Figure 2.7 Relaxation and emission of X-ray fluorescence radiation.

On the other hand, XPS is limited to surface analysis, as it detects photoelectrons, which have very shallow escape depths due to strong interactions with surrounding atoms. These interactions restrict the detectable signal to only the top few nanometres of the material. Therefore, XRF is better suited for analysing the overall composition of a sample and is capable of detecting elements from Be-U in concentrations from PPM range to 100%. Because X-rays are used to excite the sample, depths as great as 10 µm can be analysed. Through the use of appropriate reference standards, XRF analysis can accurately quantify the elemental composition of both solid and liquid samples.[21] Sample preparation is crucial for obtaining accurate and reliable results. The goal is to ensure that the sample is homogeneous, representative of the material, and appropriately prepared for optimal XRF analysis. For instance, powders samples are fine grounded to help to create a uniform surface, as the technique works best when the X-rays interact with a flat, uniform surface. XRF instrument is made of an X-ray source, a sample holder, a detector and a control system. The X-ray tube generates a beam of high-energy X-rays, which is directed toward the sample. As these X-rays strike the sample, they impart energy to the atoms, causing the ejection of inner-shell electrons through the photoelectric effect. Once the fluorescent X-rays are emitted, the detector captures it and measures both their energy and intensity. Energy dispersive detectors (ED) are commonly used for this purpose, functioning as converters that transform the radiation's energy into an electrical signal. The control system then processes this information, using the distinct energy levels and intensities of

the X-rays to identify which elements are present in the sample and to quantify their concentrations. By analysing these signals, the XRF instrument provides detailed insights into the elemental composition of the material being examined.

2.3.4 Inductively coupled plasma-optical emission spectroscopy (ICP-OES)

Inductively coupled plasma optical emission spectroscopy (ICP-OES) is a powerful and versatile analytical technique widely used for the determination of trace elements in a variety of matrices. ICP-OES measures the concentration of elements by detecting the optical emission of characteristic wavelengths of light emitted by ions and atoms in a high-temperature plasma. The method relies on the fact that each element has a unique emission spectrum, allowing for simultaneous multi-element detection.[22]

The sample is introduced as an aerosol into the plasma using a nebulizer and spray chamber, ensuring efficient atomization. The heart of ICP emission spectrometer is the plasma, an extremely hot excitation source with a temperature of *ca.*6000 -10000 K, generated by coupling radiofrequency energy to an argon gas stream. This high temperature destroys the sample completely, so the analytical result is usually not influenced by the nature of the chemical bond. In the plasma, atoms and ions are excited to emit electromagnetic radiation. The emitted light is passed through an optical system, typically involving diffraction gratings or prisms, which resolve the light into its constituent wavelengths. A detector, such as a photomultiplier tube (PMT) or a charge-coupled device (CCD), measures the intensity of the light at each wavelength. The wavelengths are used for the identification of the elements while the intensities serve for the determination of their concentration. As a rule, there is a linear relationship between intensity and concentration over more than 4-6 decades. This intensity concentration function depends on a number of parameters, some of which are unknown. Hence, these factors have to be determined before the analysis with a calibration method.[22] It is an important prerequisite to ensure good accuracy calibration based also on the assumption that the slope of the calibration functions does not change between standards and samples.

ICP-OES is largely used for quantitative determination of bulk metal content in metal-containing samples, since this method provides accurate quantification of elemental composition, making it ideal for analysing materials like alloys, ores, and catalysts.

However, ICP requires liquid samples, and solid metal samples must first undergo preparation, often involving acid digestion. Common acids used include nitric acid, hydrochloric acid, or aqua regia, depending on the metal's solubility and reactivity. After the analysis the metal content can be obtained by converting the measured concentration, often reported in mg/L or ppm, into the total metal content in the solution based on the dilution factor.[23]

Although ICP is a powerful technique for trace metal analysis, offering high sensitivity (ppb range), multi-element detection, and a wide dynamic range, it can also face some challenges. Spectral interferences, matrix effects, and operational costs are some examples. Also, solid samples require digestion, which can be time-consuming and risk contamination. While less sensitive than ICP-MS, ICP-OES balances performance and cost effectively for most routine analyses. Its versatility and efficiency make it invaluable for applications requiring accurate and rapid trace metal determination, though careful calibration and preparation are essential for optimal performance.

2.4 Spectroscopic characterisation

2.4.1 Fourier Transform Infrared Spectroscopy (FTIR)

Fourier Transform Infrared Spectroscopy (FTIR) is a non-destructive analytical technique used to obtain an infrared spectrum of absorption or emission of a solid, liquid, or gas. It is fundamentally based on the principle that molecular bonds vibrate at specific frequencies, and these vibrations can absorb infrared radiation at characteristic energies. The core component of an FTIR instrument is the interferometer, typically a Michelson-type, which modulates the infrared beam and generates an interferogram that is mathematically transformed (via Fourier Transform) into an absorbance spectrum. This allows for rapid and simultaneous collection of a wide range of frequencies, improving both signal-to-noise ratio and speed compared to traditional dispersive IR spectroscopy.[24]

In the context of graphitised carbon materials, FTIR is primarily used to probe the chemical functionalities present on the carbon surface, especially those introduced during oxidative treatment or surface functionalisation. Although the highly ordered graphitic structure has minimal IR activity due to its symmetry and low dipole moment changes,

FTIR is very sensitive to polar functional groups such as hydroxyl (-OH), carbonyl (C=O), carboxyl (-COOH), and ether (C-O-C) groups, which may exist on the surface or at the edges of graphitic domains.[25] These groups influence the physicochemical properties of carbon materials, including their wettability, catalytic behaviour, and interaction with other components in composite systems or electrochemical cells.

2.4.2 Raman Spectroscopy

Raman spectroscopy is a complementary vibrational technique based on the inelastic scattering of photons, known as the Raman effect. When monochromatic light, usually from a laser source, interacts with a sample, most photons are elastically scattered (Rayleigh scattering), but a small fraction undergoes energy shifts corresponding to the vibrational modes of the molecules.[26] This shift provides a molecular fingerprint of the material. Raman systems typically consist of a laser excitation source (commonly in the visible or near-infrared range), a high-resolution spectrograph, and a sensitive detector. The technique is particularly advantageous due to its minimal sample preparation requirements and its ability to analyse samples through transparent containers.[26]

Raman spectroscopy is one of the most informative and widely used methods for characterising carbon-based materials, especially in determining the degree of graphitisation, structural disorder, and crystallite size. In graphitised carbon, two main features dominate the Raman spectrum: the G-band (~1580 cm^{-1}), attributed to the E_2g phonon of sp^2-hybridised carbon atoms in graphitic planes, and the D-band (~1350 cm^{-1}), which arises from A_1g symmetry vibrations near defects or edges in the lattice. The intensity ratio I_D/I_G is a widely accepted metric for quantifying structural disorder: higher values suggest more defects or less graphitic ordering.[27] In addition, the presence of a 2D band (~2700 cm^{-1}) and its shape can indicate the number of graphene layers or stacking order in multilayered structures. Due to its high sensitivity to crystallinity and bonding environment, Raman spectroscopy is extensively used to monitor thermal treatments, doping, and chemical modifications in carbon materials.[27] Together with FTIR, Raman provides a comprehensive understanding of both the chemical and structural attributes of carbon materials, making it an indispensable tool in the study of graphitised carbon for applications in energy storage, catalysis, and nanocomposites.

2.5 Electrochemical techniques

In Chapter 1, it was explained that electrochemical reactions and current flow arise from the mutual exchange of electrons at the interface between an electrode and an electrolyte. This current is influenced by the applied potential, which acts as the driving force for the reaction at the electrode. The rate of electron transfer is also affected by the applied potential, as described by the Butler-Volmer kinetic equation discussed earlier.

By manipulating the applied potential at the electrodes while measuring the resulting current, it possible to analyse the relationship between current and potential.[28] Electrochemical techniques that rely on the application of specific potentials to an electrode and monitor the corresponding current response are referred to as voltammetric methods.[29] These methods are typically performed using a potentiostat and a three-electrode setup, which comprises a working electrode (WE), a counter electrode (CE), and a reference electrode (RE). **Figure 2.8** illustrates a schematic representation of a basic three-electrode cell circuit using a potentiostat.

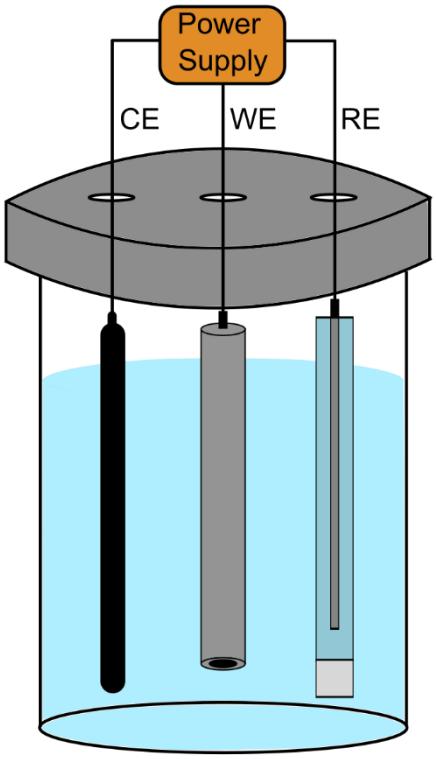

Figure 2.8 Scheme of a three-electrode cell circuit with counter (CE), working (WE) and reference (RE) electrodes.

The potentiostat's role is to maintain a well-defined potential difference between the WE and RE while facilitating the required current between the CE and WE electrodes to maintain electroneutrality in the solution. The RE serves to provide a stable reference potential, enabling the potential of the WE to be accurately defined within the electrochemical system. Notably, the actual potential experienced by the WE can differ from the set value due to the iR drop (also known as ohmic drop). This refers to the voltage drop that occurs due to the resistance of the electrolyte solution and other circuit components when a current flows through an electrochemical cell. For a correct interpretation of the electrochemical measurements is then important to correct iR drop via automatic or manual compensation.

In voltammetric methods, the relationship between current (j) time (t), and potential (E) is fundamental in understanding electrochemical behaviour. Different potential profiles applied to the WE allow for the exploration of various regions of the j-t-E surface, providing insight into reaction kinetics, mass transport effects, and capacitive behaviours.[28,29]

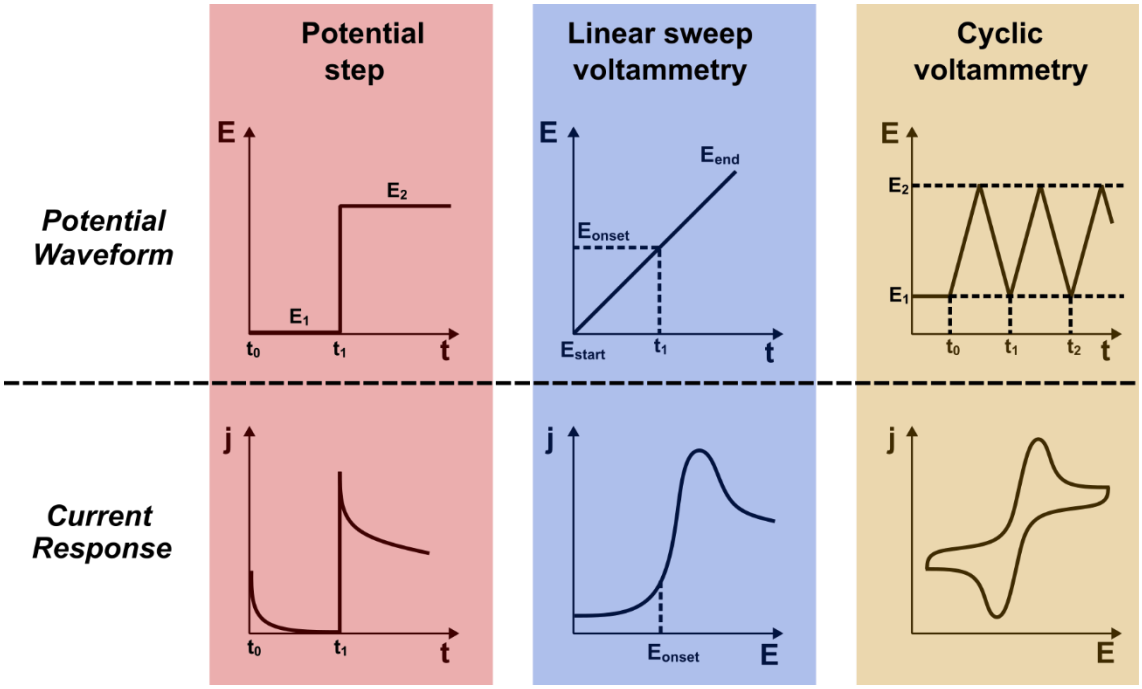

Figure 2.9 Potential waveforms and current responses for: (a) potential steps, (b) linear sweep voltammetry and (c) cyclic voltammetry methods.

Potential step techniques involve holding the potential constant for a specified period before stepping it to another value. The applied potential waveform follows a step

function, as illustrated in **Figure 2.9**. Chronoamperometry is a common potential step technique that involves measuring the current-time response at a stationary WE potential. This method captures both capacitive and Faradaic currents arising from Nernstian reactions. Capacitive currents, characterised by their large magnitude over a short duration, decay rapidly as charge redistributes at the electrode interface. Faradaic currents, associated with electron transfer reactions, may vary over time due to mass transport limitations. For macroscale electrodes, mass transport follows a linear diffusion pattern, and according to the Cottrell equation (Eq 2.7), the current decreases over time as the reactants near the electrode surface get consumed and must be replenished by diffusion from the bulk solution.

$$i(t) = \frac{zFAc_0\sqrt{D}}{\sqrt{\pi t}} \qquad \text{(Eq 2.7)}$$

Where z the number of electrons, F is the Faraday constant, A is the area of the electrode in cm^2, c_0 initial concentration of the analyte, D is the diffusion coefficient of the analyte and t is the time. Chronoamperometry can give useful information regarding electrode stability since very slow decreases of Faradaic current over time suggests that the electrode material is not degrading or undergoing unwanted side reactions. Additionally, a stable current implies that the electrode surface maintains its activity, meaning the reaction kinetics are not changing over time. Conversely instabilities, such as electrode fouling, dissolution, or passivation, typically cause a rapid drop in current.

Another class of voltammetric methods is voltammetry, which involves continuously varying the applied potential over a defined range at a fixed sweep rate. In linear sweep voltammetry (LSV), the potential is varied at fixed scan rate (ν, V s^{-1}) while measuring the resulting current. The applied potential waveform, presented in **Figure 2.9** increases (or decreases) linearly over time, with the slope equal to the scan rate. During LSV, the electrochemical reaction begins at a characteristic potential, known as the onset potential (E_{onset}), where an increase in current indicates the initiation of the reaction. Beyond a certain potential, the reaction rate becomes limited by diffusion, meaning that reactants are consumed at the electrode surface faster than they can be replenished from the bulk solution. This results in the formation of a current peak, referred to as Faradaic peak current, representing the point at which the oxidation or reduction process reaches its maximum rate. The peak occurs when electron transfer is at its fastest, after which the current stabilises due to the restricted availability of reactants near the electrode.

A closely related technique is cyclic voltammetry (CV), which extends the principles of linear sweep voltammetry (LSV) by incorporating a reversing potential scan. Unlike LSV, where the potential is swept in one direction only, CV involves scanning the potential forward to a set limit and then reversing it back to the initial value (**Figure 2.9**). This approach provides additional information about the reversibility of electrochemical reactions and the kinetics of electron transfer. CVs experiments allow for the observation of both oxidation and reduction processes. As the potential is scanned in the forward direction, an oxidation (or reduction) reaction occurs, generating a peak similar to that observed in LSV. When the scan direction is reversed, any electrochemically reversible species at the electrode surface can undergo the opposite reaction, producing a second peak in the current response. The ratio and separation of these peaks offer insights into the reversibility of the redox couple, diffusion coefficients, and reaction mechanisms.

CVs serves as a valuable technique for assessing electrochemical capacitance, which is crucial for evaluating charge storage properties in materials used for electrocatalysis, supercapacitors, and energy storage applications. Electrochemical capacitance arises primarily from two mechanisms: double-layer capacitance and pseudocapacitance. Double-layer capacitance is associated with the accumulation of charge at the electrode/electrolyte interface, resembling the behaviour of a conventional capacitor, and is largely influenced by the surface area. In contrast, pseudocapacitance results from fast, reversible redox reactions occurring at or near the electrode surface, contributing additional charge storage beyond simple electrostatic effects. The measurement of electrochemical capacitance is particularly significant when comparing different electrocatalysts, as it provides insights into their effective surface area, the density of active sites, and overall charge storage capacity. Since catalytic performance is often linked to the accessibility of active sites, materials with higher electrochemical capacitance tend to facilitate higher faradaic currents.

In practical applications, CV is used to determine capacitance by analysing the current response in a non-faradaic potential window, where no significant redox reactions occur. Within this region, the measured current is primarily attributed to the charging and discharging of the electrochemical double layer. The capacitance can be derived from the relationship between capacitive current and scan rate, where plotting the average current against scan rate yields a linear trend, the slope of which corresponds to the specific capacitance of the material. This method is particularly useful when comparing catalysts

with different surface areas, and to ensure a fair comparison current is usually normalised by the electrochemical surface area (ECSA). This normalization allows to account for differences in specific surface area, although it is underpinned by an assumption of the specific areal capacitance of the material, C_s. However, such C_s values are not always unambiguously established, as discussed in more detail by Connor et al.[30]

2.6 Quantitative analysis: Gas chromatography

Chromatography is an analytical technique employed to separate, identify, and purify individual components within a mixture. This separation is achieved by distributing the components (solutes or analytes) between two phases: a mobile phase, which moves in a define direction, and a stationary phase, which remains fixed. The differing affinities of each component for these phases result in distinct migration rates, facilitating their separation. This type of chromatographic process is called elution, and is defined as a procedure in which the mobile phase is continuously passed through or along the chromatographic bed and the sample is fed into the system as a fine slug.[31]

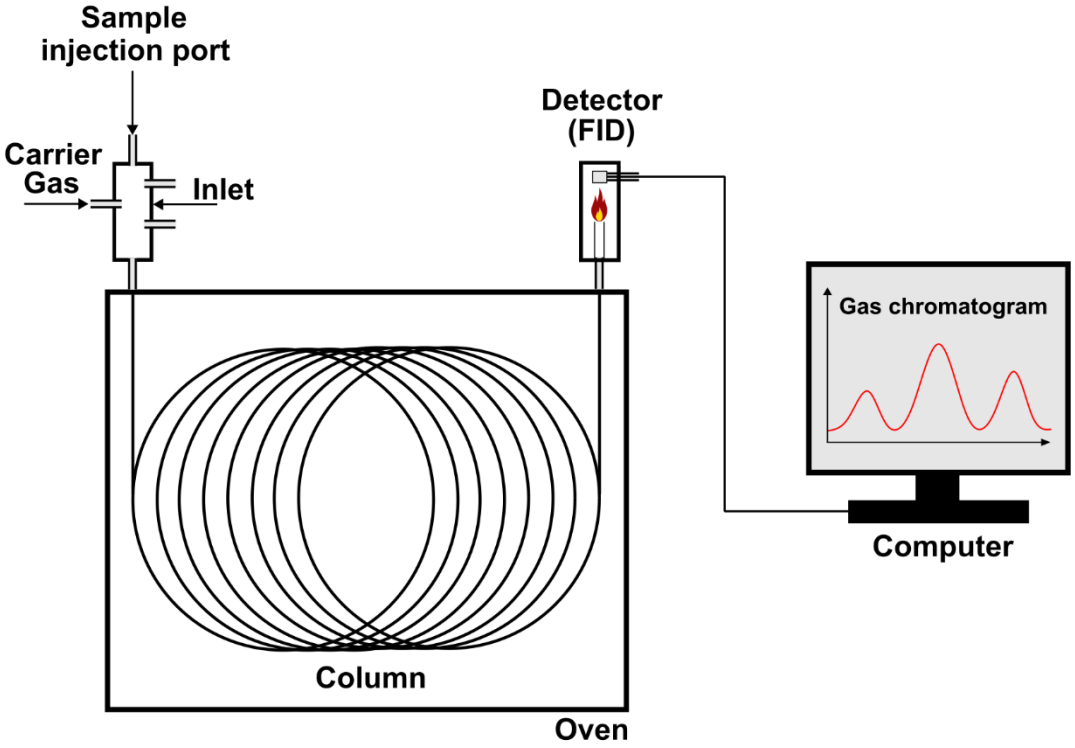

Figure 2.10 Schematic of a typical gas chromatograph

The various chromatographic processes are named according to the physical state of the mobile phase. Thus, gas chromatography (GC) is a specific type of chromatography where the mobile phase is an inert gas (also called carrier gas), which transports vaporised samples through a column containing the stationary phase. A schematic representation of a generic GC system with highlighted primary components is reported in **Figure 2.10**. The first main component is the GC inlet, which ensures accurate and reproducible sample introduction into the column. Sample is introduced through an injection port, where it is vaporised in a heated area to prepare it for transport. Depending on the application, different types of inlets are used. For instance, a split inlet is employed for high-concentration samples, allowing only a portion of the sample to enter the column while venting the rest, preventing column overloading. For trace-level analysis, a splitless inlet directs the entire sample into the column, maximising sensitivity. Once the sample is vaporised in the inlet, it is mixed with the carrier gas. The mixture is transported through the column, which is typically a coiled tube housed within a temperature-controlled oven. The column contains the stationary phase where the separation of compounds occurs based on their interactions with the stationary phase. Solutes arrive at the detector, which identifies and quantifies the separated components as they elute from the column. The Flame Ionization Detector (FID) is commonly used for detecting organic compounds; it operates by ionizing carbon-containing compounds in a hydrogen flame and measuring the resulting ions to produce a signal proportional to the concentration of the analyte. In GC-FID the inlet ensures the accurate delivery of a representative sample into the column. The consistent vaporization and transfer of the analytes are critical for the sensitivity and accuracy of the detection process. Hydrogen as the carrier gas further enhances the process by providing fast, efficient, and reproducible separation of compounds, which are then ionised in the FID for detection. This signal is transferred to the computer, where data are processed and graphically represented in a gas chromatogram. The repartition of the components between stationary phase and mobile phase in the column is mathematically described and controlled by the distribution constant K_c. This is defined as the concentration of the solute A in the stationary phase divided by its concentration in the mobile phase (Eq 2.8).[32]

$$K_c = \frac{[A]_S}{[A]_M} \qquad \text{(Eq 2.8)}$$

The distribution constant is a thermodynamic value that depends on temperature, and governs the migration rates of solutes through the column. It is influenced by the molecular properties of the analytes and their interactions with the stationary phase. This constant directly determines the retention time (R_t), which is the duration a compound spends in the column before reaching the detector. To optimise separations, GC systems commonly use temperature ramps, gradually increasing the oven temperature during the analysis. At higher temperatures, analytes exhibit reduced retention in the stationary phase, allowing compounds with stronger interactions to elute more quickly. By applying a temperature program, compounds with a wide range of volatilities can be efficiently separated in a single run. Less volatile components are driven out of the column faster as the temperature rises. This combination of the temperature-dependent distribution constant and temperature ramps ensures optimal resolution of analytes while reducing overall analysis time.

One of the key advantages of gas chromatography is its high sensitivity, particularly when paired with detectors like FID, which is ideal for organic compound detection. GC offers excellent resolution, the ability to separate complex mixtures efficiently, and the capability to analyse samples quickly. The use of temperature programming further enhances its effectiveness, allowing the separation of compounds with a wide range of volatilities within a single run. Additionally, the technique is relatively cost-effective for routine analyses, particularly when using hydrogen as the carrier gas, which is both efficient and readily available. However, gas chromatography has its limitations. It is restricted to volatile and thermally stable compounds, making it unsuitable for certain analytes that decompose under high temperatures. Sample preparation may be extensive, especially for compounds requiring derivatization to increase their volatility. The method also requires the right combination of optimised parameters such as the inlet type, temperature program, and carrier gas flow rate for accurate and reproducible results. Lastly, while detectors like the FID are highly sensitive to hydrocarbons, they are less effective for non-organic or polar compounds, often requiring the use of additional detection techniques.

2.7 Methods and operative conditions

X-ray photoelectron spectroscopy. XPS was carried out in a monochromated OmicronXM1000MK II X-ray photoemission spectrometer, with an EA125 analyser and an Al Kα (1486.7 eV) source; pass energies of 50 and 15 eV were used for survey and high-resolution spectra, respectively. Spectra were analysed using CasaXPS; best fits were carried out on spectra after Shirley background correction using mixed Gaussian-Lorentzian functions. Elemental compositions were obtained from peak areas of the high-resolutions cans.

Brunauer–Emmett–Teller surface area. BET specific surface area was determined from N_2 adsorption at 77 K with a Nova 2200e Surface Area Analyzer (Quantachrome, UK). The specific surface area was calculated from data in an optimal relative pressure range according to the method proposed by Rouqueral et al.,[33] by way of the Micropore BET Assistant feature of the NovaWin software. Pore size distributions were determined using the density functional theory (DFT) method[12,13] based on the calculation model: N_2 at 77 K on carbon (slit pore, NLDFT equilibrium model). Prior to analysis, the samples were outgassed at 250 °C under vacuum for 2 h.

Scanning electron microscopy. SEM was performed using a Zeiss Ultra microscope at 5 kV accelerating voltage, with InLens or SE2 detector.

Transmission electron microscopy. TEM was performed using a Jeol JEM 2100HR with an acceleration voltage of 200 kV, EDS SDD Oxford X–Max 80T detector and Jeol HAADF detector.

Raman spectroscopy. Raman spectroscopy was carried out using a Witec alpha 300R confocal scanning Raman system using 532 nm excitation; peak areas were analyzed using commercial software (CasaXPS).

Powder X-ray diffraction. XRD was performed using a D2 Phaser diffractometer with LynxEye detector (Bruker) and a CuKα source.

Thermogravimetric analysis. TGA was carried out using a Pyris 1 Thermogravimetric Analyzer (PerkinElmer) with a hold time of 10 min at 150 °C, followed by a 10 °C/min ramp in air to 900 °C.

Inductively coupled plasma-optical emission spectroscopy. ICP-OES was performed in a iCAP 7000 ICP-OES Analyser (Thermo Fisher); samples were treated in HNO_3 (≥ 65 %) overnight and diluted in Millipore water to a nominal concentration of 10 mg/L.

Energy-dispersive X-ray fluorescence analysis. XRF was performed using a Rigaku ED-XRF in He atmosphere on bulk solid samples; samples were prepared by selecting an appropriate sample cup with an XRF-transparent film (TF-240 polypropylene). The cup was then filled with the sample, ensuring a smooth and level surface, and sealed with the film to prevent sample loss.

Fourier-transform infrared spectroscopy. FTIR, was carried out on a FTIR Spectrum 100 spectrometer (PerkinElmer) using an attenuated total internal reflectance (ATR) diamond crystal;4 scans between the ranges of 4000 cm^{-1} and 400 cm^{-1} were collected and ratioed against background spectra obtained in air

Gas chromatography. Product analysis was carried out using an Agilent 8860 Gas Chromatograph coupled to a flame ionization detector (GC-FID), H_2 as carrier gas, split injection (1 :10,2 mL/min flow) anda DB-WAX UI column (30 m×0.250 mm×0.50 μm, Agilent J&W).

2.8 References

1. Hertz, H. Ueber einen Einfluss des ultravioletten Lichtes auf die electrische Entladung. *Annalen der Physik* **1887**,*267* (8),983-1000.

2. Hüfner, S. *Photoelectron spectroscopy: principles and applications*; Springer Science & Business Media,**2013**.

3. Chastain, J.; King Jr, R. C. Handbook of X-ray photoelectron spectroscopy. *Perkin-Elmer Corporation* **1992**,*40*,221.

4. Briggs, D. *Handbook of X-ray and ultraviolet photoelectron spectroscopy*;**1977**.

5. Hollander, J. M.; Jolly, W. L. X-ray photoelectron spectroscopy. *Accounts of chemical research* **1970**,*3* (6),193-200.

6. Eland, J. H. *Photoelectron spectroscopy: an introduction to ultraviolet photoelectron spectroscopy in the gas phase*; Elsevier,**2013**.

7. Shallenberger, J. R.; Smith, N. J.; Banerjee, J. Derivation of empirical XPS relative sensitivity factors from silicate glasses. *Surface and Interface Analysis* **2021**,*53* (6),569-579.

8. Brunauer, S.; Emmett, P. H.; Teller, E. Adsorption of gases in multimolecular layers. *Journal of the American chemical society* **1938**,*60* (2),309-319.

9. Sing, K. S. W. Adsorption methods for the characterization of porous materials. *Advances in Colloid and Interface Science* **1998**,*76-77*,3-11.

10. Galarneau, A.; Mehlhorn, D.; Guenneau, F.; Coasne, B.; Villemot, F.; Minoux, D.; Aquino, C.; Dath, J.-P. Specific Surface Area Determination for Microporous/Mesoporous Materials: The Case of Mesoporous FAU-Y Zeolites. *Langmuir* **2018**,*34* (47),14134-14142.

11. Barrett, E. P.; Joyner, L. G.; Halenda, P. P. The Determination of Pore Volume and Area Distributions in Porous Substances. I. Computations from Nitrogen Isotherms. *Journal of the American Chemical Society* **1951**,*73* (1),373-380.

12. Fierro, V.; Bosch, G.; Siperstein, F. R. Pore size distribution in microporous carbons obtained from molecular modeling and density functional theory. In *Studies in Surface Science and Catalysis*, Llewellyn, P. L., Rodriquez-Reinoso, F., Rouqerol, J., Seaton, N. Eds.; Vol.160; Elsevier,2007; pp 519-526.

13. Kupgan, G.; Liyana-Arachchi, T. P.; Colina, C. M. NLDFT Pore Size Distribution in Amorphous Microporous Materials. *Langmuir* **2017**,*33* (42),11138-11145.

14. Goldstein, J. I.; Newbury, D. E.; Michael, J. R.; Ritchie, N. W.; Scott, J. H. J.; Joy, D. C. *Scanning electron microscopy and X-ray microanalysis*; springer,**2017**.

15. Williams, D. B.; Carter, C. B.; Williams, D. B.; Carter, C. B. *The transmission electron microscope*; Springer,**1996**.

16. Stout, G. H.; Jensen, L. H. *X-ray structure determination: a practical guide*; John Wiley & Sons,**1989**.

17. Harris, K. D. M.; Tremayne, M.; Kariuki, B. M. Contemporary Advances in the Use of Powder X-Ray Diffraction for Structure Determination. *Angewandte Chemie International Edition* **2001**,*40* (9),1626-1651.

18. Coats, A.; Redfern, J. Thermogravimetric analysis. A review. *Analyst* **1963**,*88* (1053),906-924.

19. Bevis, J.; Bottom, R.; Duncan, J.; Farhat, I.; Forrest, M.; Furniss, D.; MacNaughton, B.; Nazhat, S.; Saunders, M.; Seddon, A. *Principles and applications of thermal analysis*; Wiley Online Library,**2008**.

20. Hollas, J. M. *Modern spectroscopy*; John Wiley & Sons,**2004**.

21. Beckhoff, B.; Kanngießer, B.; Langhoff, N.; Wedell, R.; Wolff, H. *Handbook of practical X-ray fluorescence analysis*; Springer Science & Business Media,**2007**.

22. Nölte, J. *ICP Emission Spectrometry: a practical guide*; John Wiley & Sons,**2021**.

23. Douvris, C.; Vaughan, T.; Bussan, D.; Bartzas, G.; Thomas, R. How ICP-OES changed the face of trace element analysis: Review of the global application landscape. *Science of The Total Environment* **2023**,*905*,167242.

24. Stuart, B. H. Infrared Spectroscopy: Fundamentals and Applications; John Wiley & Sons: Chichester, **2004**.

25. Smith, B. C. Fundamentals of Fourier Transform Infrared Spectroscopy; CRC Press: Boca Raton, FL, **2011**.

26. Ferraro, J. R. Introductory Raman Spectroscopy; Elsevier: Amsterdam, **2003**.

27. Ferrari, A. C.; Robertson, J. Interpretation of Raman Spectra of Disordered and Amorphous Carbon. *Phys. Rev. B* **2000**, *61* (20), 14095–14107.

28. Bard, A. J.; Faulkner, L. R.; White, H. S. *Electrochemical methods: fundamentals and applications*; John Wiley & Sons,**2022**.

29. Compton, R. G.; Banks, C. E. *Understanding voltammetry*; World Scientific,**2018**.

30. Connor, P.; Schuch, J.; Kaiser, B.; Jaegermann, W. The Determination of Electrochemical Active Surface Area and Specific Capacity Revisited for the System MnOx as an Oxygen Evolution Catalyst. *Zeitschrift für Physikalische Chemie* **2020**,*234* (5),979-994.

31. Ettre, L. S. Nomenclature for chromatography (IUPAC Recommendations 1993). *Pure and Applied Chemistry* **1993**,*65* (4),819-872.

32. McNair, H. M.; Miller, J. M.; Snow, N. H. *Basic gas chromatography*; John Wiley & Sons,**2019**.

33. Rouquerol, J.; Llewellyn, P.; Rouquerol, F. Is the BET equation applicable to microporous adsorbents? In *Studies in surface science and catalysis*, Vol.160; Elsevier,2007; pp 49-56.

CHAPTER 3

Design of M@C:N architectures: synthesis, characterisation and electrochemical study of Fe@C:N

Carbon porous materials containing nitrogen functionalities and encapsulated iron-based active sites (Fe@C:N) have been suggested as electrocatalysts for energy conversion, however their applications to the hydrogenation of organic substrates via ECH remain unexplored. This chapter examines the design and synthesis of Fe@C:N materials, offering detailed insights into the optimal annealing conditions and the impact of various carbon nanoscaffolds on the structural and electrochemical performance of the resulting materials.

This chapter presents result and contents reported in the candidate's first-author publication, titled:

Porous N-Doped Carbon-encapsulated Iron as Novel Catalyst Architecture for the Electrocatalytic Hydrogenation of Benzaldehyde

Pota, F.; Costa de Oliveira, M. A.; Schröder, C.; Brunet Cabré, M.; Nolan, H.; Rafferty, A.; Jeannin, O.; Camerel, F.; Behan, J. A.; Barrière, F.; Colavita, P. E.

ChemSusChem 2025,18 (1), e202400546

With the exception of specified contributions, the candidate conducted the primary investigation reported in the published work and prepared the first draft of the paper, along with subsequent revisions, under the supervision of Prof. Paula E. Colavita. The contributions of the other coauthors are as follows: M.A.C.O. development of the sample preparation methodology, C.S. & H.N. XPS analysis, M.B.C. computational study with COMSOL simulations, A.R. BET and PSD analysis, O.J. & F.C. SAXS analysis, J.A.B. & F.B. writing - review and editing, P.E.C conceptualization and supervision.

3.1 Introduction

Encapsulated metals within porous N-doped carbon frameworks (M@C:N) have received significant attention over the years as potential low-cost electrocatalyst for the HER and ORR.[1-4] However, their use in ECH of model organic compounds remains unexplored. M@C:N architectures are designed by carefully selecting the metal core, the type of carbon precursor, the annealing procedure and, if applicable, a carbon nanoscaffold. Each of these components plays a critical role in producing a stable electrode material with practical applications in ECH, ensuring a balanced trade-off between cost and potential performance.

Most electrode materials are able to yield some level of organic hydrogenation at high overpotentials; this has been shown e.g. for Hg or for pure graphitic carbons which are poor at activating hydrogen.[5-7] Therefore, in a M@C:N architecture at low overpotentials, the metal centres are expected to be the active sites, determining its effectiveness and usability as electrocatalyst for ECH. An ideal metal should possess activity for the HER so as to facilitate the Volmer step without fully suppressing ECH. Iron is a good example in this sense since it displays moderate HER activity leaving room for potential ECH applications.[2,8] Additionally, iron is highly appealing due to its abundance, sustainability, and relatively uniform geographic distribution, which contributes to its low criticality index.[9,10] Indeed, iron-based catalysts have been largely studied in the hydrogenation of several model organic compounds. HMF and glucose hydrogenations were studied by Kwonet al.[11-13] at Fe electrodes; crotonaldehyde and hydroxyacetone hydrogenations were reported on Fe catalysts;[14,15] while Fe supported on graphite was used in the hydrogenation of acetophenone.[16] Furfural was hydrogenated on Fe electrodes with high selectivity in acid electrolyte towards the pinacol dimerization product;[17] however ECH experiments with Fe cathodes reported methylfuran (MF) as the preferred product.[18] Most recently, an iron-molybdenum phosphide heterostructured electrode was demonstrated for the electrocatalytic reduction of nitro groups.[19] In a M@C:N structure the metal core can be protected by a carbon shell that prevents air oxidation, degradation and corrosion of the active sites so as to preserve the activity of the catalyst itself. This carbon shell can be generated during the annealing step of a carbon precursor which is usually an organic sol-gel resin. The most popular resin is a resorcinol-formaldehyde resin that can be further modified including melamine as source of nitrogen to generate an N-doped carbon

framework. N-doping has been suggested to enhance the rate of the Volmer step relative to a N-free carbon surface.[20] While the above effects have been extensively studied in the context of HER, their potential to enhance ECH activity in M@C:N architectures remains unexplored. To date, no studies have tested M@C for ECH, and its applicability has not been suggested in the literature.

The annealing step is also important because it results in the graphitisation of the porous material. This process enhances the material's properties for electrode applications by creating a more ordered, robust, and conductive carbon structure. One of the key objectives during annealing is to minimise the oxidation of both carbon and metal centre during evolution of decomposition products, as a less oxidised structure is generally more beneficial for performance in terms of conductivity, stability, and catalytic activity.[21] High oxygen content in carbon-based materials, such as graphene or carbon nanotubes, can disrupt their conductive properties by introducing defects into the sp^2 carbon network. These defects interrupt the continuous pathways necessary for efficient electron transport, significantly reducing electrical conductivity.[22] Oxidation also impacts the chemical stability of the material. Materials with high oxygen content are more susceptible to degradation under harsh conditions, such as acidic or basic environments, making them less suitable for long-term applications. In catalytic processes, oxygenated groups on the surface can impede performance by blocking active sites or altering the material's intrinsic electrochemical properties. A less oxidised structure helps to preserve a high density of accessible active sites, thereby improving the catalytic efficiency. However, excessive surface stability can be detrimental, as it may hinder adsorption. Overall performance is therefore a balance between these factors: surface functionalities are needed for activation, but their density and type must be carefully controlled to prevent excessive reactivity, which often leads to degradation and loss of conductivity in carbon materials.

Finally the carbon nanoscaffold is a crucial component in a M@C:N designs since it acts as a substrate onto which encapsulated architectures are dispersed, and can have a strong impact on the final properties of the catalyst. For large-scale applications, the use of commercial carbon blacks as a carbon nanoscaffold is advantageous in terms of commercial availability, low cost and their good properties (e.g. conductivity, surface area) compared with other carbon nanostructures, such as carbon nanofibers and carbon nanotubes, which are more expensive and primarily restricted to academic purposes.

Commercially available carbon blacks such us Black Pearl 2000® (BP) and Vulcan XC72R® (VUL) are then attractive as conductive and porous support for metal cores. The above two carbon materials however differ in terms of morphology/properties. First, their BET specific surface areas are 1400 m^2/g vs 240 m^2/g for BP and VUL, respectively.[23] Second, BP shows an average particle size of 15 nm[24] while VUL has particles in the 50-60 nm range.[25] Finally, BP has high surface area and pore volume, while VUL has a low surface area and pore volume.[26] These properties have a strong impact on the conductivity of the carbon material as well as on the electrochemical response of the final electrocatalyst. In fact, it has been shown that an increase in porosity decreases the conductivity and can bring high ohmic losses;[24] nevertheless, high values in surface area can be advantageous to increase the density of active sites and, as a consequence, the effective activity of fabricated electrodes.[27,28] Notably, this effective activity depends not only on the intrinsic activity of the material but also on factors such as loading of catalyst. Trade-offs between these parameters must therefore be considered in the choice of the carbon scaffold in order to optimise electrocatalytic and material performances.

In this chapter, the design and synthesis of M@C:N materials with Fe as the metal core are examined in detail. Four distinct Fe@C:N architectures are prepared by combining two types of carbon nanoscaffolds with different annealing processes. Optimal conditions for pyrolysis are identified using XPS as a diagnostic analysis. The optimised samples undergo further structural characterisation through a combination of surface, bulk, and electron microscopy techniques. Electrochemical characterisation is carried out for both the HER and ECH cathodic reactions using BZH as a model compound. Cyclic voltammetry (CV) and linear sweep voltammetry (LSV) experiments are performed on glassy carbon disk (GC disk) electrodes in two supporting electrolytes to evaluate the effects of pH changes. The results presented in this chapter establish a foundation for understanding the design and synthesis of M@C:N architectures using Fe as the active site. Insights are provided into the optimal annealing conditions and the role of different carbon nanoscaffolds in influencing the structural and electrochemical performance of the resulting materials.

3.2 Experimental section

Materials. Iron (II) acetate (95%), Nafion® 117 solution (5%), resorcinol (99%), Pluronic F-127, melamine (99%), hydrochloric acid (37%), sulfuric acid (95–98%), nitric acid (≥ 65%), formaldehyde solution (37 wt.%), hydrogen peroxide (30%), sodium sulphate (> 99%); benzaldehyde (BZH, > 99%) were all purchased from Sigma Aldrich and used as received. Ethanol (>99%) was purchased from Fisher and used as received. Black Pearls 2000® (BP) and Vulcan XC72R® (VUL) were purchased from Cabot.

Catalyst Synthesis. BP and VUL were initially pre-treated through oxidative purification to remove metal impurities and improve hydrophilicity[29,30]. The carbon black materials underwent a 4 h reflux in concentrated HNO_3 at 90 °C, followed by filtration and washing with distilled water until reaching a neutral pH. The resulting carbon paste was dried at 50 °C for two days, then ground in an agate mortar for further use.[1,31] Porous carbon-based catalysts were prepared as follows: Resorcinol (1.65 g), Pluronic F-127 (2.5 g), and melamine (0.84 g) were dissolved in a 40 mL water-ethanol solution (1:1 by volume) and stirred for 15 minutes. $Fe(CH_3COO)_2$ (1.5 g) was added as the metal precursor, followed by 0.2 g of concentrated HCl, with stirring continued for 1 hour. A formaldehyde solution (2.5 g) was then added dropwise, and the mixture was vigorously stirred for another hour to form a homogeneous slurry. Purified BP or VUL (1.5 g) were added to this mixture and stirred for 15 more minutes. The resulting mixture was placed in a Teflon-lined autoclave and heated at 50 °C for 2 days. Samples were then dried at 50 °C for two days and ground in a mortar. Finally, the product was pyrolysed at 800 °C for 2 h in an N_2/NH_3 flow (1:1 vol.,200 sccm) using two different methods referred to as annealing procedure-(α) and annealing procedure-(β) (see **Figure 3.2**).

Electrochemical characterisation. Catalyst (0.0100 g ± 0.0003) was used for the preparation of an ink dispersion, adding 135 µL of Millipore water, 270 µL of isopropyl alcohol (IPA) and 50 µL of Nafion solution. The ink was sonicated at room temperature prior to drop casting on glassy carbon disk working electrode (GC disk, Ø 5 mm, HTW GmbH), finally let it dry under N_2 flow, as shown in **Figure 3.1**. GC disks were polished with decreasing grades of alumina slurry (Ted Pella) according to published procedures;[32] disks were thoroughly sonicated and rinsed between polishing steps to remove any residue from the preceding step. GC disks were mounted in a Teflon disc holder (Pine instruments) and modified with the ink dispersion (10 µL), then dried under inert gas,

resulting in a loading of 1.10 mg cm^{-2}. A Pt disk electrode (Ø 3 mm, eDAQ) was used for comparison; prior to experiments using Pt as electrode, the disk was polished and then cleaned by cycling into the anodic region until the characteristic response of polycrystalline Pt was obtained.[33-35] CVs and LSVs experiments were carried out using a standard 3-electrode cell controlled by a potentiostat (Metrohm Autolab), using graphite rods (Morgan Advanced Materials) as counter electrodes (CE) and Ag/AgCl (1 M KCl) as reference electrode (RE,0.235 V vs SHE). All potentials are reported vs the relative hydrogen electrode (RHE) based on the experimentally determined pH of the electrolyte. The cell was cleaned with piranha and Millipore water prior to each experiment, then filled with 250 mL volume of supporting electrolytes (0.100 M H_2SO_4 or 0.100 M Na_2SO_4); the electrolyte was purged with N_2 for at least 15 min prior to characterization.

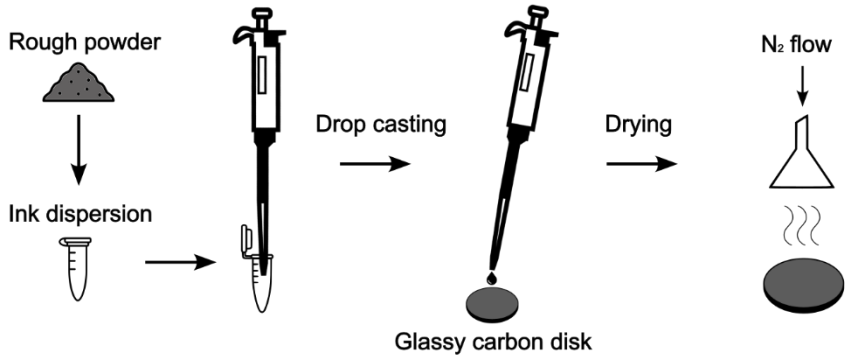

Figure 3.1 Schematic representation of working electrode preparation from ink preparation, drop casting and drying under nitrogen flow.

3.3 Results and discussion

3.3.1 Synthesis of Fe@C:N and optimisation of annealing procedure

Electrode materials were synthesised using a protocol[1] based on hydrothermal reactions of a resorcinol resin[36] in the presence of metal precursor, soft template and conductive carbon black, as schematically shown in **Figure 3.2a**. Resorcinol resin is synthesised via polycondensation of resorcinol and formaldehyde in a mixture of alcohol and water containing BP or VUL as conductive carbon black support. The presence of melamine and Pluronic F-127 leads to nitrogen incorporation in the carbon network and increases the surface area of the material,[37,38] yielding a carbon-supported resin here onwards

referred to as FeRPM/BP or FeRPM/VUL, based om which carbon black support used in the preparation.

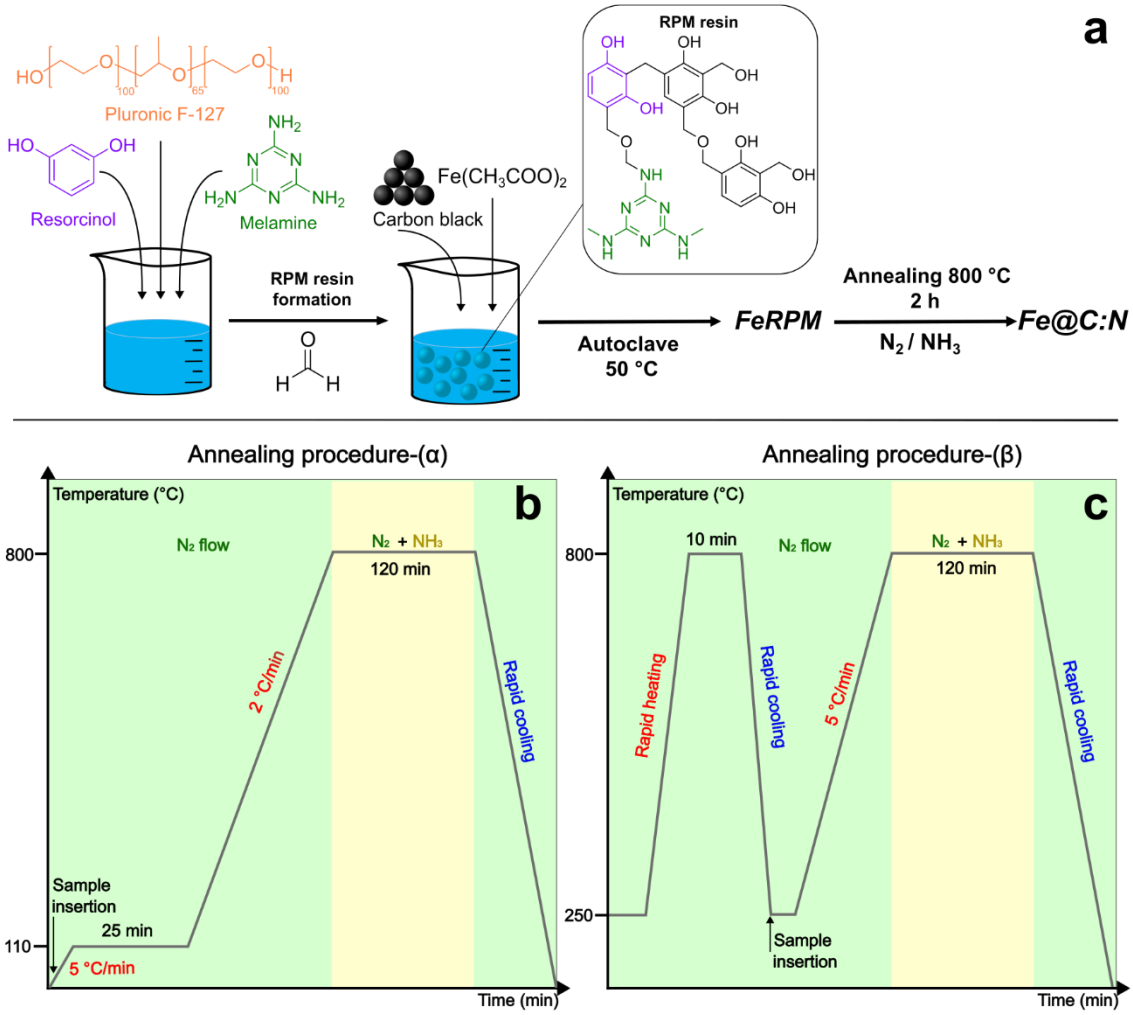

Figure 3.2 (a) Scheme showing the main steps in the materials synthesis protocol. Schematic representation of annealing procedure-(α) and annealing procedure-(β). Figure adapted from Pota et al. reference 39.

The resin was then pyrolysed using two different thermal annealing protocols named annealing procedure-(α) and annealing procedure-(β), and schematically illustrated in **Figure 3.2b** and **Figure 3.2c**, respectively. These two annealing procedures mainly differ in their temperature ramping and sample insertion timing. In annealing procedure-(α), the sample is placed in the furnace at room temperature, and the temperature is gradually increased in two stages: first at 5 °C/min, then at 2 °C/min, until it reaches 800 °C. The temperature is then held constant for 2 h in a mixed N_2/NH_3 atmosphere. This procedure had been previously used in the group for the synthesis of M@C:N electrocatalysts for the ORR and was therefore first investigated for ECH applications in this thesis.[1] In contrast, annealing procedure-(β) includes a pre-annealing step where the furnace is

rapidly heated to 800 °C, followed by rapid cooling before inserting the sample. After insertion, the temperature is ramped up at 5 °C/min to 800°C and held constant for 2 h in N_2/NH_3 atmosphere. The final result of these pyrolysis processes is a graphitised carbon matrix surrounding the N-functionalities and Fe-rich clusters. From this point forward, the annealed samples will be referred to as Fe@BP:N-(α), Fe@BP:N-(β), Fe@VUL:N-(α), and Fe@VUL:N-(β), based on the carbon nanoscaffold (BP or VUL) and the annealing procedure (α or β) used in their synthesis.

XPS surface analysis was used to characterise annealed samples and compare the outcomes of the different pyrolysis procedures in order to determine optimal conditions; a more detailed XPS characterisation of the optimised samples is presented in the next paragraph. **Figure 3.3** shows the XPS survey spectra for Fe@BP:N-(α), Fe@BP:N-(β) and Fe@VUL:N-(α), Fe@VUL:N-(β) normalised by the carbon peak intensity (285 eV) to allow for easier comparison. Characteristic peaks corresponding to Fe $2p_{3/2}$ (710 eV), N 1s (398 eV), C 1s (284 eV), and O 1s (531 eV) are observed, with additional peaks attributed to the indium foil used as support.[40]

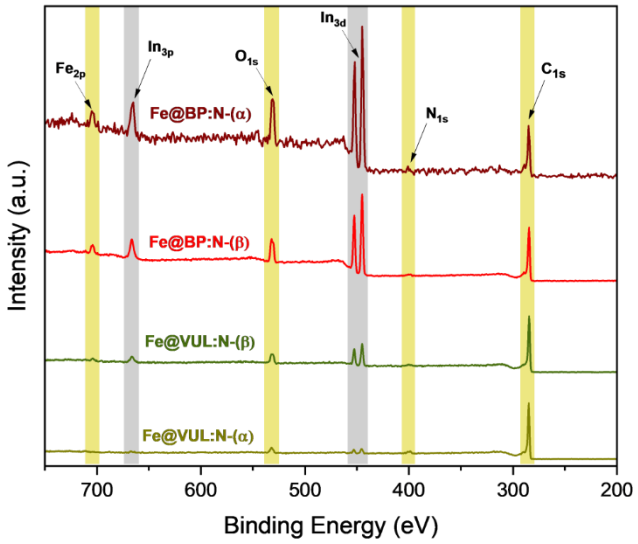

Figure 3.3 XPS survey overlays for annealed samples. Peaks corresponding to the In foil used as support are highlighted in grey, while peaks of interest are marked in yellow.

The elemental composition, detailed in **Table 3.2**, was calculated from the area ratios of high-resolution scans of core level excitations, after correcting for relative sensitivity factors. **Figure 3.4a** shows the best-fit of the C 1s obtained using five components, attributed to sp^2 (284.4 eV) and sp^3 (285.3 eV) carbon, C-O/C-N (286.0 eV), C=O/COOH

(287.5 eV) groups, and π- π* transitions (289.5 eV).[40-43] For all samples the C sp^2 component is larger than the C sp^3, suggesting that the majority of carbon observed is part of a graphitised network as the result of the annealing processes.

Table 3.1 Elemental composition in atomic-% obtained from XPS high-resolution spectra for annealed samples.

Sample	C (%)	O [a] (%)	N (%)	Fe (%)	C_{sp^2}/C_{tot} [b] (%)	O/C (%)
Fe@BP:N-(α)	78.5	18.3	2.85	0.34	39.4	23.3
Fe@BP:N-(β)	88.5	7.39	2.25	1.82	60.8	8.34
Fe@VUL:N-(α)	91.7	4.21	3.85	0.21	68.4	4.59
Fe@VUL:N-(β)	91.8	3.92	3.50	0.71	70.3	4.26

a – atomic-% content calculated from the contribution to the O 1s area that does not arise from In_2O_3.

b – Calculated as area ratio of the best-fit component at 284.4 eV over the total C 1s peak.

The degree of graphitisation can be assessed by examining the percentage of the peak at 284.4 eV (C sp^2) relative to the total C 1s peak area, with a higher %-contribution suggesting a higher degree of graphitisation. Comparing the two preparation methods, the annealing procedure-(β) results in a higher degree of graphitisation for both BP- and VUL-based materials (**Table 3.1**). This effect is especially pronounced in the BP-based samples, where procedure-(β) produces a degree of graphitisation 1.5 times greater than procedure-(α); for Fe@VUL:N although a difference is still observed, it is less significant. **Figure 3.4b** shows the best-fit of the O 1s obtained using two components at 532.2 and 530.2 eV, that can be assigned to O^{2-} from C=O groups and OH^- from oxides/hydroxides, respectively.[44,45] Both contributions may be affected by the formation of In_2O_3 due to the use of indium foil for sample mounting.[32] For this reason, the oxygen content in the samples was determined by subtracting the oxide contribution from the indium foil from the total area of the O 1s peak (**Table 3.1**). To estimate the level of oxidised species in the samples, O/C ratio was calculated, and results align with the degree of graphitisation presented in **Table 3.1**. Fe@BP:N-(β) results to have O-containing functionalities almost three times lower than Fe@BP:N-(α). For VUL-based samples the difference in O/C is instead negligible, with values consistent with the typical O/C content observed for air exposed graphitic carbons.[32] Additionally, the total amount of Fe incorporated in the subsurface is higher for procedure-(β) compared to procedure-(α) for both BP- and VUL-based samples, as shown in **Table 3.1**; suggesting that procedure-(β) has a greater capacity for metal incorporation than procedure-(α).

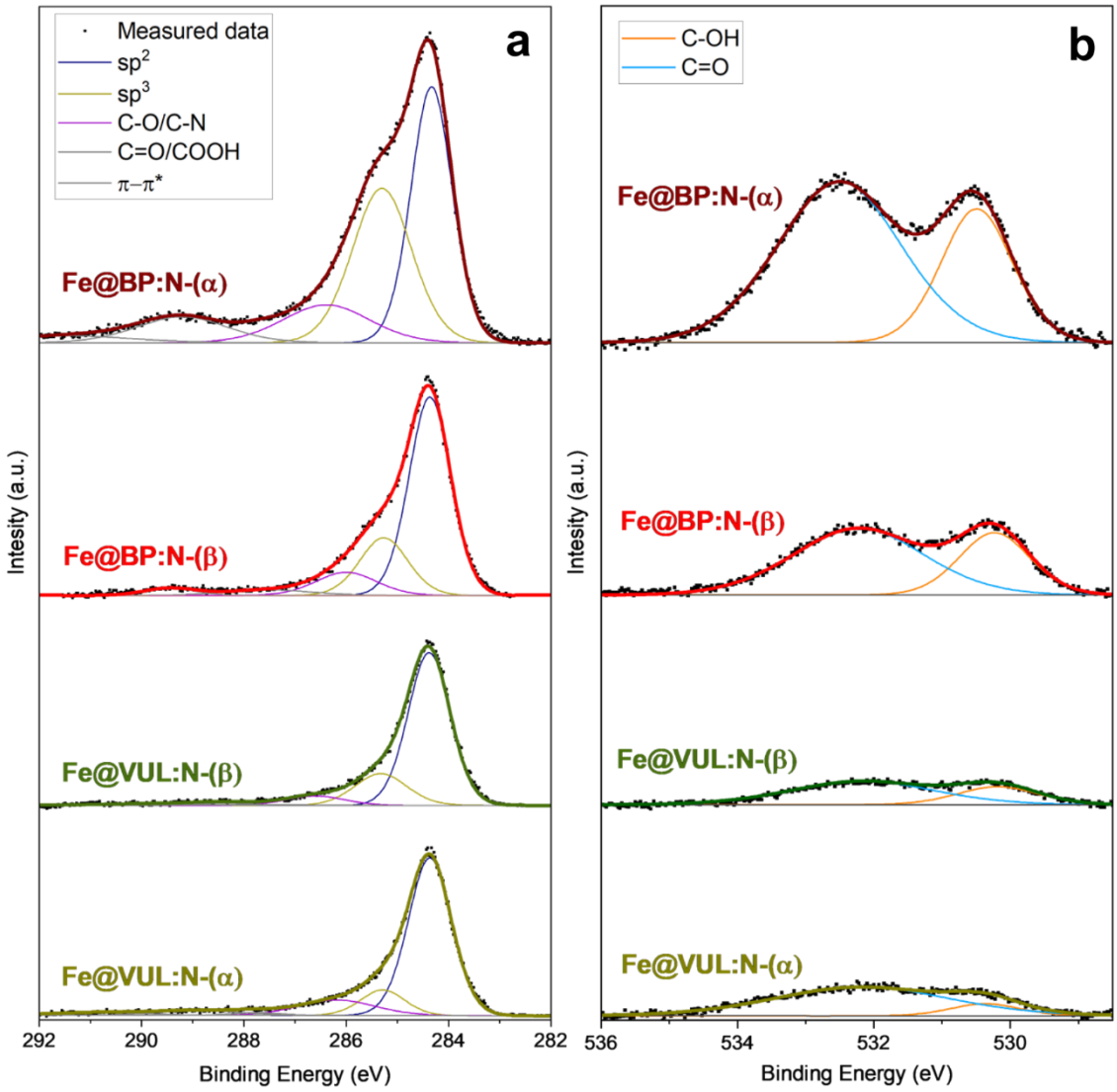

Figure 3.4 Best-fit components and simulated spectral envelope from XPS analysis for (a) C 1s and (b) O 1s of annealed samples.

It is therefore reasonable to conclude that annealing procedure-(β) is more effective and performing for preparing Fe@C:N architectures compared to procedure-(α), since it results in a higher degree of graphitisation, greater metal incorporation, and a lower or similar level of oxidised species. For these reasons, samples obtained by annealing procedure-(α) were excluded from further structural characterization in favour of the optimised samples obtained by procedure-(β). For simplicity, Fe@BP:N-(β) and Fe@VUL:N-(β) will be referred to as Fe@BP:N and Fe@VUL:N from this point forward.

3.3.2 Comparison of carbon black nanoscaffolds

After identifying the optimal annealing conditions, a series of characterisation techniques were conducted to examine the impact of using BP or VUL as carbon black nanoscaffolds on the structure, composition, and electrochemical performance of the samples.

The specific surface area and pore structure of the annealed samples were determined using BET analysis and DFT method applied to N_2 sorption isotherms.[46-48] The BET surface area for Fe@BP:N was measured at 430 m^2/g, while Fe@VUL:N exhibited a lower value of 371 m^2/g. This is consistent with BP possessing a BET area >1400 m^2/g compared to 240 m^2/g for VUL.[23] The pore structure of annealed samples can be analysed using the adsorption/desorption isotherms shown in **Figure 3.5a**.

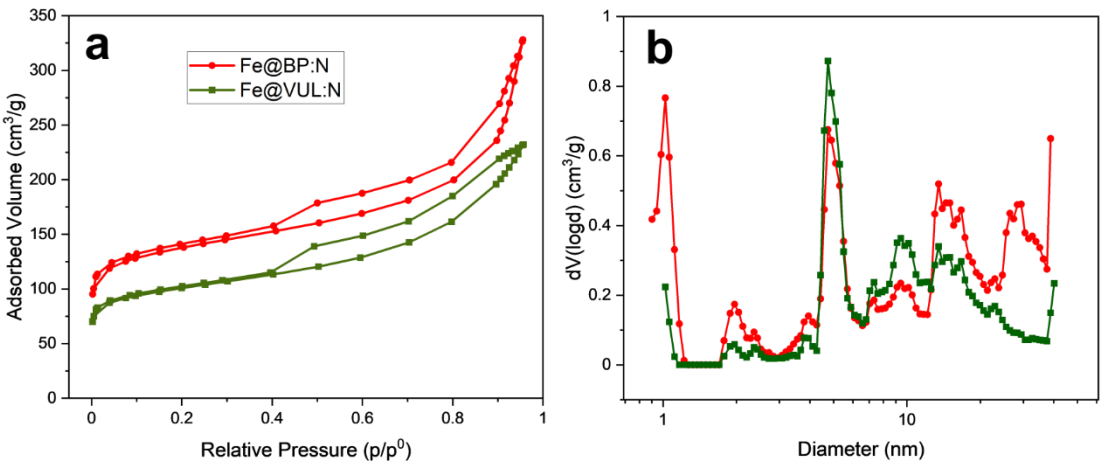

Figure 3.5 (a) Nidrogen adsorbion isotherms and (b) pore size distributions obtained for Fe@BP:N and Fe@VUL:N

Both materials displaying similar hysteresis loops characteristic of type IV isotherms associated with capillary condensation, and type H4 loops reported for narrow slit-like mesopores.[49,50] At high relative pressure ($p/p^0 > 0.8$) Fe@BP:N shows a steeper isotherm compared to Fe@VUL, suggesting higher macroporosity in the BP-based sample. This is consistent with the sharp increase in adsorption typically observed at high relative pressures, which indicates significant macroporosity as large pores fill rapidly when the pressure approaches saturation ($p/p^0 = 1$). Moreover Fe@BP:N results in a higher adsorbed volume compared to Fe@VUL:N and this is coherent with higher surface area recorded for the BP-based sample. Pore size distributions (PSDs) reported in **Figure 3.5b**

for both samples show similar distributions, with a prominent peak at 4.7 nm and smaller peaks across the measured range. Fe@BP:N demonstrates a higher pore volume in the range of 7.34 to 39 nm, aligning with the higher surface area measured for this sample compared to the VUL-based sample.

Figure 3.6a shows TGA curves in air for FeRPM/BP and Fe@BP:N samples, i.e. before and after the annealing process; data for the BP scaffold materials is also shown for comparison. Pure BP particles undergo a single combustion process at high temperature yielding a negligible residual mass of 3.7%. The FeRPM/BP solid obtained from the hydrothermal reaction yielded two broad weight loss processes, a first one at *ca.*230 ºC and a second one at *ca.*430 ºC, with a final residual mass of 9.5%. After graphitisation, Fe@BP:N materials show a single well defined mass loss at *ca.* 360 ºC with a final residue of 20.6%. This observation is consistent with the sample undergoing graphitisation, yielding a more crystalline and stable carbon structure that is oxidised at higher temperatures than the partially graphitised FeRPM/BP. Assuming that the inorganic residue from Fe@BP:N consists of Fe_2O_3 exclusively, the observed 20.6% corresponds to an estimated Fe-content of 14.4% by wt. This value is in excellent agreement with that determined by ICP-OES after accounting for the BP solid residue, yielding in an Fe-content of 10.7% by wt. Notably, a lower decomposition temperature was observed for Fe@BP:N compared to BP; this is likely due to the presence of iron oxides which are known to catalyse the oxidation of carbons.[51] Similar results are observed for VUL-based samples, as shown in **Figure 3.6b**. FeRPM/VUL shows two processes, a first one at *ca.*230 ºC and a second one at *ca.*475 ºC; while, the annealed sample Fe@VUL:N shows two processes at *ca.*390 ºC and 560 ºC, with the second process likely due to oxidation of the carbon scaffold, which in this case is observed probably due to the structural differences between BP and VUL nanomaterials. For Fe@VUL:N and FeRPM/VUL residues of 16.7% and 6.62% were observed, respectively, yielding estimated Fe% content of 11.8% wt. and 4.6% wt. Also in this case the annealed sample shows a lower degradation temperature compared to the pure carbon scaffold, and this can be justified as discussed above in relation to previous reports for Fe@BP:N.[51] **Figure 3.6c and 3.6d** present FTIR transmittance spectra for BP- and VUL-based samples, respectively, in the 1800 - 450 cm^{-1} range. Pure BP and VUL nanomaterials show mostly feature-less spectra due to the absence of oxidised groups or other functionalities. For both carbon scaffolds, the spectra of samples before annealing (FeRPM/BP and FeRPM/VUL) show broad peaks

consistent with the presence of an RPM resin.[38,52] The absence of peaks in the annealed samples (Fe@BP:N and Fe@VUL:N) further supported TGA results indicating that materials undergo significant graphitisation. Finally, Raman spectroscopy performed on Fe@BP:N also confirmed graphitisation as evidenced by an increase after annealing of the D-band contribution that is associated with the breathing mode of six-membered rings in graphitic carbons (Appendix I, **Figure A.1**), and in agreement with graphitisation trends in amorphous carbon materials.[53]

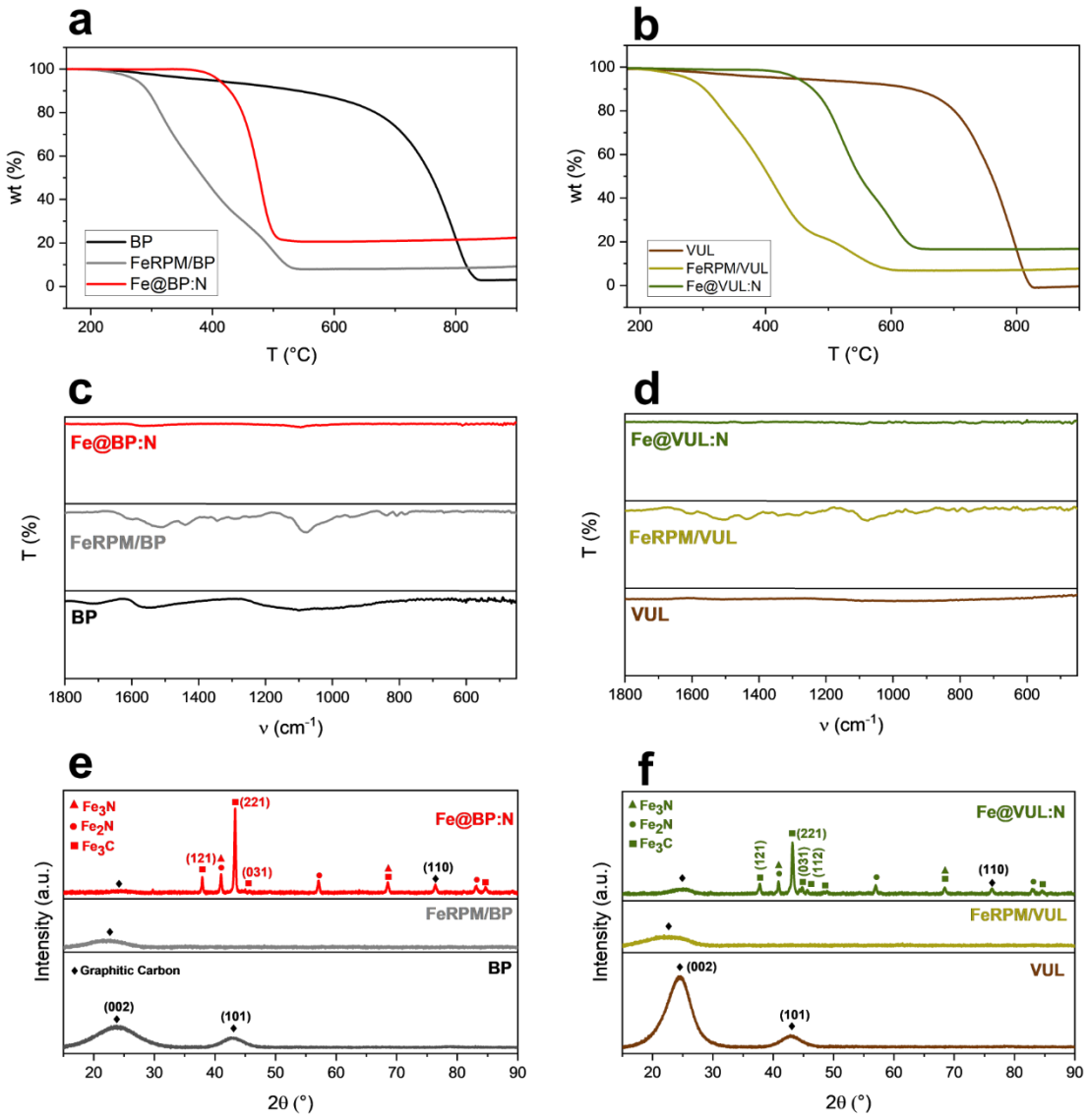

Figure 3.6 TGA curves (a), FTIR spectra (c) and XRD profiles (e) measured for BP, FeRPM/BP and Fe@BP:N. TGA curves (b), FTIR spectra (d) and XRD profiles (f) measured for VUL, FeRPM/VUL and Fe@VUL:N. Figure adapted from Pota et al. reference 39.

Figure 3.6e shows XRD data for BP, FeRPM/BP and Fe@BP:N materials. The only prominent peaks in the patterns of BP and FeRPM/BP can be indexed as (002) at 23.7º with d =3.75 Å, and (101) at 42.9º with d = 2.10 Å, reflections of the graphite structure, in agreement with literature values.[54,55] The large fwhm observed is indicative of structural disorder in the carbon phase. In the case of Fe@BP:N the pattern is instead dominated by relatively narrow and intense peaks; reflections at 2θ = 37.8º,43.3º and 44.5º are in good agreement with (121), (211) and (031) reflections, respectively, of Fe_3C;[1] peaks at 2θ = 41.0º,57.1º,68.5º,83.0º and 84.7º are assigned to contributions from nitrides and carbides in agreement with reference patterns for Fe_2N (PDF#73–2102), Fe_3N (PDF#01–1236) and Fe_3C (PDF#89–2005). The formation of nitrides and carbides is consistent with a process involving carbonisation of the organic resin under the ammonia-rich atmosphere while in the presence of iron salts. XRD does not show evidence of crystalline Fe^0, given the absence of any of the characteristic peaks at 65.2° and 85.2°, or at 63.4° and 80.1° of metallic iron patterns PDF#87-0722 and PDF#89-4186, respectively (Appendix I, **Figure A.2**). Therefore, the XRD pattern indicates that the annealing process results in the decomposition of the iron salt and its reduction to carbide-nitride solids. A similar analysis applies to the XRD patterns of the VUL-based samples, as shown in **Figure 3.6f**. Pure VUL shows graphite reflections (002) and (101) at 24.4º (d =3.63 Å) and 42.9º (d = 2.10 Å), respectively; while FeRPM/BP shows a single peak at 22.7º indexed as (002). For Fe@VUL:N peaks similar to those in Fe@BP:N are observed: peaks at 2θ =37.8º,43.3º,44.7º and 45.7º correspond to the (121), (221), (031) and (112) reflections of Fe_3C, while those at 2θ = 40.8º,56.9º,58.4º,82.9º, and 84.6º are attributed to contributions from nitrides and carbides. The crystallite size for the Fe phase was estimated in both annealed materials using the Scherrer equation, taking into account the well resolved peaks at 43º. For Fe@BP:N the crystallite size was estimated at 30.3 nm, and for Fe@VUL:N at 23.6 nm. The average crystallite size for Fe@BP:N is therefore larger than for Fe@VUL:N, which is consistent with results from TGA analysis.

Surface analysis of the annealed samples was performed using XPS**. Figure 3.7** shows survey spectra for Fe@BP:N and Fe@VUL:N already presented in **Figure 3.3**, revisited now in a larger binding energy range and normalised by the carbon peak intensity. Characteristic peaks are labelled as before with the addition of the peak at 18 eV assigned to In 4d. **Table 3.2** revisits the elemental composition of the two samples calculated from

the area ratios of high-resolution scans of core level excitations (as in **Table 3.1**), with the addition of N-composition details.

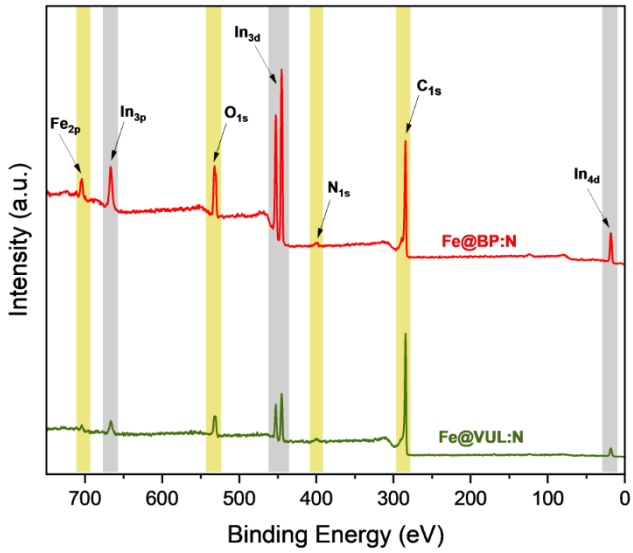

Figure 3.7 XPS survey overlays for Fe@BP:N and Fe@VUL:N. Peaks corresponding to the In foil used as support are highlighted in grey, while peaks of interest are marked in yellow. Figure adapted from Pota et al. reference 39.

Table 3.2 Elemental composition in atomic-%, obtained from XPS high-resolution spectra of Fe@BP:N and Fe@VUL:N.

Sample	C (%)	O [a] (%)	N (%)	Fe (%)	Graphitic-N (%)	Pyridinic-N (%)	Pyrrolic-N (%)	C_{sp^2}/C_{tot} [b] (%)
Fe@BP:N	88.5	7.39	2.25	1.82	14.9	42.5	42.6	60.8
Fe@VUL:N	91.8	3.92	3.50	0.71	10.1	43.6	46.3	70.3

a – atomic-% content calculated from the contribution to the O 1s area that does not arise from In_2O_3.

b – Calculated as area ratio of the best-fit component at 284.4 eV over the total C 1s peak.

Figure 3.8a and 3.8b show best-fits of the Fe $2p_{3/2}$ spectra of Fe@BP:N and Fe@VUL:N, respectively; these display two maxima at 704 and 710 eV. The peak at 704 eV was best-fit using a single component that can be assigned to Fe, Fe_xC or Fe_xN species based on its binding energy.[56-58] Iron carbides, its nitrides and metallic iron all have similar binding energies and cannot be fully resolved via XPS,[56-58] however, based on the XRD results the contribution at 704 eV likely arises from carbides and/or nitrides. The envelope with maximum at 710 eV is consistent with the presence of Fe(III) oxides/oxyhydroxides, which typically give rise to multiple peaks and an overall asymmetric line shape;[59] accordingly, the best-fit was obtained using multiple peaks (709.8,710.8,711.6,711.9 and

713.0 eV) all assigned to Fe(III) oxide species. For both samples the 704 eV peak has significantly higher intensity than the oxide components, thus indicating that most of the iron present at the surface/sub-surface is in a low oxidation state. Importantly, metallic iron and its carbides/nitrides are known to be easily oxidised in air;[60,61] therefore, the absence of significant FeO_x contributions in the Fe 2p spectrum strongly suggests that iron-rich phases are encapsulated and thus protected from oxidation by a carbon shell when using either of BP or VUL as nanoscaffolds. Values in **Table 3.2** show that Fe@BP:N has a higher surface %Fe content compared to Fe@VUL:N, and this is consistent with Fe being able to penetrate more deeply inside the carbon scaffold.

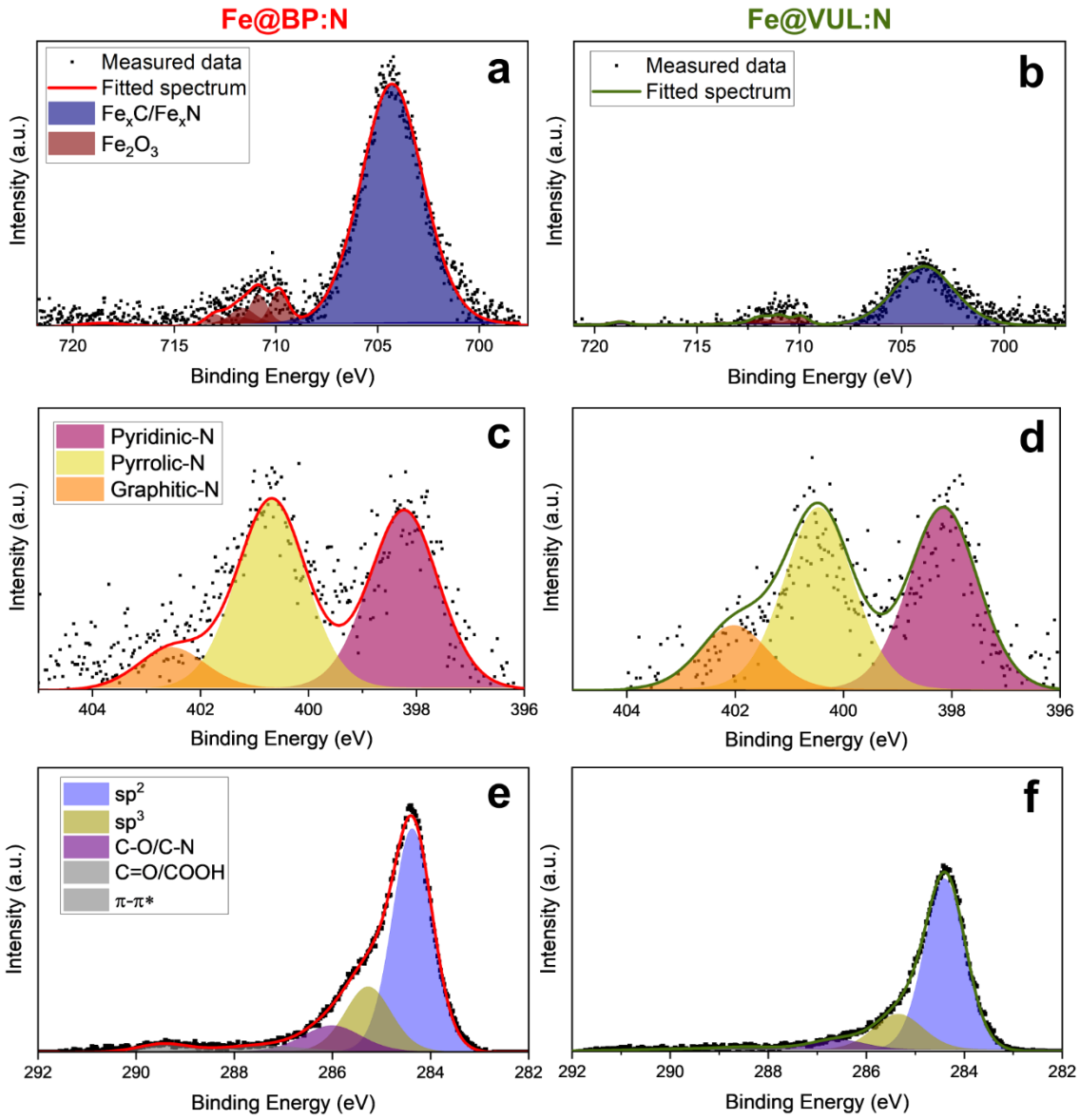

Figure 3.8 XPS high resolution spectra of Fe $2p_{3/2}$ (a), N 1s (c) and C 1s (e) for Fe@BP:N; and of Fe $2p_{3/2}$ (b), N 1s (d) and C 1s (f) for Fe@VUL:N. Figure adapted from Pota et al. reference 39.

For Fe@BP:N most of the Fe remains at the surface and is encapsulated inside the resorcinol resin with a thinner layer as previously reported using a similar protocol.[1] **Figure 3.8c and 3.8d** show best-fits of the N 1s spectra of Fe@BP:N and Fe@VUL:N, respectively, which were obtained using three components attributed to graphitic-N (400.9 eV), pyrrolic-N (400.0 eV) and pyridinic-N (398.0 eV).[41,62] The relative contributions of these three functionalities are reported in **Table 3.2** and indicate that the majority of the nitrogen is present in the form of pyrrolic/pyridinic groups for both analysed samples, while Fe@VUL:N displays a larger total nitrogen content compared to Fe@BP:N. It was not possible to resolve any contributions at 397 eV expected for Fe-N species;[58] this is likely due to their relative contributions being much smaller than those arising from N-functionalities in the carbon scaffold. **Figure 3.8e and 3.8f** show best-fits of the C 1s spectra of Fe@BP:N and Fe@VUL:N, respectively, already presented in **Figure 3.4** and obtained using the same five components. The absence of a carbide peak indicates that most of the C 1s intensity arises from the graphitised scaffold, consistently with a surface Fe-content of *ca*.1.8% and 0.71% for Fe@BP:N and Fe@VUL:N, respectively. Indeed, this indicates that the contribution arising from carbide should account for <0.7% and <0.2% of the total C 1s peak based on the Fe_3C stoichiometry for Fe@BP:N and Fe@VUL:N, respectively. Fe@VUL:N shows a higher Csp^2/C_{tot} ratio as reported in **Table 3.2**, suggesting a higher graphitisation compared to Fe@BP:N. This is consistent with TGA results, where Fe@VUL:N shows a higher temperature to reach the residual plateau resulting from the degradation of the carbon scaffold, when compared to Fe@BP:N, thus suggesting greater stability of the scaffold.

The morphology of materials was investigated via electron microscopies. **Figure 3.9a and 3.9b** show SEM images of BP and VUL, respectively, which indicate samples are characterised by a rough and irregular surface with a porous structure more evident for BP compared to VUL. **Figure 3.9c and 3.9d** shows the SEM images collected for Fe@BP:N and Fe@VUL:N, respectively, displaying a complex matrix with dispersed/embedded nanoparticles. Fe@BP:N presents a higher porosity than Fe@VUL:N and this is consistent with BET results that display a higher surface area for the BP-based sample. Further investigation via TEM for Fe@BP:N reveals that the sample consists of nanoparticles with size similar to those of the primary BP particles, as shown **Figure 3.9e and 3.9g**, and additional larger and denser particles with diameter of 0.15 ± 0.06 μm. **Figure 3.9h,3.9i,3.9l** show TEM-EDX images of the Fe, C and O signals,

respectively, showing that the larger particles are rich in Fe and are dispersed over a graphitised carbon scaffold support.

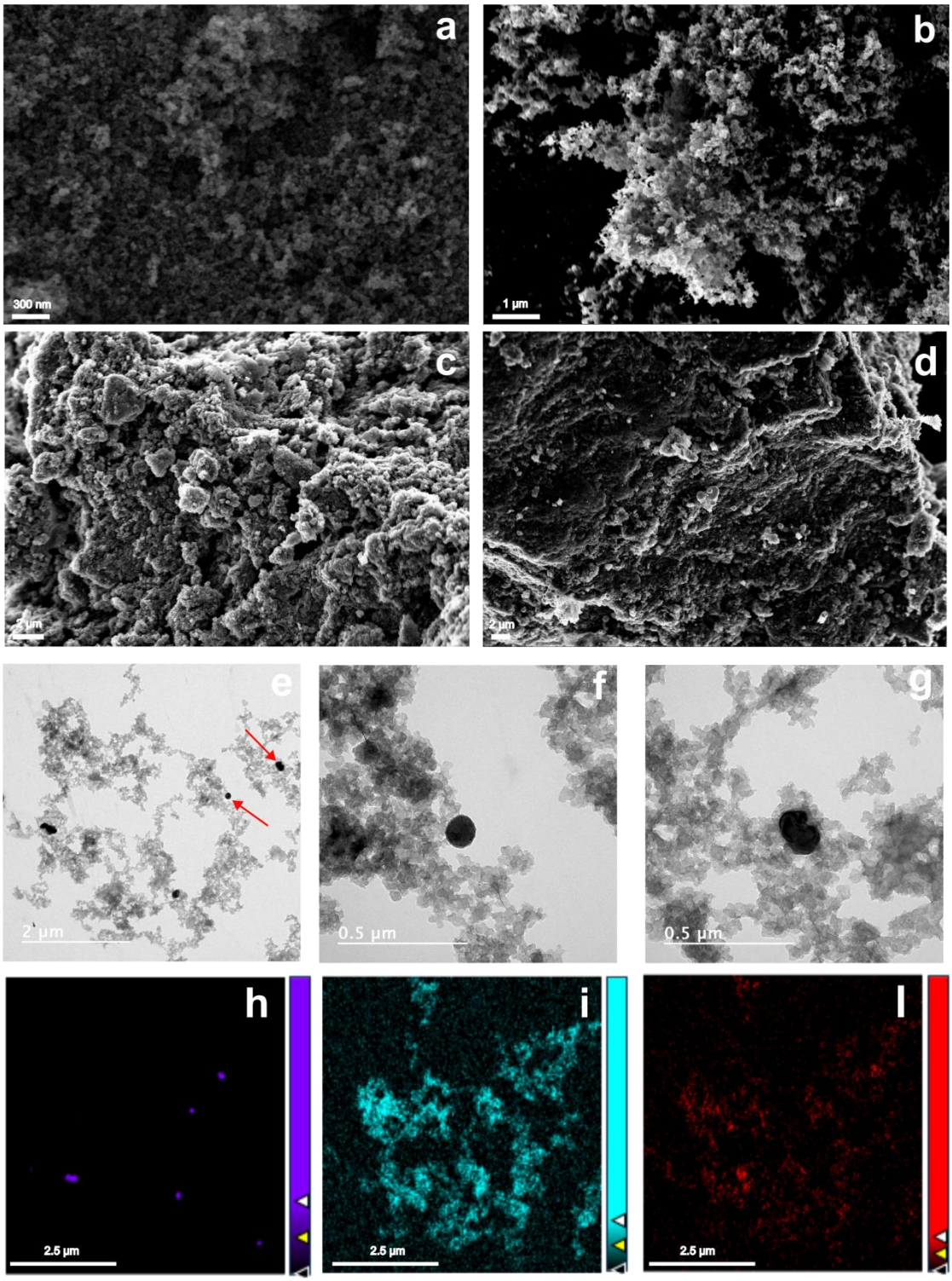

Figure 3.9 SEM images collected for (a) BP, (b) VUL, (c) Fe@BP:N and (d) Fe@VUL:N. TEM images of (e) Fe@BP:N and (f,g) expanded images with details of metal-rich nanoparticles (indicated with arrows in (e)) resulting from the annealing process. TEM-EDX chemical mapping of the image in (e) in the (h) Fe, (i) C and (l) O spectral regions. Figure adapted from Pota et al. reference 39.

3.3.3 Electrochemical study on glassy carbon disk

To evaluate the electrochemical response in both HER and ECH reactions, voltammetry experiments were carried out in H_2SO_4 aqueous electrolytes using BZH as a diagnostic organic compound. **Figure 3.10a** shows the LSV collected in the cathodic region for Fe@BP:N and Fe@VUL:N, measured after drop casting of ink dispersion on a polished GC disk at a scan rate of 5 mV/s, in only supporting electrolyte. For comparison, data of bare GC disk and Pt disk electrodes are also included. Fe@BP:N and Fe@VUL:N show overpotentials at 1 mA cm^{-2} of -0.30 and -0.58 V vs RHE, respectively and no evidence of faradaic peaks. This indicates a higher HER activity of BP-based compared to VUL-based electrocatalysts, and an improved HER current relative to the bare GC disk ($\eta \approx$ -0.99 V at 1 mA cm^{-2}), albeit below those observed at Pt disk under the same conditions.[33] HER activity in the -0.3 to -0.5 V region is attributable to the incorporation of iron carbide/nitride nanoparticles at the surface/subsurface of the electrode material. Indeed, the overpotential at 10 mA cm^{-2}, Tafel slope and exchange current density values estimated for Fe@BP:N disk electrodes are 123 mV/dec and -2.4 mA/cm^2, respectively (**Figure 3.10b**). These values are in good agreement with those reported in literature for mild steel and cast iron in acid,[63-66] suggesting that HER currents are dominated by Fe/FexC sites. This also justifies the lower HER current measured for Fe@VUL:N, that as reported in **Table 3.2** displays less than half of Fe/FexC in the surface/subsurface composition compared to Fe@BP:N. **Figure 3.10c** shows the response of electrode materials in the presence of 10 mM BZH, revealing changes in cathodic current densities with overpotentials $\eta \approx$ -0.57 V and -0.67 V vs RHE at 1 mA cm^{-2}, for Fe@BP:N and Fe@VUL:N respectively. This suppression in current suggests that benzaldehyde adsorbs onto the electrode surface, blocking sites involved in proton reduction and quenching the HER activity, a behaviour previously observed with precious metal electrocatalysts[67,68] and base metal electrodes in acidic aldehyde solutions.[69] A similar suppression of HER current is observed for both the bare GC disk and Pt disk electrode, as show in **Figure 3.10c**. Notably, a cathodic peak at *ca.* -0.64 V is observed more pronounced for Fe@BP:N than for Fe@VUL:N, and is likely associated with BZH reduction.[70] The bare GC disk exhibits a cathodic peak at *ca.* -0.92 V, while the Pt disk electrode does not show a clear reduction peak, due to the high HER current background that dominates the cathodic response below -0.4 V on these surfaces.

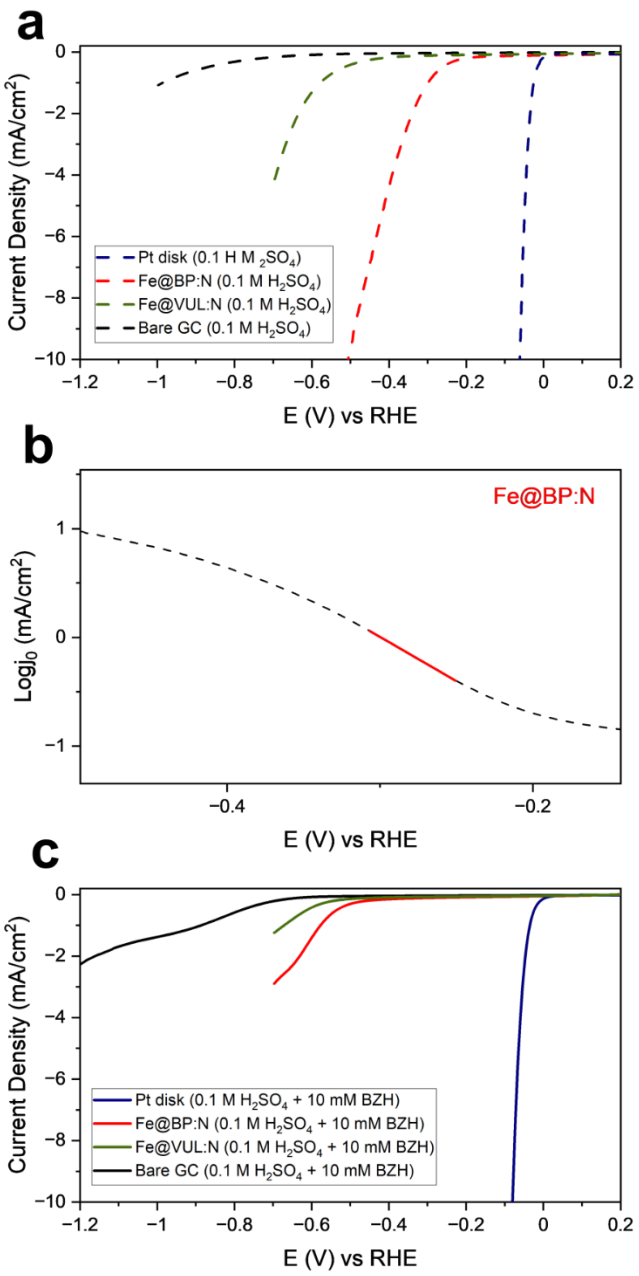

Figure 3.10 (a) LSV collected in supporting electrolyte 0.1 M H_2SO_4 and (b) Tafel plot for Fe@BP:N. (c) LSV collected in 0.1 M H_2SO_4 + 10 mM BZH at 5 mV s^{-1} scan rate. Figure adapted from Pota et al. reference 39.

Additional investigations were carried out in Na_2SO_4, to study the effect of pH changing and different BZH concentration on the HER and ECH performances. **Figure 3.11a and 3.11b** shows CVs recorded in 0.1 M Na_2SO_4 and in presence of 10 mM BZH for Fe@BP:N and Fe@VUL:N, respectively, on polished GC disk at a scan rate of 10 mV/s. In background electrolyte a lower capacitive current is recorded for Fe@VUL:N compared to Fe@BP:N. Since the loading per mass of both electrodes is the same, this

means that the electrochemical specific surface areas (ECSA) of Fe@BP:N is higher than that of Fe@VUL:N, in agreement with BET results. Materials display presence of faradaic peaks: an anodic peak is observed at *ca.*0 V, while a cathodic peak is observed at *ca* -0.42 V and -0.45V for Fe@BP:N and Fe@VUL:N, respectively.

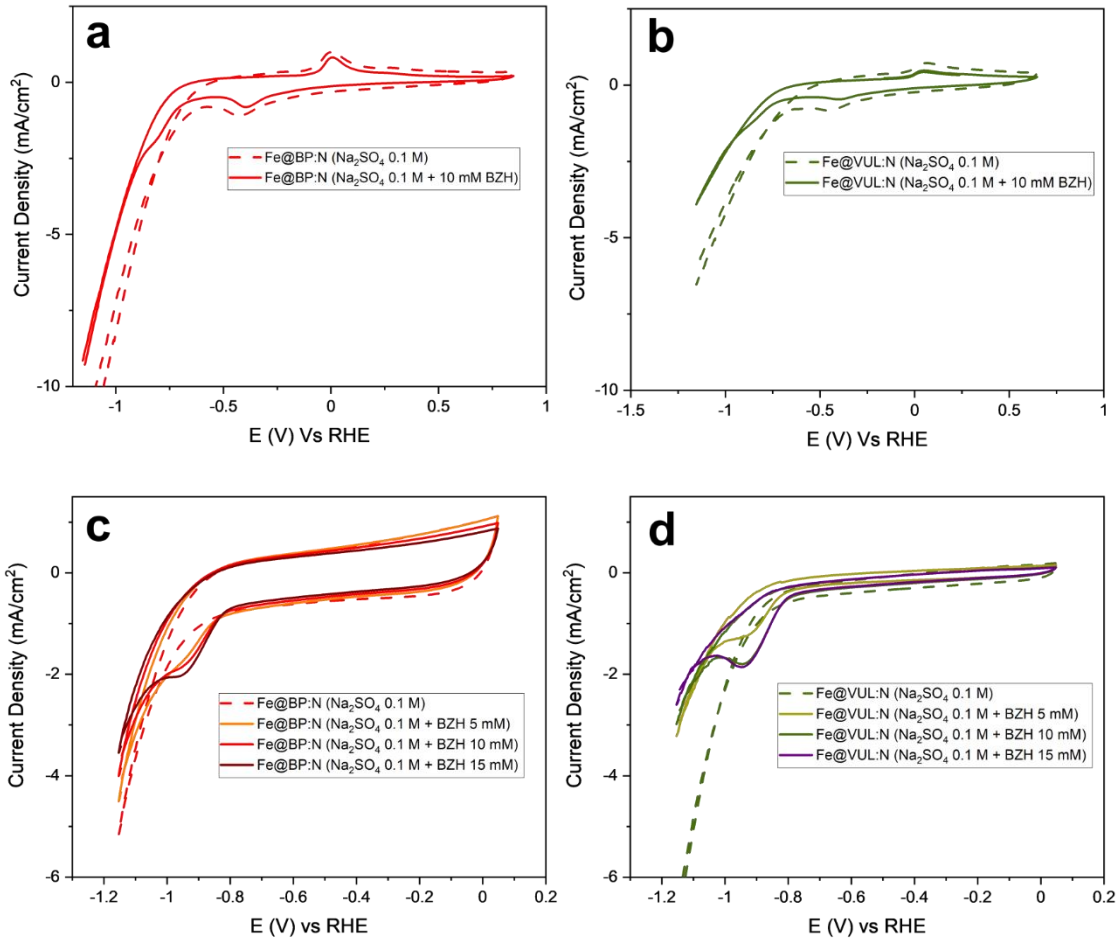

Figure 3.11 CVs collected for (a) Fe@BP:N and (b) Fe@VUL:N in 0.1 M Na_2SO_4 (dashed line) and in 0.1 M Na_2SO_4 + 10 mM BZH (solid line) at 10 mV s^{-1} scan rate . CVs recorded in 0.1 M Na_2SO_4 for different BZH concentration 5.0, 10.0, 15.0 mM BZH for (c) Fe@BP:N and (d) Fe@VUL:N.

These peaks were absent in acid electrolytes and are likely due to redox-active species present in the electrode materials and in no way associated to BZH. Indeed, given the presence of iron-species they are possibly associated with surface oxides or hydroxides. These species could result in iron couples that undergo redox processes at the surface of the electrode. It has been reported that Fe_2O_3 display Fe(III)/Fe(II) oxidation at *ca.*0.32 V vs RHE and Fe(II)/Fe(I) oxidation at *ca.*0.2 V vs RHE,[71,72] while cathodic reactions to obtain mixed Fe(III)/Fe(II) species were reported at *ca.*0 V vs RHE.[73] In the presence of

10 mM of BZH both electrocatalysts show a decrease of capacitive currents and of faradaic response associated with the HER. The anodic and cathodic peaks attributed to iron redox switch species, even if affected by this suppression, are still present after the addition of the BZH. A cathodic peak at *ca.* – 0.9 V vs RHE is observed and attributed to a BZH reduction process. This result agrees with literature reported by Cantu. et al. on reduction of benzaldehyde at glassy carbon electrodes, which was observed as a peak at -1.53 V vs Ag Nafion/AgCl at pH 5.[70]

Figure 3.11c and 3.11d show CVs recorded for different concentration of BZH (5.0, 10.0, 15.0 mM) in Na_2SO_4 0.1 M using a narrower potential windrow from 0 to -1.15 V vs RHE, for Fe@BP:N and Fe@VUL:N, respectively; the CV in supporting electrolyte is also reported for comparison. There are differences in terms of capacitive current between the two nanoscaffolds, along with a decrease of the capacitive current as consequence of the increase of BZH concentration due to adsorption effects. No additional cathodic peaks are observed at *ca*. -0.4 V vs RHE even in the pure background electrolyte, and this is consistent with previous hypotheses according to which these peaks are associated to Fe(III)/Fe(II) redox activity. Notably, the use of a potential window with a *ca.*0 V anodic limit appears to prevent formation of the switching redox species. Both samples display an increase of the peak current density at *ca.* -0.9 V as the concentration of the BZH increases indicating that this peak arises in the presence of BZH, and probably associated to ECH of the organic compound.

Considering results obtained from preliminary electrochemical study, Fe@BP:N shows a higher response in current density for low concentration of BZH even with a higher capacitive contribution compared to Fe@VUL:N in Na_2SO_4 (**Figure 3.11c and 3.11d**). While in H_2SO_4, Fe@BP:N displays a higher HER activity and a higher current density at the same BZH concentration (**Figure 3.10a**). For these reasons, Fe@BP:N material was chosen as candidate to carry out further determinations of efficiency and selectivity in BZH hydrogenation as discussed in the next chapter, while Fe@VUL:N was no longer investigated; finally, for simplicity from this point forward in this thesis, Fe@BP:N will be referred to as Fe@C:N.

3.4 Conclusion

In this chapter, Fe@C:N materials were synthesised, characterised and investigated as potential electrocatalysts for ECH, with benzaldehyde used as a diagnostic compound. Two hydrothermal methods were applied to M@C:N architectures prepared using BP or VUL as carbon nanoscaffolds. XPS analysis was employed to determine optimal conditions based on the degree of graphitisation, metal incorporation, and level of oxidised species. The annealing method that included a pre-annealing step proved more efficient and was selected as the definitive procedure. The optimised samples underwent structural analysis to evaluate the influence of BP and VUL as carbon black nanoscaffolds on the final material.

Based on BET analysis, Fe@BP:N exhibits a higher surface area, macroporosity, and pore volume compared to Fe@VUL:N, consistent with BP possessing a greater surface area than VUL. TGA analysis shows an estimated Fe wt% of 14.4% for Fe@BP:N and 11.8% for Fe@VUL:N, suggesting greater Fe bulk incorporation in the BP-based sample. Moreover, the results indicate graphitisation, as confirmed by the FT-IR spectra collected before and after annealing. XRD spectra reveal that the bulk of the annealed samples predominantly consists of Fe_3C, with contributions from Fe_2N and Fe_3N. The formation of nitrides and carbides aligns with a process involving carbonisation of the organic resin in an ammonia-rich atmosphere in the presence of iron salts. The average crystallite size for Fe@BP:N was found to be larger than that for Fe@VUL:N, in agreement with the TGA results. Surface analyses were performed on the annealed samples, indicating the encapsulation of iron-rich phases within a protective carbon shell. Fe@BP:N exhibits a higher surface atomic %Fe content compared to Fe@VUL:N, consistent with Fe penetrating more deeply into the carbon scaffold. For both samples, the majority of nitrogen within the carbon framework is present in the form of pyrrolic/pyridinic groups; however, Fe@VUL:N displays a higher total nitrogen content compared to Fe@BP:N. Additionally, Fe@VUL:N shows a higher Csp^2/C_{tot} graphitisation level than Fe@BP:N, as confirmed by TGA analysis. SEM analysis revealed a complex matrix morphology containing dispersed or embedded nanoparticles for both annealed samples. TEM-EDX analysis of Fe@BP:N further revealed larger and denser Fe-rich particles, with a diameter of 0.15 ± 0.06 μm, dispersed over a graphitised carbon scaffold support.

Electrochemical studies conducted on a glassy carbon disk revealed higher HER activity for the BP-based material compared to the VUL-based material in H_2SO_4 supporting

electrolyte. This is attributed to the greater incorporation of iron carbide/nitride nanoparticles at the surface and subsurface of the electrode material in Fe@BP:N relative to Fe@VUL:N. In the presence of 10 mM BZH, both electrocatalysts exhibit a cathodic peak at *ca.* -0.64 V, which is more pronounced for the BP-based material and likely associated with the ECH of the organic diagnostic compound. When using Na_2SO_4 as the supporting electrolyte, the electrochemical response changes, displaying diagnostic peaks corresponding to iron redox couples active on the electrode surface. More importantly, a cathodic peak at *ca.* -0.9 V is observed, which increases with rising BZH concentration, indicating that this peak arises in the presence of BZH and is likely associated with the ECH of the organic compound. Taking into account the higher current density response for low concentration of BZH in Na_2SO_4, along with higher HER activity in H_2SO_4 of Fe@BP:N compared to Fe@VUL:N, the BP-based material, renamed as Fe@C:N, has been selected to carry out quantitative analysis of benzaldehyde hydrogenation, as discussed in detail in the next chapter.

3.5 References

1. Iannaci, A.; Ingle, S.; Domínguez, C.; Longhi, M.; Merdrignac-Conanec, O.; Ababou-Girard, S.; Barrière, F.; Colavita, P. E. Nanoscaffold effects on the performance of air-cathodes for microbial fuel cells: Sustainable Fe/N-carbon electrocatalysts for the oxygen reduction reaction under neutral pH conditions. *Bioelectrochemistry* **2021**,*142*,107937.

2. Tavakkoli, M.; Kallio, T.; Reynaud, O.; Nasibulin, A. G.; Johans, C.; Sainio, J.; Jiang, H.; Kauppinen, E. I.; Laasonen, K. Single-Shell Carbon-Encapsulated Iron Nanoparticles: Synthesis and High Electrocatalytic Activity for Hydrogen Evolution Reaction. *Angewandte Chemie International Edition* **2015**,*54* (15),4535-4538.

3. Wei, H.; Wang, J.; Lin, Q.; Zou, Y.; Chen, X. a.; Zhao, H.; Li, J.; Jin, H.; Lei, Y.; Wang, S. Incorporating ultra-small N-doped Mo2C nanoparticles onto 3D N-doped flower-like carbon nanospheres for robust electrocatalytic hydrogen evolution. *Nano Energy* **2021**,*86*,106047.

4. Han, N.; Yang, K. R.; Lu, Z.; Li, Y.; Xu, W.; Gao, T.; Cai, Z.; Zhang, Y.; Batista, V. S.; Liu, W.; et al. Nitrogen-doped tungsten carbide nanoarray as an efficient bifunctional electrocatalyst for water splitting in acid. *Nature Communications* **2018**,*9* (1),924.

5. Mairanovskii, S. G.; Rubinskaya, T. Y.; Gul'tyai, V. P.; Proskurovskaya, I. V. Electrochemical reduction of benzaldehyde to benzyl alcohol at a mercury cathode. *Bulletin of the Academy of Sciences of the USSR, Division of chemical science* **1976**,*25* (10),2203-2205.

6. Chen, H.; Iyer, J.; Liu, Y.; Krebs, S.; Deng, F.; Jentys, A.; Searles, D. J.; Haider, M. A.; Khare, R.; Lercher, J. A. Mechanism of Electrocatalytic H2 Evolution, Carbonyl Hydrogenation, and Carbon–Carbon Coupling on Cu. *Journal of the American Chemical Society* **2024**,*146* (20),13949-13961.

7. Chan-Shing, E. S.; Boucher, D.; Lessard, J. The electrochemical reduction of α-nitrocumene in a protic and basic medium on large surface area (porous) electrodes: electronation-protonation or electrocatalytic hydrogenation? *Canadian Journal of Chemistry* **1999**,*77* (5-6),687-694.

8. Fan, X.; Peng, Z.; Ye, R.; Zhou, H.; Guo, X. M3C (M: Fe, Co, Ni) Nanocrystals Encased in Graphene Nanoribbons: An Active and Stable Bifunctional Electrocatalyst for Oxygen Reduction and Hydrogen Evolution Reactions. *ACS Nano* **2015**,*9* (7),7407-7418.

9. Carbonell, J. V.; de las Mercedes Menéndez, M.; Pietrobelli, C. *Critical minerals and countries' mining competitiveness: An estimate through economic complexity techniques*; UNU-MERIT,**2023**.

10. Commission, E.; Directorate-General for Internal Market, I., Entrepreneurship; SMEs; Grohol, M.; Veeh, C. *Study on the critical raw materials for the EU 2023 – Final report*; Publications Office of the European Union,**2023**.

11. Kwon, Y.; Birdja, Y. Y.; Raoufmoghaddam, S.; Koper, M. T. M. Electrocatalytic Hydrogenation of 5-Hydroxymethylfurfural in Acidic Solution. *ChemSusChem* **2015**,*8* (10),1745-1751.

12. Kwon, Y.; de Jong, E.; Raoufmoghaddam, S.; Koper, M. T. M. Electrocatalytic Hydrogenation of 5-Hydroxymethylfurfural in the Absence and Presence of Glucose. *ChemSusChem* **2013**,*6* (9),1659-1667.

13. Kwon, Y.; Koper, M. T. M. Electrocatalytic Hydrogenation and Deoxygenation of Glucose on Solid Metal Electrodes. *ChemSusChem* **2013**,*6* (3),455-462.

14. Ting, L. R. L.; Peng, Y.; Yeo, B. S. Mechanistic Insights into the Selective Electroreduction of Crotonaldehyde to Crotyl Alcohol and 1-Butanol. *ChemSusChem* **2021**,*14* (14),2963-2971.

15. Sauter, W.; Bergmann, O. L.; Schröder, U. Hydroxyacetone: A Glycerol-Based Platform for Electrocatalytic Hydrogenation and Hydrodeoxygenation Processes. *ChemSusChem* **2017**,*10* (15),3105-3110.

16. Calado Galvão de Melo, S.; da Silva, M. E. P.; da Silva, M. E. B.; da Paz, J. A.; de Menezes Barbosa, C. M. B.; de Menezes, F. D.; Loureiro, R. N. A.; Navarro, M.; da Costa, J. Â. P.; da Silva, G. F.; et al. Ultrasound as a tool for reducing energy consumption in electrocatalytic hydrogenation of aromatic ketones using graphite as catalyst support. *International Journal of Hydrogen Energy* **2020**,*45* (43),22855-22872.

17. Nilges, P.; Schröder, U. Electrochemistry for biofuel generation: production of furans by electrocatalytic hydrogenation of furfurals. *Energy & Environmental Science* **2013**,*6* (10),2925-2931.

18. Li, Z.; Kelkar, S.; Lam, C. H.; Luczek, K.; Jackson, J. E.; Miller, D. J.; Saffron, C. M. Aqueous electrocatalytic hydrogenation of furfural using a sacrificial anode. *Electrochimica Acta* **2012**,*64*,87-93.

19. Yang, G.; Jiao, Y.; Yan, H.; Xie, Y.; Tian, C.; Wu, A.; Wang, Y.; Fu, H. Unraveling the mechanism for paired electrocatalysis of organics with water as a feedstock. *Nature Communications* **2022**,*13* (1),3125.

20. Deng, J.; Ren, P.; Deng, D.; Bao, X. Enhanced Electron Penetration through an Ultrathin Graphene Layer for Highly Efficient Catalysis of the Hydrogen Evolution Reaction. *Angewandte Chemie International Edition* **2015**,*54* (7),2100-2104.

21. Kipling, J. J.; Sherwood, J. N.; Shooter, P. V.; Thompson, N. R. Factors influencing the graphitization of polymer carbons. *Carbon* **1964**,*1* (3),315-320.

22. Kolahdouz, M.; Xu, B.; Nasiri, A. F.; Fathollahzadeh, M.; Manian, M.; Aghababa, H.; Wu, Y.; Radamson, H. H. Carbon-Related Materials: Graphene and Carbon Nanotubes in Semiconductor Applications and Design. *Micromachines* **2022**,*13* (8),1257.

23. Carmo, M.; dos Santos, A. R.; Poco, J. G. R.; Linardi, M. Physical and electrochemical evaluation of commercial carbon black as electrocatalysts supports for DMFC applications. *Journal of Power Sources* **2007**,*173* (2),860-866.

24. Macías-García, A.; Díaz-Díez, M. A.; Alfaro-Domínguez, M.; Carrasco-Amador, J. P. Influence of chemical composition, porosity and fractal dimension on the electrical conductivity of carbon blacks. *Heliyon* **2020**,*6* (6).

25. Liu, Z. Y.; Zhang, J. L.; Yu, P. T.; Zhang, J. X.; Makharia, R.; More, K. L.; Stach, E. A. Transmission Electron Microscopy Observation of Corrosion Behaviors of Platinized Carbon Blacks under Thermal and Electrochemical Conditions. *Journal of The Electrochemical Society* **2010**,*157* (6), B906.

26. Leonard, N.; Nallathambi, V.; Barton, S. C. Carbon supports for non-Precious metal oxygen reducing catalysts. *Journal of The Electrochemical Society* **2013**,*160* (8), F788.

27. Timperman, L.; Feng, Y. J.; Vogel, W.; Alonso-Vante, N. Substrate effect on oxygen reduction electrocatalysis. *Electrochimica Acta* **2010**,*55* (26),7558-7563.

28. Ferrero, G. A.; Preuss, K.; Fuertes, A. B.; Sevilla, M.; Titirici, M. M. The influence of pore size distribution on the oxygen reduction reaction performance in nitrogen doped carbon microspheres. *Journal of Materials Chemistry A* **2016**,*4* (7),2581-2589,10.1039/C5TA10063A.

29. Nguyen, M.-T.; Mecheri, B.; D'Epifanio, A.; Sciarria, T. P.; Adani, F.; Licoccia, S. Iron chelates as low-cost and effective electrocatalyst for oxygen reduction reaction in microbial fuel cells. *International Journal of Hydrogen Energy* **2014**,*39* (12),6462-6469.

30. Chang, W.-C.; Nguyen, M. T. Investigations of a platinum–ruthenium/carbon nanotube catalyst formed by a two-step spontaneous deposition method. *Journal of Power Sources* **2011**,*196* (14),5811-5816.

31. Ota, K.-i.; Kreysa, G.; Savinell, R. F. *Encyclopedia of applied electrochemistry*; Springer New York,**2014**.

32. Behan, J. A.; Iannaci, A.; Domínguez, C.; Stamatin, S. N.; Hoque, M. K.; Vasconcelos, J. M.; Perova, T. S.; Colavita, P. E. Electrocatalysis of N-doped carbons in the oxygen reduction reaction as a function of pH: N-sites and scaffold effects. *Carbon* **2019**,*148*,224-230.

33. Nolan, H.; Schröder, C.; Brunet-Cabré, M.; Pota, F.; McEvoy, N.; McKelvey, K.; Perova, T. S.; Colavita, P. E. MoS2/carbon heterostructured catalysts for the hydrogen evolution reaction: N-doping modulation of substrate effects in acid and alkaline electrolytes. *Carbon* **2023**,*202*,70-80.

34. Daubinger, P.; Kieninger, J.; Unmüssig, T.; Urban, G. A. Electrochemical characteristics of nanostructured platinum electrodes–a cyclic voltammetry study. *Physical Chemistry Chemical Physics* **2014**,*16* (18),8392-8399.

35. Glarum, S.; Marshall, J. An A-C admittance study of the platinum/sulfuric acid interface. *Journal of The Electrochemical Society* **1979**,*126* (3),424.

36. Liu, J.; Qiao, S. Z.; Liu, H.; Chen, J.; Orpe, A.; Zhao, D.; Lu, G. Q. Extension of the Stöber method to the preparation of monodisperse resorcinol–formaldehyde resin polymer and carbon spheres. *Angewandte Chemie* **2011**,*123* (26),6069-6073.

37. Heydaripour, J.; Gazi, M.; Oladipo, A. A.; Gulcan, H. O. A novel magnetic mesoporous resorcinol–melamine–formaldehyde resin for removal of phenols from aqueous solution. *Journal of Porous Materials* **2019**,*26*,1249-1258.

38. Shao, Y.; Chen, H.; Li, Y.; Xie, S.; Li, B. Sintered metal fibers@ carbon molecular sieve membrane (SMFs@ CMSM) composites for the adsorptive removal of low concentration isopropanol. *RSC advances* **2017**,*7* (60),37604-37611.

39. Pota, F.; Costa de Oliveira, M. A.; Schröder, C.; Brunet Cabré, M.; Nolan, H.; Rafferty, A.; Jeannin, O.; Camerel, F.; Behan, J. A.; Barrière, F.; et al. Porous N-Doped Carbon-encapsulated Iron as Novel Catalyst Architecture for the Electrocatalytic Hydrogenation of Benzaldehyde. *ChemSusChem* **2025**,*18* (1), e202400546.

40. Bomben, K.; Moulder, J.; Sobol, P. E.; Stickle, W. Handbook of X-ray photoelectron spectroscopy: a reference book of standard spectra for identification and interpretation of XPS data. *Eden Prairie, MN (USA): Physical electronics* **1995**.

41. Hellgren, N.; Haasch, R. T.; Schmidt, S.; Hultman, L.; Petrov, I. Interpretation of X-ray photoelectron spectra of carbon-nitride thin films: New insights from in situ XPS. *Carbon* **2016**,*108*,242-252.

42. Qu, L.; Liu, Y.; Baek, J.-B.; Dai, L. Nitrogen-doped graphene as efficient metal-free electrocatalyst for oxygen reduction in fuel cells. *ACS nano* **2010**,*4* (3),1321-1326.

43. Titantah, J.; Lamoen, D. Carbon and nitrogen 1s energy levels in amorphous carbon nitride systems: XPS interpretation using first-principles. *Diamond and related materials* **2007**,*16* (3),581-588.

44. Detweiler, Z. M.; Wulfsberg, S. M.; Frith, M. G.; Bocarsly, A. B.; Bernasek, S. L. The oxidation and surface speciation of indium and indium oxides exposed to atmospheric oxidants. *Surface Science* **2016**,*648*,188-195.

45. Dupin, J.-C.; Gonbeau, D.; Vinatier, P.; Levasseur, A. Systematic XPS studies of metal oxides, hydroxides and peroxides. *Physical Chemistry Chemical Physics* **2000**,*2* (6),1319-1324.

46. Brunauer, S.; Emmett, P. H.; Teller, E. Adsorption of Gases in Multimolecular Layers. *Journal of the American Chemical Society* **1938**,*60* (2),309-319.

47. Fierro, V.; Bosch, G.; Siperstein, F. R. Pore size distribution in microporous carbons obtained from molecular modeling and density functional theory. In *Studies in Surface Science and Catalysis*, Llewellyn, P. L., Rodriquez-Reinoso, F., Rouqerol, J., Seaton, N. Eds.; Vol.160; Elsevier,2007; pp 519-526.

48. Kupgan, G.; Liyana-Arachchi, T. P.; Colina, C. M. NLDFT Pore Size Distribution in Amorphous Microporous Materials. *Langmuir* **2017**,*33* (42),11138-11145.

49. Sing, K. S. W. Reporting physisorption data for gas/solid systems with special reference to the determination of surface area and porosity (Recommendations 1984).**1985**,*57* (4),603-619.

50. Thommes, M.; Kaneko, K.; Neimark, A. V.; Olivier, J. P.; Rodriguez-Reinoso, F.; Rouquerol, J.; Sing, K. S. W. Physisorption of gases, with special reference to the evaluation of surface area and pore size distribution (IUPAC Technical Report). *Pure and Applied Chemistry* **2015**,*87* (9-10),1051-1069.

51. Tavakkoli, M.; Kallio, T.; Reynaud, O.; Nasibulin, A. G.; Johans, C.; Sainio, J.; Jiang, H.; Kauppinen, E. I.; Laasonen, K. Single-shell carbon-encapsulated iron nanoparticles: synthesis and high electrocatalytic activity for hydrogen evolution reaction. *Angewandte Chemie International Edition* **2015**,*54* (15),4535-4538.

52. Socrates, G. *Infrared and Raman characteristic group frequencies: tables and charts*; John Wiley & Sons,**2004**.

53. Ferrari, A. C.; Robertson, J. Interpretation of Raman spectra of disordered and amorphous carbon. *Physical Review B* **2000**,*61* (20),14095-14107.

54. Karthik, M.; Faik, A.; Doppiu, S.; Roddatis, V.; D'Aguanno, B. A simple approach for fabrication of interconnected graphitized macroporous carbon foam with uniform mesopore walls by using hydrothermal method. *Carbon* **2015**,*87*,434-443.

55. Zhao, M.; Song, H.; Chen, X.; Lian, W. Large-scale synthesis of onion-like carbon nanoparticles by carbonization of phenolic resin. *Acta Materialia* **2007**,*55* (18),6144-6150.

56. Zhu, J.; Wang, P.; Zhang, X.; Zhang, G.; Li, R.; Li, W.; Senftle, T. P.; Liu, W.; Wang, J.; Wang, Y. Dynamic structural evolution of iron catalysts involving competitive oxidation and carburization during CO2 hydrogenation. *Science Advances* **2022**,*8* (5), eabm3629.

57. Lu, F.; Chen, X.; Lei, Z.; Wen, L.; Zhang, Y. Revealing the activity of different iron carbides for Fischer-Tropsch synthesis. *Applied Catalysis B: Environmental* **2021**,*281*,119521.

58. Biwer, B.; Bernasek, S. Electron spectroscopic study of the iron surface and its interaction with oxygen and nitrogen. *Journal of electron spectroscopy and related phenomena* **1986**,*40* (4),339-351.

59. McIntyre, N.; Zetaruk, D. X-ray photoelectron spectroscopic studies of iron oxides. *Analytical Chemistry* **1977**,*49* (11),1521-1529.

60. Libenská, H.; Hanuš, J.; Košutová, T.; Dopita, M.; Kylián, O.; Cieslar, M.; Choukourov, A.; Biederman, H. Plasma-based synthesis of iron carbide nanoparticles. *Plasma Processes and Polymers* **2020**,*17* (11),2000105.

61. Dong, Y.; Wang, B.; Zhao, K.; Yu, Y.; Wang, X.; Mai, L.; Jin, S. Air-stable porous Fe2N encapsulated in carbon microboxes with high volumetric lithium storage capacity and a long cycle life. *Nano Letters* **2017**,*17* (9),5740-5746.

62. De Oliveira, M. A. C.; Schröder, C.; Cabré, M. B.; Nolan, H.; Forner-Cuenca, A.; Perova, T. S.; McKelvey, K.; Colavita, P. E. Effects of N-functional groups on the electron transfer kinetics of VO2+/VO2+ at carbon: Decoupling morphology from chemical effects using model systems. *Electrochimica Acta* **2024**,*475*,143640.

63. Trasatti, S. Work function, electronegativity, and electrochemical behaviour of metals: III. Electrolytic hydrogen evolution in acid solutions. *Journal of Electroanalytical Chemistry and Interfacial Electrochemistry* **1972**,*39* (1),163-184.

64. Zeradjanin, A. R.; Narangoda, P.; Masa, J.; Schlögl, R. What controls activity trends of electrocatalytic hydrogen evolution reaction?─ Activation Energy Versus Frequency Factor. *ACS Catalysis* **2022**,*12* (19),11597-11605.

65. Miyata, Y.; Kuwahara, Y.; Asakura, S.; Shinohara, T.; Yakou, T.; Shiimoto, K. Hydrogen evolution reaction on spheroidal graphite cast iron with different pearlite areas in sulphuric acid solutions. *Corrosion Engineering, Science and Technology* **2014**,*49* (4),269-274.

66. Kelly, E. J. The active iron electrode: I. Iron dissolution and hydrogen evolution reactions in acidic sulfate solutions. *Journal of the Electrochemical Society* **1965**,*112* (2),124.

67. Sanyal, U.; Yuk, S. F.; Koh, K.; Lee, M. S.; Stoerzinger, K.; Zhang, D.; Meyer, L. C.; Lopez-Ruiz, J. A.; Karkamkar, A.; Holladay, J. D. Hydrogen bonding enhances the electrochemical hydrogenation of benzaldehyde in the aqueous phase. *Angewandte Chemie* **2021**,*133* (1),294-300.

68. Song, Y.; Sanyal, U.; Pangotra, D.; Holladay, J. D.; Camaioni, D. M.; Gutiérrez, O. Y.; Lercher, J. A. Hydrogenation of benzaldehyde via electrocatalysis and thermal catalysis on carbon-supported metals. *Journal of Catalysis* **2018**,*359*,68-75.

69. Kwon, Y.; Birdja, Y. Y.; Raoufmoghaddam, S.; Koper, M. T. Electrocatalytic hydrogenation of 5-hydroxymethylfurfural in acidic solution. *ChemSusChem* **2015**,*8* (10),1745-1751.

70. Cantu, D. C.; Padmaperuma, A. B.; Nguyen, M.-T.; Akhade, S. A.; Yoon, Y.; Wang, Y.-G.; Lee, M.-S.; Glezakou, V.-A.; Rousseau, R.; Lilga, M. A. A combined experimental and theoretical study on the activity and selectivity of the electrocatalytic hydrogenation of aldehydes. *ACS Catalysis* **2018**,*8* (8),7645-7658.

71. Roberts, J. J.; Westgard, J. A.; Cooper, L. M.; Murray, R. W. Solution voltammetry of 4 nm magnetite iron oxide nanoparticles. *Journal of the American Chemical Society* **2014**,*136* (30),10783-10789.

72. Nagasaka, M.; Yuzawa, H.; Horigome, T.; Hitchcock, A. P.; Kosugi, N. Electrochemical reaction of aqueous iron sulfate solutions studied by Fe L-edge soft X-ray absorption spectroscopy. *The Journal of Physical Chemistry C* **2013**,*117* (32),16343-16348.

73. Bülter, H.; Denuault, G.; Mátéfi-Tempfli, S.; Mátéfi-Tempfli, M.; Dosche, C.; Wittstock, G. Electrochemical analysis of nanostructured iron oxides using cyclic voltammetry and scanning electrochemical microscopy. *Electrochimica Acta* **2016**,*222*,1326-1334

CHAPTER 4

Development of stable Fe@C:N electrocatalysts and quantitative analysis of benzaldehyde hydrogenation

---

The fabrication of stable Fe@C:N materials is a crucial aspect for their practical application as electrocatalysts in ECH processes. This chapter presents a methodology for preparing stable and durable electrocatalysts, along with a comprehensive analysis of key ECH performance parameters. The results highlight that these materials could serve as a viable, cost-effective alternative to the commonly used precious metal electrocatalysts.

This chapter presents result and contents reported in the candidate's first-author publication, titled:

Porous N-Doped Carbon-encapsulated Iron as Novel Catalyst Architecture for the Electrocatalytic Hydrogenation of Benzaldehyde

Pota, F.; Costa de Oliveira, M. A.; Schröder, C.; Brunet Cabré, M.; Nolan, H.; Rafferty, A.; Jeannin, O.; Camerel, F.; Behan, J. A.; Barrière, F.; Colavita, P. E.

ChemSusChem 2025,18 (1), e202400546

With the exception of specified contributions, the candidate conducted the primary investigation reported in the published work and prepared the first draft of the paper, along with subsequent revisions, under the supervision of Prof. Paula E. Colavita. The contributions of the other coauthors are as follows: M.A.C.O. development of the sample preparation methodology, C.S. & H.N. XPS analysis, M.B.C. computational study with COMSOL simulations, A.R. BET and PSD analysis, O.J. & F.C. SAXS analysis, J.A.B. & F.B. writing - review and editing, P.E.C conceptualization and supervision.

4.1 Introduction

As discussed in Chapter 1, ECH offers a sustainable electrochemical approach to biomass valorisation, providing an alternative to conventional industrial processes that predominantly depend on fossil fuels.[1-4] To realise the potential advantages of ECH, electrocatalysts with good performance in terms of faradaic efficiency (FE), yield and selectivity are needed. FE of ECH processes is typically limited by competition with the HER.[5,6] The main difference between the HER and ECH is how the H_{ads} is used: Tafel and Heyrovsky steps consume electrons and H_{ads} species and may drastically suppress the FE of organic hydrogenations.[7] Therefore, electrocatalysts must be materials capable of facilitating the Volmer step but that also inhibit the H_2 evolution pathways. Several electrocatalyst materials have been proposed as good candidates for the hydrogenation of organic substrates.[8,9] Precious metals like Pd, Pt, Au[10-12] and carbon-supported Pt-group metals (M/C) such as Pt/C, Pd/C, and Ru/C[13-15] have been reported as good electrocatalysts for the hydrogenation of aldehydes and phenols. Despite these encouraging results, the use of precious and/or critical metals is not desirable at scale. For this reason, there is interest in developing abundant and low-cost electrocatalysts as a suitable replacement. For instance, Ni and Cu have been reported as base metals that can either operate as the active phase or that can be alloyed to modulate the activity of precious metals in ECH processes.[16,17]

The previous chapter have discussed the application of Fe-based electrocatalysts for hydrogenating benzaldehyde, which due to its good solubility in water[18] and its moderate reactivity,[19] stands out among various potential organic derivatives of biomass as a relevant candidate for studying the reactivity of new electrocatalyst materials for ECH. The ECH of benzaldehyde has been previously investigated using Pt-group electrocatalysts and is reported to result information of benzyl alcohol (BA) and/or in dimerization to hydrobenzoin (HBZ).[11] In Chapter 3 promising preliminary electrochemical results were observed utilised Fe@C:N material drop casted on a glassy carbon disk as a conductive support, and tested in different supporting electrolytes. Glassy carbon is an excellent choice for small-scale electrochemical studies due to its smooth, inert surface and low background current, providing a stable and controlled environment for evaluating porous materials.[20] However, when working with larger surface areas, such as 1 cm^2 or more, challenges arise in achieving uniform ink dispersion

and film stability. These difficulties often make glassy carbon less practical for these applications. In contrast, carbon cloth (CC) with a microporous layer (MPL) offers significant advantages for larger surfaces.[21] Its textured and slightly porous surface helps improve adhesion and stability of the ink dispersion, making it less prone to cracking or detachment. Additionally, the flexibility and robustness of carbon cloth make it well-suited for larger experimental setups, where its structural integrity can handle the increased demands. Unlike the rigid and costly glassy carbon, CC is more economical and adaptable, allowing for easier handling and better compatibility with large-scale studies. This makes CC with an MPL a more appropriate choice for applications that require larger electrode surfaces, such as the evaluation of the ECH quantitative performances and, ultimately, any prototype devices for studying performance with real biomass feeds.

The first part of this chapter evaluates glassy carbon plate (GC plate) and CC as high surface area conductive supports for the Fe@C:N material, while also identifying a methodology for the preparation of stable and durable electrocatalysts. Electrochemical studies, along with chronoamperometry coupled with gas chromatography analysis, are conducted to determine the FE response in two different supporting electrolytes. Finally, a detailed analysis of quantitative ECH performance parameters, such as faradic efficiency and selectivity, product rate, and turnover frequency (TOF), is performed as a function of the applied potential, exclusively in the supporting electrolyte displaying higher efficiency. The results presented in this chapter demonstrated that is possible to achieve high faradaic efficiency and good selectivity towards the alcohol product using Fe@C:N heterostructures. A comparison of TOF estimates obtained from these results suggests that these materials could be viable as electrocatalysts for the ECH of bio-derived organics.

4.2 Experimental section

Materials. Nafion® 117 solution (5%), sulfuric acid (95–98%) sodium sulphate (> 99%); benzaldehyde (BZH, > 99%); hydrobenzoin (HBZ,99 %); acetophenone (ACP > 99 %); ethyl acetate (> 99 %) were all purchased from Sigma Aldrich and used as received. Ethanol(> 99 %), benzyl alcohol (BA, > 99 %) were purchased from Fisher and used as received.

Electrochemical characterisation. The ink dispersion was prepared as described in Chapter 3 and then drop-cast onto two different conductive supports. The first one, GC plate (2 cm^2 geometric area, Signadur®G) was polished following the same procedure as for the GC disk, using alumina slurry of decreasing grades (Ted Pella) with sonication and rinsing between each polishing step to remove any residual material. The unpolished surfaces (back and edges) were covered with insulating polyimide tape, and a portion of the polished surface was also masked with the same tape to create a final exposed geometric area of 1 cm^2. 50 µL of the ink were drop casted on the polished glassy carbon plate, then dried under inert gas for 15 min. Additional tests on glassy carbon plate were performed drop-casting Nafion solution onto the dried ink layer and further dried under inert gas for 5 min (see **Figure 4.1**). Flags of CC with MPL (1 cm^2 geometric area, FuelCellStore) were used as alternative conductive support. The CC was used as received after covering the back side (woven carbon fibre side) with insulating polyimide tape. 50 µL of the ink were drop cast in two equal aliquots, drying the ink after each step in a hot plate (80 °C) followed by compression of the CC in a hydraulic press (Specac) at room temperature. For both conductive supports, preparation methods resulted in loadings of 1.09 mg cm^{-2} for all experiments. CV, LSV and chronoamperometry experiments were conducted using graphite rods as CE and Ag/AgCl (1 M KCl) as RE (0.235 V vs SHE), cleaning the cell with piranha and Millipore water prior to each experiment. GC disk was employed as WE for CVs and LSV experiments, while CC was used as WE for chronoamperometry experiments. Estimates of ECSA were obtained from capacitive CV curves in Na_2SO_4 0.100 M over a no-Faradaic potential window; the double layer capacitance was normalised by an average value of 40 µF cm^{-2}.[22,23] Electrolysis experiments were performed in an costumed H-cell, with compartments separated by an ion-conducting membrane (FKE-50 Fumasep) to minimise cross contamination (**Figure 4.6a**).WE and RE were inserted in 34 mL of catholyte (BZH in 0.1 M H_2SO_4 or 0.1 M

Na_2SO_4), and the CE was inserted in 34 mL of anolyte (0.1 M H_2SO_4 or Na_2SO_4). Before starting the electrolysis both compartments were purged with N_2 for at least 15 min;2 mL of catholyte were aliquoted for quantitative analysis at t_0 = 0 s. CVs at 100 mV/s and 10 mV/s were first collected to condition the electrode surface, followed by measurement of the iR drop via the i-interrupt method (NOVA). Potentiostatic electrolysis was carried out for 2 h, followed by analysis via GC-FID of a 2 mL aliquot of the catholyte; the catholyte was extracted in ethyl acetate (2 mL,99.1% and 89.9% efficiency for BZH and BA, respectively) adding ACP as internal standard. Calibrations lines and extraction efficiency estimations used for quantitative analysis are presented in Appendix I (**Figure A.3 and A.4**). Appendix I includes also the equations used to calculate the key ECH performance parameters discussed throughout this chapter.

4.3 Results and discussion

4.3.1 Ink stabilization on conductive supports

To optimise the production and detection of target products by combining chronoamperometry experiments with gas chromatography analysis, it was essential to use electrode supports with a large surface area. However, this introduced challenges in stabilising the ink dispersion on such supports. The GC disk (Ø 5 mm), discussed in the previous chapter as a conductive support, exposes too small an area to the electrolyte solution for this purpose, i.e.0196 cm^2. Therefore, a GC plate with a larger surface area (1 cm^2) was first selected as conductive support. The drop-casting electrode preparation on the polished GC plate followed the same procedure used for the GC disk described in the previous chapter and reproposed in **Figure 4.1a**. After drying under a nitrogen flow for 15 minutes, the ink dispersion appeared uniformly distributed across the entire electrode surface, as shown in **Figure 4.1b**. However, preliminary electrochemical tests revealed low stability of the ink on these larger supports. In particular, the production of H_2 at negative potentials led to bubble formation, which caused the ink to deteriorate and fragment, eventually detaching in pieces from the electrode surface. **Figure 4.1c** illustrates the response of the drop-cast electrode in the electrochemical cell under applied voltage, highlighting the instability caused by bubble formation during hydrogen evolution. To address the issue of ink instability, additional tests were conducted by applying an extra layer of Nafion to prevent disintegration and improve adhesion to the

electrode surface (**Figure 4.1d**). **Figure 4.1e and Figure 4.1f** shows the modified electrode and the corresponding results of applying potential, respectively.

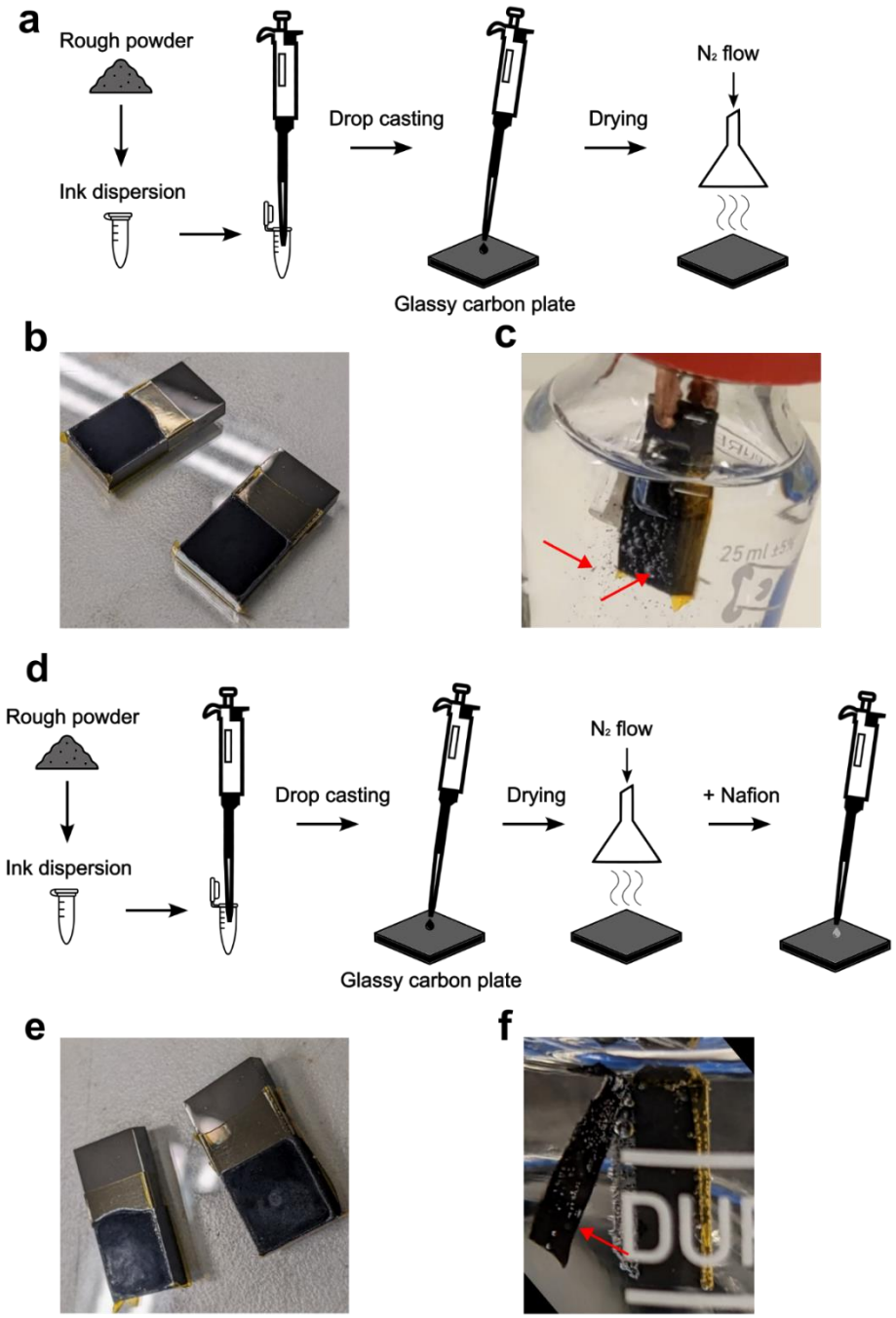

Figure 4.1 (a) Schematic representation of drop-casting electrode preparation on GC plate 1 cm^2. (b) Drop-cast electrode after 15 min drying under N_2 flow. (c) Response of the drop-cast electrode under applied voltage showing ink disintegration (indicated with red arrows). (d) Modified preparation with Nafion coverage. (e) Electrode appearance after 15 minutes of drying under N_2 flow. (f) Response of the drop-cast electrode under applied voltage showing detachment from GC plate.

Although the Nafion layer kept the ink intact, it still detached from the glassy carbon support. The high volume of bubbles produced, particularly during hydrogen evolution, continued to exert enough force to dislodge the ink layer from the electrode surface. Hence, GC plate was excluded from further use as conductive support for electrolysis experiments, and CC support was tested as an alternative candidate.

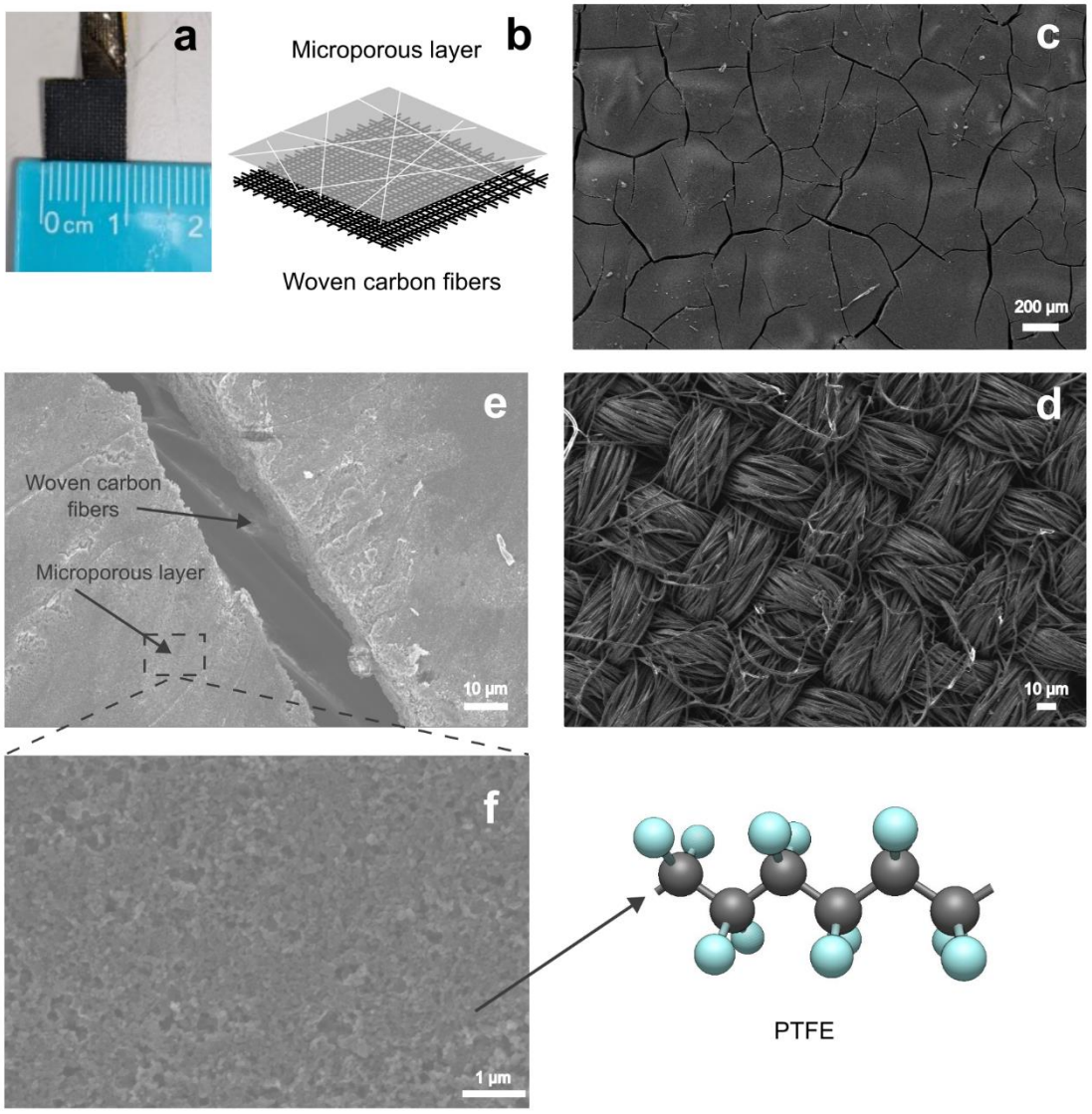

Figure 4.2 (a) Picture of 1 cm^2 bare CC and (b) schematic representation of the MPL (top layer) and woven carbon fibres (back layer). SEM images of (c) MPL, (d) woven carbon fibres layer, (e) close-up view of mud-cracks and (f) magnification of MPL layer with PTFE 3D structure.

Figure 4.2a presents an example of a 1 cm^2 bare CC composed of two layers: the top one is a microporous layer formed by carbon black particles usually bound together by a polymer, while the second layer (backing) is made of woven carbon fibres (**Figure 4.2b**).

Figure 4.2c shows the SEM image collected for the top layer revealing the non-uniformity of the MPL, characterised by so-called "mud-cracking",[21,24,25] while an image for the backing layer of woven carbon fibres is showed in **Figure 4.2d**. A close-up view of the MPL cracks is showed in **Figure 4.2e**, making the woven carbon fibre layer beneath more visible. The MPL has a measured thickness of 9.12 µm ±1.9, and the magnification in **Figure 4.2f** highlights the microporous structure. The most common binder polymer used in MPLs is polytetrafluoroethylene (PTFE), which is both chemically inert and hydrophobic**. Figure 4.3a** shows the XPS survey collected for the CC support on MPL side, displaying characteristic peaks corresponding to C 1s (284 eV), O 1s (532 eV) and F 1s (689 eV),[26] confirming the presence of fluorinated groups. The elemental composition was determined from the area ratios of high-resolution scans of core-level excitations, showing the sample consists of 53.0 at.% C,46.2 at.% F, and 0.80 at.% O.

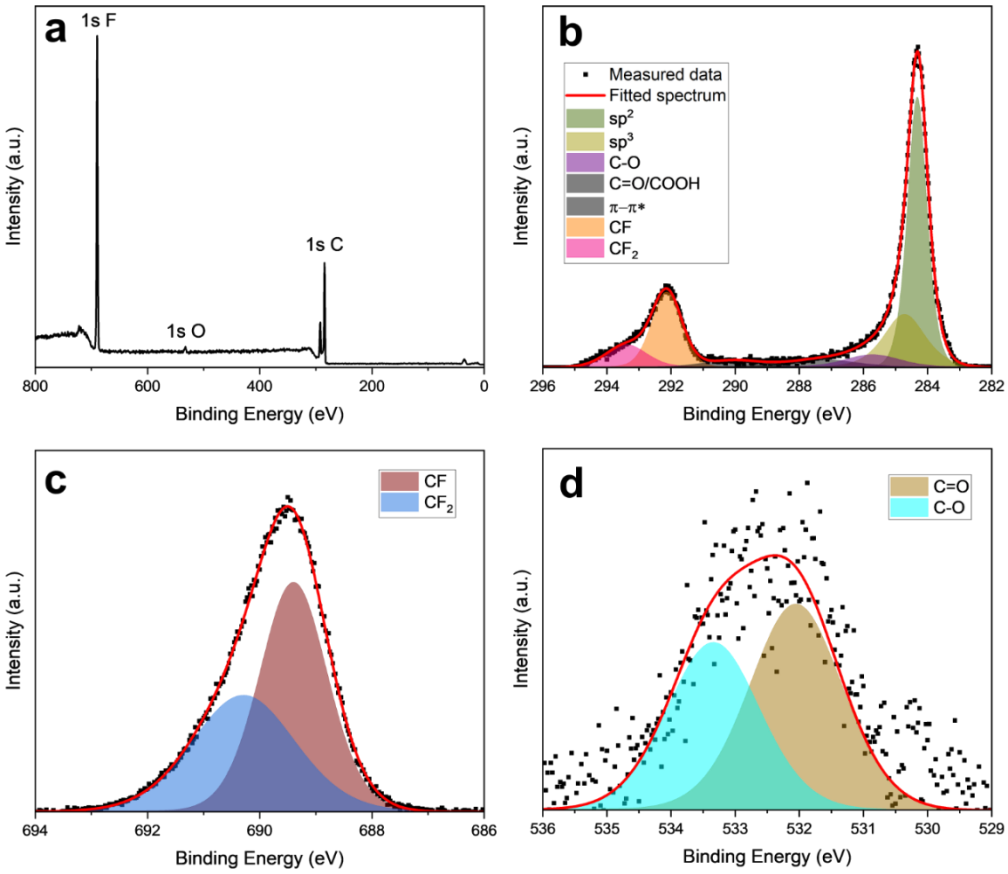

Figure 4.3 XPS (a) survey, (b) C 1s, (c) F 1s and (d) O 1s spectra of MPL side of bare CC; best-fit components and simulated spectral envelope are also shown where relevant.

Figure 4.3b shows the best-fit of the C 1s highlighting two clear pecks at 284.5 and 292 eV corresponding to the non-fluorinated and fluorinated region of MPL layer,

respectively. The non-fluorinated region was deconvoluted as discussed in the previous chapter using five components, attributed to sp^2 (284.3 eV) and sp^3 (284.7 eV) carbon, C-O (285.7 eV), C=O/COOH (287.3 eV) groups, and π- π* transitions (290.0 eV).[26-29] The fluorinated region was deconvoluted using two contributions attributed to CF (292.1 eV) and CF_2 (293.4 eV).[30-32] Similarly the F 1s best-fit region was deconvoluted using two component assigned to CF and CF_2,[31,33] as showed in **Figure 4.3c**. Finally, **Figure 4.3d** shows the O 1s best-fit region obtained using two components attributed to C=O (532.1 eV) and C-O (533.3 eV)[32,34] in fact surface functional groups like quinones, carbonyls, and carboxyls are commonly found in carbon-based materials. While PTFE is considered chemically inert, these oxygenated functional groups can be reduced at negative potentials[35] with the electrochemical behaviour highly dependent on the pH and the specific type of carbon to which they are attached.

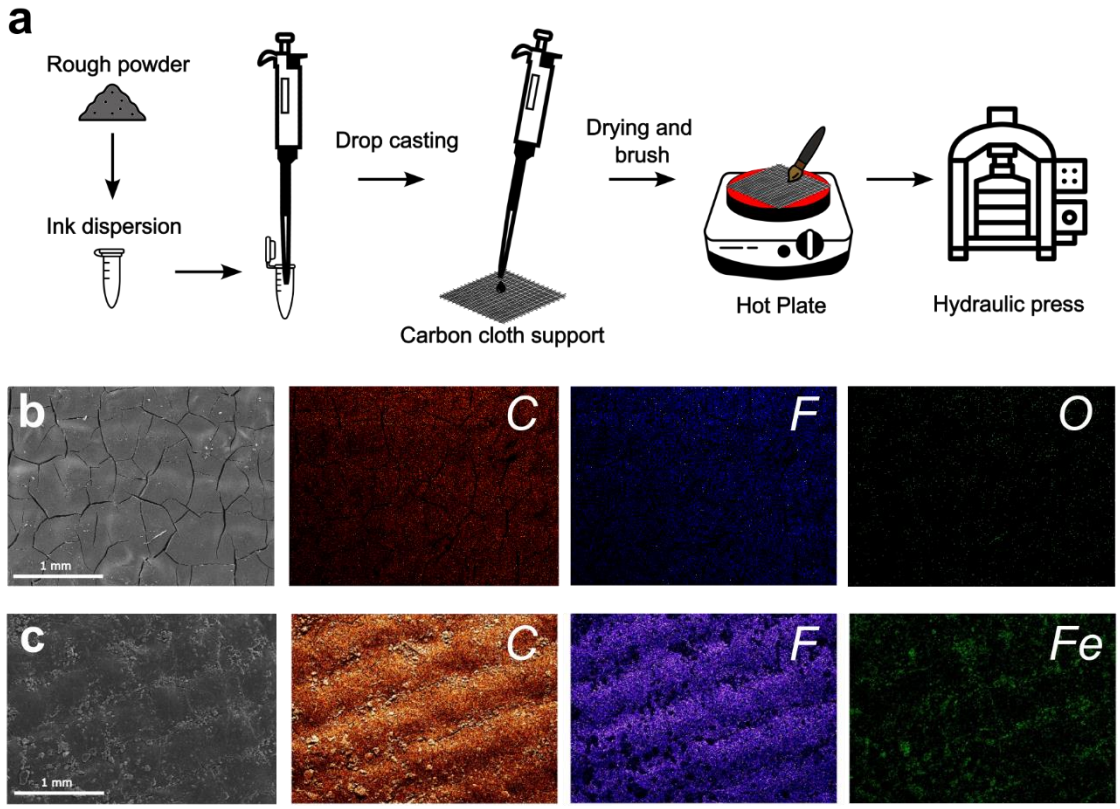

Figure 4.4 (a) Schematic representation of drop-casting electrode preparation on CC 1 cm^2, with brushing and pressing steps. SEM image of unmodified bare CC (b) and CC coated with drop-cast ink (c). SEM-EDX mapping for C, F and O atomic species of the unmodified bare CC in (b); and SEM-EDX mapping for C, F and Fe atomic species of the Fe@C:N surface in (c). Figure adapted from Pota et al. reference 36.

The MPL side of the CC was selected for drop-casting the ink dispersion due to its higher porosity and surface area compared to the back side of woven carbon fibres; and from

this point onward, any reference to CC will refer specifically to the MPL side. The greater hydrophobicity of CC compared to the GC plate, along with structural differences, required a modified approach for preparing drop-cast electrodes. **Figure 4.4a** illustrates the newly developed protocol, which involves brushing the electrocatalyst ink onto the CC support, followed by drying on a hot plate; then to ensure stability and adhesion the support was pressed at 3 tons using a hydraulic press. **Figure 4.4b and 4.4c** show SEM images of the unmodified CC surface and the CC surface coated with a uniform drop-cast layer of the Fe@C:N electrocatalyst ink, respectively. A comparison of the SEM-EDX mapping for both samples at C, O, F and Fe energies, reveals a uniform distribution of the ink across the CC surface, with a low Fe signal from the metal centres and a distinct F signal from the Nafion binder and/or MPL layer. Notably, F and O signals also appear in the unmodified CC sample, further confirming the presence of the PTFE binder polymer and surface oxygenated groups.

4.3.2 Electrochemical behaviour and faradaic efficiency in H_2SO_4 and Na_2SO_4

To assess the stability of the Fe@C:N ink dispersion on the CC support and investigate its electrochemical response, measurements were first carried out using H_2SO_4 as supporting electrolytes. **Figure 4.5a** presents uncompensated LSV of bare CC (1 cm^2) recorded at a scan rate of 10 mV s^{-1} in 0.1 M H_2SO_4, both in the absence and presence of 30 mM BZH. In the background electrolyte, bare CC exhibits moderate activity toward HER, with an overpotential of *ca.* -0.6 V (at 1 mA/cm^2). Upon the addition of 30 mM BZH, a cathodic peak appears at *ca.* -0.8 V, consistent with observations made for a GC disk electrode in Chapter 3. **Figure 4.5b** shows the response of CC modified with Fe@C:N (Fe@C:N/CC) under the same conditions. In the supporting electrolyte a cathodic peak is detected at *ca.* -0.1 V which shifts cathodically to -0.26 V in presence of 30 mM BZH. Moreover, in presence of the organic compound a distinct cathodic peak appears at *ca.* -0.8 V in agreement with prior results observed for bare CC. **Figure 4.5c** displays LSVs for Fe@C:N/CC at varying BZH concentrations (1.0,10.0, and 30.0 mM) at 10 mV s^{-1}. The peak at -0.26 V remains unaffected by BZH concentration, suggesting it is dominated by surface redox processes; conversely, the peak at -0.8 V increases with BZH concentration, indicating that it is associated with an organic reduction process. The same set of experiments were repeated under different pH conditions (pH 5.3) using 0.1

M Na_2SO_4 as supporting electrolyte. **Figure 4.5d** shows the response of bare CC in the presence and absence of BZH. In the supporting electrolyte a peak appears at approximately 0.1 V, which shifts cathodically in the presence of BZH.

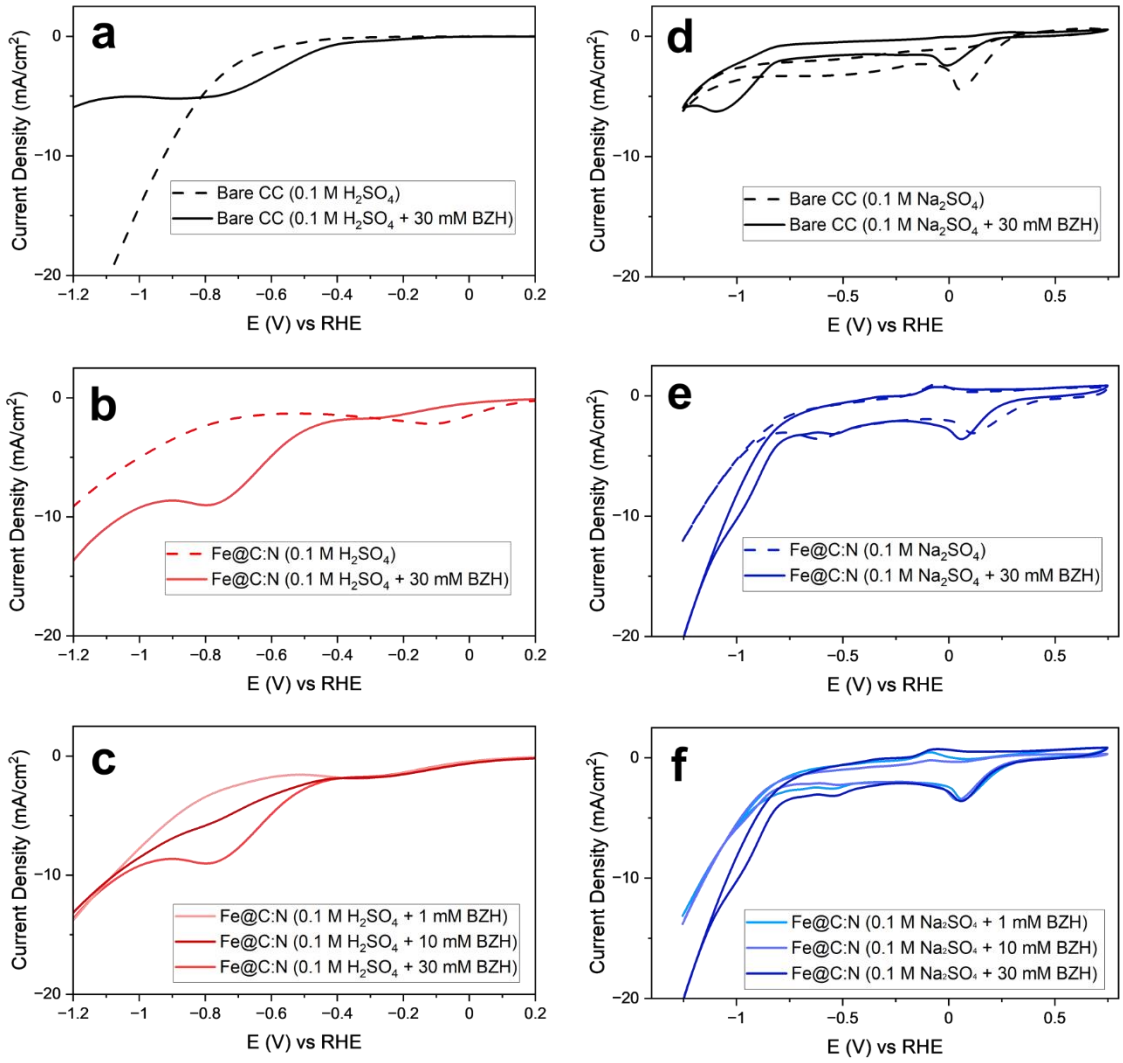

Figure 4.5 (a) LSV collected for bare CC in 0.1 M H_2SO_4 (dashed line) and in 0.1 M H_2SO_4 + 30 mM BZH (solid line) at 10 mV s^{-1}. (b) LSV collected for Fe@C:N/CC in 0.1 M H_2SO_4 (dashed line) and in 0.1 M H_2SO_4 + 30 mM BZH (solid line) at 10 mV s^{-1}. (c) LSV collected for Fe@C:N/CC 0.1 M H_2SO_4 + 1.0, 10.0 and 30.0 mM BZH. (d), (e) and (f) CVs collected in the same conditions as (a),(b) and (c) but using 0.1 M Na_2SO_4 as supporting electrolyte instead of H_2SO_4. Figure adapted from Pota et al. reference 36.

Additionally, a new cathodic peak at *ca.* – 1.1 V is observed with BZH, likely corresponding to its reduction. In contrast, the peak at *ca.*0.1 V is not attributed to BZH, but rather to surface functional groups such as quinones/carbonyls/carboxyls present in the MPL layer.[35] **Figure 4.5e** shows the CVs of Fe@C:N/CC in Na_2SO_4 with a similar response to that observed with the GC disk as discussed in the previous chapter. Two

faradaic peaks are visible, one anodic at *ca.*0 V and one cathodic at *ca.* -0.6 V, which are attributed to the redox processes of iron species on the electrode surface; additionally, a cathodic peak at *ca.*0.1 V is observed. Similarly to what was argued for measurements in H_2SO_4 the peak at ca 0.1 V in Na_2SO_4 shifts cathodically to *ca.*0.06 V in presence of 30 mM BZH together with the appearance of an additional cathodic peak at *ca.* -1.0 V. **Figure 4.5f** shows the CVs collected at various BZH concentrations for Fe@C:N/CC (1.0,10.0 and 30.0 mM) in 0.1 M Na_2SO_4. The results indicate that the faradaic peak associated with the iron redox couple (at *ca.*0 V and -0.6 V) decreases in intensity as the BZH concentration decreases, likely due to adsorption effects. Meanwhile, the peak at 0.06 V remains unaffected by the BZH concentration, further suggesting that it is unrelated to the organic compound. More importantly, the peak at *ca.* -1.0 V increases as the concentration of BZH increases, strongly suggesting that it is associated with an organic reduction process.

CVs obtained at varying scan rates were conducted in Na_2SO_4 supporting electrolyte in a non-faradaic potential window, as shown in Appendix I **(Figure A.5)**. The double-layer capacitance (Cdl) was estimated from a linear fit of the capacitive currents and found to be 1.32 and 5.57 mF cm^{-2} for bare CC and Fe@C:N/CC, respectively. This suggests that drop-casting of the catalyst ink increases the ECSA; assuming the specific double-layer capacitance to remain constant,[22,23] the microscopic area can be estimated to increase approximately four-fold after deposition of Fe@C:N/C on the CC support. This higher value is consistent with high porosity developed during the synthesis of the catalyst material. Notably, across all electrochemical tests in both H_2SO_4 and Na_2SO_4 solutions, the stable current density observed even at negative potentials suggest the robust stability of the ink dispersion on the CC support.

To further evaluate reactions taking place at cathodic potentials, electrolysis experiments with product analysis were carried out using an H-cell setup as showed in **Figure 4.6a**. Chronoamperometry experiments were carried out at the peak potential of -0.8 V and -1.0 V in 0.1 M H_2SO_4 and 0.1 M Na_2SO_4 solutions, respectively; containing three concentrations of BZH for 2 h reaction time and under static conditions. The current density remained stable over the entire duration of the experiment, thus confirming that the electrodes prepared display high stability even when subject to the mechanical stresses associated with evolution of hydrogen bubbles in the HER region (**Figure 4.6b**). Stability

tests were also conducted for longer times (4 h) at constant potential always displaying a solid and stable response in current density over the time (Appendix I**, Figure A.6**).

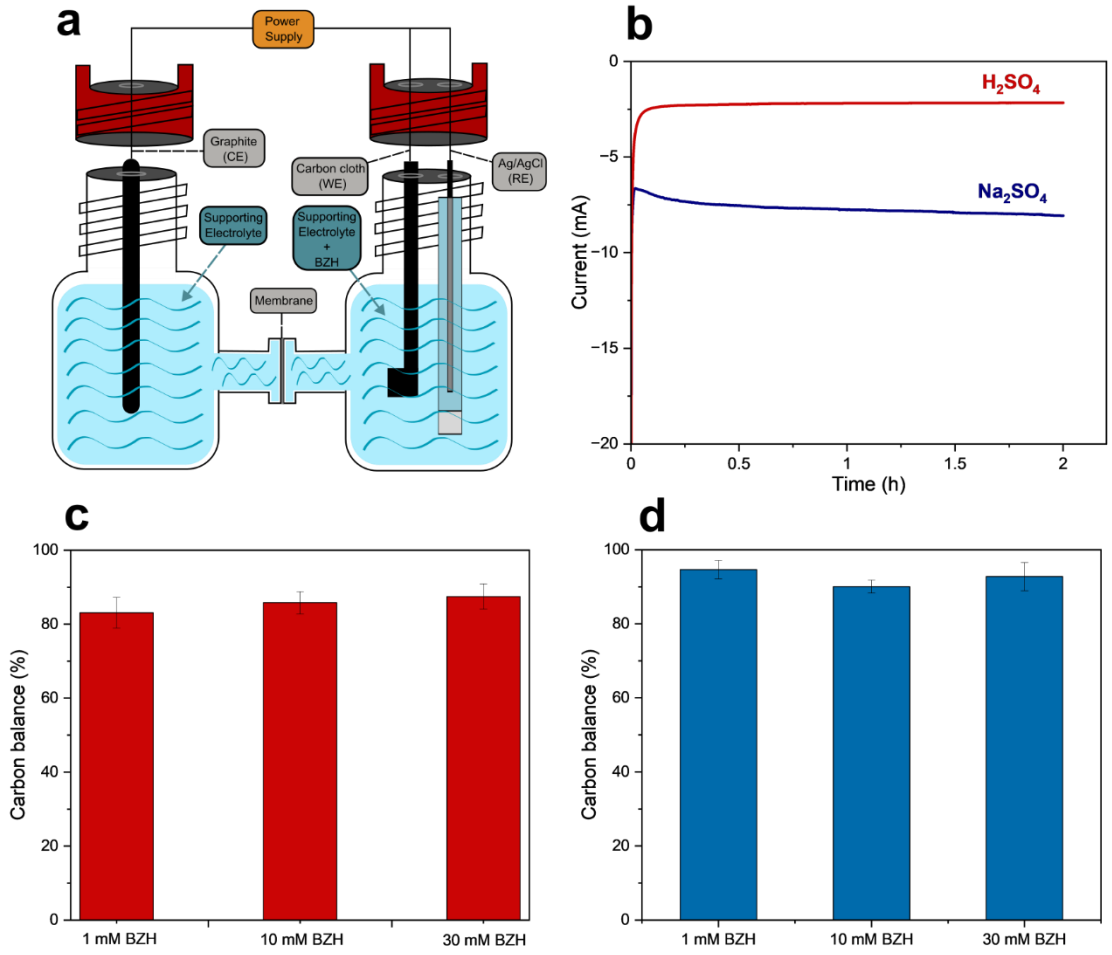

Figure 4.6 (a) Schematic representation of H-cell setup. (b) Chronoamperometry recorded in 0.1 M H_2SO_4 + 30 mM BZH at -0.8 V vs RHE (red line), and 0.1 M Na_2SO_4 + 30 mM BZH at -1.0 V vs RHE (blue line). Carbon balance for 1,10, and 30 mM BZH in (c) 0.1 M H_2SO_4 and (d)0.1 M Na_2SO_4

Two products were identified from the chromatogram at t_{2h}: BA and HBZ, thus confirming that hydrogenation of the organic substrate takes place at the peak potential (Appendix I**, Figure A.7**). For all the experimental conditions the carbon balance was *ca.*90% (**Figure 4.6c and 4.6d**), suggesting only a small mass loss likely resulting from diffusion of the organic through the membrane in the half-cell and/or partitioning into the headspace. **Figure 4.7a and 4.7b** shows the total FE_{ECH} associated with BZH reductions obtained as a function of BZH concentration in H_2SO_4 and Na_2SO_4, respectively. FE_{ECH} values increased linearly with rising BZH concentrations, reaching 70.1 % at 30.0 mM BZH in H_2SO_4, but only 23.5% at the same BZH concentration in Na_2SO_4; higher concentrations were not tested to remain well below the solubility limit of the reactant

(65 mM).[18] It is important to note that although a cathodic peak can be observed at bare CC electrodes (**Figure 4.5a**), the hydrogenation performance summarised in **Figure 4.7a** can be largely attributed to the presence of Fe@C:N; in fact, a control experiment in acid conditions (Appendix I, **Figure A.8**) shows that the bare support yields less than half of the FE_{ECH} at Fe@C:N.

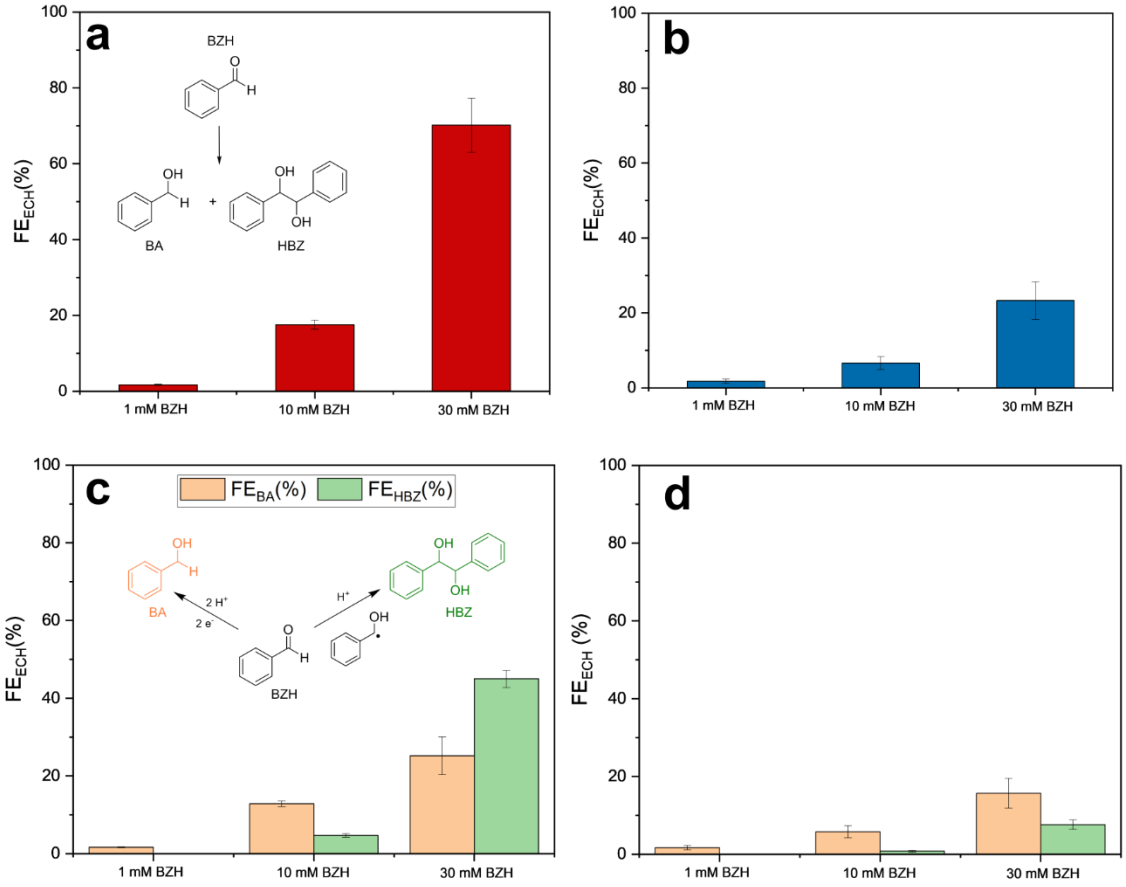

Figure 4.7 Total faradaic efficiency (FE) given by the sum of BA and HBZ contributions in 0.1 M H_2SO_4 at -0.8 V applied potential (a) and 0.1 M Na_2SO_4 at -1.0 V applied potential (b), for 1.0,10.0 and 30.0 mM BZH. Contributions of benzyl alcohol (BA) and hydrobenzoin (HBZ) to the total FE in 0.1 M H_2SO_4 (c) and 0.1 M Na_2SO_4 (d). Figure adapted from Pota et al. reference 36.

Further, in H_2SO_4 supporting electrolyte the faradaic selectivity towards BA is highest at the lowest BZH concentrations, whereas the dimer becomes the preferred product at the highest concentration investigated (**Figure 4.7c**). This suggests that when the BZH concentration increases from 1 to 30 mM the cathodic process results in increased ketyl radical concentrations leading to higher probability of dimerization via pinacolic coupling.[37] On the other hand, at 1 mM the ketyl radicals should have a higher probability of reacting with protons or H_{ads} species at the electrode surface thus enhancing the

selectivity towards BA. Conversely, in Na_2SO_4 supporting electrolyte, BA is the preferred product for all tested BZH concentrations (**Figure 4.7d**). Indeed, the availability of H_{ads} on the surface strictly depended by the pH conditions and potential applied. In Na_2SO_4, despite the higher pH, the potential applied is also more cathodic, allowing a lower probability of dimerization even at higher BZH concentration.

Based on these results and taking into account that acidic electrolytes are suggested to favour ECH processes by generating high proton concentrations,[38] Na_2SO_4 was excluded from further quantitative analysis due to its lower efficiency, focusing on H_2SO_4 as the only supporting electrolyte.

4.3.3 Quantitative analysis in H_2SO_4 supporting electrolyte

Yield values were calculated for H_2SO_4 supporting electrolyte and showed in **Figure 4.8a**. The total yield for the hydrogenation ($Yield_{ECH}$) decreases from 16.3 % to 7.2 % when the BZH concentration is increased from 1 to 30 mM. Additionally, the BA yield contribution result to be higher at lower BZH concentration showing a linear decline as BZH concentration increased, favouring the production of HBZ (**Figure 4.8b**). This trend aligns with previous observations for faradaic selectivity.

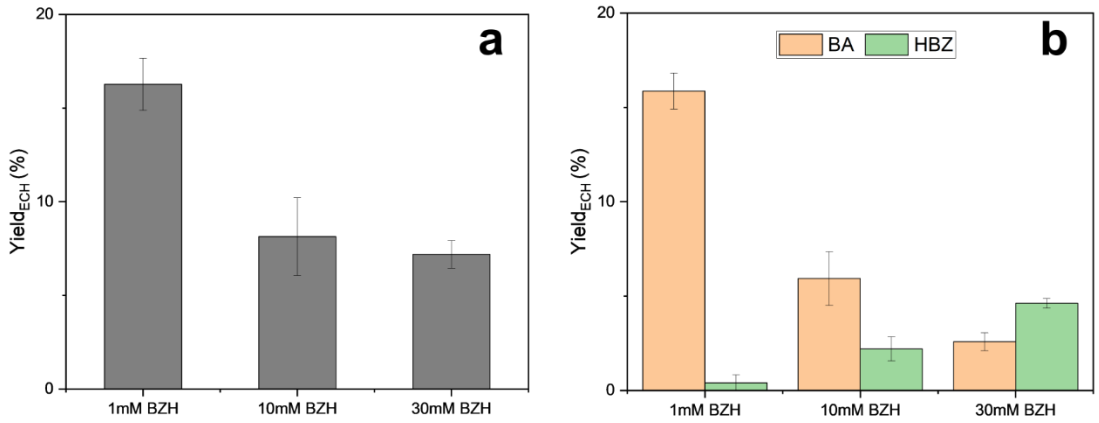

Figure 4.8 (a) Total ECH Yield given by the sum of BA and HBZ contributions and (b) BA and HBZ Yield for 1,10,30 mM in 0.1 M H_2SO_4. Figure adapted from Pota et al. reference 36.

Figure 4.9a shows the BZH conversion as a function of its concentration displaying a decrease from 33.6% to 24.3% as the concentration increases. These results were

compared to estimates for a diffusion-controlled reaction using a smooth 1 cm^2 electrode with comparable cell and electrode geometry to those used experimentally. **Figure 4.9b and 4.9c** provides the details of the model implemented to simulate diffusive mass transport through Finite Element Analysis (FEA) by COMSOL Multiphysics version 5.4.

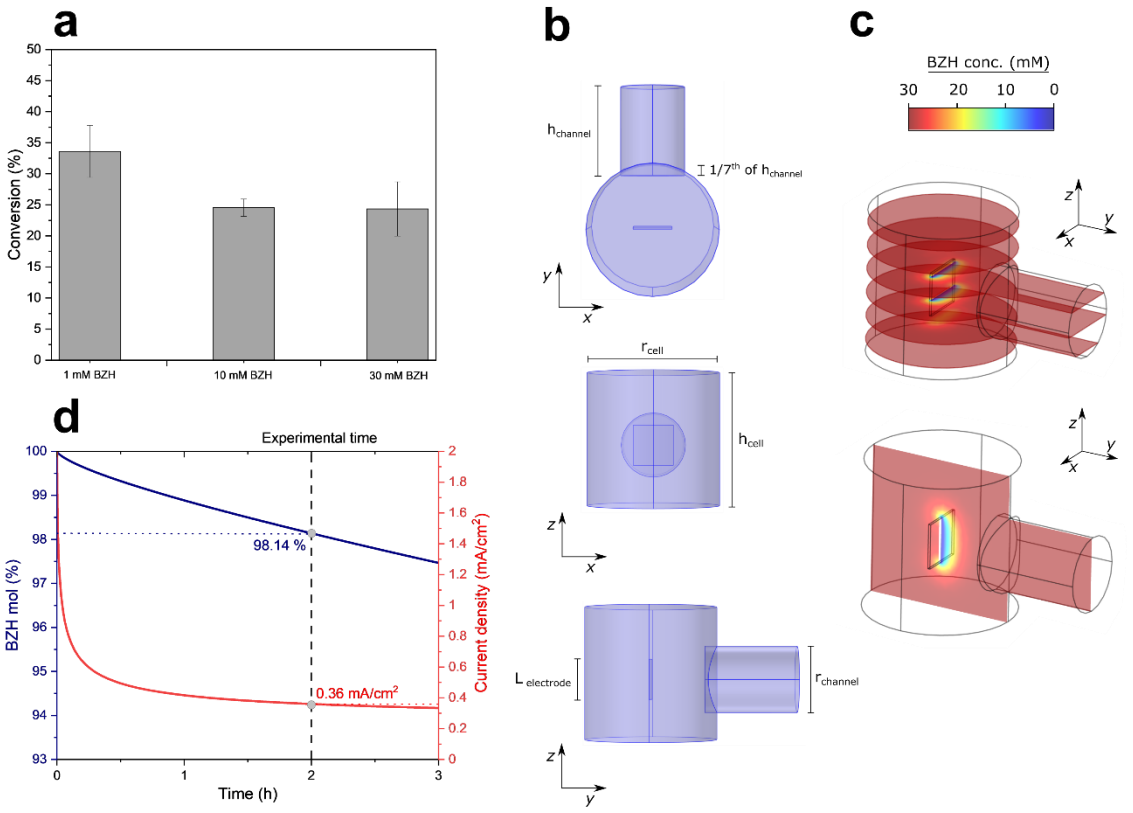

Figure 4.9 (a) Conversion of BZH as function of its concentration. (b) Geometry of the cell simulated from different plane view perspectives with key geometric parameters identified. (c) Cell cross-sections profile showing BZH concentration on the cell after 2 h reaction considering only diffusive mass transport. (d) On the left axis, evolution of the percentage of BZH moles remaining (from 30 mM BZH initial concentration) in the cell vs reaction time. On the right axis, evolution of current density vs reaction time. Figure adapted from Pota et al. reference 36.

The model takes into account the diffusion coefficient of BZH, the specific geometry of the cell used and ensures the same volume of electrolyte as for experimental determinations (32 mL). A comprehensive description of the boundary conditions and parameters is provided in **Table A.1** and **A.2**. The maximum conversion achievable solely through diffusive processes over a 2 h period was determined to be 1.86 % (**Figure 4.9d**). Considering that mass losses typically observed at open circuit are only *ca.*7.4% (Appendix I, **Figure A.9**), then the *ca.*24% conversion measured at 30 mM BZH (**Figure 4.9a**) is much higher than values expected based on a diffusion-controlled reaction alone.

Thus, reduction rates are facilitated by convection due to the generation of H_2 bubbles, as previously reported.[39]

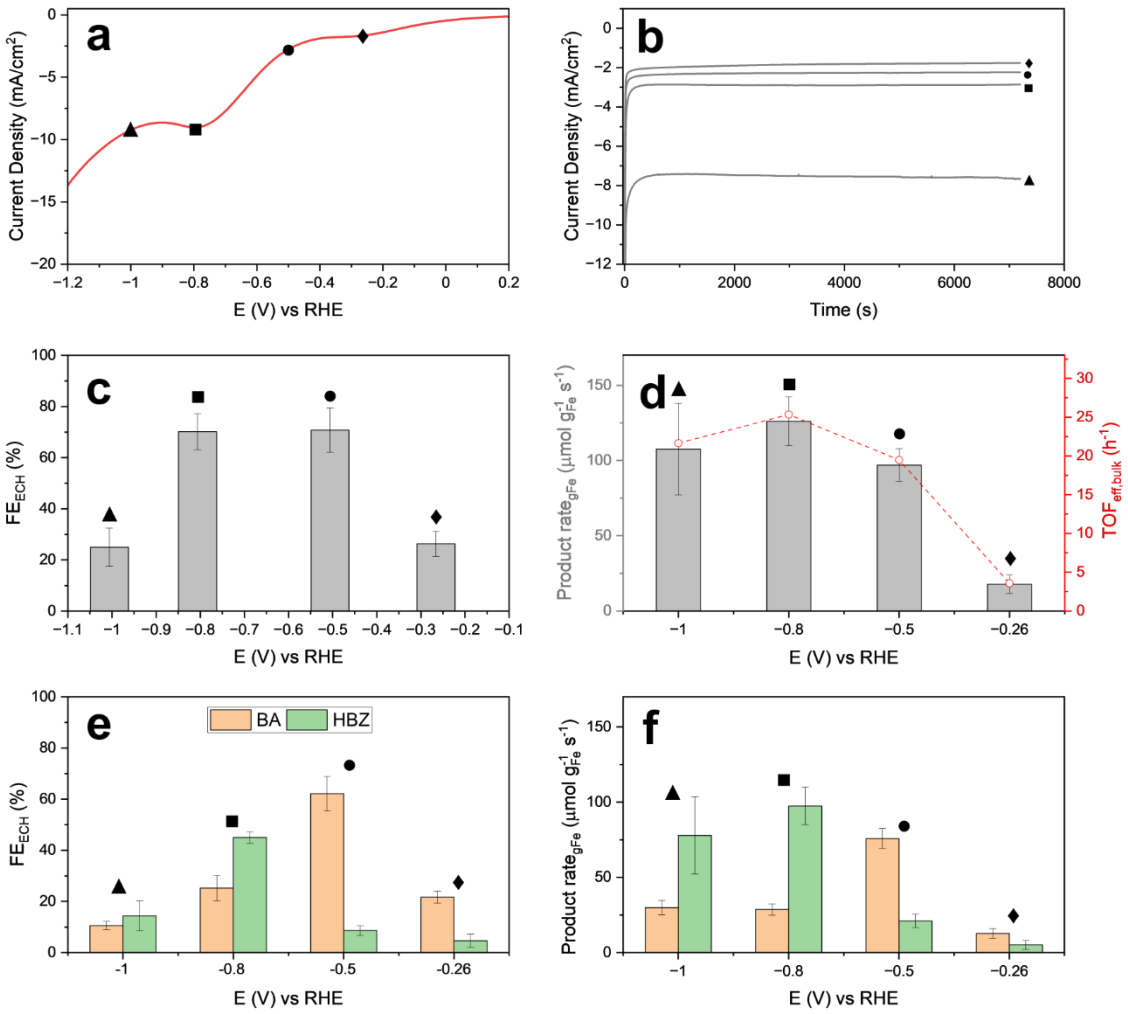

Figure 4.10 (a) CV collected for Fe@C:N on CC-MPL in 0.1 M H_2SO_4/ 30 mM BZH at 10 mV/s. (b) Chronoamperometries collected for each potential for 2 h. Total ECH FE% (c) and total product rate with $TOF_{eff,bulk}$ values (d) for -0.26, -0.5, -0.8, -1 V vs RHE. Contribution of BA and HBZ to ECH FE% (e) and to product rate (f) for each potential. Figure adapted from Pota et al. reference 36.

To better understand the interplay among product selectivity, FE and potential, a more detailed investigation of hydrogenation performance indicators was carried out using the electrolyte composition that yielded the highest FE performance in H_2SO_4, i.e.30 mM BZH. **Figure 4.10a** shows the uncompensated CV of a Fe@C:N/CC electrode in the above electrolyte, obtained in the H-cell, with potentials marked at -0.26, -0.50, -0.80 and -1.00 V to indicate values chosen for further chronoamperometry experiments. The corresponding chronoamperograms are shown in **Figure 4.10b**; all plots display nearly

constant currents, which is diagnostic of a highly stable electrode performance over the entire duration of the experiments.

Figure 4.10c shows the change in total FE of the organic hydrogenations as a function of potential. First, it is interesting to note that there is detectable organic hydrogenation activity at potentials as high as -0.26 V vs RHE. A control experiment run under identical conditions but at open circuit confirmed that the products observed are indeed the result of an electrochemical hydrogenation process (Appendix I**, Figure A.9**). As the potential is lowered, the FE first increases and then decreases significantly at -1.00 V; in contrast, the rate of production (Product rate$_{gFe}$) and effective turn over frequency (TOF$_{eff,bulk}$) both normalised by bulk metal content remain approximately constant, as shown in **Figure 4.10d** (see also summary of equations in Appendix I). These results are consistent with improvements in hydrogenation efficiency at -0.50 and -0.80 V, and the drop at -1.00 V being attributable to competition from increased rates of HER.[40] Therefore, for potentials below -0.80 V, any further increases in cathodic current are almost exclusively due to increased rates of HER rather than to enhanced rates of organic hydrogenation. Finally, a control experiment using a bare CC in 30 mM BZH/0.1 M H_2SO_4 (Appendix I**, Figure A.10**) further confirms that the FE at -0.50 V results from an improvement of more than a factor of two in the intrinsic efficiency of Fe@C:N surfaces towards ECH relative to that of a graphitic carbon support.

The trends in FE vs potential for the two products, BA and HBZ, are particularly interesting and are shown in **Figure 4.10e**. It is clear that under experimental conditions, BA is the preferred product at more anodic potentials whereas HBZ is instead favoured at the more cathodic potentials. This is also evident by examining the rates of production for the two compounds, shown in **Figure 4.10f**; the corresponding TOF$_{eff,bulk}$ values are reported in Appendix I (**Table A.3**). Notably, at -0.56 V the selectivity towards BA is very high, while also achieving a close to maximum average rate of production of hydrogenated organics and high total FE. This suggests that it is possible to tailor the electrolysis conditions to achieve electrochemical hydrogenations with high selectivity and high efficiency.

Optimal conditions are likely to be found at intermediate potentials that are sufficiently cathodic to result in H_{ads} coverage,[2,41] but also sufficiently anodic to inhibit uncontrolled/too fast reduction rates of BZH to α-hydroxybenzyl radicals and,

consequently, fast dimerization. In fact, greater selectivity for BA in **Figure 4.10** is achieved at the lowest overpotentials relative to the thermodynamic value for the conversion of BZH to BA ($E° = 0.14 - 0.19$ V).[42,43] A similar mechanism for increased selectivity towards dimerization at base metals was proposed by Andrews et al.[44] based on product trends in continuous flow cell experiments. Results presented in this chapter therefore suggests that using metal-encapsulated Fe@C:N heterostructured materials it is possible to achieve hydrogenation via an electrocatalytic mechanism, as opposed to a direct electronation-protonation pathway. This can take place over a selected potential range that enables fast rates of hydrogenation via surface-activated proton transfer. It is important to note that the specific influence of nitrides and carbides on the ECH performances cannot be easily discriminated/resolved and fundamental studies on pure carbides and nitrides would be desirable in order to clarify this aspect.

Prior work on the reduction of BZH indicates that achieving high FE values while controlling selectivity for BA and/or HBZ remains a challenge in the literature, particularly when balanced against the choice of metal in terms of their cost and abundance.[8,16,17,44-46] Electrode materials with high HER activity, such as Pt/C, catalyse hydrogenation selectively to BA at low overpotentials; however, as the potential is shifted to more cathodic values, competition from the HER lowers the FE of hydrogenations.[17] This is similar to observed trends in **Figure 4.10e**, further supporting the idea that BA production at Fe@C:N surfaces and low overpotentials takes place via H_{ads} transfers. It is interesting to note that FE values for Fe@C:N at -0.26 V are only slightly inferior to those for Rh/C and Pt/C in pH 5 batch cells at similar potentials (vs. RHE) reported by Song et al., while the performance appears comparable or better at -0.50 V.[17] $TOF_{eff,bulk}$ values at Fe@C:N are approximately two orders of magnitude lower than those reported for Rh/C and Pt/C in the same work, as expected from the much higher HER activity at these Pt-group metals compared to Fe.[47] However, using a continuous flow cell configuration with carbon felt electrodes, Lopez-Ruiz et al.[48] reported TOF_{ECH} values at pH 2 and 5 mA cm^{-2} using Pd/C, one of the best metal electrodes for ECH of BZH, that are only ~12 times larger than those observed with Fe@C:N/CC at similar current density. Anibal et al.[11] also investigated BZH reduction studies on metal foils in pH 4.6 electrolyte at -0.5 V vs RHE; interestingly, rates of production at -0.56 V with Fe@C:N found experimentally are intermediate between those reported in the study for Pd and Pt, and are similar to those measured at Au foils. Given the well-known difference in cost and criticality between Fe

and Pt-group metals, the performances observed at Fe@C:N appear promising to further develop novel Fe-based composite electrocatalysts with selectivity towards the alcohol. ECH of BZH using base metal electrodes has been previously investigated and the performance of Fe@C:N compares very well to those of e.g. Ni[17] and Cu[11] in terms of TOF values and production rates in aqueous electrolytes. The use of iron electrodes for the reduction of other aldehydes have been previous reported by several studies, showing a lower selectivity towards the simple alcohol product.[49-52] For instance, in acid electrolyte the ECH of furfural using iron electrodes has been shown to lead almost exclusively to the pinacolic dimer[51] or to the highly hydrogenated methylfuran product.[52] Hydrogenation of glucose to sorbitol is somewhat of an exception, as it was observed to take place with high selectivity using Fe at neutral pH, but no hydrogenated products were detected in sulfuric acid solutions, as the hydrogenation was proposed to require a local alkaline pH to proceed.[50] Mixed product streams with different degree of hydrogenation were detected at Fe electrodes using HMF as a substrate in acid electrolyte.[49]

The results presented in this chapter demonstrate strong selectivity for BA at intermediate potentials, with no evidence of aromatic ring hydrogenation or hydrogenolysis to toluene. The BA-selectivity is likely due to a combination of higher stability of phenyl vs. furanyl rings and differences in the organic-surface adsorption strengths. Although this argument is consistent with descriptors and reactivity trends observed in the literature,[40,53] further studies aimed at modulating the partitioning of BZH onto the surface are needed to support this hypothesis. An interesting aspect of the M@C:N electrocatalyst architecture is the wide range of metal cores that can be used as catalytic centre, and also the rich library of surface functionalization strategies applicable to carbon nanomaterials available to fine tune the binding strengths of substrate and intermediates[54-56]. In the following chapters, these architectures will be tested with different metal centres to assess their impact on ECH performance and compare the results with similar electrocatalysts.

4.4 Conclusion

In this chapter, a protocol for fabricating stable Fe@C:N material on a large surface area conductive substrate was developed. The GC support was set aside due to ink instability, and CC was chosen as the definitive substrate for quantitative studies of Fe@C:N as electrocatalyst for benzaldehyde hydrogenation. LSV and CV measurements performed

on the prepared material showed results consistent with those obtained using the GC disk in Chapter 3, with cathodic peaks observed at *ca.* -0.8 V and -1.1 V for H_2SO_4 and Na_2SO_4, respectively. These peaks were attributed to benzaldehyde reduction, as confirmed by chronoamperometry carried out in a customised H-cell for 2 h at constant potential. Gas chromatography analysis identified two possible products: BA and HBZ. Faradaic efficiency evaluation for both pH conditions revealed superior performance in H_2SO_4, consistent with literature reports,[38] while Na_2SO_4 was excluded from further quantitative analysis.

A more detailed investigation of hydrogenation performance indicators was conducted at various potentials in H_2SO_4. Results showed that the applied potential can influence the contribution to the total FE for hydrogenations of the two products, thus indicating that electrolysis conditions can be tailored to achieve both high product selectivity and high efficiency. Optimal conditions were identified at intermediate potentials that enable control over the competition between ECH and HER, with BA and HBZ being the preferred products at low and high overpotentials, respectively. Estimates of $TOF_{eff,bulk}$ and production rates compare extremely well to those reported using base metal electrodes such Ni and Cu for the ECH of BZH in aqueous electrolytes.[11,16] Notably, $TOF_{eff,bulk}$ values for Fe@C:N were only an order of magnitude smaller than those observed for a carbon supported precious metal electrocatalysts such as Pd/C (pH 2) in previous reports.[16] Given that this experiments are not carried out under conditions that necessarily maximise mass transport, the calculated $TOF_{eff,bulk}$ values for Fe@C: N are likely to represent a lower boundary value.

The results presented in this chapter are the first report of an Fe-based N-doped electrocatalyst for the ECH of benzaldehyde. No comparable or superior performances using iron-carbon composites have been reported to date. Given the potential for implementing these architectures with various functionalisations, these findings could pave the way for the development of improved M@C:N architectures for the hydrogenation of organic compounds. This approach utilises low-cost and abundant metals not yet explored in this configuration and expands the scope of catalysts for a range of organic substrates.

4.5 References

1. Zhang, L.; Rao, T. U.; Wang, J.; Ren, D.; Sirisommboonchai, S.; Choi, C.; Machida, H.; Huo, Z.; Norinaga, K. A review of thermal catalytic and electrochemical hydrogenation approaches for converting biomass-derived compounds to high-value chemicals and fuels. *Fuel Processing Technology* **2022**,*226*,107097.

2. Ota, K.-i.; Kreysa, G.; Savinell, R. F. *Encyclopedia of applied electrochemistry*; Springer New York,**2014**.

3. Akhade, S. A.; Singh, N.; Gutiérrez, O. Y.; Lopez-Ruiz, J.; Wang, H.; Holladay, J. D.; Liu, Y.; Karkamkar, A.; Weber, R. S.; Padmaperuma, A. B.; et al. Electrocatalytic Hydrogenation of Biomass-Derived Organics: A Review. *Chemical Reviews* **2020**,*120* (20),11370-11419.

4. Zhou, P.; Zhang, J. Electrochemical transformation of biomass-derived oxygenates. *Science China Chemistry* **2023**,*66* (4),1011-1031.

5. Ďurovič, M.; Hnát, J.; Bouzek, K. Electrocatalysts for the hydrogen evolution reaction in alkaline and neutral media. A comparative review. *Journal of Power Sources* **2021**,*493*,229708.

6. Wang, S.; Lu, A.; Zhong, C.-J. Hydrogen production from water electrolysis: role of catalysts. *Nano Convergence* **2021**,*8* (1),4.

7. zhao, B.; Chen, M.; Guo, Q.; Fu, Y. Electrocatalytic hydrogenation of furfural to furfuryl alcohol using platinum supported on activated carbon fibers. *Electrochimica Acta* **2014**,*135*,139-146.

8. Zeng, Y.; Zhao, M.; Zeng, H.; Jiang, Q.; Ming, F.; Xi, K.; Wang, Z.; Liang, H. Recent progress in advanced catalysts for electrocatalytic hydrogenation of organics in aqueous conditions. *Escience* **2023**,*3* (5),100156.

9. Catizane, C.; Jiang, Y.; Sumner, J. Improving plastic pyrolysis oil quality via an electrochemical process for polymer recycling: a review. *Energy Advances* **2024**,*3* (2),366-388,10.1039/D3YA00389B.

10. Cantu, D. C.; Padmaperuma, A. B.; Nguyen, M.-T.; Akhade, S. A.; Yoon, Y.; Wang, Y.-G.; Lee, M.-S.; Glezakou, V.-A.; Rousseau, R.; Lilga, M. A. A Combined Experimental and Theoretical Study on the Activity and Selectivity of the Electrocatalytic Hydrogenation of Aldehydes. *ACS Catalysis* **2018**,*8* (8),7645-7658.

11. Anibal, J.; Malkani, A.; Xu, B. Stability of the ketyl radical as a descriptor in the electrochemical coupling of benzaldehyde. *Catalysis Science & Technology* **2020**,*10* (10),3181-3194.

12. Andrews, E.; Lopez-Ruiz, J. A.; Egbert, J. D.; Koh, K.; Sanyal, U.; Song, M.; Li, D.; Karkamkar, A. J.; Derewinski, M. A.; Holladay, J.; et al. Performance of Base and Noble

Metals for Electrocatalytic Hydrogenation of Bio-Oil-Derived Oxygenated Compounds. *ACS Sustainable Chemistry & Engineering* **2020**,*8* (11),4407-4418.

13. Amouzegar, K.; Savadogo, O. Electrocatalytic hydrogenation of phenol on dispersed Pt: reaction mechanism and support effect. *Electrochimica Acta* **1998**,*43* (5),503-508.

14. Cleghorn, S. J. C.; Pletcher, D. The mechanism of electrocatalytic hydrogenation of organic molecules at palladium black cathodes. *Electrochimica Acta* **1993**,*38* (2),425-430.

15. Li, Z.; Kelkar, S.; Raycraft, L.; Garedew, M.; Jackson, J. E.; Miller, D. J.; Saffron, C. M. A mild approach for bio-oil stabilization and upgrading: electrocatalytic hydrogenation using ruthenium supported on activated carbon cloth. *Green Chemistry* **2014**,*16* (2),844-852,10.1039/C3GC42303D.

16. Yu, J.; Zhang, P.; Li, L.; Li, K.; Zhang, G.; Liu, J.; Wang, T.; Zhao, Z.-J.; Gong, J. Electroreductive coupling of benzaldehyde by balancing the formation and dimerization of the ketyl intermediate. *Nature Communications* **2022**,*13* (1),7909.

17. Song, Y.; Sanyal, U.; Pangotra, D.; Holladay, J. D.; Camaioni, D. M.; Gutiérrez, O. Y.; Lercher, J. A. Hydrogenation of benzaldehyde via electrocatalysis and thermal catalysis on carbon-supported metals. *Journal of Catalysis* **2018**,*359*,68-75.

18. Mitchell, A. G.; Wan, L. S. C.; Bjaastad, S. G. The solubility of benzaldehyde in water. *Journal of Pharmacy and Pharmacology* **1964**,*16* (9),632-633.

19. Hammerich, O.; Speiser, B. *Organic electrochemistry*; CRC press Boca Raton,**2016**.

20. Ofoegbu, S. U.; Ferreira, M. G. S.; Nogueira, H. I. S.; Zheludkevich, M. Comparison of the Electrochemical Response of Carbon-Fiber-Reinforced Plastic (CFRP), Glassy Carbon, and Highly Ordered Pyrolytic Graphite (HOPG) in Near-Neutral Aqueous Chloride Media. *C* **2023**,*9* (1),7.

21. Nagy, K. A.; Tóth, I. Y.; Ballai, G.; Varga, Á. T.; Szenti, I.; Sebők, D.; Kopniczky, J.; Hopp, B.; Kukovecz, Á. Wetting and evaporation on a carbon cloth type gas diffusion layer for passive direct alcohol fuel cells. *Journal of Molecular Liquids* **2020**,*304*,112698.

22. Nolan, H.; Schröder, C.; Brunet-Cabré, M.; Pota, F.; McEvoy, N.; McKelvey, K.; Perova, T. S.; Colavita, P. E. MoS2/carbon heterostructured catalysts for the hydrogen evolution reaction: N-doping modulation of substrate effects in acid and alkaline electrolytes. *Carbon* **2023**,*202*,70-80.

23. McCrory, C. C.; Jung, S.; Peters, J. C.; Jaramillo, T. F. Benchmarking heterogeneous electrocatalysts for the oxygen evolution reaction. *Journal of the American Chemical Society* **2013**,*135* (45),16977-16987.

24. Arvay, A.; Yli-Rantala, E.; Liu, C. H.; Peng, X. H.; Koski, P.; Cindrella, L.; Kauranen, P.; Wilde, P. M.; Kannan, A. M. Characterization techniques for gas diffusion layers for proton exchange membrane fuel cells – A review. *Journal of Power Sources* **2012**,*213*,317-337.

25. Li, Y. S.; Zhao, T. S.; Xu, J. B.; Shen, S. Y.; Yang, W. W. Effect of cathode micro-porous layer on performance of anion-exchange membrane direct ethanol fuel cells. *Journal of Power Sources* **2011**,*196* (4),1802-1807.

26. Bomben, K.; Moulder, J.; Sobol, P. E.; Stickle, W. Handbook of X-ray photoelectron spectroscopy: a reference book of standard spectra for identification and interpretation of XPS data. *Eden Prairie, MN (USA): Physical electronics* **1995**.

27. Hellgren, N.; Haasch, R. T.; Schmidt, S.; Hultman, L.; Petrov, I. Interpretation of X-ray photoelectron spectra of carbon-nitride thin films: New insights from in situ XPS. *Carbon* **2016**,*108*,242-252.

28. Qu, L.; Liu, Y.; Baek, J.-B.; Dai, L. Nitrogen-doped graphene as efficient metal-free electrocatalyst for oxygen reduction in fuel cells. *ACS nano* **2010**,*4* (3),1321-1326.

29. Titantah, J.; Lamoen, D. Carbon and nitrogen 1s energy levels in amorphous carbon nitride systems: XPS interpretation using first-principles. *Diamond and related materials* **2007**,*16* (3),581-588.

30. Golub, M. A.; Lopata, E. S.; Finney, L. S. X-ray Photoelectron Spectroscopy Study of Argon Plasma-Treated Fluoropolymers. *Langmuir* **1994**,*10* (10),3629-3634.

31. Chen, G.; Zhang, J.; Yang, S. Fabrication of hydrophobic fluorinated amorphous carbon thin films by an electrochemical route. *Electrochemistry Communications* **2008**,*10* (1),7-11.

32. Zahiri, B.; Felix, R. M.; Hill, A.; Kung, C. H.; Sharma, T.; Real, J. D.; Mérida, W. Through-plane wettability tuning of fibrous carbon layers via O2 plasma treatment for enhanced water management. *Applied Surface Science* **2018**,*458*,32-42.

33. Dai, Y.; Cai, S.; Wu, L.; Yang, W.; Xie, J.; Wen, W.; Zheng, J.-C.; Zhu, Y. Surface modified CFx cathode material for ultrafast discharge and high energy density. *Journal of Materials Chemistry A* **2014**,*2* (48),20896-20901,10.1039/C4TA05492J.

34. Jernigan, G. G.; Nolde, J. A.; Mahadik, N. A.; Cleveland, E. R.; Boercker, J. E.; Katz, M. B.; Robinson, J. T.; Aifer, E. H. Physical properties of nanometer graphene oxide films partially and fully reduced by annealing in ultra-high vacuum. *Journal of Applied Physics* **2017**,*122* (7).

35. Jerigová, M.; Odziomek, M.; López-Salas, N. “We Are Here!” Oxygen Functional Groups in Carbons for Electrochemical Applications. *ACS Omega* **2022**,*7* (14),11544-11554.

36. Pota, F.; Costa de Oliveira, M. A.; Schröder, C.; Brunet Cabré, M.; Nolan, H.; Rafferty, A.; Jeannin, O.; Camerel, F.; Behan, J. A.; Barrière, F.; et al. Porous N-Doped Carbon-encapsulated Iron as Novel Catalyst Architecture for the Electrocatalytic Hydrogenation of Benzaldehyde. *ChemSusChem* **2025**,*18* (1), e202400546.

37. Mairanovskii, S.; Rubinskaya, T. Y.; Gul'tyai, V.; Proskurovskaya, I. Electrochemical reduction of benzaldehyde to benzyl alcohol at a mercury cathode. *Bulletin of the Academy of Sciences of the USSR, Division of chemical science* **1976**,*25* (10),2203-2205.

38. Wijaya, Y. P.; Grossmann-Neuhaeusler, T.; Dhewangga Putra, R. D.; Smith, K. J.; Kim, C. S.; Gyenge, E. L. Electrocatalytic Hydrogenation of Guaiacol in Diverse Electrolytes Using a Stirred Slurry Reactor. *ChemSusChem* **2020**,*13* (3),629-639.

39. Hreiz, R.; Abdelouahed, L.; Fünfschilling, D.; Lapicque, F. Electrogenerated bubbles induced convection in narrow vertical cells: A review. *chemical engineering research and design* **2015**,*100*,268-281.

40. Lopez-Ruiz, J. A.; Andrews, E.; Akhade, S. A.; Lee, M.-S.; Koh, K.; Sanyal, U.; Yuk, S. F.; Karkamkar, A. J.; Derewinski, M. A.; Holladay, J. Understanding the role of metal and molecular structure on the electrocatalytic hydrogenation of oxygenated organic compounds. *ACS Catalysis* **2019**,*9* (11),9964-9972.

41. Cheong, A. K.; Bolduc, Y.; Lessard, J. Electrocatalytic hydrogenation of ketones and of α-and β-diketones on Raney metal electrodes. *Canadian journal of chemistry* **1993**,*71* (11),1850-1856.

42. Akhade, S. A.; Singh, N.; Gutiérrez, O. Y.; Lopez-Ruiz, J.; Wang, H.; Holladay, J. D.; Liu, Y.; Karkamkar, A.; Weber, R. S.; Padmaperuma, A. B. Electrocatalytic hydrogenation of biomass-derived organics: a review. *Chemical reviews* **2020**,*120* (20),11370-11419.

43. Nutting, J. E.; Gerken, J. B.; Stamoulis, A. G.; Bruns, D. L.; Stahl, S. S. "How Should I Think about Voltage? What Is Overpotential?": Establishing an Organic Chemistry Intuition for Electrochemistry. *The Journal of organic chemistry* **2021**,*86* (22),15875-15885.

44. Andrews, E.; Lopez-Ruiz, J. A.; Egbert, J. D.; Koh, K.; Sanyal, U.; Song, M.; Li, D.; Karkamkar, A. J.; Derewinski, M. A.; Holladay, J. Performance of base and noble metals for electrocatalytic hydrogenation of bio-oil-derived oxygenated compounds. *ACS Sustainable Chemistry & Engineering* **2020**,*8* (11),4407-4418.

45. Jiang, Y.; Catizane, C. R.; Sumner, J. Improving plastics pyrolysis oil quality via electrochemical process for polymer recycling: A review. *Energy Advances* **2024**.

46. Sanyal, U.; Yuk, S. F.; Koh, K.; Lee, M. S.; Stoerzinger, K.; Zhang, D.; Meyer, L. C.; Lopez-Ruiz, J. A.; Karkamkar, A.; Holladay, J. D. Hydrogen bonding enhances the electrochemical hydrogenation of benzaldehyde in the aqueous phase. *Angewandte Chemie* **2021**,*133* (1),294-300.

47. Trasatti, S. Work function, electronegativity, and electrochemical behaviour of metals: III. Electrolytic hydrogen evolution in acid solutions. *Journal of Electroanalytical Chemistry and Interfacial Electrochemistry* **1972**,*39* (1),163-184.

48. Lopez-Ruiz, J. A.; Sanyal, U.; Egbert, J.; Gutiérrez, O. Y.; Holladay, J. Kinetic investigation of the sustainable electrocatalytic hydrogenation of benzaldehyde on Pd/C: effect of electrolyte composition and half-cell potentials. *ACS Sustainable Chemistry & Engineering* **2018**,*6* (12),16073-16085.

49. Kwon, Y.; Birdja, Y. Y.; Raoufmoghaddam, S.; Koper, M. T. Electrocatalytic hydrogenation of 5-hydroxymethylfurfural in acidic solution. *ChemSusChem* **2015**,*8* (10),1745-1751.

50. Kwon, Y.; Koper, M. T. Electrocatalytic hydrogenation and deoxygenation of glucose on solid metal electrodes. *ChemSusChem* **2013**,*6* (3),455-462.

51. Nilges, P.; Schröder, U. Electrochemistry for biofuel generation: production of furans by electrocatalytic hydrogenation of furfurals. *Energy & Environmental Science* **2013**,*6* (10),2925-2931.

52. Li, Z.; Kelkar, S.; Lam, C. H.; Luczek, K.; Jackson, J. E.; Miller, D. J.; Saffron, C. M. Aqueous electrocatalytic hydrogenation of furfural using a sacrificial anode. *Electrochimica Acta* **2012**,*64*,87-93.

53. Singh, N.; Sanyal, U.; Ruehl, G.; Stoerzinger, K. A.; Gutiérrez, O. Y.; Camaioni, D. M.; Fulton, J. L.; Lercher, J. A.; Campbell, C. T. Aqueous phase catalytic and electrocatalytic hydrogenation of phenol and benzaldehyde over platinum group metals. *Journal of Catalysis* **2020**,*382*,372-384.

54. Behan, J. A.; Hoque, M. K.; Stamatin, S. N.; Perova, T. S.; Vilella-Arribas, L.; Garcia-Melchor, M.; Colavita, P. E. Experimental and computational study of dopamine as an electrochemical probe of the surface nanostructure of graphitized N-doped carbon. *The Journal of Physical Chemistry C* **2018**,*122* (36),20763-20773.

55. De Oliveira, M. A. C.; Schröder, C.; Cabré, M. B.; Nolan, H.; Forner-Cuenca, A.; Perova, T. S.; McKelvey, K.; Colavita, P. E. Effects of N-functional groups on the electron transfer kinetics of VO2+/VO2+ at carbon: Decoupling morphology from chemical effects using model systems. *Electrochimica Acta* **2024**,*475*,143640.

56. Behan, J. A.; Mates-Torres, E.; Stamatin, S. N.; Domínguez, C.; Iannaci, A.; Fleischer, K.; Hoque, M. K.; Perova, T. S.; García-Melchor, M.; Colavita, P. E. Untangling cooperative effects of pyridinic and graphitic nitrogen sites at metal-free N-doped carbon electrocatalysts for the oxygen reduction reaction. *Small* **2019**,*15* (48),1902081.

CHAPTER 5

Effect of metal concentration in M@C:N architectures: investigating structural and electrochemical differences

---

M@C:N architectures using Fe as metal core have shown promising results in the electrocatalytic hydrogenation of BZH. However, other low-cost metal cores have yet to be explored for similar applications. In this Chapter, W and Mo are investigated as active sites for the preparation of M@C:N, with the methodology developed in previous chapters being adapted for their synthesis. The structural properties and electrochemical behaviour of both Mo- and W-based materials are evaluated, revealing the significant impact of metal concentration on performances and composition.

This chapter presents result and contents reported in the candidate's first-author publication, titled:

Electrocatalytic hydrogenation of unsaturated organics using Mo and W porous carbon-encapsulated nanostructures: impact of metal type on properties and performances

Pota, F.; Costa de Oliveira, M. A.; Schröder, C.; Rafferty, A.; De Castro C.; Rault L.; Behan, J. A.; Barrière, F.; Colavita, P. E.

Journal of Materials Chemistry A, 2025, Advance Article

With the exception of specified contributions, the candidate conducted the primary investigation reported in the published work and prepared the first draft of the paper, along with subsequent revisions, under the supervision of Prof. Paula E. Colavita. The contributions of the other coauthors are as follows: M.A.C.O. development of the sample preparation methodology, C.S. XPS analysis, A.R. BET and PSD analysis, C.D.C XRF analysis, L.R. TEM-EDX analysis, J.A.B. & F.B. writing - review and editing, P.E.C conceptualization and supervision.

5.1 Introduction

The advantages of utilising low-cost metal cores in M@C:N architectures were discussed in Chapter 1. In particular, the use of Fe as an active site was extensively explored in Chapters 3 and 4, yielding encouraging results in terms of performance and material stability. This has prompted a review of catalyst preparation methods using alternative low-cost metal cores. Indeed, as highlighted in Chapter 1, transition metals such as Mo and its carbide, Mo_2C, have demonstrated promising HER activity in both acidic and neutral media.[1,2] Similarly, W_2C has also been reported as an effective HER electrocatalyst in acidic media, albeit with slightly lower performance compared to Mo.[2] Notably, encapsulating Mo or W within an M@C:N structure has shown enhanced HER performance,[3,4] however no report on their use as electrocatalyst for benzaldehyde hydrogenation are reported to date. HER activity is a key requirement in the design of new ECH electrocatalysts, while simultaneously striving to balance the competition between these two electrochemical processes. To develop an optimised procedure for preparing such electrocatalysts, it is essential to understand how metal concentration affects ECH performance and HER competition. Specifically, for a given metal, it is crucial to determine the impact of concentration variations on hydrogenation processes.

In this chapter, Mo and W were selected as metal cores for the preparation of M@C:N architectures with varying metal concentrations. For each metal, two materials were synthesised with lower –(L) and higher –(H) atomic %-content of active sites, allowing for an internal comparison of how changes in the concentration of the same metal affect electrochemical performance, composition and nanostructure. The use of ammonium salt precursors also resulted in different dispersibility of the final catalyst powders, which were assessed to develop a new ink preparation recipe. The results and discussion section of this Chapter is divided into subsections for Mo- and W-based electrocatalysts. These sections evaluate the impact of varying metal concentrations on both the composition (surface and bulk) and structure, and how these affect the ECH performance for each metal core. The results presented in this chapter demonstrated that differences in metal concentration significantly influence the structural properties and electrochemical behaviour of both Mo- and W-based materials.

5.2 Experimental section

Materials. Nafion® 117 solution (5%), resorcinol (99%), Pluronic F-127, melamine (99%), hydrochloric acid (37%), sulfuric acid (95–98%), nitric acid (≥ 65%), formaldehyde solution (37 wt%), hydrogen peroxide (30%), sodium sulfate (> 99%); benzaldehyde (BZH, > 99%); hydrobenzoin (HBZ,99%); acetophenone (> 99%); ethyl acetate (>99%); ammonium heptamolybdate tetrahydrate ($(NH_4)_6Mo_7O_{24} \cdot 4\ H_2O$,99%) were all purchased from Sigma Aldrich and used as received. Methanol (>99%), benzyl alcohol (BA, >99%) and ammonium metatungstate hydrate ($(NH_4)_6W_{12}O_{39} \cdot H_2O$,99%) were purchased from Fisher and used as received. Black Pearls 2000® (BP, > 1400 m^2/g) were purchased from Cabot.

Catalyst synthesis. BP were purified as mentioned in Chapter 3. Porous carbon-based catalysts were synthesised by first dissolving resorcinol (0.83 g), Pluronic F-127 (1.25 g), and melamine (0.42 g) in 20 mL of a 1:1 water:methanol solution and stirring for 15 min. Ammonium heptamolybdate tetrahydrate $(NH_4)_6Mo_7O_{24} \cdot 4H_2O$, or ammonium metatungstate hydrate $(NH_4)_6W_{12}O_{39} \cdot H_2O$, were then added as metal precursors in amounts summarised in **Table 5.1**, followed by the addition of concentrated HCl (0.2 g) and stirring for 1 h. Formaldehyde (1.25 g) was introduced dropwise, resulting in a homogeneous slurry after vigorous stirring for another hour. Purified BP (0.75 g) was added to the mixture and stirred for an additional 15 min. The mixture was heated in a Teflon-lined autoclave at 50 °C for 2 days, then the vessel was opened and the solid was thoroughly dried at the same temperature. The sample was ground in a mortar, inserted in a tube furnace at 250 °C under N_2 flow and, finally, annealed at 800 °C for 2 h in a N_2:NH_3 flow (1:1 vol.,200 sccm total) following the procedure reported previously.

Electrochemical characterisation. Ink dispersions contained catalyst (0.0100 g ± 0.0003), 270 µL of deionised water, 160 µL of methanol (MeOH) and 53 µL of Nafion solution. Each addition was followed by 10 min of sonication in a cooling bath; the resulting dispersion was drop-cast on carbon working electrodes for further analysis. GC disks (Ø 5 mm, HTW GmbH) were used as working electrodes for CV experiments. GC disks were polished as described in Chapter 3 and modified with the ink dispersion (10 µL), then dried under inert gas, resulting in a loading of 1.06 mg cm^{-2}. Flags of CC (1 cm^2 geometric area, FuelCellStore) with microporous layer were used as current collectors for electrolysis experiments. The CC was used as received after covering the

back side with insulating polyimide tape.52 μL of the ink were drop-cast in two equal aliquots following the same preparation procedure used for Fe@C:N, yielding a loading of 1.07 mg cm^{-2} across all samples. Voltammetry and chronoamperometry experiments were carried out as described in previous Chapters, utilising the same three-electrode configuration.

5.3 Results and discussion

Carbon-based materials were prepared using the optimised procedure described in Chapter 3 for Fe@C:N. Briefly, materials were synthesised via polycondensation of resorcinol and formaldehyde with the addition of BP carbon black as a conductive scaffold, Pluronic F-127 as a soft template and melamine as a nitrogen source. Annealing at 800 °C under N_2/NH_4 atmosphere resulted in graphitisation of the prepared samples. Mo and W metal precursors were integrated into the established protocol and varied their amount to prepare two distinct electrode materials per metal. **Table 5.1** shows the precursor quantities used for the synthesis of each sample, as well as the metal content obtained after the final graphitisation step, by weight and by atomic percent. The bulk composition of Mo-based materials was investigated via ICP-OES, while for W-based electrodes ED-XRF analysis was performed. The atomic-% content in the bulk was calculated assuming carbon and metal to be the main components. Mo-based materials are referred to as Mo@C:N and Mo@C:N-(L), with the latter having a lower metal concentration. W-based electrocatalysts are labelled as W@C:N and W@C:N-(H), with the latter having a higher metal concentration.

Table 5.1 Summary of samples, details of the metal precursors used, metal content after the final graphitisation step by weight-% and by atomic-%, and BET specific surface area.

Material	Metal Precursor	Initial metal precursor (g)	wt. (%)	at. (%)	BET (m^2/g)
Mo@C:N	$(NH_4)_6Mo_7O_{24} \cdot 4H_2O$	1.78	10.8[a]	1.51	229
Mo@C:N-(L)	$(NH_4)_6Mo_7O_{24} \cdot 4H_2O$	0.36	3.59[a]	0.46	509
W@C:N	$(NH_4)_6W_{12}O_{39} \cdot H_2O$	0.61	17.7[b]	1.41	450
W@C:N-(H)	$(NH_4)_6W_{12}O_{39} \cdot H_2O$	2.5	29.3[b]	2.71	198

a – Data obtained by ICP-OES on the graphitised material. *b* – Data obtained by ED-XRF on the graphitised material.

5.3.1 Mo-based electrode materials

The bulk structure of Mo-based materials was first investigated via XRD; **Figure 5.1a** reports patterns collected for Mo@C:N and Mo@C:N-(L). The Mo@C:N pattern indicates the presence of crystalline phases consisting of mostly Mo_2C, with contributions from MoO_2 oxide. Peaks at 34.4º,37.8º,39.3º,51.9º,61.5º,69.3º,74.4º,75.6º, match well those Mo_2C reference (PDF#35-0787) and are assigned to reflections (100), (002), (101), (102), (110), (103), (112) and (201), respectively. The broad peak at 25.3º is assigned to (002) reflection of graphitic carbon while the small broad peak at 36.9º indicates the presence of MoO_2 (PDF#65-5787).[5]

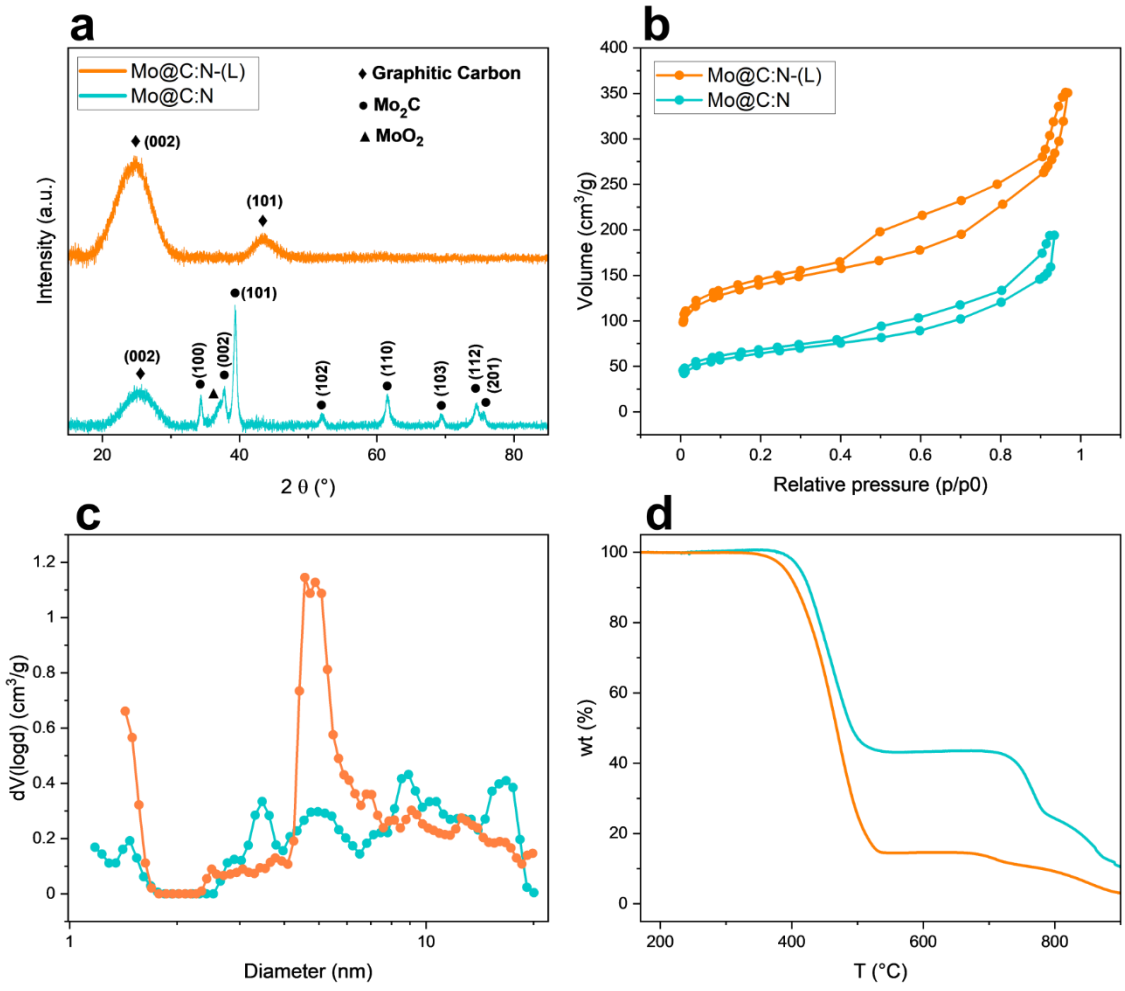

Figure 5.1 (a) XRD patterns, (b) nitrogen adsorption-desorption isotherm, (c) pore size distribution, and (d) TGA curves, collected for Mo@C:N and Mo@C:N-(L).

The XRD pattern of Mo@C:N-(L), synthesised with a lower metal content, shows only peaks associated with the graphitised carbon phase at 25.3º and 43.2º, indexed as (002) and (101) reflections,[5] thus suggesting that Mo-containing phases are either below the detection limit or highly amorphous when the metal is introduced at these lower concentrations. Both samples were found to be porous as expected based on previous results using related protocols for M@C incorporation.[6,7] Materials display similar hysteresis loops characteristic of type IV isotherms associated with capillary condensation, and type H4 loops reported for narrow slit-like micro-/mesopores (**Figure 5.1b**).[8,9] The BET specific surface values calculated from the isotherms are summarised in **Table 5.1**. Mo@C:N display a lower specific surface area compared to Mo@C:N-(L) due to the higher metal incorporation. The differences in hysteresis profiles reveal significant differences in pore structure among the materials. This is confirmed by comparison of PSDs in **Figure 5.1c**, where the capability of Mo centres to catalyse pore opening is evident at lower concentrations, as the PSD for Mo@C:N-(L) shows already a significant shift in the maximum contribution from *ca.*3.5 nm to 5 nm. This suggests that the progressive introduction of metals has a marked effect on the pore distribution, particularly in the range 3.5 – 4.5 nm, as these tend to be suppressed in favour of the formation of larger pores. **Figure 5.1d** shows the TGA curves collected in air for Mo@C:N and Mo@C:N-(L). The TGA of Mo@C:N yields multiple processes: the first one at *ca.*360 °C is marked by a small 0.7% mass increase that suggests formation of MoO_x species, as previously reported in the case of Mo_2C materials,[10,11] followed by a mass loss attributable to combustion of carbon. The high temperature mass losses starting at *ca.*700 °C are likely due to oxidation combined with sublimation of MoO_3, which is known to take place above 700 °C.[12,13] Indeed, the solid residue of 10.5% at 900 °C would account for an estimated Mo-content of only 7%, assuming a residual consisting of MoO_3. This value is lower than the Mo-content in **Table 5.1** obtained from ICP-OES, as expected after partial sublimation during the temperature ramp. The TGA curve for Mo@C:N-(L) displays a first combustion starting at *ca.*320°C without any discernible mass increase resulting from MoO_x formation, likely due to lower metal incorporation compared to Mo@C:N. As for Mo@C:N, the process starting at *ca.*700 °C is assigned to sublimation of MoO_3 species with possible combustion of any residual highly graphitised carbon. The final residual of MoO_2 was found to be 3.04 wt%, that corresponds to *ca.*2 wt.% of Mo, which is again lower than the Mo-content in **Table 5.1**, obtained via ICP-MS.

Figure 5.2 show survey spectra of Mo-containing materials; peaks associated with Mo 4p (41 eV), Mo 3d (231 eV), Mo $3p_{1/2}$ (398 eV), Mo 3s (511 eV), C 1s (284 eV), N 1s (414 eV), O 1s (531 eV) ionisations are clearly identified. The In foil support contributes additional peaks at 18.4 eV,444.5 and 452.7 eV,667.4 and 704.6 eV, corresponding to In In 4d, In 3d and In 3p emissions.[14] The O-content of Mo@C:N materials was therefore obtained by subtracting the oxide contribution from the indium foil (In_2O_3) from the total area of the O 1s peak.

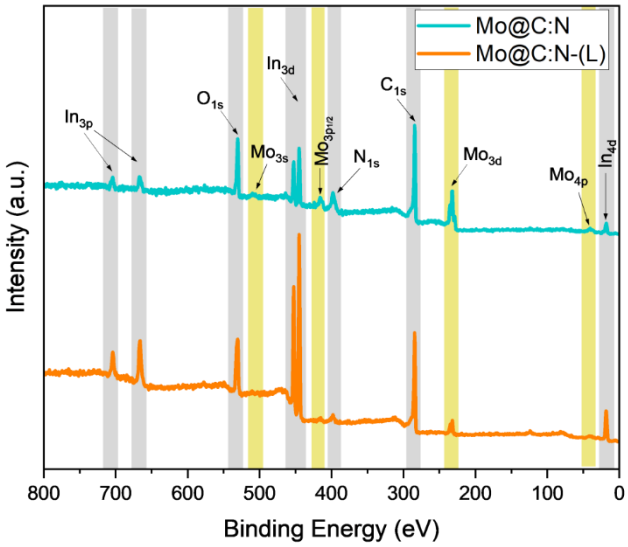

Figure 5.2 Survey XPS spectra of Mo-based electrocatalysts. Pecks associated to Mo are highlighted in yellow, while all other contributions are marked in grey.

As showed in **Figure 5.3a-b**, the C 1s peak was deconvoluted using six components attributed to sp^2 (284.2 eV) and sp^3 (285.3 eV) carbon, C-O (286.6 eV) and C=O (288.0 eV) groups, π-π* excitations (289.0 eV) and COOH groups (290.0 eV).[15-18] For both materials, the sp^2 peak constitutes the largest contribution to the total intensity, as shown in **Table 5.2**. $C_{sp}{}^2/C_{tot}$ ratio indicate that Mo@C:N undergo higher graphitisation during the annealing step compare to Mo@C:N-(L). N 1s spectra are shown in **Figure 5.3c-d**. Best-fits were obtained using three components attributed to graphitic-N, pyrrolic-N and pyridinic-N; **Table 5.2** report the binding energies and %-contributions to the total nitrogen content for each component.[16,19] Notably, the peak associated with pyrrolic-N could not be resolved for Mo@C:N-(L), likely due to the strong contribution of pyridinic-N (**Figure 5.3d**). Indeed, for both Mo@C:N and Mo@C:N-(L) pyridinic-N accounts for

the majority component. An additional well-resolved peak at *ca.*394.6 eV is also observed and is assigned to Mo $3p_{3/2}$ ionizations.[10,20,21]

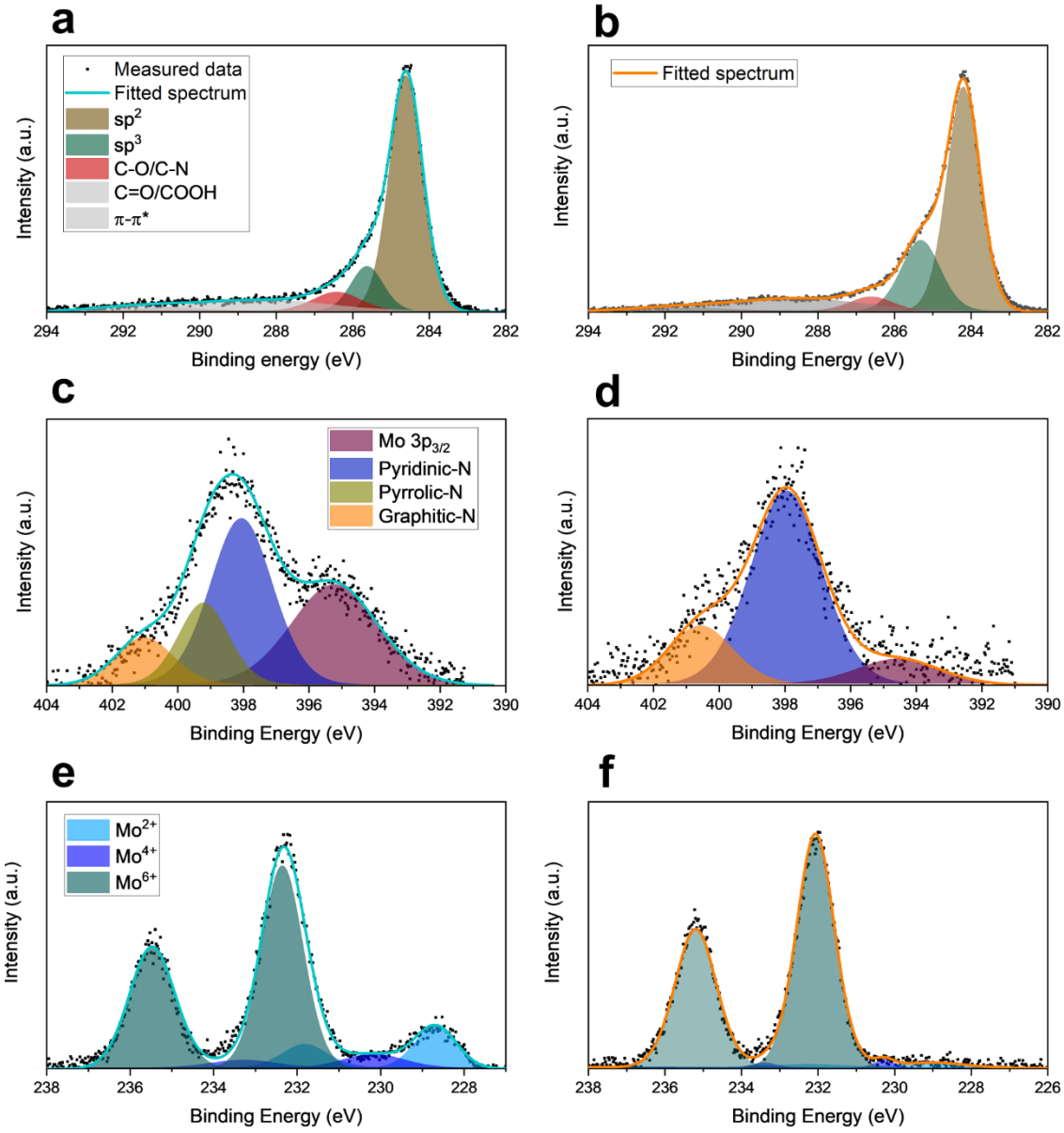

Figure 5.3 XPS high resolution spectra of C 1s (a), N 1s (c) and Mo 3d (e) for Mo@C:N; and of C 1s (b), N 1s (d) and Mo 3d (f) for Mo@C:N-(L).

The Mo 3d spectrum of Mo@C:N, **Figure 5.3e-f**, was deconvoluted using three doublets with an energy splitting of *ca.*3 eV, assigned to Mo^{2+} (228 eV), Mo^{4+} (230 eV), and Mo^{6+} (232 eV) species. Mo^{2+} components indicate the presence of molybdenum carbides in the form of Mo_2C and/or MoC, whereas Mo^{4+} and Mo^{6+} arise from oxide species due to surface oxidation in air, as previously reported for Mo carbides.[10,22,23] **Table 5.2** report %-contributions to the total metal content for each component. Peak area ratios, **Table**

5.2, indicate that the majority of surface Mo centers (>80%) are indeed oxidised after air exposure, in contrast with the predominance of carbide phases in the bulk evidenced by XRD studies.

Table 5.2 Summary of atomic elemental compositions and selected best-fit results, along with nitrogen content and Mo %-contents calculated from best-fits of high resolution XPS spectra of Mo-based materials.

Material	C (at.%)	O [a] (at.%)	N (at.%)	Mo (at.%)	C_{sp^2}/C_{tot} [b] (%)	M/C (at.%)	MC_x/M_{tot} (at.%)	M-O/M_{tot} (at.%)
Mo@C:N	68.9	13.6	13.5	4.30	63.4	5.7	16.3	83.7
Mo@C:N-(L)	86.4	6.01	6.04	1.49	56.6	1.7	3.9	96.0
	Pyri-N[c] (%)	**Pyrr-N[c] (%)**	**Gra-N[c] (%)**		**Mo^{2+} (%)**	**Mo^{4+} (%)**	**Mo^{6+} (%)**	
Mo@C:N	397.6 eV 61	398.8 eV 24	400.6 eV 15		16.3	8.5	75.2	
Mo@C:N-(L)	397.9 eV 78	NA	400.7 eV 22		3.9	1.6	94.4	

a – atomic-% content calculated from the contribution to the O 1s area that does not arise from In_2O_3

b – Calculated as area ratio of the best-fit component 284.4 eV over the total C 1s peak

c – Pyri-N = Pyridinic-N, Pyrr-N = Pyrrolic-N, Gra-N= Graphitic-N.

The morphology of the materials was investigated via electron microscopies. **Figure 5.4a-b** shows an SEM image of Mo@C:N and Mo@C:N-(L), respectively. Materials consist of nanostructured particles with rough and irregular surfaces; Mo is uniformly distributed in the carbon matrix as shown in the SEM-EDX mapping at C, O and Mo energies. HR-TEM, performed on Mo@C:N showed in **Figure 5.4c-d**, indicates that the sample consists of opaque nanoparticles (~5 nm diameter), embedded within a graphitised carbon matrix: nanoparticles exhibit lattice *d*-spacing of 0.138 nm, in **Figure 5.4e**, closely matching (103) reflections of Mo_2C at 0.135 nm (PDF#35- 0787).

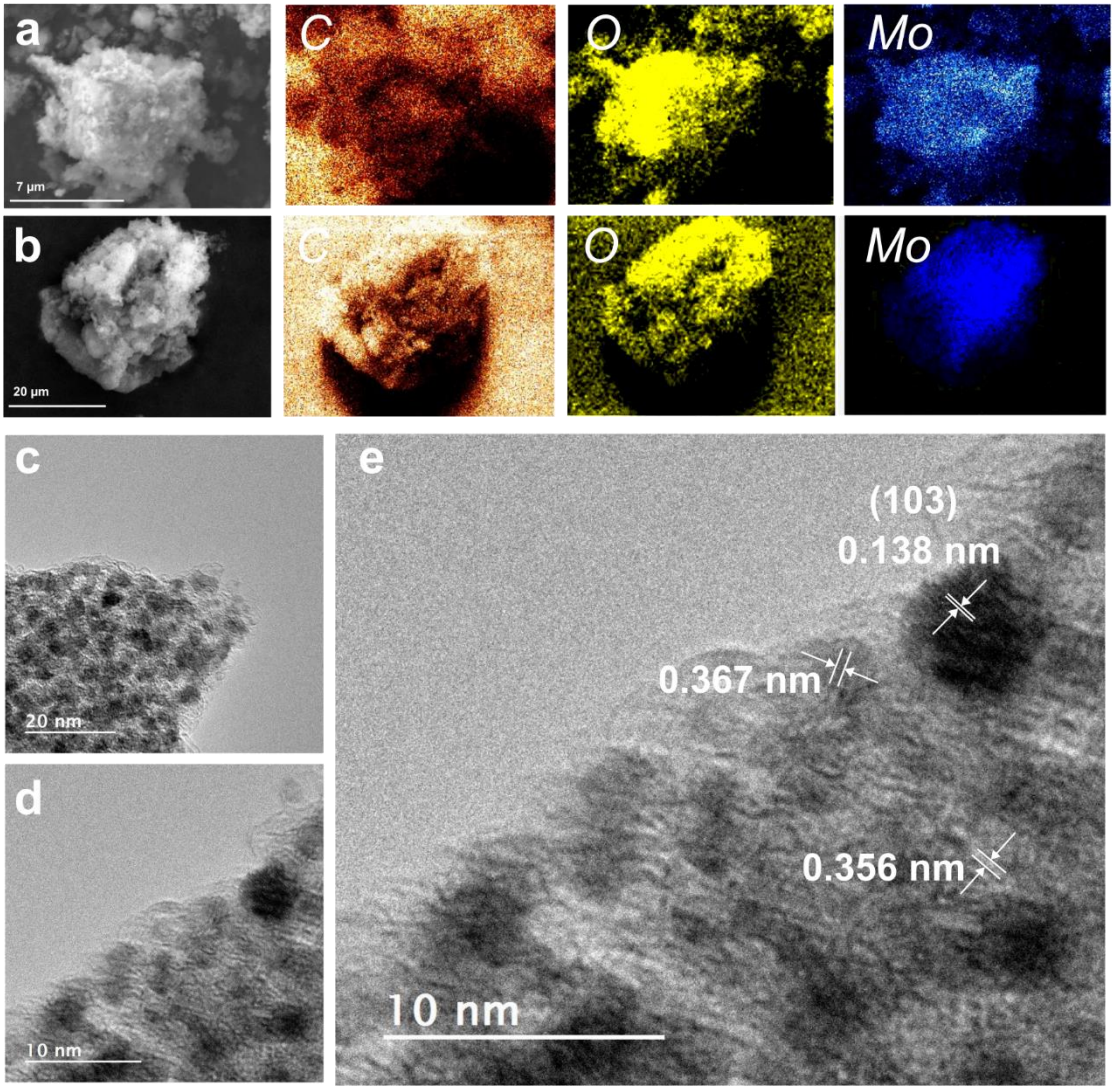

Figure 5.4 SEM images for (a) Mo@C:N and (b) Mo@C:N-(L) with SEM-EDX mapping in the C, O, Mo spectral regions. HR-TEM (c-d) of Mo@C:N and (e) HR-TEM for Mo@C:N with measured d-spacings (white arrow).

Electrochemical analysis was conducted using an ink dispersion, which was prepared and drop casted onto a polished GC disk. The procedure for ink preparation was consistent with the method used for Fe@C:N, as described in Chapter 3. However, the results were less satisfactory due to the lower dispersibility of the catalyst powders compared to Fe-based materials. Consequently, the drop-casting approach was unsuccessful, as the ink dispersion exhibited an uneven distribution and poor adhesion to the carbon support (**Figure 5.5a**). To improve dispersion, various tests were conducted, highlighting the importance of the water to organic solvent ratio. Prepared Mo-based samples showed better dispersion in water compared to organic solvents. Unlike the Fe@C:N ink dispersion, which used 59% IPA as the main solvent, the Mo-based ink dispersion

primarily utilised water, constituting 56% of the mixture. Furthermore, replacing IPA with methanol and incorporating ice-bath sonication during the preparation significantly enhanced the ink's stability and ensured a more uniform distribution on the glassy carbon disk. The finalised ink dispersion protocol was established as follows: 270 µL of Millipore water, 160 µL of methanol, and 53 µL of Nafion. Each addition was followed by 10 min in ice bath sonicator. An example of ink dispersion and drop cast electrode prepared following this procedure is presented in **Figure 5.5b.**

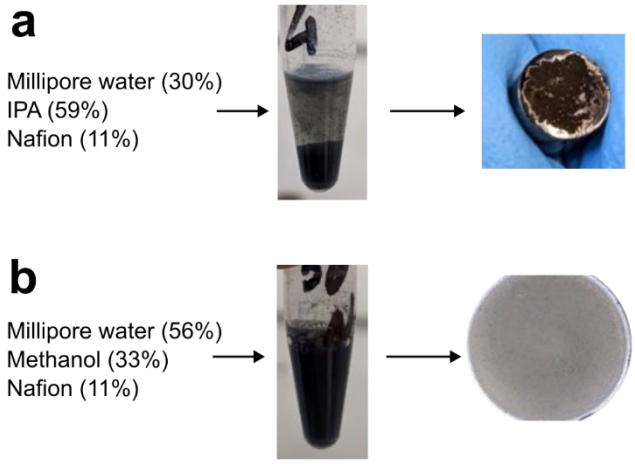

Figure 5.5 (a) Recipe used for Fe@C:N applied to Mo-based catalyst powder, and (b) optimised recipe developed for Mo-based materials.

The electrochemical response for the HER reaction was investigated via voltammetry experiments, carried out in 0.1 M H_2SO_4 electrolyte after drop casting the ink dispersion on polished GC disk with identical loadings by weight. **Figure 5.6a** shows LSV in the cathodic region obtained for Mo@C:N and Mo@C:N-(L) at 2 mV s^{-1}. Mo@C:N show an overpotential $\eta \cong$ -0.17 V at 1.5 mA cm^{-2}, while Mo@C:N-(L) displays a lower HER performances with $\eta \cong$ -0.31 V at the same current density. Measurements conducted in the same conditions for bare GC disk result in higher overpotential ($\eta \cong$ - 1 V at 1 mA cm^{-2}), as already discussed in Chapter 3.[6,14] Then the HER activity of the prepared materials is strongly influenced by the incorporation of the metal and its concentration within the carbon nanoscaffold. Specifically, Mo@C:N-(L), which contains a lower metal concentration compared to Mo@C:N, also exhibits reduced HER activity. Furthermore, the presence of a cathodic peak at -0.078 V, characteristic of proton-coupled reductions of MoO_3 at low pH,[24-26] is consistent with a significant concentration of Mo^{6+} at the electroactive surface of Mo@C:N and with evidence from XPS characterisation. Mo_2C is

reported to be activated under cathodic polarisation,[24] while MoO_2/MoO_3 are sluggish in the HER;[24] therefore the observed activity of Mo@C:N in acid electrolytes is likely to be dominated by Mo^{2+} centres at the electrolyte interface. As a preliminary study of the ECH response, electrochemical measurements were repeated in the presence of 30 mM of BZH at 2 mV s^{-1} (**Figure 5.6b**), and higher concentrations were not tested to remain well below the solubility limit of the reactant (65 mM).[27] Mo@C:N remains stable in the HER response and does not show any cathodic peaks associated with the presence of the organic, thus suggesting low ECH activity. Anyway, Mo@C:N shows a suppression of the peak at -0.078 V, and this could likely be due to adsorption of the BZH, blocking surface sites involved in the electrochemical activity of molybdenum oxides. Mo@C:N-(L) shows a similar behaviour to Mo@C:N with suppression of cathodic peaks attributed to MoO_x species at -0.078 V, and absence of diagnostic peaks associated with the organic compound.

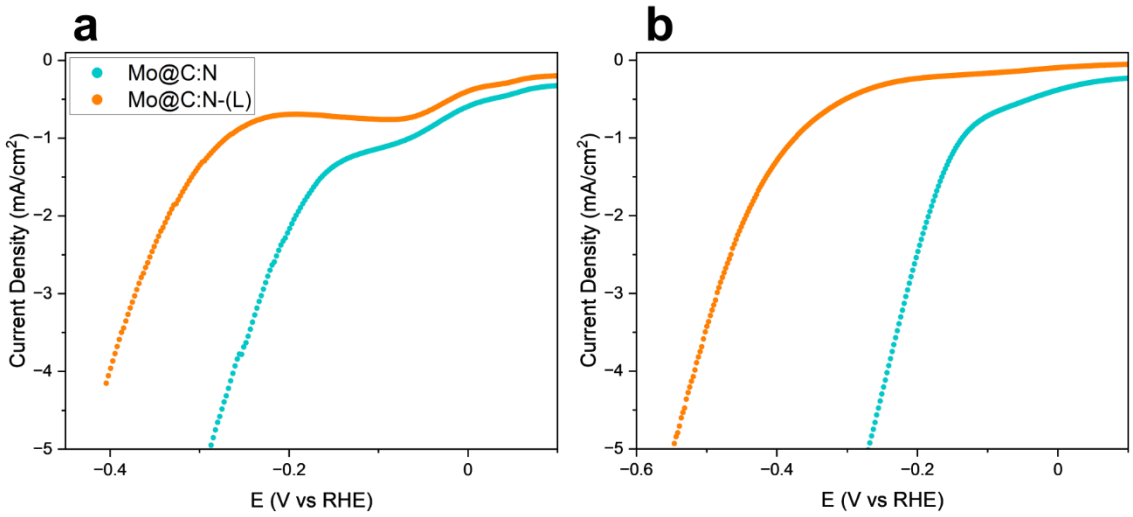

Figure 5.6 LSVs collected for Mo-based materials ink dispersion drop-casted on polished GC disk in (a) 0.1 M H_2SO_4 and (b)0.1 M H_2SO_4 + 30 mM BZH at 2 mV s^{-1}.

The catalyst ink dispersion was drop-cast onto 1 cm^2 CC supports using the procedure introduced in Chapter 4 and was tested in 0.1 M H_2SO_4 / 30 mM BZH in the H-cell discussed in the same Chapter. Mo@C:N does not show any diagnostic peak associated with BZH, in good agreement with results obtained at drop-cast disk electrodes, while Mo@C:N-(L) displays a cathodic peak at *ca.* -0.8 V similarly to Fe@C:N (**Figure 5.7**).

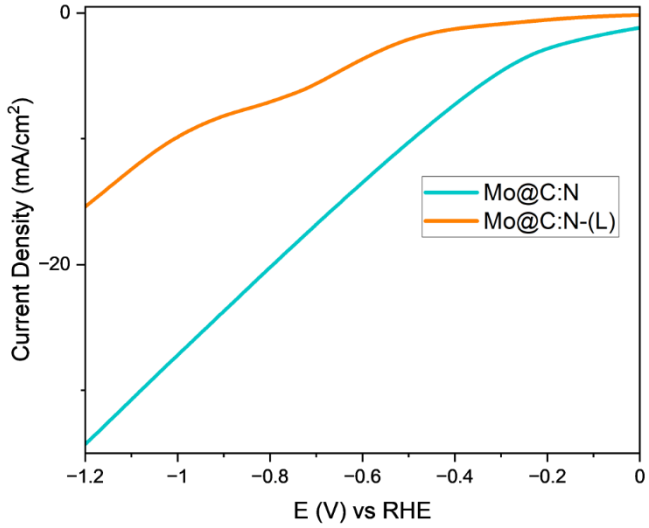

Figure 5.7 LSVs collected for Mo-based materials ink dispersion drop-casted on CC in 0.1 M H_2SO_4 + 30 mM BZH at 10 mV s^{-1}.

Electrolysis experiments were performed for 2 h at three selected potentials: -0.56 V, -0.8 V, and -1.1 V vs RHE, for both samples, to investigate and compare the influence of applied potential and metal concentration on BZH hydrogenation. Gas chromatography was used for diagnostic analysis, and FE was calculated to determine the optimal conditions. At the anodic potential of -0.56 V vs RHE, Mo@C:N-(L) exhibited a FE of *ca.*30%, with BA as the major product. In contrast, Mo@C:N showed negligible efficiency at this potential (**Figure 5.8a-b**). A similar trend was observed at the intermediate potential of -0.8 V vs RHE, **Figure 5.8c-d**, where Mo@C:N remained inactive, whereas Mo@C:N-(L) displayed a FE comparable to that at -0.56 V. At the more cathodic potential of -1.1 V vs RHE, both materials demonstrated activity toward benzaldehyde ECH, with FEs of *ca.*20% and 60% for Mo@C:N and Mo@C:N-(L), respectively (**Figure 5.8e**). Notably, Mo@C:N exhibited higher selectivity for BA, while Mo@C:N-(L) showed a higher FE for HBZ (**Figure 5.8f**). This behaviour can be attributed to differences in HER activity and the reaction pathways leading to the final products. Specifically, Mo@C:N, with its higher HER competition, favours a direct reduction pathway to BA as the preferred product. Conversely, Mo@C:N-(L), due to its lower HER activity at this potential, generates a high concentration of radical intermediates that readily dimerise to form HBZ.

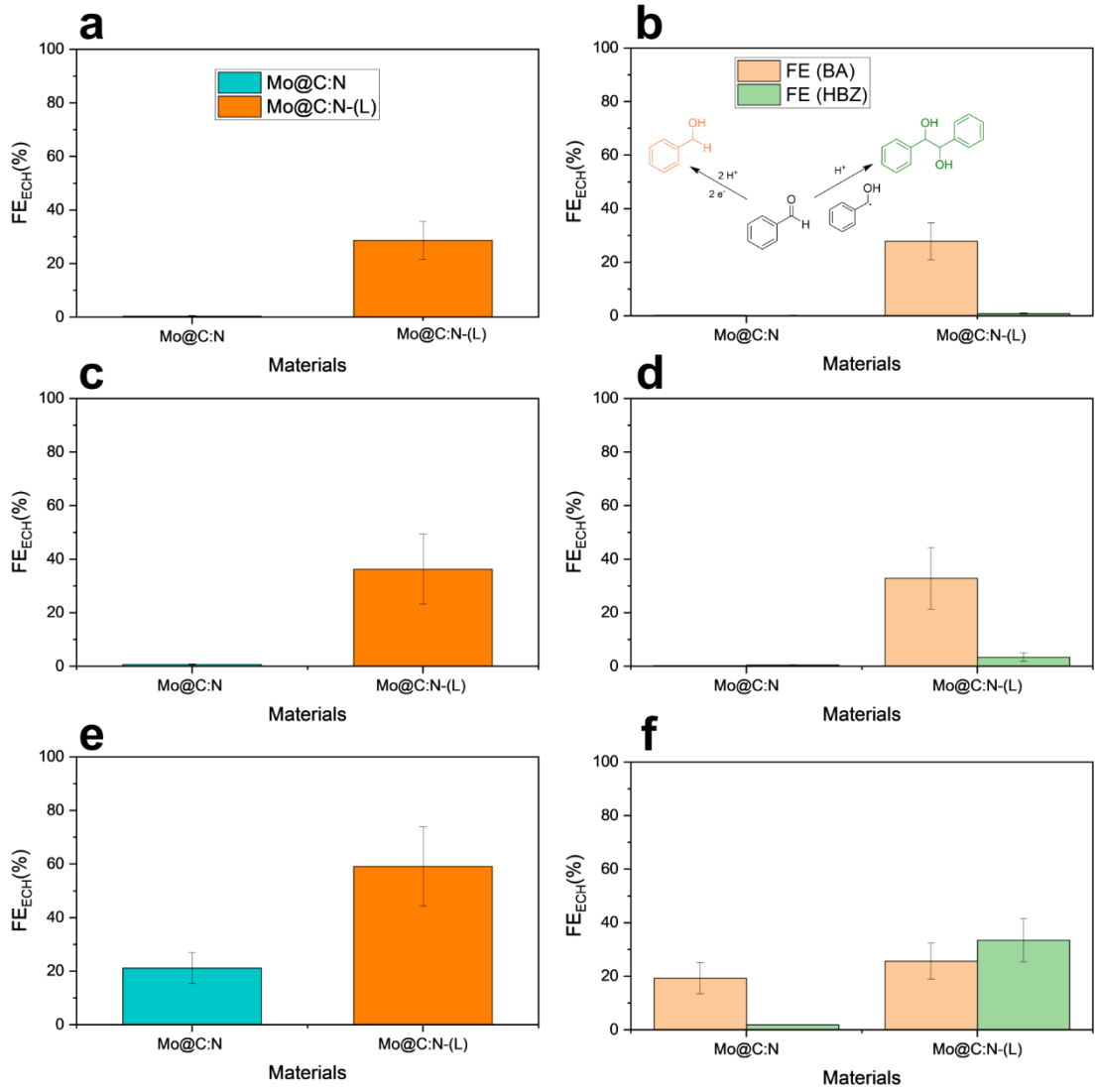

Figure 5.8 Faradaic efficiency of ECH for Mo@C:N and Mo@C:N-(L) at (a) -0.56 V, (c) -0.8 V, and (e) -1.1 V vs. RHE, and Faradaic selectivity for BA and HBZ at (b) -0.56 V, (d) -0.8 V, and (f) -1.1 V vs. RHE.

It might be tempting to conclude from the FE results that metal centres inhibit ECH catalytic activity and that a metal-free material would be preferable for ECH. However, as discussed in Chapter 4, bare CC exhibits lower FE compared to Fe@C:N at equal potential conditions, confirming that the metal centre in M@C:N architectures serves as the active site (Appendix I, **Figure A.10**). Additionally, it is important to emphasise that FE results reflect the strong competition from HER, which becomes particularly significant at higher metal concentrations. Therefore, additional studies focusing on accurately assessing the catalytic activity of the prepared materials, by incorporating other performance parameters such as product rate and TOF, would be highly beneficial.

5.3.2 W-based electrode materials

W-based electrode materials were characterised using methods similar to those employed for Mo-based electrocatalysts. Bulk analysis was performed by XRD. **Figure 5.9a** shows the pattern for W@C:N with peaks at 37.4º,43.6º,63.3º,76.1º and 80.1º, that match those of the WN reference pattern (PDF#65-2898) and are assigned to reflections (111), (200), (220), (311), and (222), respectively.[28,29] The (002) reflection of graphitic carbon is also detectable at 24.6º. At higher W concentrations, the XRD pattern of W@C:N-(H) yields similar WN peaks and additional ones assigned to W_2C (PDF#35-0776) at 34.5º,39.5º,61.6º,69.7º and 74.7º (**Figure 5.9a**). Therefore, the synthesis protocol results in mixed nitride/carbide phases with carbide phases more evident at higher W concentrations. Hysteresis loops obtained by BET analysis are similar with those reported for Mo-based materials, characteristic of micro-/mesopore structures (**Figure 5.9b**).

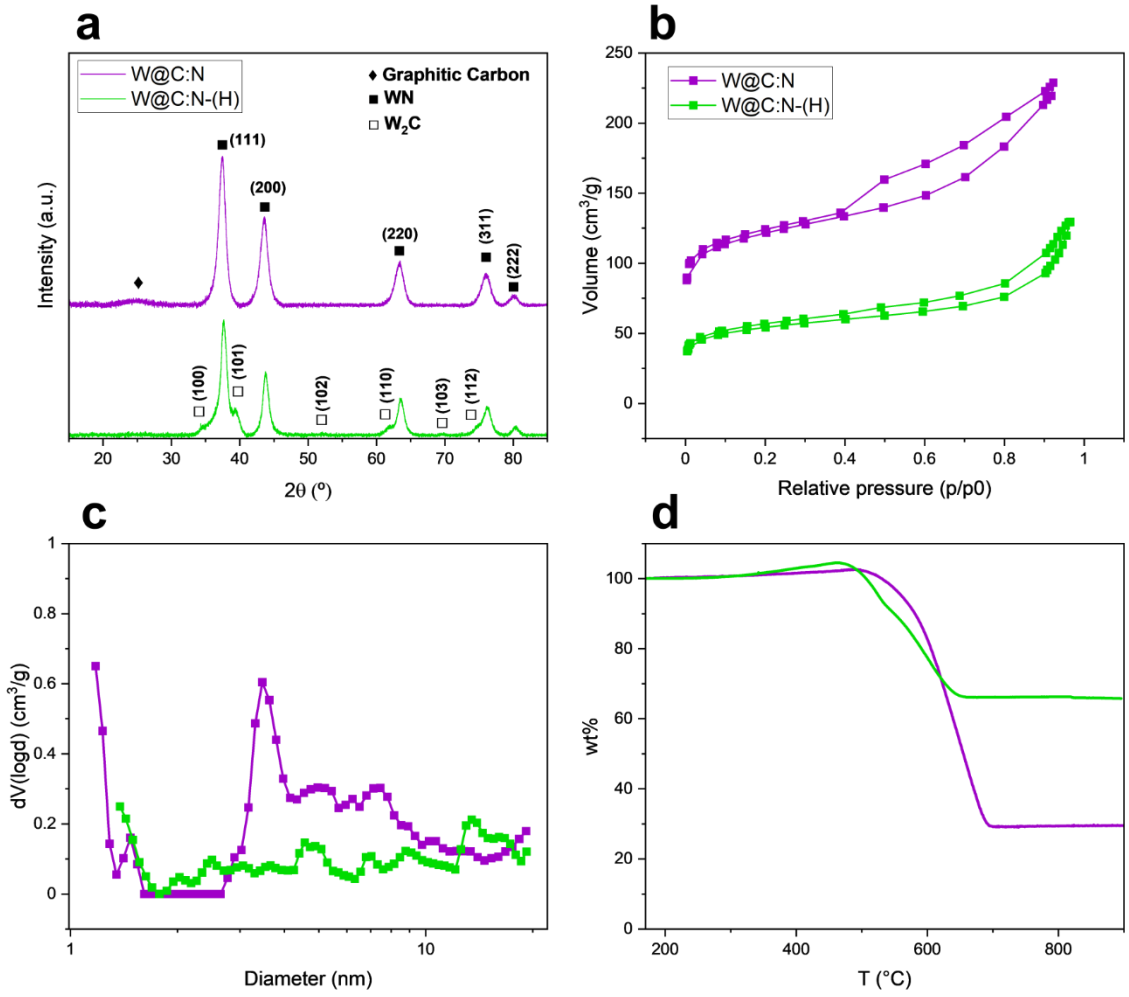

Figure 5.9 (a) XRD patterns, (b) nitrogen adsorption-desorption isotherm, (c) pore size distribution, and (d) TGA curves, collected for W@C:N and W@C:N-(H).

The higher W concentration in W@C:N-(H) it translated into decrease in BET area that is more evident than those reported for Mo-based materials suggesting that effects on pore development require higher metal concentrations when using W relative to Mo. **Figure 5.9c** illustrates the PDS for the W-based material. The results align with those observed for the Mo-based electrocatalyst, highlighting a significant effect of high metal concentration on pore distribution. Specifically, W@C:N-(H) predominantly exhibits larger pores, whereas W@C:N shows smaller pore dimensions. **Figure 5.9d** shows the TGA curves for W@C:N and W@C:N-(H). W@C:N displays a mass loss at *ca.*493 °C preceded by a 2.6% wt. increase due to the formation of WO_x, in agreement with previous reports.[30] The final inorganic residual of 29.4 wt% was attributed to WO_3 and corresponds to 18.5 wt.% of W in the sample, in good agreement with results in **Table 5.1** from ED-XRF analysis. W@C:N-(H) leads to a first mass loss at *ca.*464 °C and a second at *ca.*534 °C, followed by a constant residual weight until 900 °C. Such behaviour is attributed to the higher incorporation of metal in the structure compared to W@C:N, as confirmed by the higher mass increase equal to 4.5 wt.% due to the formation of WO_x species. The residual assigned to WO_3 was found to be 65.7 wt.%, corresponding to 41.4 wt.% of W in the sample, i.e. a higher value than obtained from ED-XRF (see **Table 5.1**).

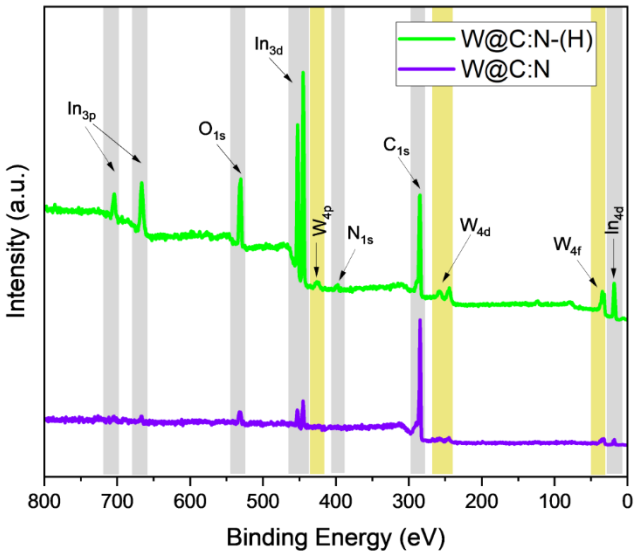

Figure 5.10 Survey XPS spectra of W-based electrocatalysts. Pecks associated to W are highlighted in yellow, while all other contributions are marked in grey.

Surface analysis was performed by XPS. **Figure 5.10** shows surveys of both W-based materials with peaks for W 4f (33.4 eV), W 4d (244.4 eV,256.8 eV), and W 4p (426.7 eV), along with C, O, N, and In peaks previously mentioned for the Mo-based electrocatalysts. C 1s spectra of W-based material was deconvoluted as done for Mo-based materials. Also in this case the sp^2 peak constitutes the largest contribution to the total intensity, with W@C:N-(H) that displays a lower degree of graphitisation (**Figure 5.11a-b**, **Table 5.3**). N 1s spectra are shown in **Figure 5.11c-d**. Peaks were deconvoluted into three contributions: graphitic-, pyrrolic-, and pyridinic-N, with pyridinic-N accounting for the majority as reported in **Table 5.3**. The W 4f spectrum, **Figure 5.11e-f**, was deconvoluted into two doublets with energy splitting of *ca.*3 eV.[15,31-33] The $4f_{7/2}$ peak at low binding energy (32.2 eV) is assigned to W_2C and/or WN;[34-36] this is consistent with XRD results indicating the presence of nitrides/carbides as the main species in the bulk. The $4f_{7/2}$ peak at high binding energy (35.2 eV) is instead assigned to oxidised tungsten in the form of WO_3.[32,36]

Table 5.3 Summary of atomic elemental compositions and selected best-fit results, along with nitrogen content and W %-contents calculated from best-fits of high resolution XPS spectra of W-based materials.

Material	C (at.%)	O [a] (at.%)	N (at.%)	W (at.%)	C_{sp^2}/C_{tot} [b] (%)	M/C (at.%)	MN_x or WC_x/Mtot (at.%)	M-O/ Mtot (at.%)
W@C:N	94.7	3.25	1.64	0.43	57.1	0.45	64.3	35.7
W@C:N-(H)	83.9	9.47	3.97	2.67	47.3	3.18	68.6	31.4
	Pyri-N[c] (%)	**Pyrr-N[c] (%)**	**Gra-N[c] (%)**		**W^{3+} (%)**	**W^{6+} (%)**		
W@C:N	397.6 eV 48	400.4 eV 37	401.6 eV 15		64.3	35.7		
W@C:N-(H)	397.6 eV 63	400.4 eV 27	401.8 eV 10		68.6	31.3		

a – atomic-% content calculated from the contribution to the O 1s area that does not arise from In_2O_3.

b – Calculated as area ratio of the best-fit component 284.4 eV over the total C 1s peak.

c – Pyri-N = Pyridinic-N, Pyrr-N = Pyrrolic-N, Gra-N= Graphitic-N.

Notably, the oxide component accounts for a minority of surface W species, while carbides/nitrides constitute 64-68% of the metal centres. Tungsten carbides have been reported to oxidise in air as demonstrated by multiple studies,[22,37-39] therefore the absence of significant contributions from oxide species suggests that the majority of the

carbide/nitride phases are encapsulated within a protective carbon shell that prevents/minimises oxidation, in agreement with the observation of a W-surface/-subsurface content that is lower than that expected from bulk determinations and in contrast to evidence of a metal surface excess in Mo@C:N.

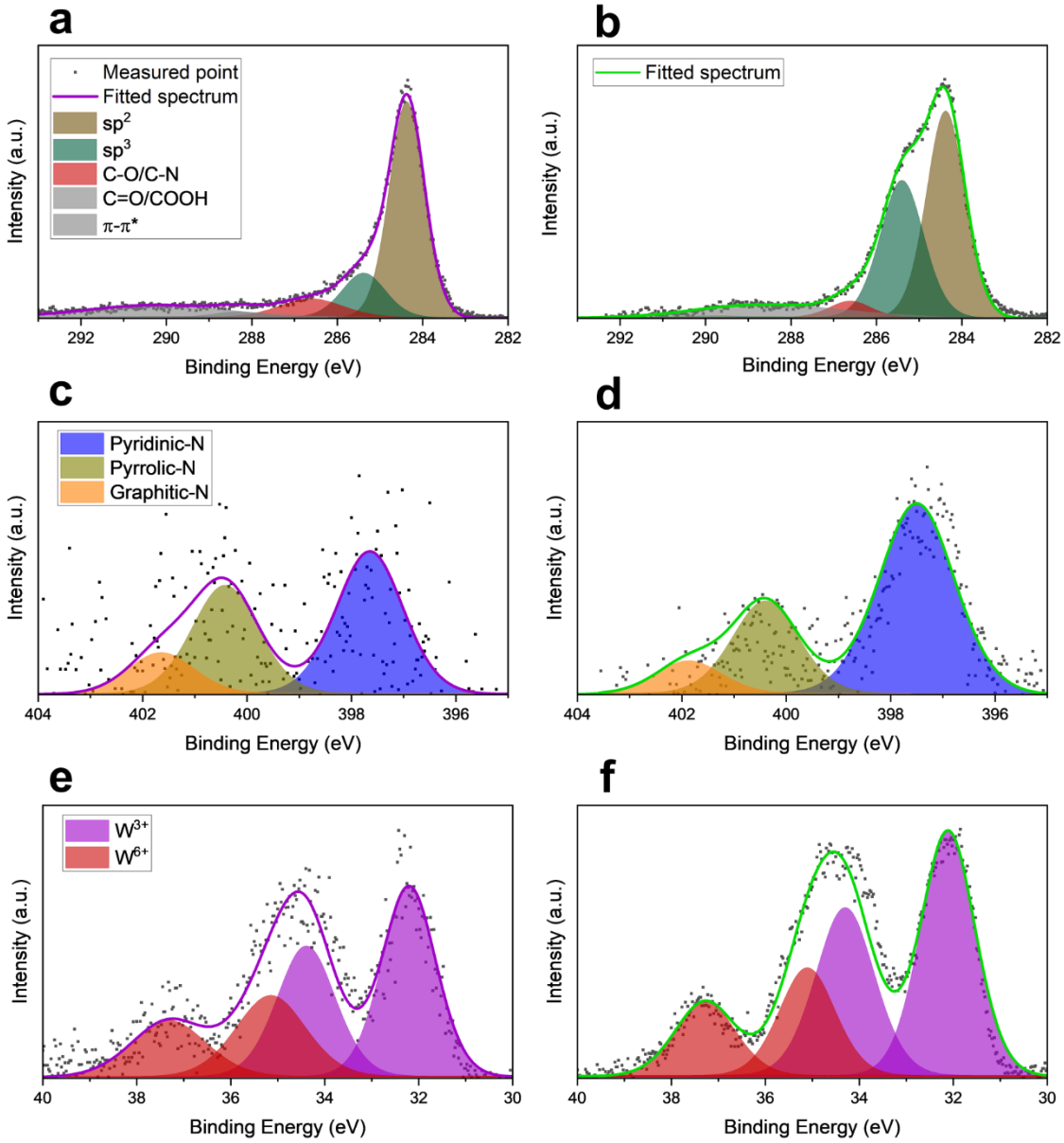

Figure 5.11 XPS high resolution spectra of C 1s (a), N 1s (c) and W 4f (e) for W@C:N; and of C 1s (b), N 1s (d) and W 4f (f) for W@C:N-(H).

Morphology analysis was performed using electron microscopy techniques. **Figure 5.12a-b** shows TEM and SEM images collected for W@C:N-(H) and W@C:N, respectively, together with EDX mapping for C, O and W elements. Both materials display a porous solid matrix with well-defined rodlike nanostructures rich in W, and with

diameters in the 50-200 nm range. HR-TEM of such features for W@C:N reveals that they display well defined crystal facets and are encapsulated within a graphitised shell 10-20 nm in thickness, as showed in **Figure 5.12c-d**. The selected area electron diffraction (SAED) pattern of nanorods, in **Figure 5.12e**, confirms *d*-spacings of 0.238 nm and 0.205 nm, consistent with the (111) and (200) reflections of WN at 0.238 nm and 0.206 nm, respectively (PDF#65-2898).

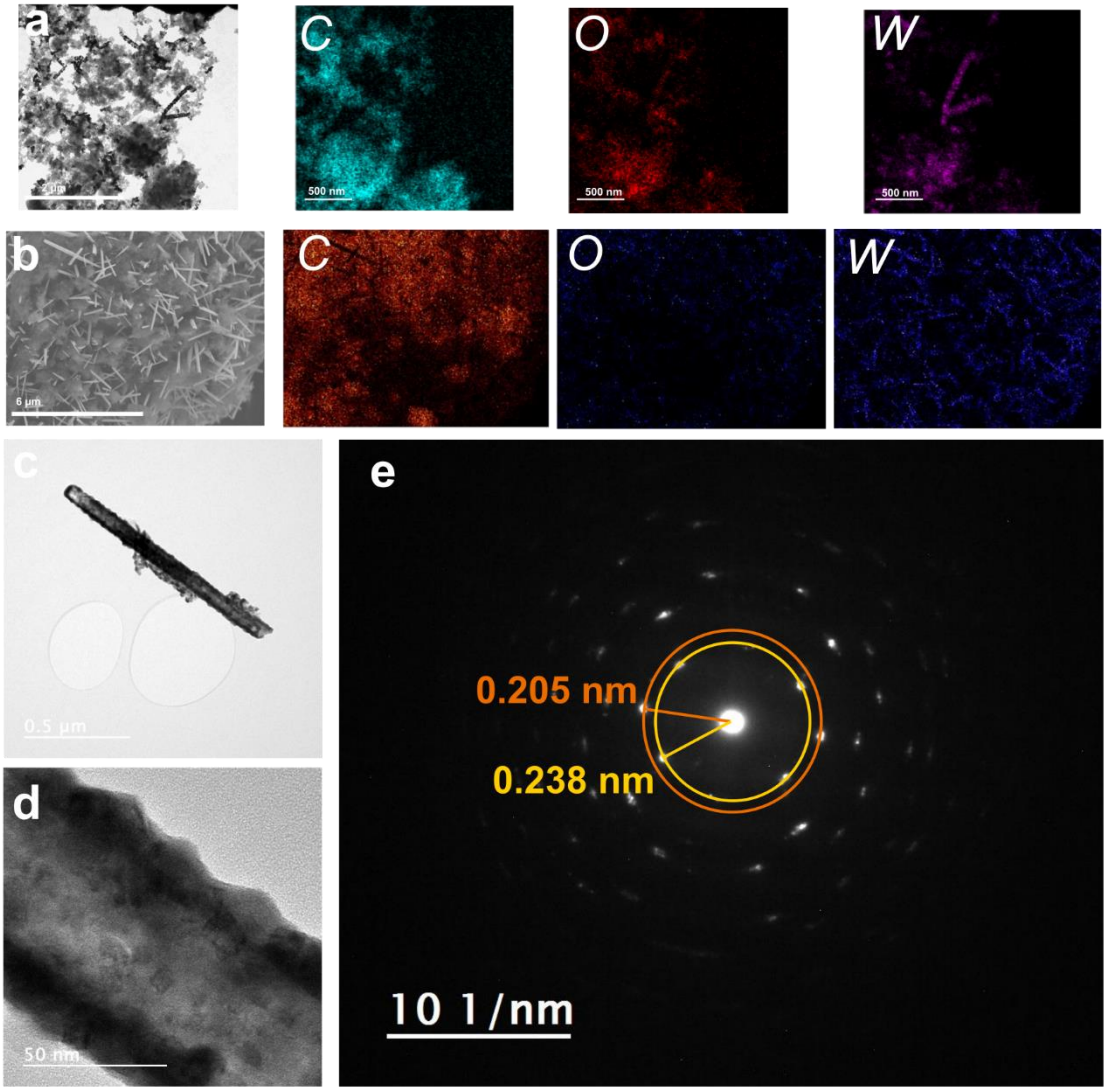

Figure 5.12 (a) TEM images for W@C:N-(H) and (b) SEM images for W@C:N with EDX mapping in the C, O, W spectral regions.(c-d) HR-TEM of W@C:N and (f) SAED pattern of WN nanorods with estimated d-spacing.

Electrochemical performance of W-based materials was first studied using GC disks as conductive supports. **Figure 5.13a** shows the LSV collected in 0.1 M H_2SO_4 at a scan rate of 2 mV s^{-1}. W@C:N-(H) shows a lower overpotential i.e. $\eta \cong$ -0.26 V at 1.5 mA

cm^{-2} compared to W@C:N $\eta \cong$ -0.50 V at the same current density, and similar to those reported for either WN,[40] or carbon-encapsuled WC electrodes.[41]

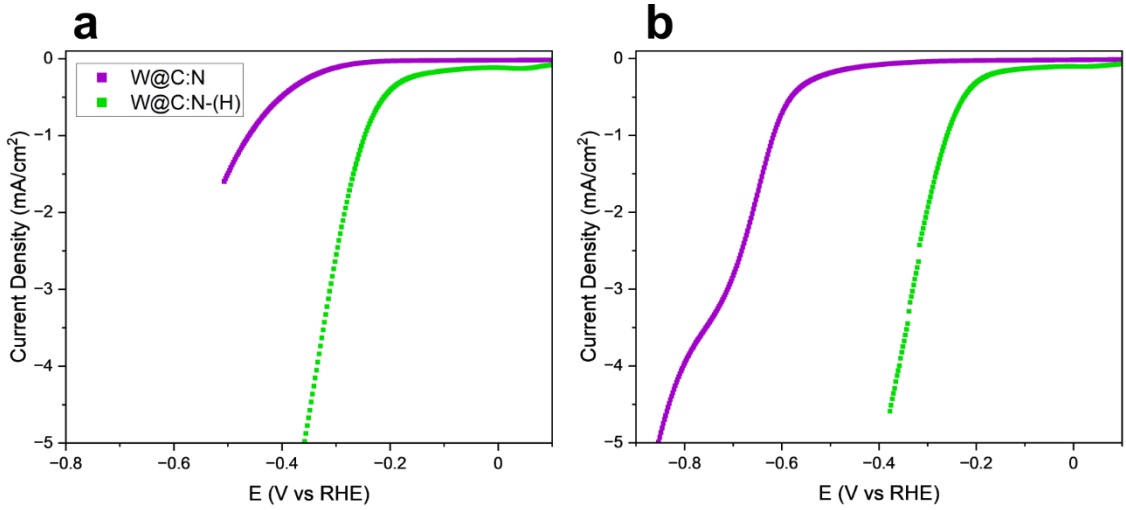

Figure 5.13 LSVs collected for Mo-based materials ink dispersion drop-casted on polished GC disk in (a)0.1 M H_2SO_4 and (b) 0.1 M H_2SO_4 + 30 mM BZH at 2 mV s^{-1}.

The difference in overpotential between the two W-based materials aligns with the discussion in the previous section for Mo-based electrocatalysts regarding the relationship between HER activity and metal concentration. Interestingly, W@C:N-(H) presents a cathodic peak at -0.1 V vs RHE characteristic of proton-coupled reductions of WO_3 species.[42] This peak is absent in W@C:N thus supporting results from XPS that show a higher metal concentration for W@C:N-(H). **Figure 5.13b** shows LSV curves collected in presence of 30 mM BZH in the same supporting electrolyte. W@C:N displays a cathodic peak associated with the organic at *ca.* -0.7 V vs. RHE, along with a change in cathodic current density with an overpotential of -0.64 V at 1.5 mA cm^{-2}. Similarly, W@C:N-(H) shows HER quenching but does not present any cathodic peaks associated with BZH reductions. Also for W-based materials,1 cm^2 CC conductive supports were selected for quantitative ECH studies. **Figure 5.14** shows LSV collected in 0.1 M H_2SO_4/ 30 mM BZH in the same cell configuration used for Mo-based materials. W@C:N-(L) does not display any cathodic peaks, while W@C:N presents small ones at -0.26 V and -0.5 V vs RHE. Electrolysis experiments were conducted as for Mo-based materials, at -0.56 V, -0.8 V, and -1.1 V vs RHE, using FE as a diagnostic parameter to assess ECH performance.

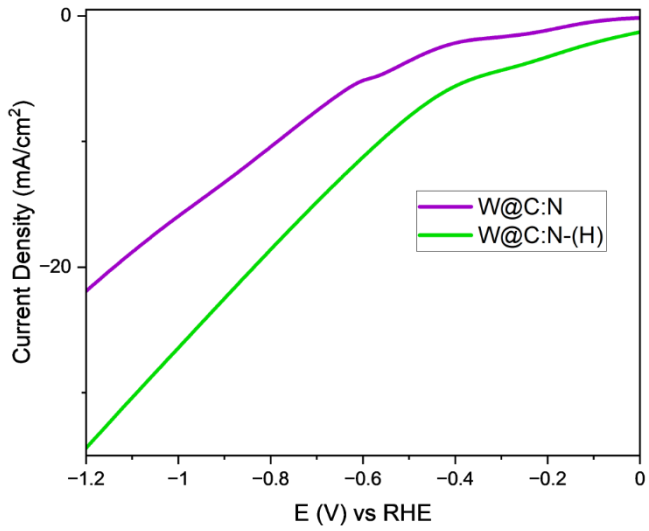

Figure 5.14 LSVs collected for W-based materials ink dispersion drop-casted on CC in 0.1 M H_2SO_4 + 30 mM BZH at 10 mV s^{-1}.

At all tested potentials W@C:N shows higher FE compared to W@C:N-(H) reaching a difference of *ca.*15 % in FE_{ECH} at -1.1 V vs RHE (**Figure 5.15a, Figure 5.15c, Figure 5.15e**). Moreover, BA results to be the preferred product in the case of either of the electrocatalysts and at all tested potentials, even if W@C:N shows higher performance toward BA selectivity compared to W@C:N-(H) (**Figure 5.15b, Figure 5.15d, Figure 5.15f**). These results align with those from the previous section, as electrocatalysts with lower metal concentrations present also higher FE_{ECH} due to reduce HER competition. However, in the case of W-based materials, the effect of the applied potential on the FE performance is less significant compared to what was observed for Mo-based electrocatalysts. This is likely due to the generally lower activity of W compared to Mo for the HER, which could in turn affect the ECH response.[2]

The results presented in this chapter highlight the critical role of metal concentrations in determining the structural composition and ECH/HER activity of M@C:N materials, using Mo and W as metal cores. Structures with higher metal content are particularly active towards the HER, which appears to limit their potential application for ECH. Conversely, materials with lower metal concentrations exhibit higher FE, indicating a more favourable balance between HER and ECH. However, as noted at the end of the previous section, these trends must be interpreted with caution, as additional performance

parameters are needed to accurately assess the true impact of the metal on the ECH reaction.

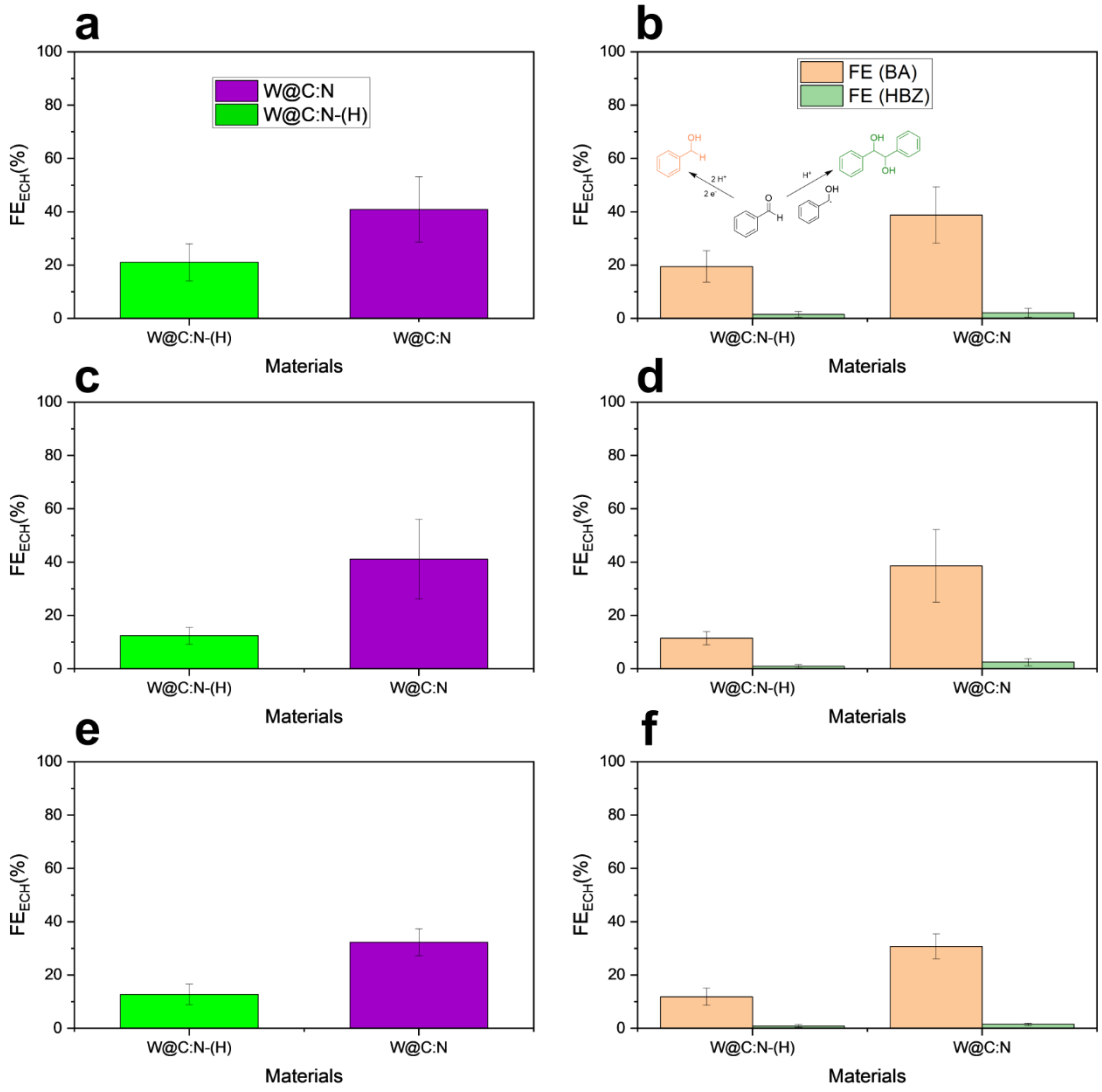

Figure 5.15 Faradaic efficiency of ECH for W@C:N and W@C:N-(H) at (a) -0.56 V, (c) -0.8 V, and (e) -1.1 V vs. RHE, and Faradaic selectivity for BA and HBZ at (b) -0.56 V, (d) -0.8 V, and (f) -1.1 V vs. RHE.

Indeed, while understanding the effect of metal concentration is essential, an even more important aspect is evaluating the impact of the metal type on properties and performance at equivalent metal concentrations. In the next chapter, these comparisons will be examined through a more detailed quantitative and structural analysis, integrating other ECH performance parameters and using a metal-free sample as a benchmark to have a clearer understanding of the specific impact of each metal on ECH performance.

5.4 Conclusion

In this chapter, Mo and W were utilised as active sites for the preparation of M@C:N architectures with varying metal concentrations. For the Mo-based electrocatalysts, Mo@C:N exhibited an atomic-% metal concentration approximately three times higher than Mo@C:N-(L), determined by ICP-MS. Significant structural differences were observed between these samples. XRD analysis of Mo@C:N revealed characteristic peaks corresponding to Mo_2C , along with minor MoO_2 impurities. In contrast, Mo@C:N-(L) displayed peaks solely associated with the graphitised carbon phase, indicating that Mo-containing phases are either below the detection limit or highly amorphous at lower metal concentrations. The higher metal incorporation in Mo@C:N was also reflected in its increased BET surface area compared to Mo@C:N-(L). Additionally, the progressive introduction of metal notably influenced the pore size distribution, with smaller pores giving way to larger ones. Finally, TGA results were consistent with ICP-OES findings, confirming the higher metal incorporation in Mo@C:N. Surface composition analysis via XPS revealed higher degree of graphitisation for Mo@C:N sample; with significant differences observed also in metal incorporation. Indeed, consistent with bulk analysis results, Mo@C:N exhibited a higher surface metal concentration compared to Mo@C:N-(L). However, most of the surface Mo centres were oxidised upon air exposure, contrasting with the predominance of carbide phases in the bulk as evidenced by XRD studies. This effect was even more pronounced for Mo@C:N-(L), where oxidised Mo species exceeded 95% on the surface. Electron microscopy techniques confirm the incorporation of Mo nanoparticles embedded within a graphitised carbon matrix.

The lower solubility of Mo-based powders using the established Fe@C:N ink preparation method prompted the development of a new procedure. This revised approach incorporated a higher water content percentage and replaced the IPA organic solvent with methanol. The ink dispersion was drop-casted onto a GC disk electrode, revealing higher HER activity for the Mo@C:N sample, attributed to its greater metal incorporation compared to Mo@C:N-(L). ECH performance was evaluated using CC as a conductive support decorated with Mo-based samples, with FE determined at three selected potentials. Mo@C:N-(L) exhibited higher FE, attributed to its reduced HER competition. However, this also led to increased generation of radical intermediates that readily

dimerize to form HBZ at cathodic potentials, explaining its lower selectivity under these conditions.

The atomic-% concentrations of W-based materials were determined using ED-XRF, revealing that the metal content in W@C:N was approximately half that of W@C:N-(H). Both samples exhibit characteristic XRD peaks associated with WN; however, the spectrum for W@C:N-(H) also aligns well with the presence of W_2C. Porosity measurements, performed similarly to those for Mo-based materials, yielded comparable results. W@C:N-(H) demonstrated a lower BET surface area and larger pores compared to W@C:N. TGA profiles aligns the ED-XRF findings, while morphological analysis revealed that the metal is encapsulated within graphitised shell structures in the form of rod-like nanostructures. This was further supported by XPS surface analysis, which indicated that oxide species account for a minor fraction of surface W species, while carbides/nitrides constitute 64–68% of the metal centers in the subsurface. Since carbides are known to oxidise in air, as shown in multiple studies,[22,37-39] the negligible presence of oxide species suggests that most carbide/nitride phases are protected by a carbon shell. Electrochemical evaluation on GC disk indicates higher HER activity for W@C:N-(H), while quantitative analysis on CC shows greater FE toward ECH for W@C:N. Notably, for W-based materials, the effect of applied potential on FE performance is less pronounced compared to Mo-based materials, and the selectivity toward BA consistently exceeds that for HBZ.

The results presented in this chapter provide valuable insights into the impact of low-cost metal concentration on the structural composition of M@C:N and the competition between ECH and HER. However, a more in depth study of the ECH performance indicators is necessary to determine the effective role of metal cores in M@C:N structures for developing active electrocatalysts. This analysis will be conducted in the next chapter.

5.5 References

1. Short, G. D.; Bishop, E. Concentration Overpotentials on Antimony Electrodes in Differential Electrolytic Potentiometry. *Analytical Chemistry* **1965**,*37* (8),962-967.

2. Hussain, S.; Vikraman, D.; Feroze, A.; Song, W.; An, K.-S.; Kim, H.-S.; Chun, S.-H.; Jung, J. Synthesis of Mo2C and W2C Nanoparticle Electrocatalysts for the Efficient Hydrogen Evolution Reaction in Alkali and Acid Electrolytes. *Frontiers in Chemistry* **2019**,*7*, Original Research.

3. Wei, H.; Wang, J.; Lin, Q.; Zou, Y.; Chen, X. a.; Zhao, H.; Li, J.; Jin, H.; Lei, Y.; Wang, S. Incorporating ultra-small N-doped Mo2C nanoparticles onto 3D N-doped flower-like carbon nanospheres for robust electrocatalytic hydrogen evolution. *Nano Energy* **2021**,*86*,106047.

4. Han, N.; Yang, K. R.; Lu, Z.; Li, Y.; Xu, W.; Gao, T.; Cai, Z.; Zhang, Y.; Batista, V. S.; Liu, W.; et al. Nitrogen-doped tungsten carbide nanoarray as an efficient bifunctional electrocatalyst for water splitting in acid. *Nature Communications* **2018**,*9* (1),924.

5. Karthik, M.; Faik, A.; Doppiu, S.; Roddatis, V.; D'Aguanno, B. A simple approach for fabrication of interconnected graphitized macroporous carbon foam with uniform mesopore walls by using hydrothermal method. *Carbon* **2015**,*87*,434-443.

6. Pota, F.; Costa de Oliveira, M. A.; Schröder, C.; Brunet Cabré, M.; Nolan, H.; Rafferty, A.; Jeannin, O.; Camerel, F.; Behan, J. A.; Barrière, F.; et al. Porous N-Doped Carbon-encapsulated Iron as Novel Catalyst Architecture for the Electrocatalytic Hydrogenation of Benzaldehyde. *ChemSusChem* **2025**,*18* (1), e202400546.

7. Iannaci, A.; Ingle, S.; Domínguez, C.; Longhi, M.; Merdrignac-Conanec, O.; Ababou-Girard, S.; Barrière, F.; Colavita, P. E. Nanoscaffold effects on the performance of air-cathodes for microbial fuel cells: Sustainable Fe/N-carbon electrocatalysts for the oxygen reduction reaction under neutral pH conditions. *Bioelectrochemistry* **2021**,*142*,107937.

8. Sing, K. S. W. Reporting physisorption data for gas/solid systems with special reference to the determination of surface area and porosity (Recommendations 1984). *Pure and Applied Chemistry* **1985**,*57* (4),603-619.

9. Thommes, M.; Kaneko, K.; Neimark, A. V.; Olivier, J. P.; Rodriguez-Reinoso, F.; Rouquerol, J.; Sing, K. S. W. Physisorption of gases, with special reference to the evaluation of surface area and pore size distribution (IUPAC Technical Report). *Pure and Applied Chemistry* **2015**,*87* (9-10),1051-1069.

10. Chen, Y.-Y.; Zhang, Y.; Jiang, W.-J.; Zhang, X.; Dai, Z.; Wan, L.-J.; Hu, J.-S. Pomegranate-like N,P-Doped Mo2C@C Nanospheres as Highly Active Electrocatalysts for Alkaline Hydrogen Evolution. *ACS Nano* **2016**,*10* (9),8851-8860.

11. Chen, Y.; Zhang, H.; Zhang, J.; Ma, J.; Ye, H.; Qian, G.; Ye, Y.; Zhong, S. Facile synthesis and thermal stability of nanocrystalline molybdenum carbide. *Materials Sciences and Applications* **2011**,*2* (09),1313.

12. Gulbransen, E. A.; Andrew, K. F.; Brassart, F. A. Vapor Pressure of Molybdenum Trioxide. *Journal of The Electrochemical Society* **1963**,*110* (3),242.

13. Wang, L.; Zhang, G.-H.; Sun, Y.-J.; Zhou, X.-W.; Chou, K.-C. Preparation of Ultrafine β-MoO3 from Industrial Grade MoO3 Powder by the Method of Sublimation. *The Journal of Physical Chemistry C* **2016**,*120* (35),19821-19829.

14. Nolan, H.; Schröder, C.; Brunet-Cabré, M.; Pota, F.; McEvoy, N.; McKelvey, K.; Perova, T. S.; Colavita, P. E. MoS2/carbon heterostructured catalysts for the hydrogen evolution reaction: N-doping modulation of substrate effects in acid and alkaline electrolytes. *Carbon* **2023**,*202*,70-80.

15. Chastain, J.; King Jr, R. C. Handbook of X-ray photoelectron spectroscopy. *Perkin-Elmer Corporation* **1992**,*40*,221.

16. Hellgren, N.; Haasch, R. T.; Schmidt, S.; Hultman, L.; Petrov, I. Interpretation of X-ray photoelectron spectra of carbon-nitride thin films: New insights from in situ XPS. *Carbon* **2016**,*108*,242-252.

17. Qu, L.; Liu, Y.; Baek, J.-B.; Dai, L. Nitrogen-Doped Graphene as Efficient Metal-Free Electrocatalyst for Oxygen Reduction in Fuel Cells. *ACS Nano* **2010**,*4* (3),1321-1326.

18. Titantah, J. T.; Lamoen, D. Carbon and nitrogen 1s energy levels in amorphous carbon nitride systems: XPS interpretation using first-principles. *Diamond and Related Materials* **2007**,*16* (3),581-588.

19. Costa de Oliveira, M. A.; Schröder, C.; Brunet Cabré, M.; Nolan, H.; Forner-Cuenca, A.; Perova, T. S.; McKelvey, K.; Colavita, P. E. Effects of N-functional groups on the electron transfer kinetics of VO2+/VO2+ at carbon: Decoupling morphology from chemical effects using model systems. *Electrochimica Acta* **2024**,*475*,143640.

20. Wei, H.; Xi, Q.; Chen, X. a.; Guo, D.; Ding, F.; Yang, Z.; Wang, S.; Li, J.; Huang, S. Molybdenum Carbide Nanoparticles Coated into the Graphene Wrapping N-Doped Porous Carbon Microspheres for Highly Efficient Electrocatalytic Hydrogen Evolution Both in Acidic and Alkaline Media. *Advanced Science* **2018**,*5* (3),1700733.

21. Yang, X.; Feng, X.; Tan, H.; Zang, H.; Wang, X.; Wang, Y.; Wang, E.; Li, Y. N-Doped graphene-coated molybdenum carbide nanoparticles as highly efficient electrocatalysts for the hydrogen evolution reaction. *Journal of Materials Chemistry A* **2016**,*4* (10),3947-3954,10.1039/C5TA09507G.

22. Preiss, H.; Meyer, B.; Olschewski, C. Preparation of molybdenum and tungsten carbides from solution derived precursors. *Journal of Materials Science* **1998**,*33* (3),713-722.

23. Malone, N.; Fiedler, H.; Mitchell, D. R. G.; Kennedy, J. V.; Waterhouse, G. I. N.; Gupta, P. High Turnover Frequency for the Hydrogen Evolution Reaction on Molybdenum Carbide Thin Films Synthesized by Ion Implantation. *ACS Applied Engineering Materials* **2023**,*1* (9),2377-2385.

24. Vrubel, H.; Hu, X. Molybdenum boride and carbide catalyze hydrogen evolution in both acidic and basic solutions. *Angewandte Chemie International Edition* **2012**,*51* (51),12703-12706.

25. Saji, V. S.; Lee, C.-W. Molybdenum, Molybdenum Oxides, and their Electrochemistry. *ChemSusChem* **2012**,*5* (7),1146-1161.

26. Wang, X.; Xie, Y.; Tang, K.; Wang, C.; Yan, C. Redox Chemistry of Molybdenum Trioxide for Ultrafast Hydrogen-Ion Storage. *Angewandte Chemie International Edition* **2018**,*57* (36),11569-11573.

27. Mitchell, A. G.; Wan, L. S. C.; Bjaastad, S. G. The solubility of benzaldehyde in water. *Journal of Pharmacy and Pharmacology* **1964**,*16* (9),632-633.

28. Zhang, M.; Qiu, Y.; Han, Y.; Guo, Y.; Cheng, F. Three-dimensional tungsten nitride nanowires as high performance anode material for lithium ion batteries. *Journal of Power Sources* **2016**,*322*,163-168.

29. Shen, L.; Wang, N. Effect of Nitrogen Pressure on the Structure of Cr-N, Ta-N, Mo-N, and W-N Nanocrystals Synthesized by Arc Discharge. *Journal of Nanomaterials* **2011**,*2011* (1),781935.

30. Liu, C.; Zhou, D.; Zhou, J.; Xie, Z.; Xia, Y. Synthesis and characterization of tungsten carbide and application to electrocatalytic hydrogen evolution. *RSC Advances* **2016**,*6* (80),76307-76311,10.1039/C6RA12545J.

31. Baker, C. C.; Shah, S. I. Reactive sputter deposition of tungsten nitride thin films. *Journal of Vacuum Science & Technology A* **2002**,*20* (5),1699-1703.

32. Wang, Z.; Liu, Z.; Yang, Z.; Shingubara, S. Characterization of sputtered tungsten nitride film and its application to Cu electroless plating. *Microelectronic Engineering* **2008**,*85* (2),395-400.

33. Shen, Y. G.; Mai, Y. W.; McKenzie, D. R.; Zhang, Q. C.; McFall, W. D.; McBride, W. E. Composition, residual stress, and structural properties of thin tungsten nitride films deposited by reactive magnetron sputtering. *Journal of Applied Physics* **2000**,*88* (3),1380-1388.

34. Ouendi, S.; Robert, K.; Stievenard, D.; Brousse, T.; Roussel, P.; Lethien, C. Sputtered tungsten nitride films as pseudocapacitive electrode for on chip micro-supercapacitors. *Energy Storage Materials* **2019**,*20*,243-252.

35. Krasovskii, P. V.; Malinovskaya, O. S.; Samokhin, A. V.; Blagoveshchenskiy, Y. V.; Kazakov, V. A.; Ashmarin, A. A. XPS study of surface chemistry of tungsten carbides nanopowders produced through DC thermal plasma/hydrogen annealing process. *Applied Surface Science* **2015**,*339*,46-54.

36. Rodella, C. B.; Barrett, D. H.; Moya, S. F.; Figueroa, S. J. A.; Pimenta, M. T. B.; Curvelo, A. A. S.; Teixeira da Silva, V. Physical and chemical studies of tungsten carbide catalysts: effects of Ni promotion and sulphonated carbon. *RSC Advances* **2015**,*5* (30),23874-23885,10.1039/C5RA03252K.

37. Kurlov, A. S.; Gusev, A. I. Oxidation of tungsten carbide powders in air. *International Journal of Refractory Metals and Hard Materials* **2013**,*41*,300-307.

38. Voitovich, R. F.; Pugach, É. A. High-temperature oxidation characteristics of the carbides of the Group VI transition metals. *Soviet Powder Metallurgy and Metal Ceramics* **1973**,*12* (4),314-318.

39. Esposito, D. V.; Chen, J. G. Monolayer platinum supported on tungsten carbides as low-cost electrocatalysts: opportunities and limitations. *Energy & Environmental Science* **2011**,*4* (10),3900-3912,10.1039/C1EE01851E.

40. Denny, S. R.; Tackett, B. M.; Tian, D.; Sasaki, K.; Chen, J. G. Exploring electrocatalytic stability and activity of unmodified and platinum-modified tungsten and niobium nitrides. *International Journal of Hydrogen Energy* **2020**,*45* (43),22883-22892.

41. Kimmel, Y. C.; Esposito, D. V.; Birkmire, R. W.; Chen, J. G. Effect of surface carbon on the hydrogen evolution reactivity of tungsten carbide (WC) and Pt-modified WC electrocatalysts. *International Journal of Hydrogen Energy* **2012**,*37* (4),3019-3024.

42. Spencer, M. A.; Holzapfel, N. P.; You, K.-E.; Mpourmpakis, G.; Augustyn, V. Participation of electrochemically inserted protons in the hydrogen evolution reaction on tungsten oxides. *Chemical Science* **2024**,*15* (14),5385-5402,10.1039/D4SC00102H.

CHAPTER 6

The role of metal core selection on the electrocatalytic hydrogenation performances of porous N-doped carbon catalysts

---

Understanding the role of the metal core in M@C:N structures is crucial for developing efficient and cost-effective catalysts for electrocatalytic hydrogenation. In this chapter, a metal-free material is used as a benchmark to compare two M@C:N structures containing nearly identical atomic amounts of Mo and W. The results suggest that W@C:N architectures have strong potential for cost-competitive ECH applications compared to precious metal. Additionally, a comparison including Fe@C:N provides a comprehensive perspective on all the metals examined in this thesis. The findings confirm that balancing HER and ECH competition is key to achieving high-performance catalysts for ECH applications, with the metal playing a crucial role in tuning this balance.

This chapter presents result and contents reported in the candidate's first-author publication, titled:

Electrocatalytic hydrogenation of unsaturated organics using Mo and W porous carbon-encapsulated nanostructures: impact of metal type on properties and performances

Pota, F.; Costa de Oliveira, M. A.; Schröder, C.; Rafferty, A.; De Castro C.; Rault L.; Behan, J. A.; Barrière, F.; Colavita, P. E.

Journal of Materials Chemistry A, 2025, Advance Article

With the exception of specified contributions, the candidate conducted the primary investigation reported in the published work and prepared the first draft of the paper, along with subsequent revisions, under the supervision of Prof. Paula E. Colavita. The contributions of the other coauthors are as follows: M.A.C.O. development of the sample preparation methodology, C.S. XPS analysis, A.R. BET and PSD analysis, C.D.C XRF analysis, L.R. TEM-EDX analysis, J.A.B. & F.B. writing - review and editing, P.E.C conceptualization and supervision

---

6.1 Introduction

The previous chapter examined the impact of metal concentration in M@C:N architectures, with a focus on the influence of varying metal concentrations on structural composition and ECH performance. However, the influence of different metal cores at equal concentrations within an M@C:N structure was not thoroughly evaluated. Hence, once identified the optimal concentration condition for the synthesis of materials with identical atomic metal loadings, addressing this gap is crucial for designing and developing efficient, high-performing catalysts for applications in the ECH of biomass-derived organics. In this thesis, three metals cores have been studied for the preparation of M@C:N architectures: Fe, Mo, W. These metals and several of their compounds, possess the ability to activate chemisorbed hydrogen through the Volmer step while displaying differences in their activity towards hydrogen evolution,[1-3] thus offering a potential route to regulating the degree of competition between HER and the ECH. Moreover, as already discussed, these transition metals are highly desirable as active sites in M@C:N structures, due to their significantly lower costs compared to precious metals. **Figure 6.1** shows market prices for these metals; iron displays the lowest cost of *ca.* 1×10^{-4} USD/g, followed by W and Mo with 0.05 USD/g and 0.07 USD/g, respectively.[4]

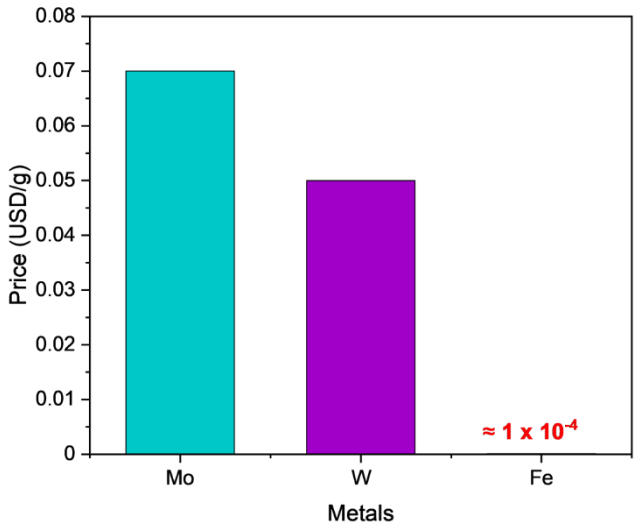

Figure 6.1 Market prices of precious and base metals in USD/g. Data sourced from reference 4.

In this chapter, two electrocatalysts introduced in Chapter 5, Mo@C:N and W@C:N, are utilised to investigate the influence of the metal centre on their electrochemical performance in HER and ECH processes. Both these samples have nearly identical metal atomic contents of *ca.*1.5%. To complement this study, a metal-free material is synthesised using the same preparation procedure as the metal-based electrocatalysts. This material serves as a benchmark for comparing the structural and electrochemical ECH performances of the metal-based catalysts. To minimise surface differences among the materials and to facilitate the preparation of ink dispersions, an additional sieving step was incorporated into the process, yielding benefits in dispersibility and ink stability. Finally, the last section presents a comparative analysis performance of all three metal cores discussed in this thesis, including Fe.

The results presented in this Chapter demonstrate that the identity of the metal core can have a profound influence on the properties of the graphitised carbon matrix and on the surface chemical composition in M@C:N materials with identical atomic metal loadings. This translates into important changes in product rates, FE and TOF, offering new insights into optimising transition metal-based heterostructured electrocatalysts for the ECH of organics.

6.2 Experimental section

Electrochemical characterisation. Materials were synthesised as discussed in Chapter 5 then mortared and sieved (20 µm) prior to the preparation of catalyst inks. The ink preparation follows the same procedure presented in previous chapter for Mo- and W-based electrocatalysts. GC disk and CC flags were used as conductive support for the preparation of drop-casted electrodes as schematised in **Figure 6.2.** For the metal-free sample 52 µL of the ink were drop-cast in two equal aliquots on CC yielding a loading of 1.07 mg cm^{-2}. Capacitance measurements were conducted in 0.1 M Na_2SO_4 supporting electrolyte in a non-faradic region at different scan rate. Voltammetry and chronoamperometry experiments were carried out as described in previous chapters, utilising the same three-electrode configuration. Appendix I includes the equations used to calculate the key ECH performance parameters discussed throughout this chapter.

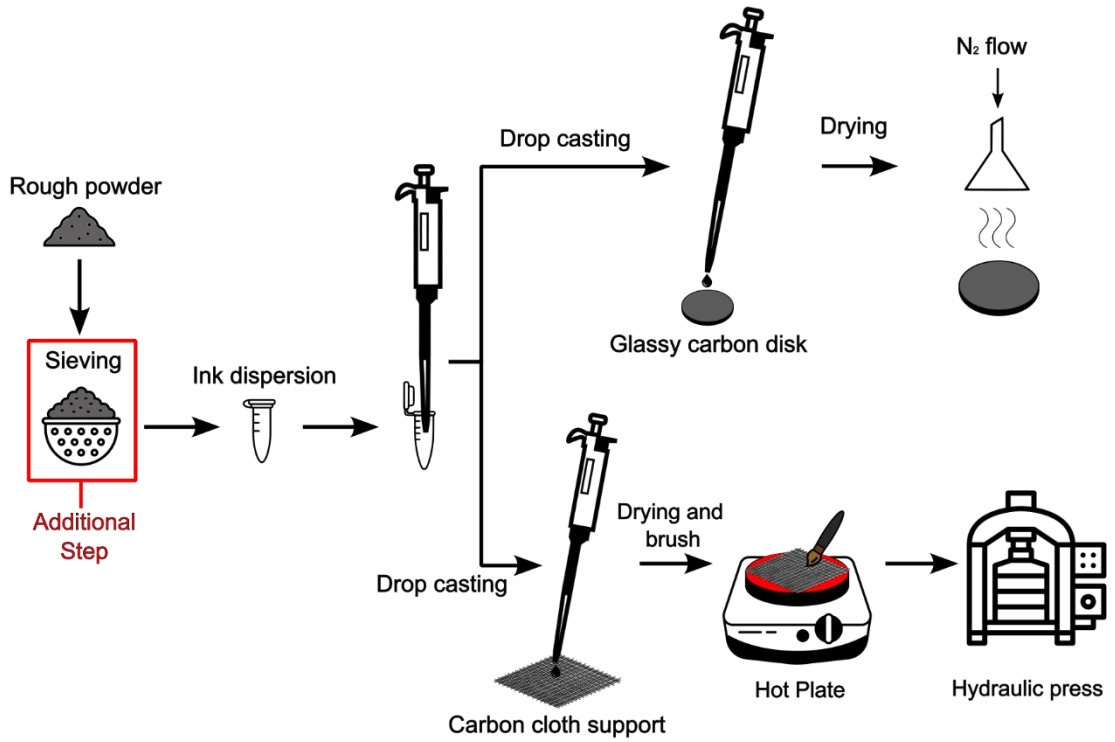

Figure 6.2 Illustration of the ink dispersion preparation procedure, highlighting the additional sieving step in red, along with schematic representation of the drop-casting process onto a glassy carbon disk or carbon cloth support, detailing the main steps involved.

6.3 Results and discussion

6.3.1 Mo and W carbon-encapsulated structures

The metal-free electrocatalyst material was synthesised according to the procedure detailed in Chapter 5. BP were purified through reflux and served as carbon nanoscaffold; while resorcinol, Pluronic F-127, and melamine were utilised for the formation of the sol-gel resin. The autoclave treatment and annealing processes were conducted in identical manner to those described in Chapter 5. The final metal-free product, named as RPM/BP, was characterised as done for metal-based samples.

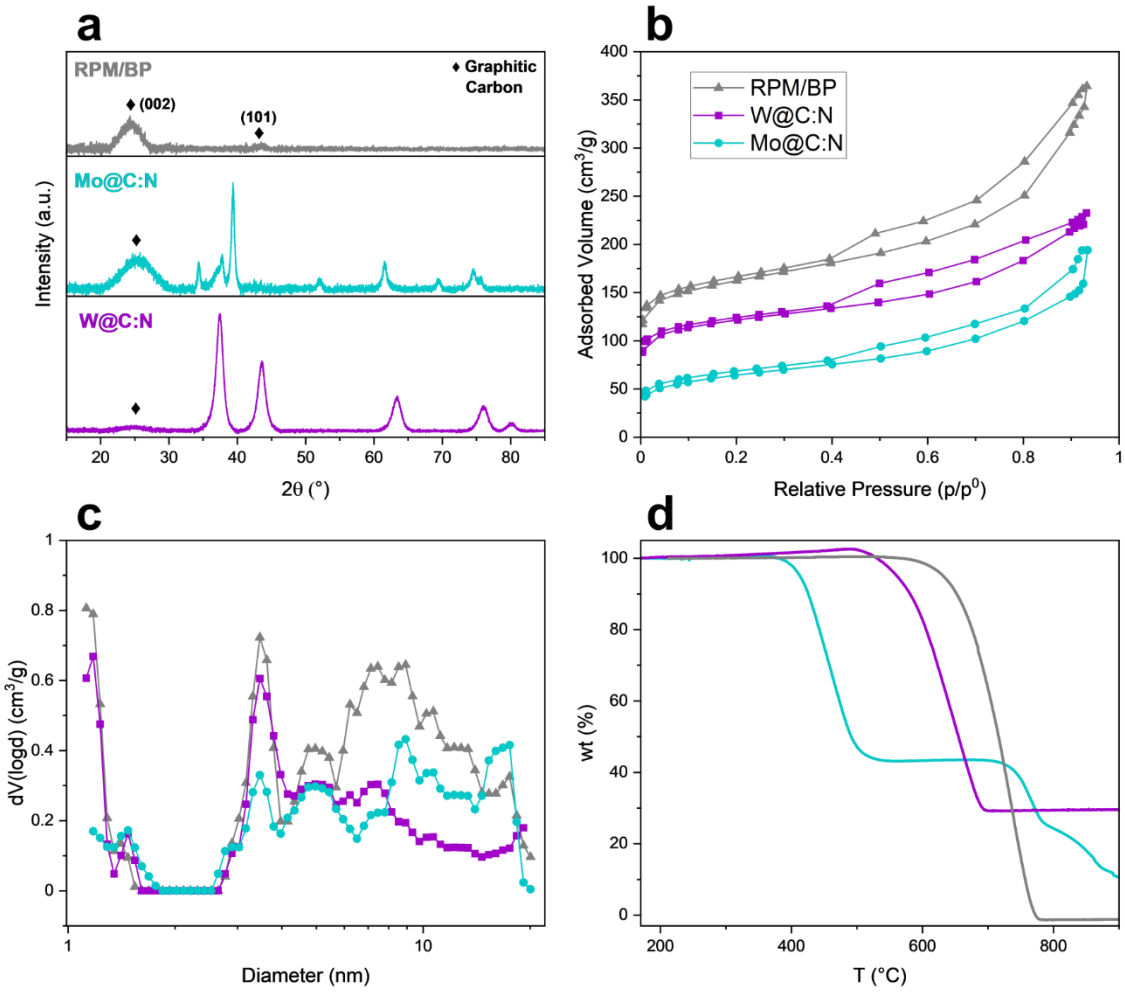

Figure 6.3 (b) XRD patterns for metal-free RPM/BP, Mo@C:N and W@C:N. (c) Nitrogen adsorption-desorption isotherm and (d) pore size distribution for RPM/BP, W@C:N and Mo@C:N materials. (d) TGA curves for RPM/BP, W@C:N and Mo@C:N electrocatalyst.

The bulk structure was first investigated via XRD. **Figure 6.3a** reports patterns collected for metal-free RPM/BP, along with Mo@C:N and W@C:N for comparison purposes.

RPM/BP yielded two peaks at 24.3º and 43.2º, indexed as (002) and (101) reflections of the graphitic carbon, respectively.[5] These peaks match really well with those observed for Mo@C:N and W@C:N and assigned to the same reflections. RPM/BP display a porous structure with similar hysteresis loops and isotherms to those reported for metal-based electrocatalysts (**Figure 6.3b**). The BET specific surface area summarised in **Table 6.1**, reveals how the incorporation of Mo or W into the structure results in a decrease in BET surface areas by 15% to 67% compared to metal-free RPM/BP. Assuming that contributions to the surface area from metal-containing phases are negligible relative to those from the carbon phases, and accounting for the metal wt.% in **Table 6.1**, it is possible to note that for W@C:N the BET area is only slightly lower than expected from a replacement of 1.4% of C atoms in RPM/BP with W (494 m^2/g). This suggests that the development of the carbon microscopic area during graphitisation is not significantly affected by the presence of the W centres at these concentrations. On the other hand, for Mo@C:N the BET area is less than half the value expected based on replacement of 1.5% of C atoms alone (535 m^2/g). This suggests that Mo centres impact the development of pores in the carbon phase to a much greater extent than W. Metal centres can have a catalytic effect on carbon gasification and graphitisation,[6-11] and such processes can enhance pore opening and lead to reductions in BET areas.

Table 6.1 Summary of samples, details of the metal precursors used, metal content after the final graphitisation step by weight-% and by atomic-%, and BET specific surface area.

Material	Metal precursor (g)	wt. (%)	at. (%)	BET (m^2/g)	Pore volume (cm^3/g)	Pore width (mode(dLog)) (nm)
RPM/BP	N/A	N/A	N/A	600	0.524	1.1
Mo@C:N	1.78	10.8[a]	1.51	229	0.280	8.9
W@C:N	0.61	17.7[b]	1.41	450	0.329	1.2

a – Data obtained by ICP-OES on the graphitised material.

b – Data obtained by ED-XRF on the graphitised material.

To better understand the impact on pore size the DFT method was used to generate pore size distributions, shown in **Figure 6.3c**. The three materials are similar insofar as they exhibit distinct occurrences of porosity in the micro (< 2 nm) and meso (2-50 nm) ranges, with broadly similar distributions, i.e. peaks at 1.5,3.5 and 5 nm, characteristic of the parent carbon phase. W@C:N and RPM/BP share the most similarities, with a significant volume of micropores, which are key contributors to the surface area. A closer inspection

of the micropore region shows differences, in that the second peak (*ca.*1.5 nm) grows according to Mo@C:N > W@C:N > RPM/BP, while the peak at 1.1 nm decreases accordingly. As also mentioned in the previous chapter, this means that larger micropores are generated at the expense of smaller ones. Notably, Mo@C:N displays limited contributions from micropores relative to both RPM/BP and W@C:N. This likely explains the lower surface area observed for this sample, as well as its low pore volume (**Table 6.1**). Further, it highlights a key difference between Mo@C:N and W@C:N: for Mo@C:N the smallest tranche of micropores have either been rendered inaccessible or have undergone enlargement. DFT pore width values (mode), in **Table 6.1**, show that pore size increases with a decrease in surface area, as expected. Of note is the fact that the values for RPM/BP and W@C:N occur in the micropore range, where that of Mo@C:N falls in the mesopore range thus confirming that pore evolution in the N-doped carbon matrix is significantly affected by the incorporation of Mo centres.

TGA analysis in air was carried out and results are reported in **Figure 6.3d**. Briefly, in the case of the metal-free RPM/BP a single combustion process with zero residual mass is observed over 650-750 °C, associated with oxidation of graphitised carbon. In the presence of metals, carbon oxidation occurs at significantly lower temperatures, with the effect on onset temperature being more pronounced in the case of Mo-containing materials. This is consistent with oxidation being catalysed by metal centres, in agreement with prior literature;[12,13] while the enhanced effect of Mo vs W in these reactions is also consistent with observations from BET and DFT analysis that suggest a greater effect of Mo centres on pore opening processes.

Table 6.2 Summary of atomic elemental compositions and selected best-fit results obtained from high resolution XPS spectra of synthesised materials.

Material	C_{sp^2}/C_{tot} [a] (%)	N/C (at.%)	M/C (at.%)	MC_x or MN_x /M_{tot} (%)	M-O /M_{tot} (at.%)
RPM/BP	51.6	4.69	NA	NA	NA
Mo@C:N	63.4	19.5	5.7	16.3	83.7
W@C:N	57.4	1.7	0.45	64.3	35.7

a – Calculated as area ratio of the best-fit component at 284.4 eV over the total C 1s peak.

Surface composition was studied using XPS, and **Table 6.2** summarises results obtained from best fits of high-resolution spectra for all materials. **Figure 6.4a** show the survey spectrum collected for RPM/BP with peaks associated with C 1s, N 1s and O 1s ionisations together with peaks coming from the In foil, as mentioned in Chapter 5.[14]

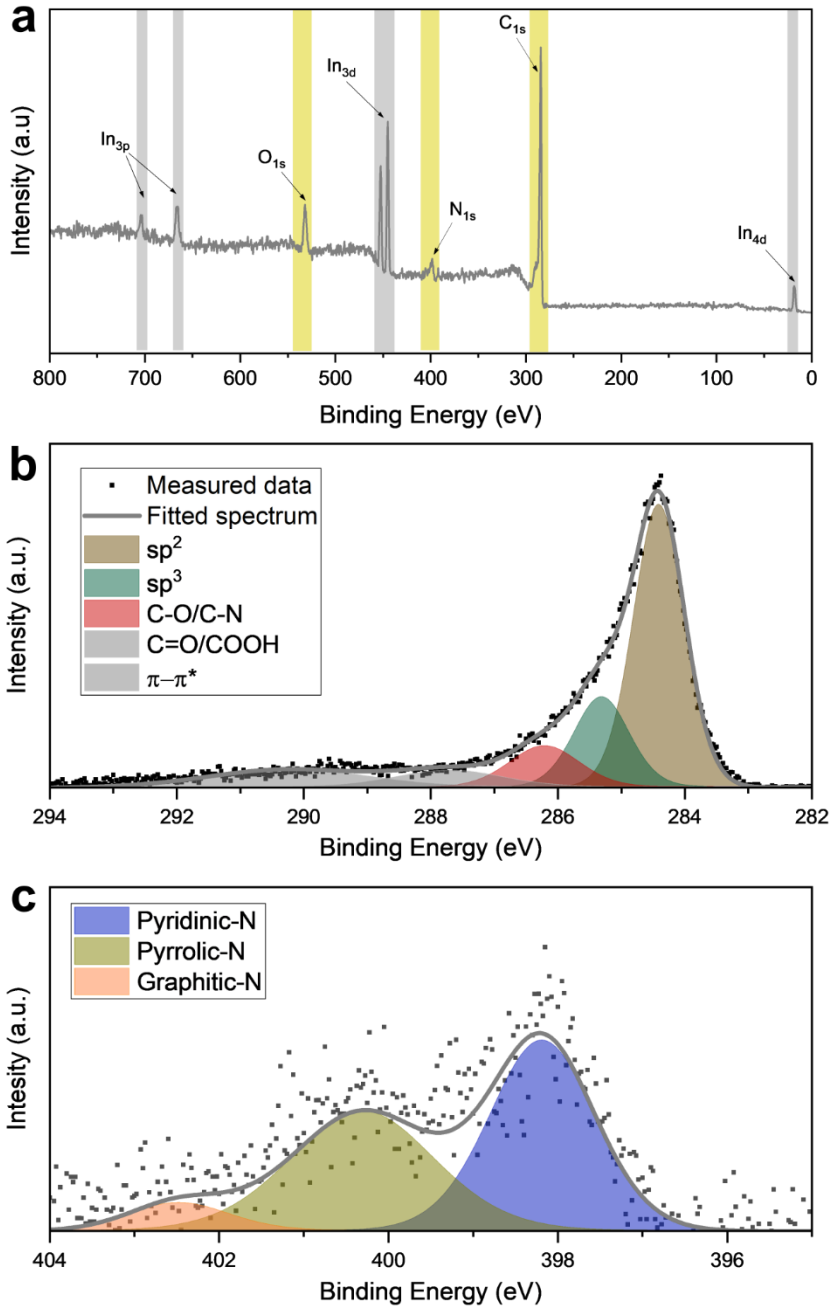

Figure 6.4 (a) Survey XPS spectrum of RPM/BP with highlighted in yellow characteristic peaks and in grey In peaks. Corresponding high-resolution spectra in the (b) C1s and (c) N 1s regions.

The C 1s peak, **Figure 6.4b**, was deconvoluted using five components attributed to sp^2 and sp^3 carbon, C-O/C-N and C=O/COOH groups, and π-π* excitations.[14-17] As observed

in Mo- and W-based materials, the sp^2 peak in RPM/BP makes the largest contribution to the total intensity (**Table 6.2**). This suggests that the material undergoes graphitisation to a similar extent during the annealing step. N 1s spectra collected for RPM/BP is shown in **Figure 6.4c.** The peak was deconvoluted using three components assigned to graphitic-N, pyrrolic-N and pyridinic-N,[15,18] Also in this case results are coherent with those coming from metal-based electrocatalysts, with pyridinic-N that accounts for the majority of contributions (49.9 at.%). Relevant is also the comparison of the metal-based materials surface composition. Both the nitrogen and metal %-contents are much lower for W@C:N than for Mo@C:N, despite the two metals being present at similar atomic bulk concentrations. Indeed, a comparison between metal/carbon atomic %-ratios obtained by XPS and those from bulk determinations (**Table 6.1**) indicates that while W remains preferentially in the bulk, or below sub-surface, Mo is found predominantly at the air interface.

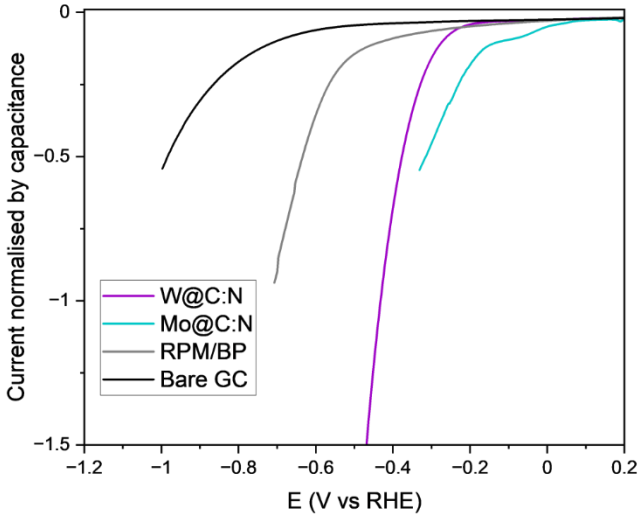

Figure 6.5 LSV of W@C:N, Mo@C:N, RPM/BP and bare GC normalised by capacitance.

The electrochemical behaviour of prepared materials was initially evaluated using a GC disk as conductive support. After the sieving step, the catalyst powder was dispersed in an ink, drop casted onto the GC disk, and tested in H_2SO_4 supporting electrolyte. Given that drop-cast films are porous, a comparison of the LSV curves was carried out after normalisation by capacitive contributions in a non-faradaic region to account for differences in microscopic area (**Figure 6.5**).[19-21] Metal-free surfaces yielded the most sluggish responses with RPM/BP providing a slightly better overpotential than GC electrodes, likely due to the presence of heteroatom functionalities.[19] Both M@C:N

materials yielded better performances than metal-free materials strongly suggest that M@C:N materials have improved intrinsic HER activity relative to metal-free graphitic carbons, and that this can be attributed to the incorporation of Mo/W centres in the form of carbides/nitrides. As also observed in Chapter 5, Mo@C:N was found to display higher HER currents than W@C:N, in agreement with prior reports of better HER performance in general for MoC_x vs WC_x electrodes in acid electrolytes.[22] The cathodic peak at -0.078 V at Mo@C:N is due to the electrochemical activity of MoO_3 species in acid media.[23] An attempt was made to calculate Tafel slopes from the LSV in 0.1 M H_2SO_4 yielding values of 225 and 166 mV for Mo@C:N, and W@C:N, respectively. However, note that the overlap between MoO_3 reductions and the rising edge of the HER current make the unambiguous determination of the HER Tafel slope challenging for Mo@C:N materials. Therefore, these values are only reported for operational comparisons vs others' in the literature. Benzaldehyde reaction was then studied using electrolysis experiments coupled to product detection. Carbon cloth current collectors were drop-coated using the same ink dispersions as for disk voltammetry studies. **Figure 6.6a** shows again the SEM image of unmodified CC presented in Chapter 4 to facilitate comparisons. **Figure 6.6b** shows the SEM image of CC coated with RPM/BP, while **Figure 6.6c** and **Figure 6.6d** display the SEM and SEM-EDX images of CC decorated with Mo@C:N and W@C:N, respectively, indicating uniform metal distribution over the CC surface. **Figure 6.6e-h** shows capacitance measurements conducted in Na_2SO_4 0.1 M supporting electrolyte in a non-faradic region for bare CC, RPM/BP, Mo@C:N and W@C:N, respectively. Bare CC displays lower capacitance values, while all prepared electrocatalysts present higher capacitances arising from their porous structures (**Table 6.3**).

Table 6.3 Capacitance values obtained from cyclic voltammograms in 0.1 M Na_2SO_4 on carbon cloth electrodes of constant mass loading (1.07 mg cm^{-2}); values shown are obtained from normalizations by geometric unit area and by areal mass loadings of catalyst ink.

Materials	**Capacitance**	
	(mF cm^{-2})	**(F g^{-1})**
Bare CC	0.34	NA
RPM/BP	24.9	23.2
Mo@C:N	11.9	11.1
W@C:N	11.1	10.4

Capacitance values were found to be comparable for Mo@C:N and W@C:N, suggesting that the two materials do not differ significantly in ECSA despite their differences in BET area.

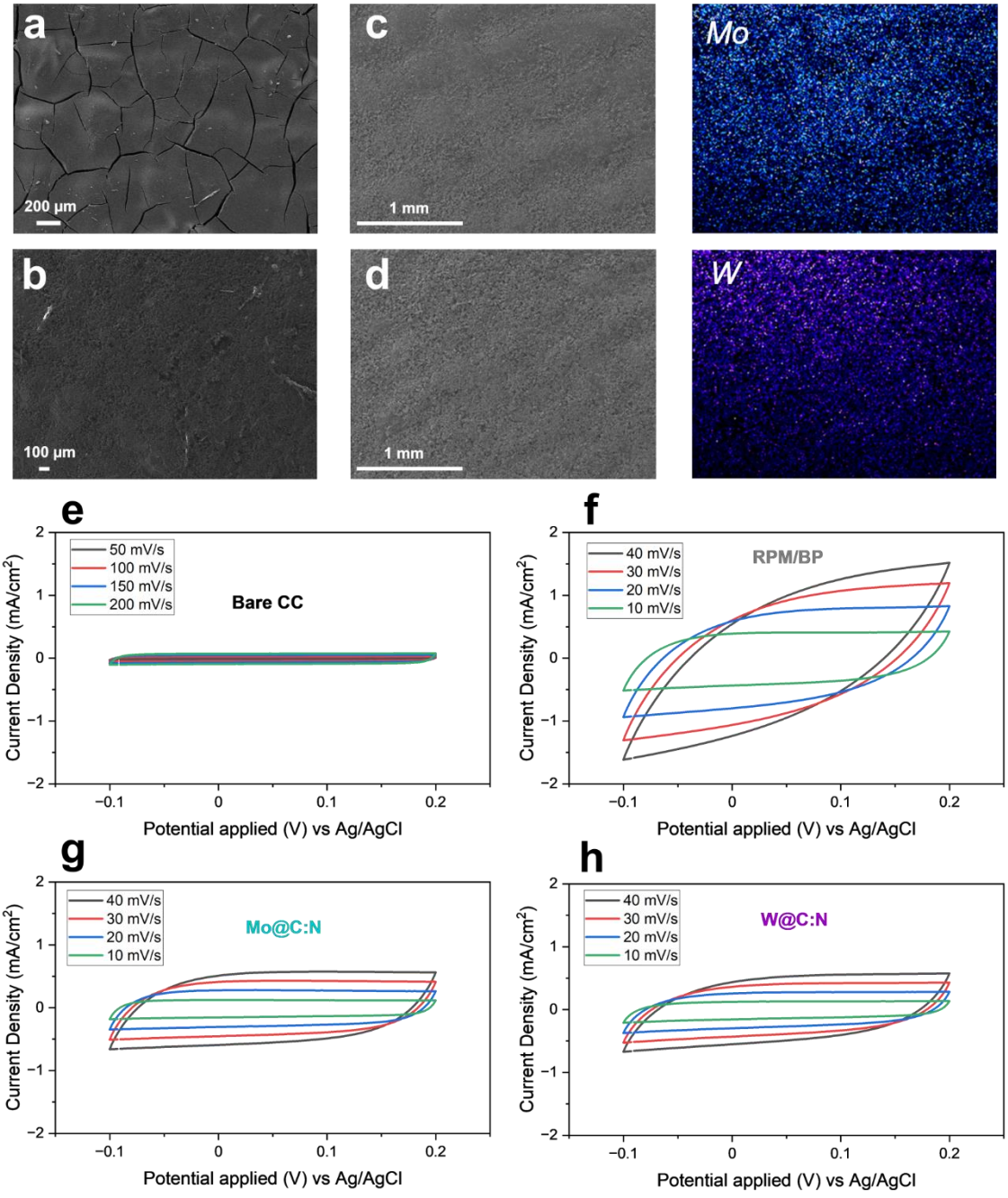

Figure 6.6 SEM images for (a) bare CC and (b) CC coated with RPM/BP, along with SEM images and EDX mapping of CC electrodes coated with (c) Mo@C:N and (d) W@C:N electrocatalyst inks. CV recorded at varying scan rates in 0.1 M Na_2SO_4 for (e) bare CC, (f) RPM/BP, (g) Mo@C:N and (h) W@C:N coated on CC supports.

LSV at electrodes prepared on CC supports were recorded in 0.1 M H_2SO_4 at 10 mV s^{-1}. In supporting electrolyte, **Figure 6.7a**, RPM/BP displays lower HER currents compared to Mo@C:N and W@C:N. Wide cathodic plateaus are observed over the -0.4 to -0.2 V range likely due to contributions from capacitive/pseudocapacitive processes at the nitrogenated porous carbon over this potential window.[24] **Figure 6.7b-d** show LSV comparisons at RPM/BP on CC, Mo@C:N on CC and W@C:N on CC with and without 30 mM benzaldehyde, respectively.

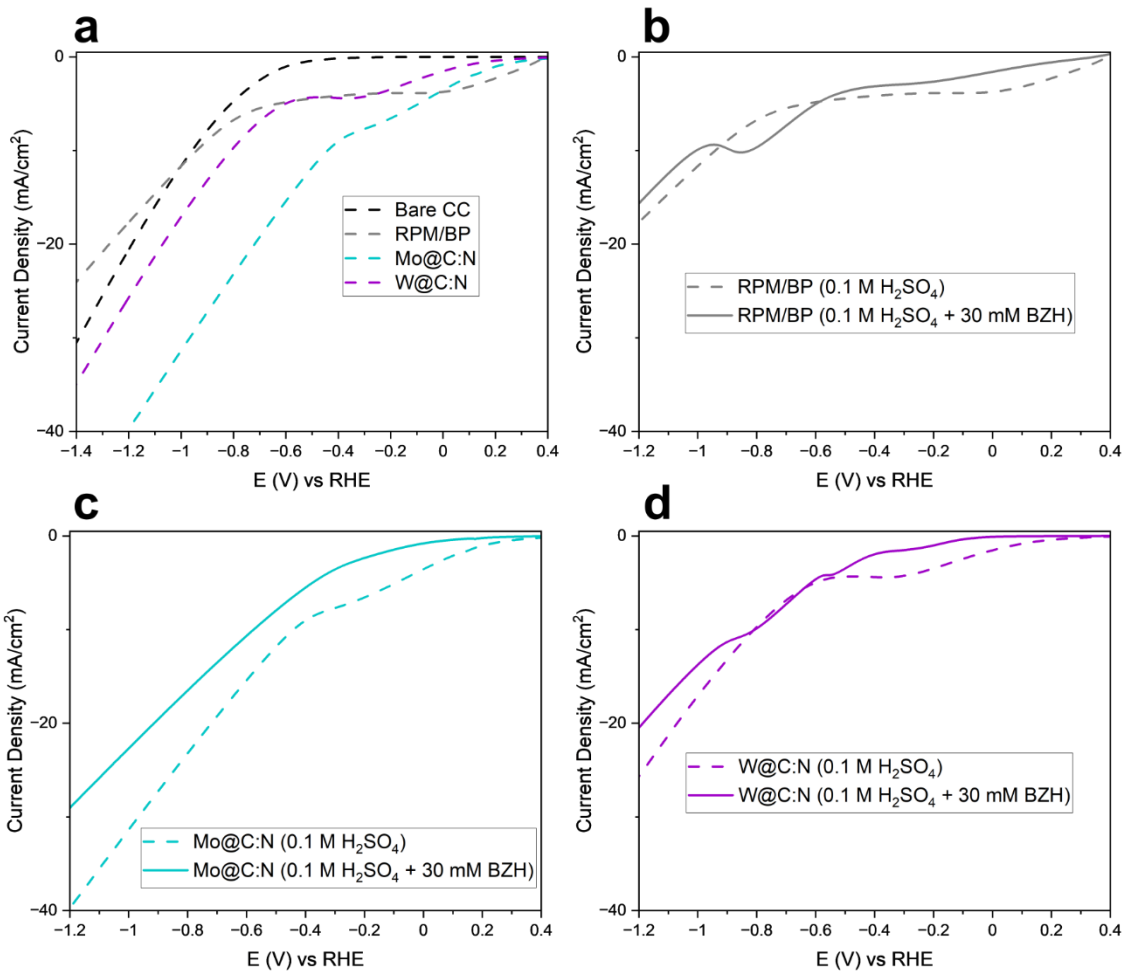

Figure 6.7 (a) LSV measured in 0.1 M H_2SO_4 supporting electrolyte for all materials on CC current collectors at 10 mV s^{-1}. LSV measured in 0.1 M H_2SO_4 in absence and presence of 30 mM BZH for (b) RPM/BP, (c) Mo@C:N, (d) W@C:N coated on CC.

In the presence of benzaldehyde RPM/BP present a single peak at *ca.* -0.8 V, likely associated to the organic and in agreement to what was observed in previous chapters. No peaks are observed for Mo@C:N likely due to HER being the dominant contribution to the LSV currents, as observed for disk electrodes. Multiple broad cathodic peaks between

-0.8 and -0.26 V and associated with BZH are observed for W@C:N, consistently with the discussion in Chapter 5 for unsieved samples. The peaks in the LSV currents could arise from either mixed mass transport regimes in the porous CC electrode,[25,26] or from reduction at different functional sites, as observed by some even at carbon disk electrodes of well-defined geometry.[27]

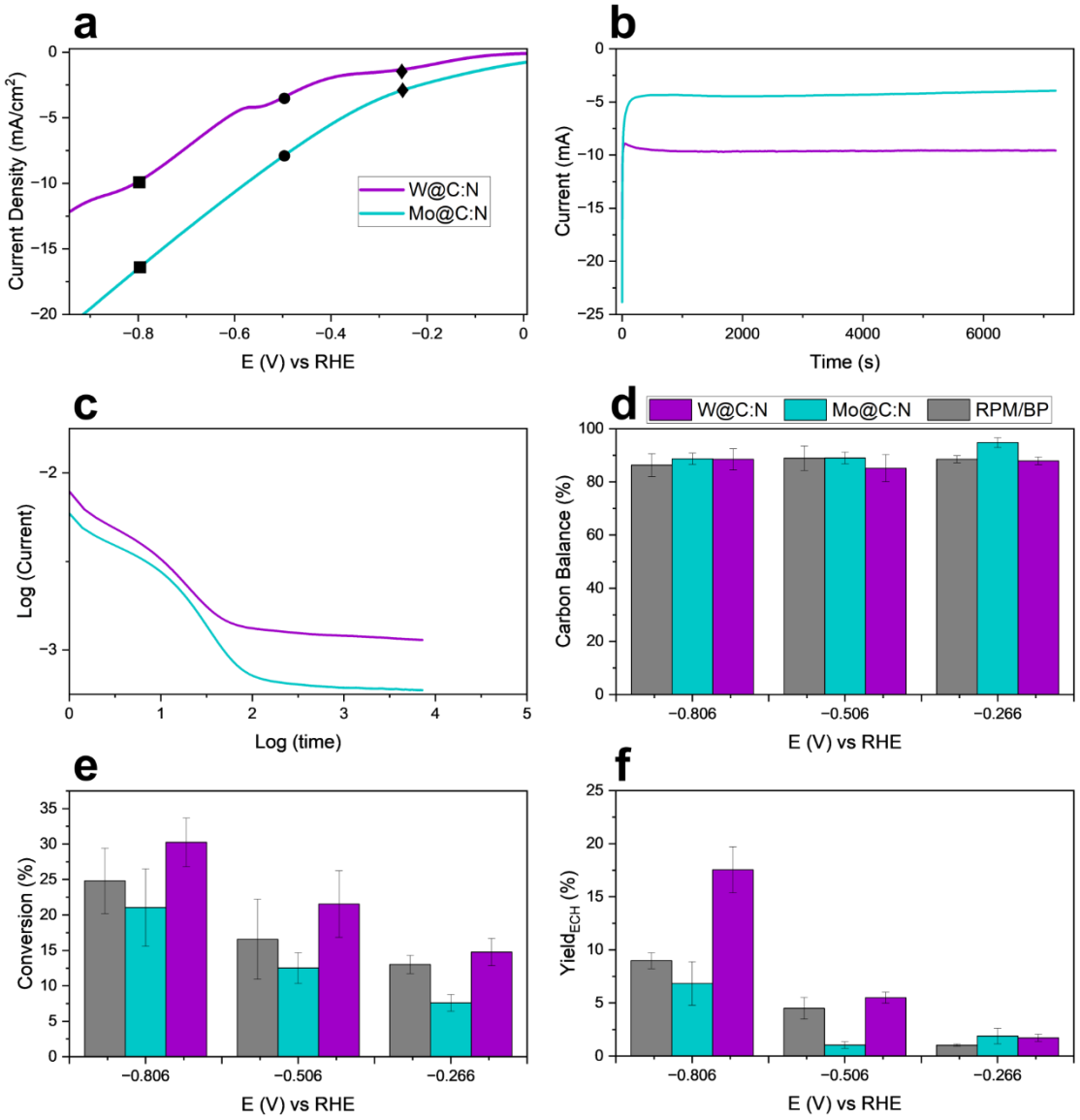

Figure 6.8 (a) LSV collected for W@C:N and Mo@C:N on CC support in 0.1 M H2SO4 + 30 mM BZH with highlighted potential at -0.26 V (♦), -0.5 V (●) and -0.8 V (■) vs RHE. (b) Representative chronoamperograms recorded for W@C:N and Mo@C:N, measured at -0.8 V. (c) Representative log-log plots of individual chronoamperograms at -0.26 V. (d) Summary of mass balance for electrolysis experiments carried out with all three investigated materials. (e) Conversion and (f) yield obtained from electrolysis experiments carried out with all three investigated materials.

An H-cell was used for electrolysis studies, as described in previous chapters. Chronoamperometry experiments were carried out in a 30 mM BZH in 0.1 M H_2SO_4

solution at three selected potentials: -0.26, -0.50 and -0.80 V vs. RHE, as shown in **Figure 6.8a**. Catalyst layers displayed high mechanical stability over the duration of the experiments thus yielding stable chronoamperogram curves as shown in **Figure 6.8b**. Log-log plots of current vs. time, **Figure 6.8c**, show that after *ca.*100-150 s, the slope of these plots transitions from a value of *ca.* -0.5 to a value close to zero, indicative of convective control. Evidence of convection is in agreement with prior work on similar electrode materials and is attributed to gas evolution during HER.[24] Both BA and HBZ were identified as reduction products via gas chromatography, confirming the hydrogenation of BZH. Carbon balance was found to be *ca.*90% for all materials, indicating negligible mass losses due to diffusion through the membrane or into the headspace (**Figure 6.8d**). Yields and conversion values were calculated for all materials and are shown in **Figure 6.8e and Figure 6.8f**.

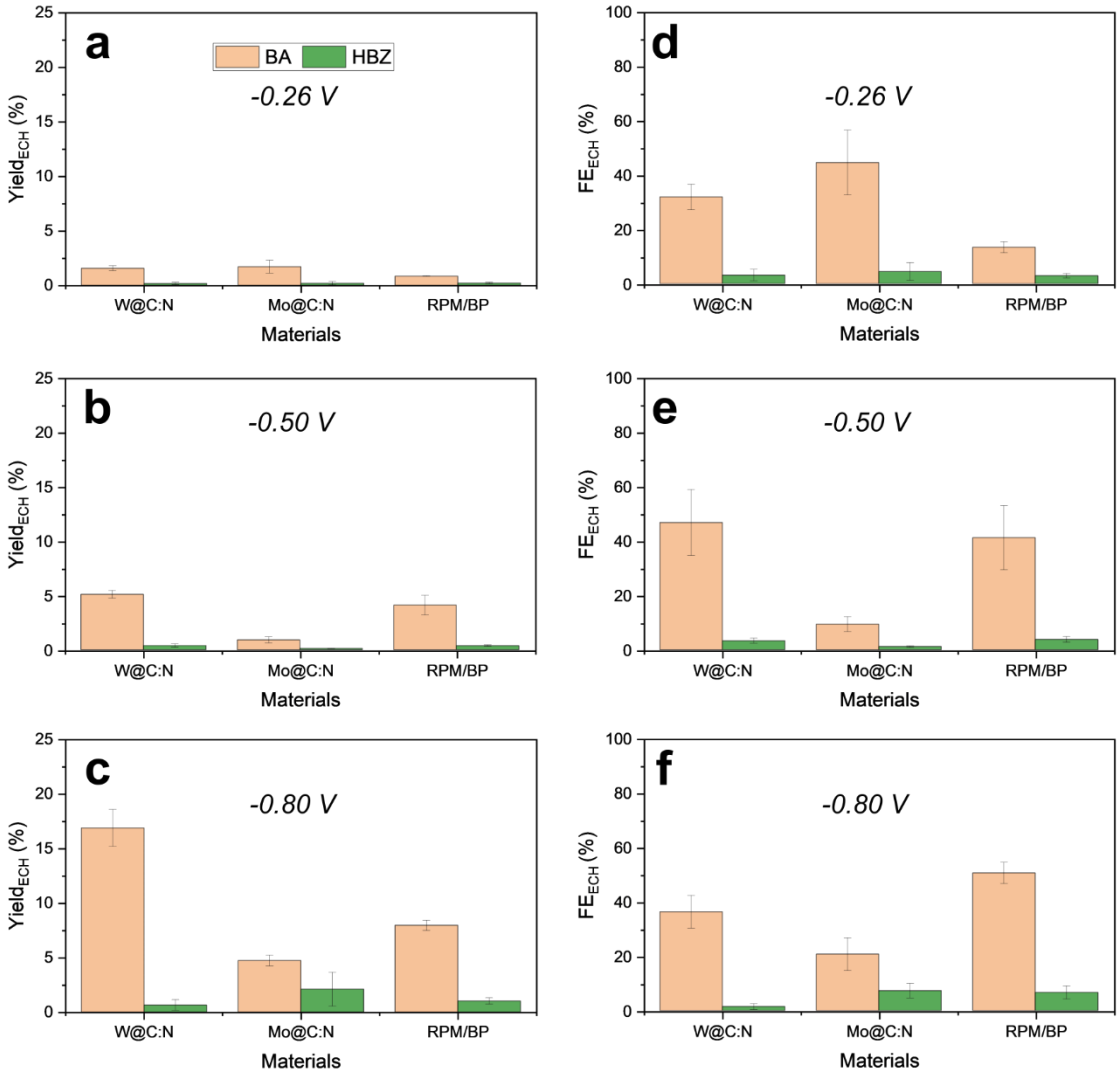

Figure 6.9 Yield by product for all materials at (a) -0.26 V (b) -0.5 V and (c) -0.8 V. Selectivity by product for all materials at (d) -0.26 V (e) -0.5 V and (f) -0.8 V.

As the potential is shifted to more cathodic values, both conversion and yield show an increase, while the preferred product remains BA (**Figure 6.9a-c**). At any given potential, better yields and conversions were observed for W@C:N vs Mo@C:N over 2 h, thus suggesting that given, the same metal atomic concentrations, W-containing catalyst layers result in better operational performances in organic hydrogenations. Faradic selectivity was calculated by considering the individual contributions of BA and HBZ, as is summarised in **Figure 6.9d-f**. BA consistently emerged as the preferred product across all tested potentials and materials, aligning with the yield results.

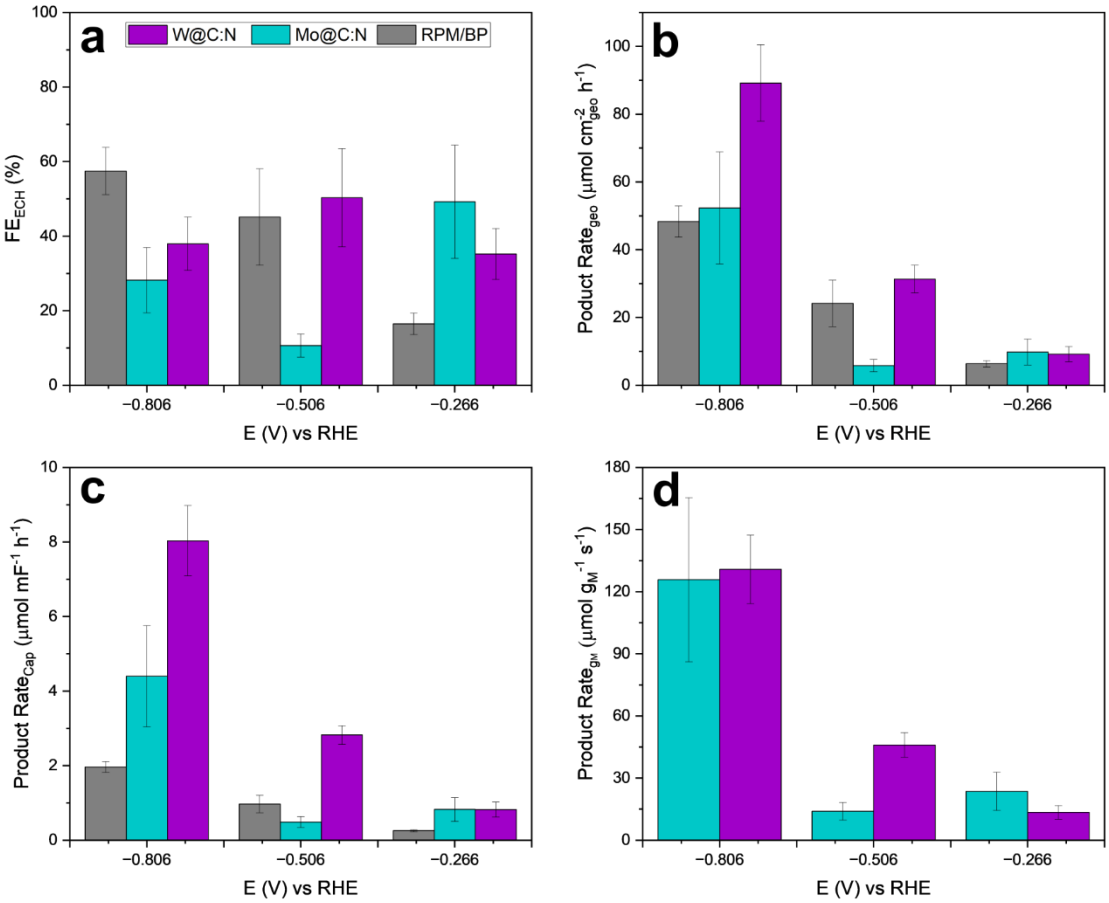

Figure 6.10 (a) Total FE_{ECH} calculated for all three investigated materials and potentials. Product rate normalised by geometric area (b), by capacitance (c), and by amount of metal in the bulk for both M@C:N (d).

The ECH faradaic efficiencies, were calculated and are summarised in **Figure 6.10a**. Mo@C:N shows good FE_{ECH} at the lowest overpotential, but the efficiency of reductions decreases significantly at -0.5 V before increasing slightly at -0.8 V again. The greater HER activity of Mo@C:N vs W@C:N and RPM/BP, enables facile H_{ads} activation even

at -0.26 V which increases rates of ECH via H_{ads} addition or concerted e-H^+ additions;[28,29] however, as the potential is shifted to more cathodic values, the HER becomes the dominant faradaic process decreasing the overall efficiency of ECH. At higher cathodic overpotentials proton coupled reductions of BZH can become an additional and energetically favourable pathway for the production of BA/HBZ particularly at carbon surfaces, as discussed in detail in computational studies by Cantu at. al.[29] This is likely to explain the increase in FE_{ECH} at -0.8 V for Mo@C:N. In the case of both W@C:N and RPM/BP, the efficiencies are low at -0.26 V but superior to that of Mo@C:N at -0.5 V, which is consistent with these materials being less effective at evolving hydrogen and with the HER being suppressed as a competing reaction at -0.5 V. Product rates normalised by geometric area (Product $Rate_{geo}$) and by capacitance (Product $Rate_{cap}$) are shown in **Figure 6.10b** and **Figure 6.10c**, respectively (see also summary of equations in Appendix I). Normalisation by capacitance puts in clear evidence the significant differences in specific electroactive area between the metal-free material and M@C:N catalysts, as well as the superior performance in organic hydrogenations obtained with the latter. W@C:N materials offer significant advantages at -0.5 and -0.8 V. Interestingly, while the Volmer step is facile and H_2 desorption limiting at WC/WN,[3,30] it is H_{ads} activation that is rate determining at carbons. Therefore, H_{ads} coverages should remain low at RPM/BP but increase readily with cathodic overpotential at WN, which likely explains why the product rate normalised by specific area is markedly superior for W@C:N at both -0.5 V and -0.8 V. **Figure 6.10d** shows product rates for Mo@C:N and W@C:N after normalisation by bulk metal contents (Product $Rate_{gM}$). These results align with trends in FE_{ECH}, showing higher performance for Mo@C:N at -0.26 V and for W@C:N at -0.5 V; while at -0.8 V the two materials show similar product rates. However, their performances diverge when considering differences in surface segregation between Mo and W centres observed for the two M@C:N. This can be taken into account by estimating a surface-effective turnover frequency ($TOF_{eff,surface}$) for W and Mo metal centres at the electrolyte interface. Assuming that the double-layer capacitance arises from the carbon matrix alone (20 $\mu F/cm^2$)[31,32] and accounting for the areal carbon density of graphite of 3.82×10^{15} atoms/cm^2,[33,34] $TOF_{eff,surface}$ values can be calculated using the atomic %-contents of 0.43% and 4.30% for W and Mo, respectively, obtained from XPS (see also summary of equations in Appendix I). $TOF_{eff,surface}$ values thus calculated are shown in **Figure 6.11** and suggest that encapsulated W centres yield significant advantages in terms of intrinsic activity.

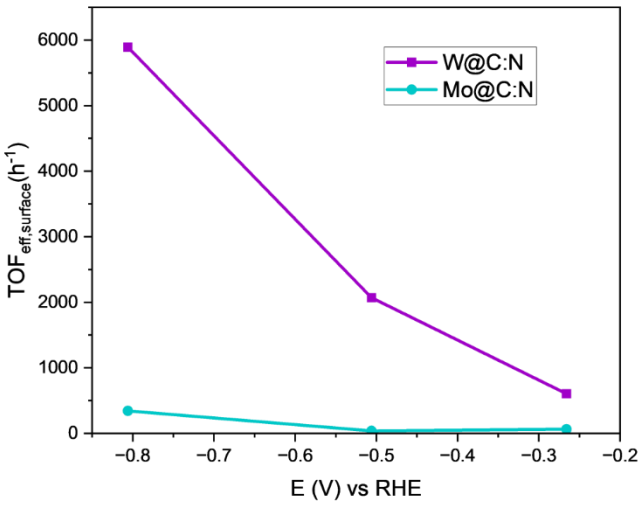

Figure 6.11 $TOF_{eff,surface}$ calculated values for Mo@C:N and W@C:N samples normalised for surface atomic concentrations.

The above results indicate that both Mo@C:N and W@C:N show activity in the hydrogenation of benzaldehyde and that W@C:N appears to be particularly promising, achieving satisfactory FE_{ECH} and good product rates at moderate potentials. At low overpotentials, FE_{ECH} values for Mo@C:N samples are comparable to those reported for Pt/C (~60%) and exceed those of similar M@C:N architectures synthesised using Fe as a metal core.[28,35] Further, W@C:N shows good FE_{ECH} at -0.5 V compared to Pt/C, as determined by Song et al. at pH 5 and similar potentials.[28] Interestingly, $TOF_{eff,surface}$ values estimated for W@C:N under operational conditions presented in this thesis are comparable to those reported for Pt/C and Rh/C catalysts at -0.5 V vs RHE in the same work. These findings therefore suggest that compositional changes can be successfully leveraged to modulate and improve ECH performance at M@C architectures based on transition metals.

It is important however to highlight that, when interpreting differences in performance between Mo and W-containing electrodes it remains challenging to disentangle the effects of a change in metal identity (W vs Mo), from those arising from morphological and compositional differences that result from metal-catalysed graphitisation. In the case of W@C:N materials, metal centres are encapsulated and protected from oxidation; the majority of them are present in the form of WN nanorods that can improve, simultaneously, H_{ads} stabilisation[3,30] and metallic character/conductivity of the porous carbon matrix. For Mo@C:N it is also possible to argue that H_{ads} coverages are stabilised

relative to RPM/BP; however, the presence of surface MoO_x indicates that only a fraction of metal sites should facilitate H_{ads} activation, while charge transfer impedances are likely to be negatively affected by surface oxidised phases.[36] Moreover, the calculation of $TOF_{eff,surface}$ values assumes implicitly that the metal sites are responsible for BZH reduction rates. This is likely an oversimplification that neglects possible activation of multiple N-/C-sites due to e.g. proximity effects of metal in the sub-surface,[1,37] as well as the fact that hydrogenation pathways are potential-dependent.[29] As mentioned in Chapter 1, several proposed hypotheses have been put forward to explain the nature of the active site at M@C:N electrodes in the HER. Both M-sites in contact with the electrolyte but with their reactivity modulated by the surrounding carbon matrix, or C/N-sites with their reactivity modulated by metals in the subsurface are considered as possible and experimentally consistent explanations for H_{ads} activation at carbon-encapsulated architectures. However, unequivocal identification of these active sites remains a topic of ongoing debate, as highlighted recently by Yoo et al.,[38] despite the HER being a considerably simpler reaction than the ECH of benzaldehyde. Nonetheless, regardless of whether the active sites are C- or M-centers, the activity remains dependent on the degree to which the metal is in proximity to, or at, the surface. Therefore, XPS atomic coverages, which reflect metal content within the first 1-3 nm from the surface, are a relevant quantity when attempting to account for metal effects on surface reactivity. A more in-depth analysis of the active site in the ECH is likely to require further experimental work, including use of poisoning/capping agents, as discussed by Yoo et al.[38] Furthermore, potential-dependence of the active site must also be contemplated, at increasing cathodic overpotentials it is reasonable to assume that the total product rate stems at least in part from proton coupled reductions, as noted when discussing FE_{ECH} values at -0.8 V. Indeed, contributions from M-site mediated H-addition and from proton coupled reduction of BZH_{ads} must both be contemplated, particularly at high overpotentials, based on the current mechanistic understanding of ECH.[29,39-41] Therefore, the validity of assumptions underpinning TOF_{eff} calculations might be limited at the most negative potentials tested and comparisons between metal TOF values are best restricted to the low overpotential range where metal catalysed pathways are expected to dominate hydrogenation rates. Also, although electrolysis experiments are performed under natural convection, well-defined convective conditions e.g. flow through electrolyser devices, would be desirable to fully account for mass transport effects and support comparative performance studies.[37]

6.3.2 Performance comparison of Mo, W, and Fe metal cores

Particularly interesting is the comparison of W- and Mo-based materials with Fe@C:N material introduced in Chapters 3 and 4 under identical conditions, i.e. after sieving. Indeed, although Fe@C:N has a different surface atomic %-contents of 2.51%, present still a similar bulk metal wt.% compared to Mo-based sample equal to *ca.*10.7% (**Table 6.4**). The ink dispersion of Fe@C:N was prepared following the sieving-based procedure presented in this chapter and then drop-cast on CC support. Electrolysis experiments were performed at identical potentials of -0.26, -0.5, and -0.8 V vs. RHE as done for W- and Mo-based materials. ECSA measurements for the sieved Fe@C:N yielded a C_{dl} of 6.86 mF cm^{-2}, higher than the values reported in Chapter 4 for the unsieved sample. This increase is consistent with enhanced surface area availability for electrochemical interactions following the sieving step. Based on the Fe surface atomic content determined by XPS and the ECSA of sieved Fe@C:N, $TOF_{eff,surface}$ calculations were performed, with the results presented in **Figure 6.12**.

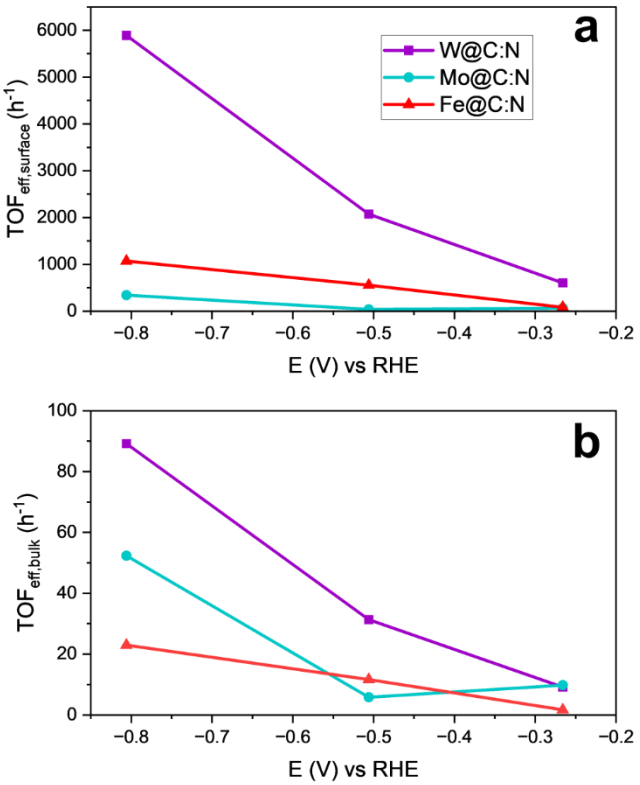

Figure 6.12 (a) $TOF_{eff,surface}$ normalised for surface atomic concentrations and (b) $TOF_{eff,bulk}$ normalised for bulk atomic concentrations, calculated for all sieved M@C:N samples.

Interestingly, Fe-based material exhibits a $TOF_{eff,surface}$ value comparable to Mo@C:N at -0.26 V. As the potential becomes more cathodic, Fe@C:N material shows a linear increase in $TOF_{eff,surface}$ surpassing Mo@C:N but remaining lower than W@C:N. This positions the Fe-based material as a viable alternative to Mo- and W-based electrocatalysts, particularly given the cost differences between these metal cores. However, to account for variations in surface metal content and to better interpret performance metrics in relation to the bulk metal contribution, bulk-effective turnover frequency ($TOF_{eff,bulk}$) calculations were also conducted, with the results presented in **Figure 6.12**. However, it is important to note that bulk metal content does not necessarily dictate electrochemical activity, as reactions occur at the solid/electrolyte interface, and is presented here purely for comparative purposes. Despite the nearly identical bulk metal content, Fe@C:N exhibits a lower $TOF_{eff,bulk}$ than Mo@C:N at -0.26 V, likely due to the intrinsically lower HER activity of Fe-based materials compared to Mo-based ones. As the potential becomes more cathodic (-0.5 V), Fe@C:N surpass Mo@C:N but remains less active than W@C:N, aligning with the trends observed in $TOF_{eff,surface}$ calculations. More cathodic potential has to be carefully interpreted, since as mentioned before pathways are likely not dominated by hydrogen activation rates at this potential.

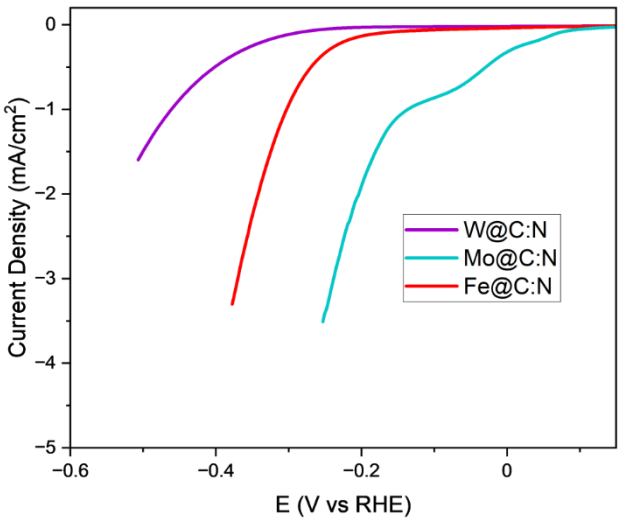

Figure 6.13 LSV measured in 0.1 M H_2SO_4 supporting electrolyte for all sieved M@C:N materials drop-casted on polished GC disk at 2 mV s^{-1}.

At -0.5 V vs. RHE, both TOF values normalised for bulk and surface follow the HER activity trends of the materials, as shown in **Figure 6.13**, which presents the LSV data collected for sieved samples in 0.1 M H_2SO_4 on GC disk. Notably, highly active HER

catalysts like Mo@C:N demonstrate poor ECH performance due to the strong competition between HER and ECH. Excessive HER activity leads to increased bubble production, which can restrict the effective surface area by blocking access to the solution, which further highlight the importance of the choice of the metal active site into the M@C:N structure.

A comprehensive comparison of all sieved metal-based electrocatalysts discussed in this thesis is provided in **Table 6.4**. Except for FE, all parameters increase as the potential becomes more cathodic. Both W@C:N and Fe@C:N exhibit similar conversions at the same potentials, although W@C:N demonstrates superior performance at -0.8 V. A similar trend is observed for yields, with W@C:N achieving the best performance at -0.8 V. For both Fe@C:N and W@C:N the highest FE values are observed at intermediate potentials where the competition between HER and ECH remains controllable. On the other hand, Mo@C:N displays lower conversions and yields, along with FE higher at anodic potentials where materials is less HER active. Finally Fe@C:N display comparable values of Product rate per grams of metals to those of the other two metal-based electrocatalysts.

Table 6.4 Summary of ECH performance parameters for sieved M@C:N, along with weight% and atomic% for each material.

Materials (wt.%) (at.%)	**Potential (V vs RHE)**	**Conversion (%)**	**$Yield_{ECH}$ (%)**	**FE_{ECH} (%)**	**Prod. $Rate_{geo}$ (µmol/ cm^2 h)**	**Prod. $Rate_{cap}$ (µmol/ mF h)**	**Prod. $Rate_{gM}$ (µmol/ g_M s)**
W@C:N	-0.26	14.7	1.71	35.2	9.15	0.82	13.4
17.7[a]	-0.50	21.5	5.50	50.3	29.9	2.82	45.9
1.41	-0.80	30.3	17.5	37.9	88.9	8.03	130.8
Fe@C:N	-0.26	14.4	0.60	11.4	3.28	0.47	8.45
10.7[b]	-0.50	21.2	4.40	46.0	21.9	3.20	57.9
2.51	-0.80	26.0	8.40	35.6	42.4	6.17	114.2
Mo@C:N	-0.26	7.60	1.88	49.2	9.81	0.82	23.5
10.8[b]	-0.50	12.5	1.03	10.6	5.80	0.48	13.9
1.51	-0.80	21.0	6.83	28.2	52.3	4.39	125.8

a – Data obtained by ED-XRF on the graphitised material.

b – Data obtained by ICP-OES on the graphitised material.

The results presented in this chapter highlight the critical role of metal core selection in determining the ECH performance of M@C:N architectures. This choice is essential not only for the structural composition but also for the metal's ability to be encapsulated at equivalent concentrations. Specifically, a high concentration of oxides on the surface hinders the ECH process, resulting in diminished performance. Furthermore, excessive HER activity increases bubble production, which can hinder the effective area available for ECH. Therefore, metal selection should prioritise those that activate hydrogen at the surface while exhibiting limited HER activity.

6.4 Conclusion

This chapter explores the effect of metal centre identity on regulating ECH performance by investigating two M@C:N architectures, Mo@C:N and W@C:N. The synthesis and properties of these materials, with nearly identical atomic metal contents of *ca.*1.5%, were examined alongside a metal-free material used as a benchmark for comparison. As demonstrated by BET analysis, the introduction of W centres resulted in minimal changes to carbon porosity compared to the metal-free analogue, while Mo centres facilitated pore opening. The RPM/BP material showed a surface composition similar to that of the metal-based catalysts, maintaining comparable graphitisation levels during the annealing process and a similar nitrogen composition, dominated by pyridinic-N sites.

Electrochemical performances were evaluated by preparing ink dispersion using a sieved-based procedure to minimise surface differences among the materials and to simplify the preparation. The incorporation of Mo and W centres enhanced HER activity in both materials relative to the metal-free benchmark RPM/BP, with Mo@C:N exhibiting higher HER cathodic currents. Electrolysis experiments coupled with gas chromatography analysis of products demonstrated that this translates into increased ECH activity at low overpotentials in the hydrogenation of benzaldehyde. Selectivity for the benzyl alcohol product was observed at all tested potentials; this is a promising result as achieving selectivity remains a challenge for most studied electrocatalysts, particularly at cathodic potentials.[28,35,42] Mo@C:N shows high FE at anodic potentials, while W@C:N is more efficient at cathodic potentials due to suppressed competition between HER and ECH pathways. Product rates and $TOF_{eff,surface}$ values were used as a basis for comparison, with W@C:N showing higher ECH performances at the investigated atomic loading,

especially when considering the differences in surface excess between the two metals. $TOF_{eff,surface}$ was also employed as the primary comparison parameter with sieved Fe@C:N. Despite its higher metal atomic concentration, Fe@C:N exhibits lower ECH activity at equivalent potentials compared to W@C:N but outperforms Mo@C:N, particularly at cathodic potentials. TOF values align with the HER activity trends of the materials, with bubble production potentially limiting the effective surface area by obstructing access to the solution. Notably, estimated $TOF_{eff,surface}$ for W-based material are comparable to those for Rh/C and Pt/C catalysts;[28] and given the four orders of magnitude difference in material cost, results suggests that W@C:N architectures are likely to be cost competitive for ECH applications and could reduce pressure on precious and critical raw materials for ECH implementation at scale.

6.5 References

1. Peng, Y.; Chen, S. Electrocatalysts based on metal@carbon core@shell nanocomposites: An overview. *Green Energy & Environment* **2018**,*3* (4),335-351.

2. Trasatti, S. Work function, electronegativity, and electrochemical behaviour of metals: III. Electrolytic hydrogen evolution in acid solutions. *Journal of Electroanalytical Chemistry and Interfacial Electrochemistry* **1972**,*39* (1),163-184.

3. Michalsky, R.; Zhang, Y.-J.; Peterson, A. A. Trends in the Hydrogen Evolution Activity of Metal Carbide Catalysts. *ACS Catalysis* **2014**,*4* (5),1274-1278.

4. https://www.dailymetalprice.com (accessed 17/01/2025).

5. Karthik, M.; Faik, A.; Doppiu, S.; Roddatis, V.; D'Aguanno, B. A simple approach for fabrication of interconnected graphitized macroporous carbon foam with uniform mesopore walls by using hydrothermal method. *Carbon* **2015**,*87*,434-443.

6. Iannaci, A.; Ingle, S.; Domínguez, C.; Longhi, M.; Merdrignac-Conanec, O.; Ababou-Girard, S.; Barrière, F.; Colavita, P. E. Nanoscaffold effects on the performance of air-cathodes for microbial fuel cells: Sustainable Fe/N-carbon electrocatalysts for the oxygen reduction reaction under neutral pH conditions. *Bioelectrochemistry* **2021**,*142*,107937.

7. Baker, R. T. K.; Chludzinski, J. J.; Dispenziere, N. C.; Murrell, L. L. Catalytic gasification of graphite by: Tungsten, rhenium, and tungsten-rhenium. *Carbon* **1983**,*21* (6),579-588.

8. Wang, T.; Tang, J.; Fan, X.; Zhou, J.; Xue, H.; Guo, H.; He, J. The oriented growth of tungsten oxide in ordered mesoporous carbon and their electrochemical performance. *Nanoscale* **2014**,*6* (10),5359-5371,10.1039/C4NR00396A.

9. Li, J.; Zhang, Z.; Wang, Z.; Cao, Q.; Guo, F.; Cao, Q. Low temperature graphitization and electrochemical properties of porous carbon catalyzed with bimetal Ni-Mo. *Diamond and Related Materials* **2022**,*123*,108862.

10. Guo, H.; Song, Y.; Chen, P.; Lou, H.; Zheng, X. Effects of graphitization of carbon nanospheres on hydrodeoxygenation activity of molybdenum carbide. *Catalysis Science & Technology* **2018**,*8* (16),4199-4208,10.1039/C8CY01136B.

11. Ōya, A.; Ōtani, S. Catalytic graphitization of carbons by various metals. *Carbon* **1979**,*17* (2),131-137.

12. Braun, S.; Appel, L. G.; Schmal, M. Molybdenum species on alumina and silica supports for soot combustion. *Catalysis Communications* **2005**,*6* (1),7-12.

13. Neeft, J. P. A.; Makkee, M.; Moulijn, J. A. Catalysts for the oxidation of soot from diesel exhaust gases. I. An exploratory study. *Applied Catalysis B: Environmental* **1996**,*8* (1),57-78.

14. Chastain, J.; King Jr, R. C. Handbook of X-ray photoelectron spectroscopy. *Perkin-Elmer Corporation* **1992**,*40*,221.

15. Hellgren, N.; Haasch, R. T.; Schmidt, S.; Hultman, L.; Petrov, I. Interpretation of X-ray photoelectron spectra of carbon-nitride thin films: New insights from in situ XPS. *Carbon* **2016**,*108*,242-252.

16. Qu, L.; Liu, Y.; Baek, J.-B.; Dai, L. Nitrogen-Doped Graphene as Efficient Metal-Free Electrocatalyst for Oxygen Reduction in Fuel Cells. *ACS Nano* **2010**,*4* (3),1321-1326.

17. Titantah, J. T.; Lamoen, D. Carbon and nitrogen 1s energy levels in amorphous carbon nitride systems: XPS interpretation using first-principles. *Diamond and Related Materials* **2007**,*16* (3),581-588.

18. Costa de Oliveira, M. A.; Schröder, C.; Brunet Cabré, M.; Nolan, H.; Forner-Cuenca, A.; Perova, T. S.; McKelvey, K.; Colavita, P. E. Effects of N-functional groups on the electron transfer kinetics of VO2+/VO2+ at carbon: Decoupling morphology from chemical effects using model systems. *Electrochimica Acta* **2024**,*475*,143640.

19. Nolan, H.; Schröder, C.; Brunet-Cabré, M.; Pota, F.; McEvoy, N.; McKelvey, K.; Perova, T. S.; Colavita, P. E. MoS2/carbon heterostructured catalysts for the hydrogen evolution reaction: N-doping modulation of substrate effects in acid and alkaline electrolytes. *Carbon* **2023**,*202*,70-80.

20. Perez Bakovic, S. I.; Acharya, P.; Watkins, M.; Thornton, H.; Hou, S.; Greenlee, L. F. Electrochemically active surface area controls HER activity for FexNi100−x films in alkaline electrolyte. *Journal of Catalysis* **2021**,*394*,104-112.

21. Kibsgaard, J.; Chen, Z.; Reinecke, B. N.; Jaramillo, T. F. Engineering the surface structure of MoS2 to preferentially expose active edge sites for electrocatalysis. *Nature Materials* **2012**,*11* (11),963-969.

22. Hussain, S.; Vikraman, D.; Feroze, A.; Song, W.; An, K.-S.; Kim, H.-S.; Chun, S.-H.; Jung, J. Synthesis of Mo2C and W2C Nanoparticle Electrocatalysts for the Efficient Hydrogen Evolution Reaction in Alkali and Acid Electrolytes. *Frontiers in Chemistry* **2019**,*7*, Original Research.

23. Saji, V. S.; Lee, C.-W. Molybdenum, Molybdenum Oxides, and their Electrochemistry. *ChemSusChem* **2012**,*5* (7),1146-1161.

24. Frackowiak, E. Carbon materials for supercapacitor application. *Physical Chemistry Chemical Physics* **2007**,*9* (15),1774-1785,10.1039/B618139M.

25. Sims, M. J.; Rees, N. V.; Dickinson, E. J. F.; Compton, R. G. Effects of thin-layer diffusion in the electrochemical detection of nicotine on basal plane pyrolytic graphite (BPPG) electrodes modified with layers of multi-walled carbon nanotubes (MWCNT-BPPG). *Sensors and Actuators B: Chemical* **2010**,*144* (1),153-158.

26. Keeley, G. P.; E G Lyons, M. The Effects of Thin Layer Diffusion at Glassy Carbon Electrodes Modified with Porous Films of Single-Walled Carbon Nanotubes. *International Journal of Electrochemical Science* **2009**,*4* (6),794-809.

27. Chandrasekaran, M.; Noel, M.; Krishnan, V. Glassy carbon surface effects on the electroreduction of aromatic carbonyl compounds: Part 1. Benzaldehyde. *Journal of Electroanalytical Chemistry and Interfacial Electrochemistry* **1991**,*303* (1),185-197.

28. Song, Y.; Sanyal, U.; Pangotra, D.; Holladay, J. D.; Camaioni, D. M.; Gutiérrez, O. Y.; Lercher, J. A. Hydrogenation of benzaldehyde via electrocatalysis and thermal catalysis on carbon-supported metals. *Journal of Catalysis* **2018**,*359*,68-75.

29. Cantu, D. C.; Padmaperuma, A. B.; Nguyen, M.-T.; Akhade, S. A.; Yoon, Y.; Wang, Y.-G.; Lee, M.-S.; Glezakou, V.-A.; Rousseau, R.; Lilga, M. A. A Combined Experimental and Theoretical Study on the Activity and Selectivity of the Electrocatalytic Hydrogenation of Aldehydes. *ACS Catalysis* **2018**,*8* (8),7645-7658.

30. Jin, H.; Zhang, H.; Chen, J.; Mao, S.; Jiang, Z.; Wang, Y. A general synthetic approach for hexagonal phase tungsten nitride composites and their application in the hydrogen evolution reaction. *Journal of Materials Chemistry A* **2018**,*6* (23),10967-10975,10.1039/C8TA02595A.

31. Fagan, D. T.; Hu, I. F.; Kuwana, T. Vacuum heat-treatment for activation of glassy carbon electrodes. *Analytical chemistry* **1985**,*57* (14),2759-2763.

32. Hoque, M. K.; Behan, J. A.; Stamatin, Serban N.; Zen, F.; Perova, T. S.; Colavita, P. E. Capacitive storage at nitrogen doped amorphous carbon electrodes: structural and chemical effects of nitrogen incorporation. *RSC Advances* **2019**,*9* (7),4063-4071,10.1039/C8RA10187F.

33. Pop, E.; Varshney, V.; Roy, A. K. Thermal properties of graphene: Fundamentals and applications. *MRS Bulletin* **2012**,*37* (12),1273-1281, From Cambridge University Press Cambridge Core.

34. Akhade, S. A.; Singh, N.; Gutiérrez, O. Y.; Lopez-Ruiz, J.; Wang, H.; Holladay, J. D.; Liu, Y.; Karkamkar, A.; Weber, R. S.; Padmaperuma, A. B.; et al. Electrocatalytic Hydrogenation of Biomass-Derived Organics: A Review. *Chemical Reviews* **2020**,*120* (20),11370-11419.

35. Pota, F.; Costa de Oliveira, M. A.; Schröder, C.; Brunet Cabré, M.; Nolan, H.; Rafferty, A.; Jeannin, O.; Camerel, F.; Behan, J. A.; Barrière, F.; et al. Porous N-Doped Carbon-encapsulated Iron as Novel Catalyst Architecture for the Electrocatalytic Hydrogenation of Benzaldehyde. *ChemSusChem* **2025**,*18* (1), e202400546.

36. Zheng, W. iR Compensation for Electrocatalysis Studies: Considerations and Recommendations. *ACS Energy Letters* **2023**,*8* (4),1952-1958.

37. Zhang, L.; Xiao, J.; Wang, H.; Shao, M. Carbon-Based Electrocatalysts for Hydrogen and Oxygen Evolution Reactions. *ACS Catalysis* **2017**,*7* (11),7855-7865.

38. Yoo, J. M.; Shin, H.; Chung, D. Y.; Sung, Y.-E. Carbon Shell on Active Nanocatalyst for Stable Electrocatalysis. *Accounts of Chemical Research* **2022**,*55* (9),1278-1289.

39. Chan-Shing, E. S.; Boucher, D.; Lessard, J. The electrochemical reduction of α-nitrocumene in a protic and basic medium on large surface area (porous) electrodes:

electronation-protonation or electrocatalytic hydrogenation? *Canadian Journal of Chemistry* **1999**,*77* (5-6),687-694.

40. Chen, H.; Iyer, J.; Liu, Y.; Krebs, S.; Deng, F.; Jentys, A.; Searles, D. J.; Haider, M. A.; Khare, R.; Lercher, J. A. Mechanism of Electrocatalytic H2 Evolution, Carbonyl Hydrogenation, and Carbon–Carbon Coupling on Cu. *Journal of the American Chemical Society* **2024**,*146* (20),13949-13961.

41. Lopez-Ruiz, J. A.; Andrews, E.; Akhade, S. A.; Lee, M.-S.; Koh, K.; Sanyal, U.; Yuk, S. F.; Karkamkar, A. J.; Derewinski, M. A.; Holladay, J.; et al. Understanding the Role of Metal and Molecular Structure on the Electrocatalytic Hydrogenation of Oxygenated Organic Compounds. *ACS Catalysis* **2019**,*9* (11),9964-9972.

42. Sanyal, U.; Yuk, S. F.; Koh, K.; Lee, M. S.; Stoerzinger, K.; Zhang, D.; Meyer, L. C.; Lopez-Ruiz, J. A.; Karkamkar, A.; Holladay, J. D. Hydrogen bonding enhances the electrochemical hydrogenation of benzaldehyde in the aqueous phase. *Angewandte Chemie* **2021**,*133* (1),294-300.

CHAPTER 7

Conclusions and future work

7.1 Conclusions

The aim of this thesis was to synthesise and evaluate the performance of M@C:N architectures as potential alternative catalyst materials for the electrocatalytic hydrogenation of benzaldehyde. Transition metals Fe, Mo, and W were chosen as active sites to be encapsulated within the M@C:N structures, due to their high activity toward HER and competitive cost.

In Chapter 3, Fe was chosen as the first metal core to be tested, due to its previously reported use in M@C:N-like structures for HER applications. First, catalyst preparation was optimised by assessing the ideal annealing conditions. The results showed that incorporating a pre-annealing step enhanced the degree of graphitisation and metal incorporation, while reducing the presence of oxidised species on the material's surface and improving catalytic efficiency. Second, a comprehensive characterisation of the structural composition and electrochemical response was conducted to determine the most suitable carbon nanoscaffold. The BP-based material was chosen over the VUL-based electrocatalyst as the final sample for the quantitative analysis of benzaldehyde hydrogenation, due to its higher response in current density for low concentration of BZH in 0.1 M Na_2SO_4, and higher HER activity in 0.1 M H_2SO_4 supporting electrolyte.

Once identified the optimised Fe-based material, ink stabilisation on different conductive supports was carefully assessed. Indeed, to enable quantitative analysis of BZH hydrogenation in detectable amounts, high surface area supports were required. Then in Chapter 4 carbon cloth was chosen as the conductive support, demonstrating superior performance over glassy carbon plates in maintaining ink dispersion integrity. A novel protocol for fabricating stable carbon-porous electrocatalysts was developed using a hydraulic press to enhance adhesion between the support and the ink dispersion. This stability persisted even at cathodic potential, despite the high generation of bubbles in this condition. Quantitative evaluations of electrocatalytic hydrogenation of BZH were conducted by combining electrolysis experiments with gas chromatography analysis. Acidic supporting electrolyte was chosen as the optimal solution along with a BZH concentration of 30 mM. A comprehensive assessment of key performance parameters, including FE, production rate, and TOF, revealed that intermediate potentials provided the best conditions by balancing the competition between ECH and HER, favouring BA at low overpotentials and HBZ at higher overpotentials. Interestingly, the TOF values for

Fe@C:N were determined to be only one order of magnitude lower than those observed for carbon-supported noble metal electrocatalysts, opening new possibilities for advancing M@C:N structures using affordable and widely available metals.

This approach was implemented in Chapter 5, where Mo and W were chosen as alternative metal cores for synthesising M@C:N structures. The influence of metal concentration on structural and electrochemical properties was examined to determine the optimal conditions for a highly efficient ECH electrocatalyst. For Mo-based materials, a highly oxygenated surface suggested a low level of encapsulation, whereas W-based materials exhibited evidence of carbide/nitride phase encapsulation. To address the low solubility of these samples in water, a new ink dispersion recipe was developed for electrode preparation on CC conductive support. Electrochemical results highlighted that a high metal concentration in M@C:N leads to excessive HER activity, which appears to limit their potential application for ECH. Indeed, this affects FE_{ECH} performances since electrocatalysts with lower metal concentrations demonstrate higher efficiency due to reduce HER competition at all tested potentials.

To clarify the role of the metal core in M@C:N and its impact on the ECH performance indicators, a more in depth study was conducted in Chapter 6, where Mo@C:N and W@C:N materials were evaluated alongside a metal-free benchmark electrocatalyst. The catalyst preparation procedure was further implemented introducing a sieving step to minimise surface differences between materials and improve ink dispersion. A structural comparison of the prepared electrocatalysts revealed a significant influence of metal incorporation on pore development and oxidation of graphitised carbon. Both Mo and W centres enhanced HER activity relative to the metal-free material, leading to increased ECH activity at low overpotentials during BZH hydrogenation. Notably, high selectivity toward BA was maintained across all tested potentials, an important finding given that achieving selectivity remains a challenge for most electrocatalysts. Mo@C:N demonstrated high FE at anodic potentials, whereas W@C:N exhibited greater efficiency at cathodic potentials due to reduced competition between HER and ECH pathways. For performance comparison, production rates and TOF values were analysed, showing that W@C:N achieved superior ECH activity at the investigated atomic loading compared to Mo@C:N. A broader evaluation, including Fe@C:N, was conducted primarily based on $TOF_{eff,surface}$ values. Despite its higher metal atomic concentration, Fe@C:N displayed lower ECH activity than W@C:N at equivalent potentials but outperformed Mo@C:N

under high cathodic conditions (> -0.5 V vs RHE). This trend follow the materials HER activity: Mo@C:N > Fe@C:N > W@C:N, confirming the crucial role of the metal core in balancing the ECH/HER competition. Indeed, an excessive high HER activity leads to bubbles formations which can hinder the effective area available for ECH, reducing the efficiency of the hydrogenation process. Notably, the estimated $TOF_{eff,surface}$ values for the W-based material were comparable to those of Rh/C and Pt/C catalysts. Given the four orders of magnitude difference in metal costs, these findings suggest that W@C:N structures offer strong cost competitiveness, while Fe@C:N presents a viable, cost-effective alternative for ECH applications, potentially reducing reliance on precious and critical raw materials for large-scale implementation.

The common theme throughout each chapter of this thesis has been the preparation, optimisation, characterisation, and investigation of novel M@C:N architectures for applications in the electrocatalytic hydrogenation of benzaldehyde. The feasibility of using non-critical metals has been explored as a sustainable approach for developing a new class of electrocatalysts. The findings presented in this thesis, shared to the scientific community through peer-reviewed articles, have significantly advanced the understanding and practicality of these structures as efficient electrocatalysts. These results open the door for the development of improved M@C:N architectures for the hydrogenation of organic compounds, utilising low-cost and abundant metals that have yet to be explored in this configuration and tested for a wider range of organic substrates.

7.2 Future work

This thesis has highlighted several potential areas for future research work in the preparation and study of M@C:N for electrocatalytic hydrogenation applications.

First, as mentioned earlier, the choice of Fe, Mo, and W transition metals has been driven by their low cost and good activity for HER. However, other metals could also be considered viable candidates in this regard. For example, the use of Cu, Co, or Ni as metal cores for preparing M@C:N architectures has shown improved HER performance compared to the corresponding metal electrocatalysts, and so these structures could be tested as well for ECH. Second, the selection of BZH as a diagnostic organic compound was based on its good solubility in water at moderate concentrations and its low toxicity. However, several other potential biomass-derived organics could serve as excellent alternatives for ECH studies using M@C:N electrocatalysts. Examples such as HMF, furfural and acetophenone have garnered significant attention in the literature as diagnostic compounds in studies using precious metal electrocatalysts, and could be then tested as well using M@C:N materials.

In Chapter 3, the use of BP or VUL as carbon nanoscaffolds could be expanded to include carbon nanotubes (CNTs) or carbon nanofibers (CNFs). In fact, these scaffolds have demonstrated promising results in the preparation of Fe@C:N structures and their performance in other cathodic reactions. However, no studies have yet explored their use in the electrocatalytic hydrogenation of organics. It could also be particularly interesting to prepare Fe@C:N at different metal concentrations, similar to the approach used in Chapter 5 for Mo and W, in order to investigate whether the effects on HER performance are reproducible for Fe as well.

In Chapter 4, other carbon supports could be tested to simplify catalyst preparation by eliminating the need for a hydraulic press to ensure adhesion. Good examples in this regard include carbon paper or carbon felt. The latter, with its higher porosity and interwoven structure, may offer benefits for ink stability. Additionally, the identification of optimal operating conditions could be further explored. For example, the use of a buffered pH in electrochemical studies, rather than an acidic one, has been shown to be an effective condition for the ECH of benzaldehyde on precious metal catalysts.

In Chapter 5, the synthesis of Mo and W materials with lower metal concentrations could be explored to determine the minimum required concentration for achieving a significantly efficient ECH catalyst. This could have important implications for reducing production costs at a large scale. Additionally, a narrower range of intermediate potentials, between -0.5 and -0.8 V vs RHE, could be tested to identify the optimal potential for maximising ECH performance.

In Chapter 6, a comparative study on the impact of sieving on ECH performance could be conducted for all tested materials. This would provide insights not only into the ink's stability due to the sieving process but also into its actual effects on catalytic performance. Further studies should be conducted to determine the identity of the active sites in M@C:N. This activity may originate from carbon sites whose reactivity is influenced by sub-surface metals or from the thinning of the carbon shell due to nitrogen-induced defects. This topic remains widely debated in the literature, even for simpler reactions such as HER. A potential approach to address this could involve synthesising identical M@C structures with and without N-functionalization. However, this presents significant challenges, as it would require rethinking the resin preparation and annealing procedures. This could also have a substantial impact on the material's solubility, affecting the preparation of the ink dispersion and, consequently, the stability of the final porous carbon electrocatalyst. Moreover, since the experiments presented this thesis were conducted under natural convection, it would be beneficial to perform tests on prototype electrolyser devices with well-defined convective conditions to fully validate the observed trends and account for mass transport effects. Finally, studying electrolysers as a function of temperature could further optimise their performance.

Appendix I

Supplementary results

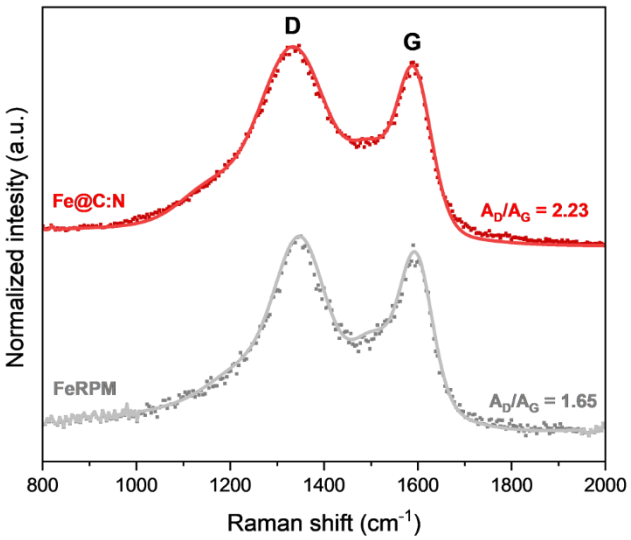

Figure A.1 Raman spectra and best-fits of FeRPM and Fe@BP:N; spectra are shown, normalised by the G-peak height to facilitate comparison.

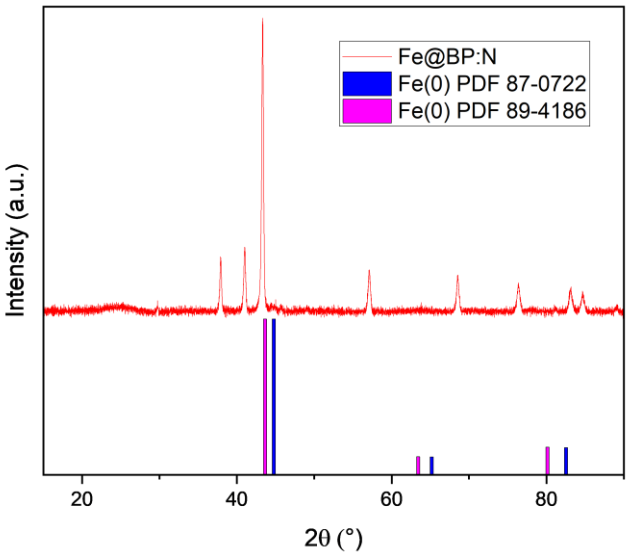

Figure A.2 XRD patterns of Fe@BP:N compared to reference patterns of Fe^0.

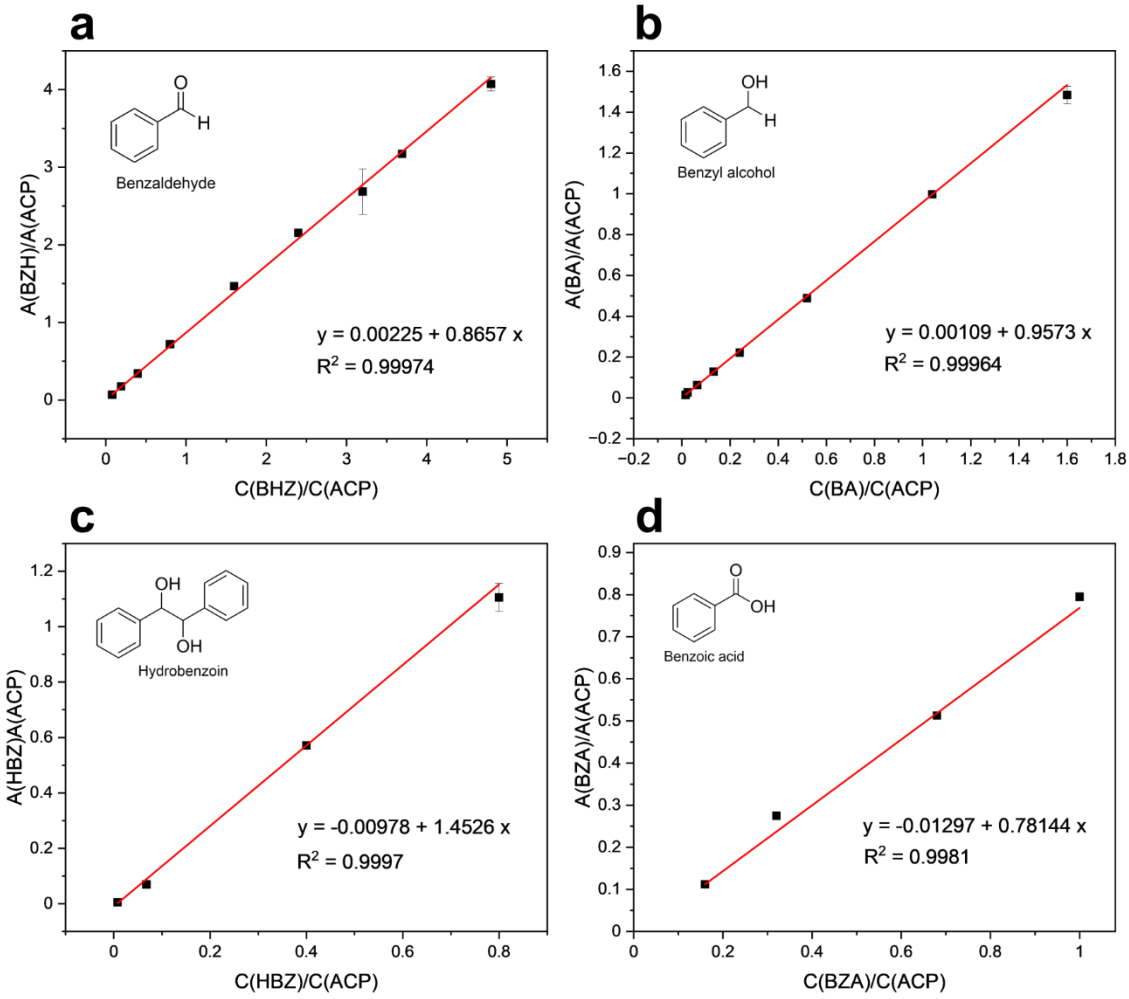

Figure A.3 Calibration curve for (a) benzaldehyde (BZH), (b) benzyl alcohol (BA), (c) hydrobenzoin (HBZ) and (d) benzoic acid (BZA).

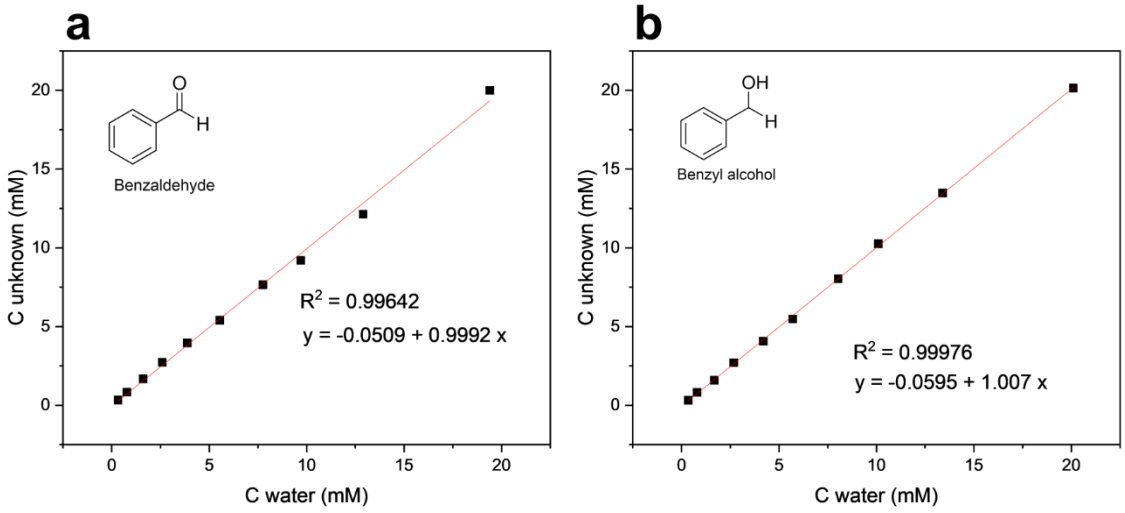

Figure A.4 Extraction efficiency for (a) benzaldehyde and (b) benzyl alcohol.

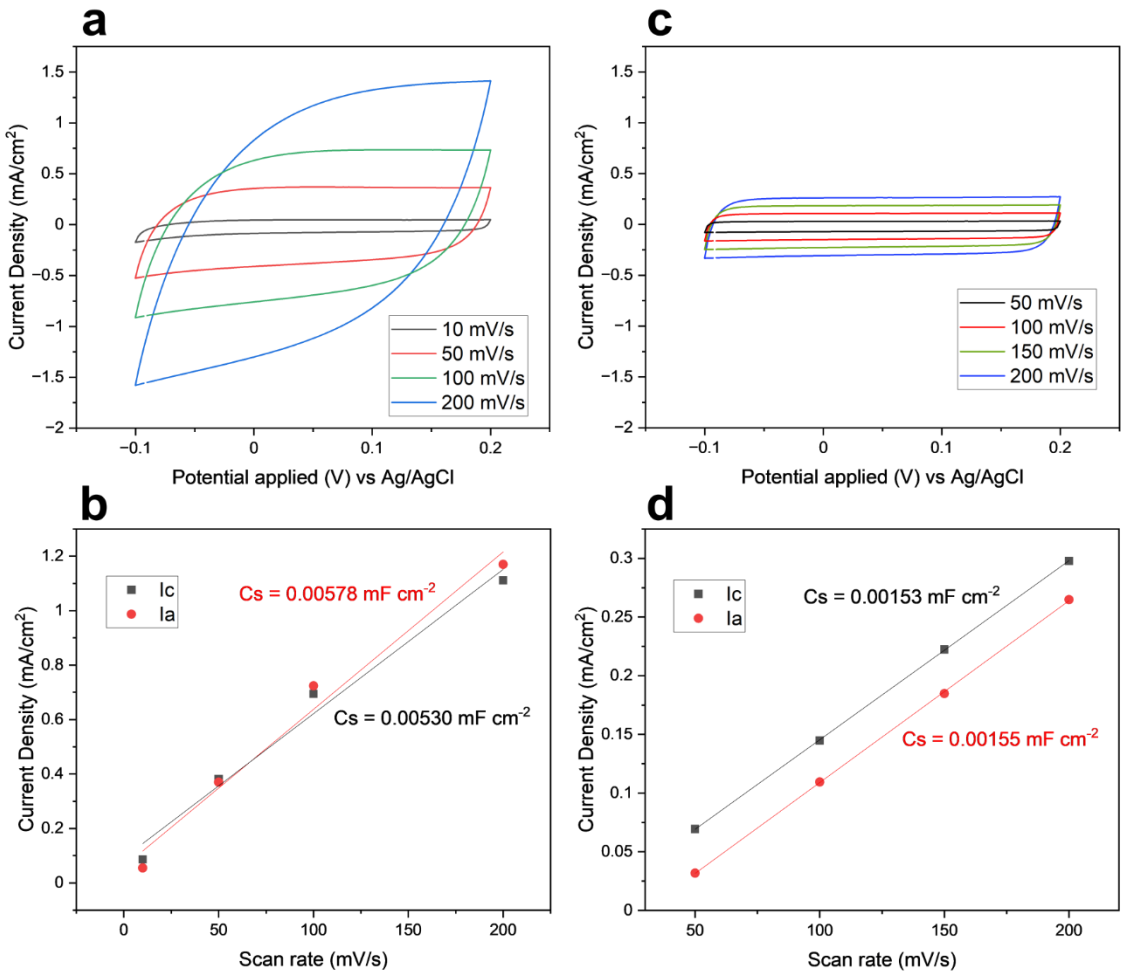

Figure A.5 Non-Faraday CV profiles and current density plotted against the scan rate for (a,b) Fe@C:N and (c, d) Bare CC. Measurements were conducted in 0.1 M Na_2SO_4.

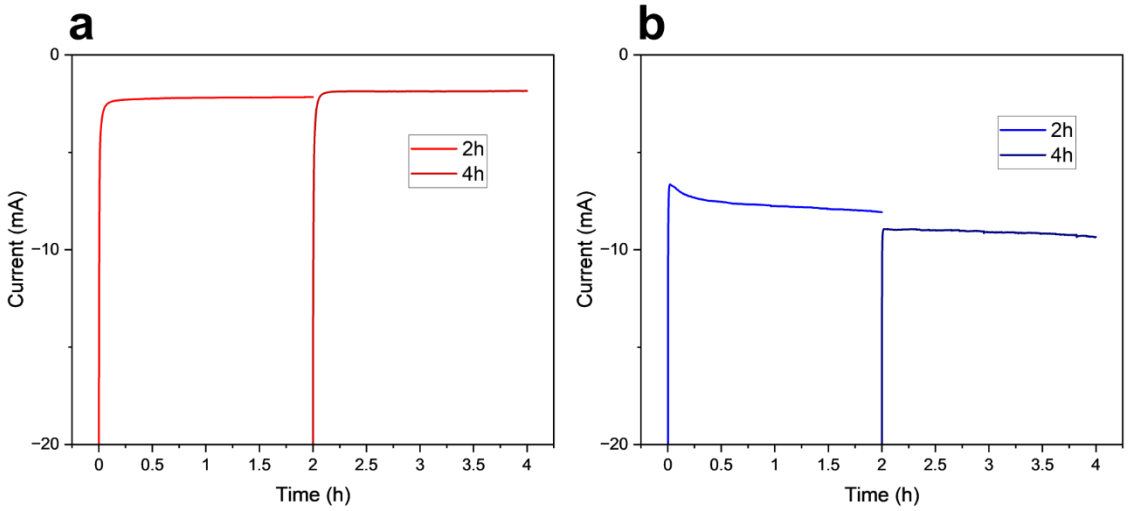

Figure A.6 Stability tests of fabricated electrodes conducted at constant potential for 4 h in (a) H_2SO_4 and (b) Na_2SO_4.

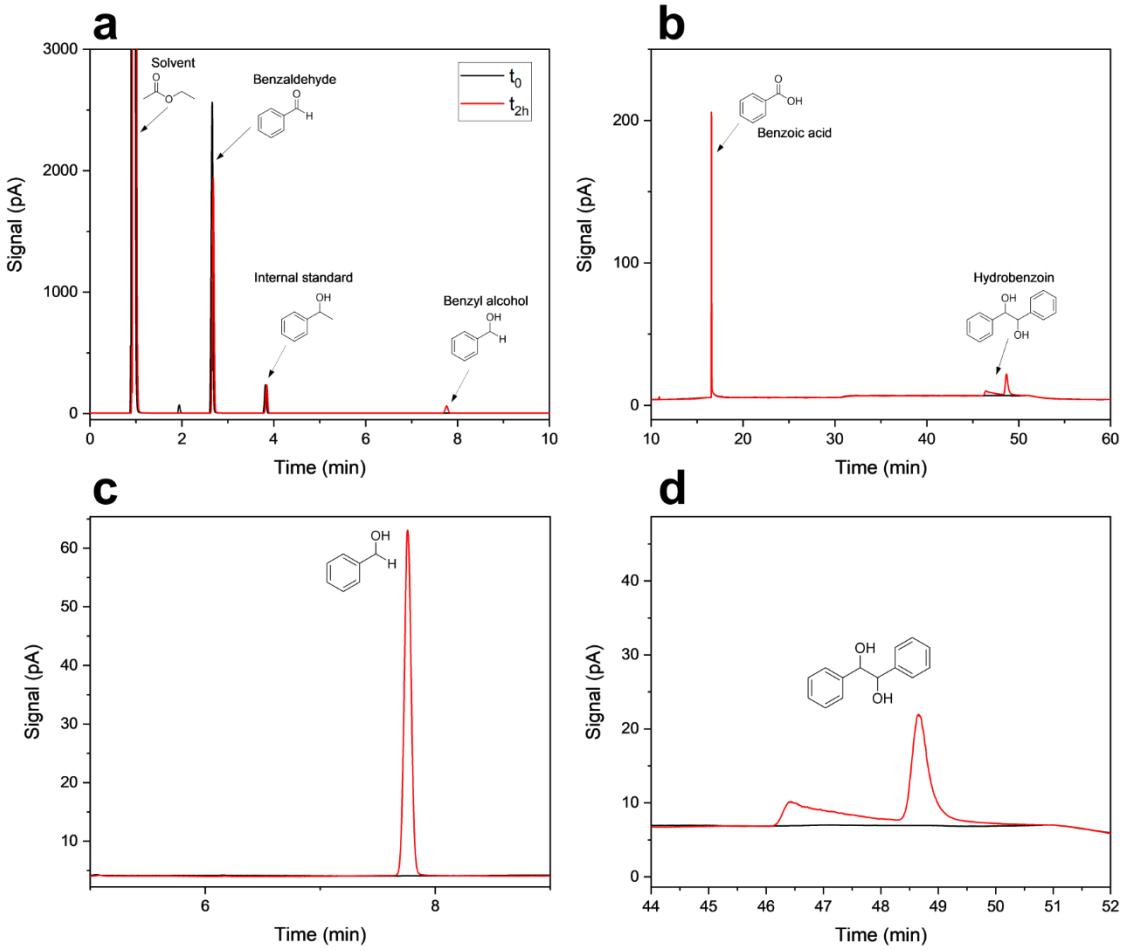

Figure A.7 Gaschromatogram collected after 2 h of electrolysis in 0.1 M H_2SO_4 + 30 mM BZH in the range of (a) 0 to 10 min and (b) 10 to 60 min. Zoom in the region of (c) BA at *ca.* 8 min and (d) HBZ at *ca.* 46 min.

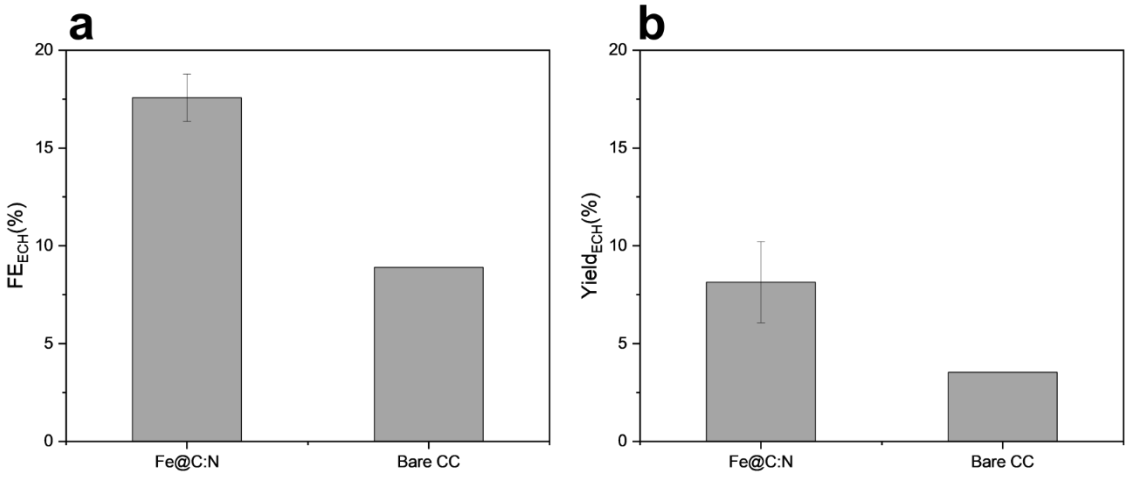

Figure A.8 (a) FE_{ECH} and (b) $Yield_{ECH}$ of Fe@C:N and Bare CC obtained at -0.8 V vs RHE for 2 h in 0.1 M H_2SO_4 with 10 mM BZH.

Table A.1 Coordinates (*z,y,z*) used to describe each boundary and domain in the finite element simulation as detailed in Fig. S14, and correspoding mass transport conditions. c_i refers to the concentration of i species.

Boundary Description		**Coordinates**	**Boundary condition**
Cell Domain	Top cap	$x^2 + y^2 \leq {r_{cell}}^2$ for $z = h_{cell}$	J = 0 (No flux)
	Bottom cap	$x^2 + y^2 \leq {r_{cell}}^2$ for $z = 0$	
	Cell wall	$x^2 + y^2 = {r_{cell}}^2$ for $0 \leq z \leq h_{cell}$	
Channel Domain	Cap	$z^2 + x^2 \leq {r_{channel}}^2$ for $y = r_{cell} + h_{channel} - \frac{h_{channel}}{7}$	J = 0 (No flux)
	Channel walls	$z^2 + x^2 = {r_{channel}}^2$ for $r_{cell} - \frac{h_{channel}}{7} \leq y \leq r_{cell} + h_{channel} - \frac{h_{channel}}{7}$	
Electrode Domain	Front Electrode Surface	$-\frac{1}{2}L_{electrode} \leq x \leq +\frac{1}{2}L_{electrode}$ $\frac{1}{2}h_{cell} - \frac{1}{2}L_{electrode} \leq z \leq \frac{1}{2}h_{cell} + \frac{1}{2}L_{electrode}$ $y = \frac{1}{2}d_{electrode}$	c_{BZH} = 0
	Back inert surface	$-\frac{1}{2}L_{electrode} \leq x \leq +\frac{1}{2}L_{electrode}$ $\frac{1}{2}h_{cell} - \frac{1}{2}L_{electrode} \leq z \leq \frac{1}{2}h_{cell} + \frac{1}{2}L_{electrode}$ $y = -\frac{1}{2}d_{electrode}$	J = 0 (No flux)
	Other inert electrode surface	The electrode has a thickness of $d_{electrode}$. There are 4 rectangular surfaces of size $d_{electrode}$ x $L_{electrode}$ that enclose the Front and back surface of the electrode.	J = 0 (No flux)

Table A.2 Summary of parameters used for finite element analysis.

Variable	Value	Units	Description
r_{cell}	16.5	mm	Radius of the cell domain.
h_{cell}	33	mm	Height of the cell domain.
$r_{channel}$	8.3	mm	Radius of the channel domain.
$h_{channel}$	23	mm	Height of the channel domain.
$L_{electrode}$	10	mm	Lateral length of the square electrode domain.
$d_{electrode}$	0.5	mm	Thickness of the electrode domain.
D_{BZH}	$8.6 \cdot 10^{-6}$	$cm^2\ s^{-1}$	Diffusion coefficient of Benzaldehyde[2]
$c0_{BZH}$	30	mM	Initial concentration of Benzaldehyde in the electrolyte solution domain. The electrode solution domain is contained within the cell and channel domain.

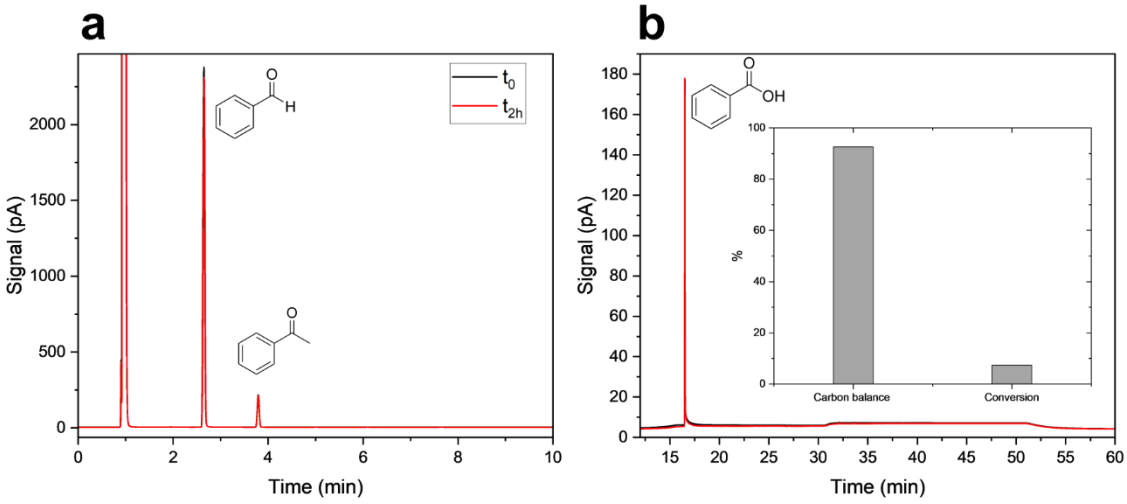

Figure A.9 Overlay of t_0 and t_{2h} gas chromatograms collected in an open circuit control experiment from (a) 0 to 10 min and (b) 12 to 60 min. Conversion and carbon balance for the same experiment are displayed in the inset of (b).

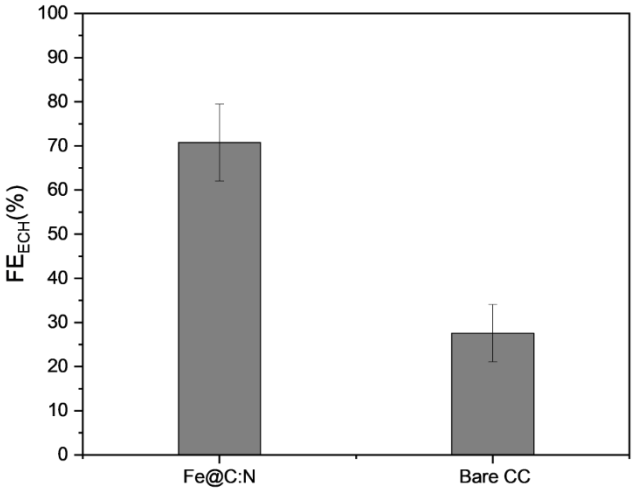

Figure A.10 FE_{ECH} of Fe@C:N and bare CC obtained at -0.5 V vs RHE for 2 h in 0.1 M H_2SO_4 with 30 mM BZH.

Table A.3 Summary reaction data for electrocatalytic hydrogenation (ECH) and hydrogen evolution reaction (HER), considering the single contribution of BA and HBZ.

E (V vs RHE)	$mol_{electrons}$ (µmol)	FE_{BA} (%)	FE_{HBZ} (%)	Prod $Rate_{BA}$ (µmol g_{Fe}^{-1} s^{-1})	Prod $Rate_{HBZ}$ (µmol g_{Fe}^{-1} s^{-1})	$^{\Delta}TOF_{BA}$ (h^{-1})	$^{\Delta}TOF_{HBZ}$ (h^{-1})
-0.26	102 ± 29	22 ± 2	5 ± 3	13 ± 3	5 ± 3	2.5 ± 0.7	1.0 ± 0.6
-0.50	214 ± 35	62 ± 7	9 ± 2	76 ± 7	21 ± 4	15 ± 1	4.2 ± 0.8
-0.80	206 ± 8	25 ± 5	45 ± 2	29 ± 4	97 ± 13	5.7 ± 0.7	20 ± 3
-1.00	490 ± 59	11 ± 2	15 ± 6	30 ± 5	78 ± 26	6 ± 1	16 ± 5

Δ = Effective turn over frequency normalised by bulk metal content for BA and for HBZ

Appendix I

Summary of equations used to calculate performance indicators

Carbon balance and Conversion

$$\textbf{Carbon balance}\ (\%) = \frac{mol_{t=2h}(BZH) + mol_{t=2h}(BA) + 2mol_{t=2h}(HBZ)}{mol_{t_0}(BZH)} \cdot 100 \quad \text{(Eq.A1)}$$

$$\textbf{Coversion}\ (\%) = \frac{mol_{t_0}(BZH) - mol_{t_{2h}}(BZH)}{mol_{t_0}(BZH)} \cdot 100 \quad \text{(Eq.A2)}$$

Yield

$$\textbf{Yield}_{\textbf{BA}}\ (\%) = \frac{mol_{t=2h}(BA)}{mol_{t_0}(BZH)} \cdot 100 \quad \text{(Eq.A3)}$$

$$\textbf{Yield}_{\textbf{HBZ}}\ (\%) = \frac{2mol_{t=2h}(HBZ)}{mol_{t_0}(BZH)} \cdot 100 \quad \text{(Eq.A4)}$$

$$\textbf{Yield}_{\textbf{ECH}}\ (\%) = Yield_{BA} + Yield_{HBZ} \quad \text{(Eq.A5)}$$

Faradaic efficiency

$$\textbf{FE}_{\textbf{BA}}(\%) = \frac{2\,mol_{t=2h}(BA)}{mol_e} \cdot 100 \quad \text{(Eq.A6)}$$

$$\textbf{FE}_{\textbf{HBZ}}(\%) = \frac{2\,mol_{t=2h}(HBZ)}{mol_e} \cdot 100 \quad \text{(Eq.A7)}$$

$$\textbf{FE}_{\textbf{ECH}}(\%) = FE_{BA} + FE_{HBZ} \quad \text{(Eq.A8)}$$

Product Rate (normalised by geometric area)

$$\textbf{Prod Rate}_{\textbf{BA,geo}}\left(\mu mol\ cm_{geo}^{-2}\ h^{-1}\right) = \frac{mol_{BA}}{A_{geo} \cdot t} \quad \text{(Eq.A9)}$$

$$\textbf{Prod Rate}_{\textbf{HBZ,geo}}\left(\mu mol\ cm_{geo}^{-2}\ h^{-1}\right) = \frac{2mol_{HBZ}}{A_{geo} \cdot t} \quad \text{(Eq.A10)}$$

$$\textbf{Prod Rate}_{\textbf{geo}}\left(\mu mol\ cm_{geo}^{-2}\ h^{-1}\right) = Product\ Rate_{BA,geo} + Product\ Rate_{HBZ,geo} \quad \text{(Eq.A11)}$$

$A_{geo} \equiv geometric\ area = 1\ cm^2, t = 2\ h$

Product Rate (normalised by capacitance)

$$\boldsymbol{Prod\ Rate_{BA,Cap}}(\mu mol\ mF^{-1}\ h^{-1}) = \frac{Prod\ Rate_{BA,geo}}{C_{dl}} \quad \text{(Eq.A12)}$$

$$\boldsymbol{Prod\ Rate_{HBZ,Cap}}(\mu mol\ mF^{-1}\ h^{-1}) = \frac{Prod\ Rate_{HBZ,geo}}{C_{dl}} \quad \text{(Eq.A13)}$$

$$\boldsymbol{Prod\ Rate_{Cap}}(\mu mol\ mF^{-1}\ h^{-1}) = Prod\ Rate_{BA,Cap} + Prod\ Rate_{HBZ,Cap} \quad \text{(Eq.A14)}$$

Product Rate (normalised by bulk metal mass)

$$\boldsymbol{Prod\ Rate_{BA,g_M}}(\mu mol\ g_M^{-1}\ s^{-1}) = \frac{mol_{BA}}{M\ \cdot t} \quad \text{(Eq.A15)}$$

$$\boldsymbol{Prod\ Rate_{HBZ,g_M}}(\mu mol\ g_M^{-1}\ s^{-1}) = \frac{2mol_{HBZ}}{M\ \cdot t} \quad \text{(Eq.A16)}$$

$$\boldsymbol{Prod\ Rate_{g_M}}(\mu mol\ g_M^{-1}\ s^{-1}) = Prod\ Rate_{BA,g_M} + Prod\ Rate_{HBZ,g_M} \quad \text{(Eq.A17)}$$

$$\boldsymbol{M}(g) = M_{wt\,\%}\ A_{geom}\ InkLoad \quad \text{(Eq.A18)}$$

$t = 2\ h.$

Bulk effective turnover frequency

$$\boldsymbol{TOF_{eff,bulk}}(\ h^{-1}) = Prod\ Rate_{gM} \times MW_M \quad \text{(Eq.A19)}$$

Surface effective turnover frequency

$$\boldsymbol{Prod\ Rate_{ECSA}}(\mu mol\ cm_{ECSA}^{-2}\ h^{-1}) = \frac{Prod\ Rate_{geo} C_s}{C_{dl}} \quad \text{(Eq.A20)}$$

$$\boldsymbol{M_{at\%\ XPS}} = \frac{100\ \frac{M}{C} at\%}{100 + \frac{M}{C} at\% + \frac{N}{C} at\% + \frac{O}{C} at\%} \quad \text{(Eq.A21)}$$

$$\boldsymbol{TOF_{eff,surface}}(\ h^{-1}) = \frac{Prod\ Rate_{ECSA}}{\frac{M_{at\%\ XPS}}{100}\Gamma_C} \quad \text{Eq.A22)}$$

$C_s = 0.02$ mF cm^{-2} is the specific double layer capacitance.

$\Gamma_C = 6.14 \times 10^{-3}$ µmol cm^{-2} is the molar density of carbon atoms in graphite.

Appendix II

Published work and conferences

Appendix II

Conference contributions

Oral Contributions

- ***Pota, F.***; Schröder, C.; Costa de Oliveira, M. A.; Nolan, H.; Iannacci, A; Domínguez, C.; Colavita, P. E. *Metal@Carbon porous electrode materials for electrocatalytic applications in biomass valorisation*. Fall meeting 2023 of Europian Material Research Society. 18-21 September 2023, Warsaw.
- ***Pota, F.***; Schröder, C.; Costa de Oliveira, M. A.; Cabré, M. B.; Nolan, H.; Behan, J. A.; Barrière, F. *Heteroatom doped carbon-based materials as non-precious metal catalysts for electrocatalytic hydrogenation of biomass-derived organics.* 9th Europian Chemical Society Chemistry Congress 2024. 7-11 July 2024, Dublin.
- ***Pota, F.***; Costa de Oliveira, M. A.; Schröder, C.; Brunet Cabré, M.; Nolan, H.; Behan, J. A.; Barrière, F.; Colavita, P. E. *Carbon-encapsulated metal N-doped porous materials: A promising architecture for electrocatalytic hydrogenation of biomass derivative organics. 75th* Irish Universities Chemistry Research Colloquium. 17-18 June 2024, Dublin.
- ***Pota, F.***; Costa de Oliveira, M. A.; Schröder, C.; Brunet Cabré, M.; Behan, J. A.; Barrière, F.; Colavita, P. E. *Hydrogenation of biomass-derived organics: a study of metal@carbon porous materials as electrocatalysts.* 34nd International Conference on Diamond and Carbon Materials 2024. 1-5 September 2024, Dresden.

Poster Contributions

- ***Pota, F.***; Schröder, C.; Ingle S.; Nolan, H.; Colavita, P. E. *Synthesis and studies of carbon-based porous nanocomposite electrode materials as electrocatalysts for organic transformations*. 32nd International Conference on Diamond and Carbon Materials 2022. 4-8 September 2022, Lisbon.
- ***Pota, F.***; Schröder, C.; Costa de Oliveira, M. A.; Nolan, H.; Colavita, P. E. *Carbon-based nanocomposite porous materials as electrocatalysts for valorisation of biomass.* Spring meeting 2023 of Europian Material Research Society. May 29th to June 2nd, 2023, Strasbourg.
- ***Pota, F.***; Schröder, C.; Costa de Oliveira, M. A.; Nolan, H.; Colavita, P. E. *Design and synthesis of carbon-based electrode materials for electrocatalytic reduction of biomass-derived organics*. 16th International Conference on Materials Chemistry 2023. 3-6 July 2023, Dublin.
- ***Pota, F.***; Schröder, C.; Costa de Oliveira, M. A.; The influence of sieving metal@carbon N-doped powder materials on electrocatalytic hydrogenation performances. 9th Europian Chemical Society Chemistry Congress 2024. 7-11 July 2024, Dublin.

Awards

- ***Young Researcher Award*** – Issued by the European Materials Research Society in September 2023 during its annual Spring Meeting in recognition of the oral contribution entitled: *Metal@Carbon porous electrode materials for electrocatalytic applications in biomass valorisation.*. Symposium L: *Frontiers in Carbon Science and Technology.*
- ***Best talk and presentation*** **–** Issued by Dublin Chemistry in May 2024 during its annual meeting in recognition of the oral contribution entitled: *Porous N-doped carbon-encapsulated metals as a novel catalyst architecture for the electrocatalytic hydrogenation of organics.*

Published works

During the course of this PhD research project, a number of peer-reviewed articles have been published on the work presented in this thesis, together with other co-authored works. They are listed here for reference. Original copies of first-author publications are included at the end of the thesis.

- ***Pota, F.***; Costa de Oliveira, M. A.; Schröder, C.; Rafferty, A.; De Castro C.; Rault L.; Behan, J. A.; Barrière, F.; Colavita, P. E. Electrocatalytic hydrogenation of unsaturated organics using Mo and W porous carbon-encapsulated nanostructures: impact of metal type on properties and performances. *Journal of Materials Chemistry A,* **2025**, Advance Article

- ***Pota, F.***; Costa de Oliveira, M. A.; Schröder, C.; Brunet Cabré, M.; Nolan, H.; Rafferty, A.; Jeannin, O.; Camerel, F.; Behan, J. A.; Barrière, F.; Colavita, P. E. Porous N-Doped Carbon-encapsulated Iron as Novel Catalyst Architecture for the Electrocatalytic Hydrogenation of Benzaldehyde. *ChemSusChem* **2025**, *18* (1), e202400546.

- Nolan, H.; Zen, F.; Gençer, A.; Henderson, L.; Kelly, M.; ***Pota, F.***; Schröder, C.; Scanlan, E. M.; Colavita, P. E. Functional organic adlayers for controlling the adhesion strength of electrolessly deposited copper on super-engineering plastics. *Applied Surface Science* **2025**, *682*, 161700.

- Cabré, M. B.; Schröder, C.; ***Pota, F.***; de Oliveira, M. A. C.; Nolan, H.; Henderson, L.; Brazel, L.; Spurling, D.; Nicolosi, V.; Martinuz, P.; et al. Carbon Thin-Film Electrodes as High-Performing Substrates for Correlative Single Entity Electrochemistry. *Small Methods* **2025**, *9* (1), 2400639.

- Costa de Oliveira, M. A.; Brunet Cabré, M.; Schröder, C.; Nolan, H.; ***Pota, F.***; Behan, J. A.; Barrière, F.; McKelvey, K.; Colavita, P. E. Single-Entity Electrochemistry of N-Doped Graphene Oxide Nanostructures for Improved Kinetics of Vanadyl Oxidation. *Small* **2025**, *21* (3), 2405220.

- Nolan, H.; Schröder, C.; Brunet-Cabré, M.; ***Pota, F.***; McEvoy, N.; McKelvey, K.; Perova, T. S.; Colavita, P. E. MoS2/carbon heterostructured catalysts for the hydrogen evolution reaction: N-doping modulation of substrate effects in acid and alkaline electrolytes. *Carbon* **2023**, *202*, 70-80.

ChemSusChem

Research Article
doi.org/10.1002/cssc.202400546

Chemistry Europe
European Chemical Societies Publishing

www.chemsuschem.org

Porous N-Doped Carbon-encapsulated Iron as Novel Catalyst Architecture for the Electrocatalytic Hydrogenation of Benzaldehyde

Filippo Pota,[a] Maida A. Costa de Oliveira,[a] Christian Schröder,[a] Marc Brunet Cabré,[a] Hugo Nolan,[a] Aran Rafferty,[a] Olivier Jeannin,[b] Franck Camerel,[b] James A. Behan,[b] Frédéric Barrière,[b] and Paula E. Colavita*[a]

Carbon porous materials containing nitrogen functionalities and encapsulated iron-based active sites have been suggested as electrocatalysts for energy conversion, however their applications to the hydrogenation of organic substrates via electrocatalytic hydrogenation (ECH) remain unexplored. Herein, we report on a Fe@C:N material synthesized with an adapted annealing procedure and tested as electrocatalyst for the hydrogenation of benzaldehyde. Using different concentrations of the organic, and electrolysis coupled to gas chromatography experiments, we demonstrate that it is possible to use such architectures for the ECH of unsaturated organics. Potential control experiments show that ECH faradaic efficiencies >70% are possible in acid electrolytes, while maintaining selectivity for the alcohol over the pinacol dimerization product. Estimates of product formation rates and turnover frequency (TOF) values suggest that these carbon-encapsulated architectures can achieve competitive performance in acid electrolytes relative to both base and precious metal electrodes.

1. Introduction

Among various explored strategies to address the increasing demand for sustainable energy, the valorization of biomass and waste feedstocks emerges as a significant alternative to produce fuels, chemicals and for reducing carbon dioxide emissions.[1,2] Biomass valorization is highlighted as a valuable approach to mitigate global warming, and its derivatives are seen as promising renewable and abundant hydrocarbon resources with potential for different applications.[3] The main strategies to convert biomass feedstocks to high-value products are based on hydrogenation processes. Thermal catalytic hydrogenation (TCH) can be an effective method however it requires high temperature, high pressure and high purity H_2 conditions, and usually the use of precious metal catalysts.[4] An alternative approach is electrocatalytic hydrogenation (ECH), an electrochemical method that can bypass the problem of activating H_2, thanks to in situ generation of adsorbed hydrogen (H_{ads}) via electroreduction of protons/water.[5] ECH can be further driven by renewable electricity, thus making it potentially an attractive alternative route to conventional TCH.[6,7]

To realize the potential advantages of ECH, electrocatalysts with good performance in terms of faradaic efficiency (FE), yield and selectivity are needed. FE is typically limited by competition with the hydrogen evolution reaction (HER),[8,9] as shown in Figure 1a. The main difference between the HER and ECH is how the H_{ads} is used: Tafel and Heyrovsky steps consume electrons and H_{ads} species and may drastically suppress the FE of organic hydrogenations.[10] Therefore, electrocatalysts must be materials capable of facilitating the Volmer step but that also inhibit the H_2 evolution pathways.

Several electrocatalyst materials have been proposed as good candidates for the hydrogenation of organic substrates.[11,12] Precious metals like Pd, Pt, Au[13–15] and carbon-supported Pt-group metals (M/C) such as Pt/C, Pd/C, and Ru/C[16–18] have been reported as good electrocatalysts for the hydrogenation of aldehydes and phenols. Despite these encouraging results, the use of precious and/or critical metals is not desirable at scale, particularly when using biomass derived feeds that often vary in composition and purity. For this reason, there is interest in developing abundant and low-cost electrocatalysts as a suitable replacement. Ni and Cu have been reported as base metals that can either operate as the active phase or that can be alloyed to modulate the activity of precious metals.[19,20] Iron-based catalysts on the other hand have received less attention, despite this being a highly abundant and sustainable metal that has a relatively uniform geographic distribution and therefore a low criticality index.[21,22] HMF and glucose hydrogenations were studied by Kwon et al.[23–25] at Fe electrodes; crotonaldehyde and hydroxyacetone hydrogenations were reported on Fe catalysts;[26,27] while Fe supported on graphite was used in the hydrogenation of acetophenone.[28] Furfural was hydrogenated on Fe electrodes with high selectivity in acid electrolyte towards the pinacol

[a] School of Chemistry, Trinity College Dublin, College Green, Dublin 2 Ireland
[b] Univ Rennes, CNRS, Institut des Sciences Chimiques de Rennes – UMR 6226, Rennes, France

Correspondence: Paula E. Colavita, School of Chemistry, Trinity College Dublin, College Green, Dublin 2 Ireland.
Email: colavitp@tcd.ie

Supporting Information for this article is available on the WWW under https://doi.org/10.1002/cssc.202400546

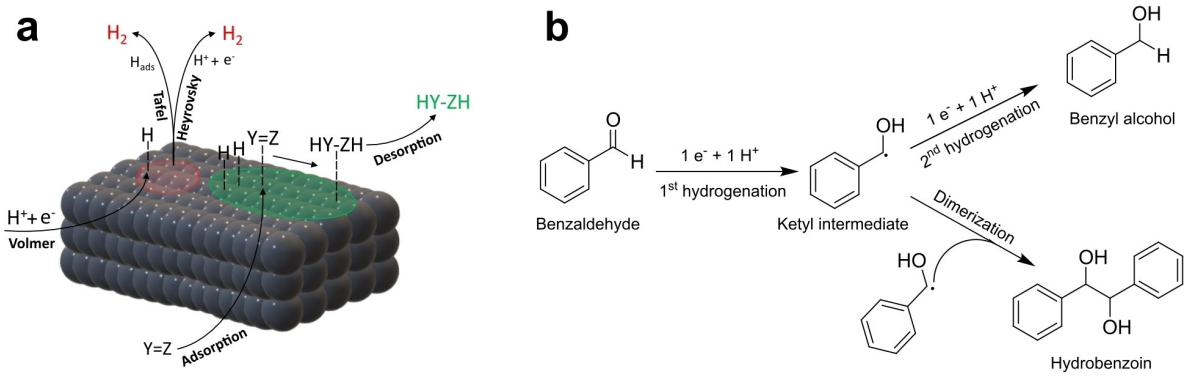

Figure 1. (a) Schematic representation of mechanisms for HER (highlight in red) and ECH (highlight in green). Y=Z is the target organic molecule. (b) Proposed mechanism for benzaldehyde hydrogenation.[14]

dimerization product;[29] however ECH experiments with Fe cathode reported methylfuran as the preferred product.[30] Most recently, an iron-molybdenum phosphide heterostructured electrode was demonstrated for the electrocatalytic reduction of nitro groups.[31]

In this work we discuss the synthesis and study of N-doped Fe-carbon heterostructured materials for electrocatalyst applications in the ECH, where the Fe serves as a metal core and the N-doped carbon matrix as a porous conductive phase in which the Fe sites are embedded (Fe@C:N). Applications of Fe@C:N heterostructures remain largely unexplored in the ECH, despite their use for the electrocatalysis of other reactions,[32] including the ORR[33] and the HER.[34] Electrocatalytic activity was studied via voltammetry and electrolysis experiments aqueous electrolyte using benzaldehyde (BZH) as a diagnostic substrate.[35] Benzaldehyde, due to its good solubility in water[36] and its moderate reactivity,[35] stands out among various potential organic derivatives of biomass as a relevant candidate for studying the reactivity of new electrocatalyst materials for ECH. Importantly, BZH and substituted BZH are commonly found in the pyrolysis of lignin[37–41] and are important representatives of biomass-derived aromatic aldehydes.[19] This justifies the recent interest in BZH, which has become the subject of intense investigation in several studies with encouraging results.[42–44] The ECH of benzaldehyde has been previously investigated using Pt-group electrocatalysts and is reported to result in formation of benzyl alcohol and/or in dimerization to hydrobenzoin, as in Figure 1b.[14] Both of these products are of interest: benzyl alcohol is the most important aromatic alcohol from a commercial perspective and a high value commodity with applications in e.g. coatings, plastics, cosmetics and food;[45,46] while hydrobenzoin is a high-value compound with applications in the pharmaceutical industry.[19,47] Achieving ECH with high faradaic efficiency and good selectivity towards one of these two products using Fe@C:N heterostructures is therefore of interest both from a mechanistic and an application perspective. Our results show that this is indeed possible with such electrocatalyst architectures thanks to potential control. A comparison of turnover frequency (TOF) estimates obtained from our results suggest that these materials could be a competitive alternative for the ECH of bio-derived organics.

2. Experimental Section

2.1. Materials

Iron (II) acetate (95%), Nafion® 117 solution (5%), resorcinol (99%), Pluronic F-127, melamine (99%), hydrochloric acid (37%), sulfuric acid (95–98%), nitric acid (≥65%), formaldehyde solution (37 wt%), hydrogen peroxide (30%), sodium sulphate (>99%); benzaldehyde (BZH, >99%); hydrobenzoin (HBZ, 99%); acetophenone (ACP, >99%); ethyl acetate (>99%) were all purchased from Sigma Aldrich and used as received. Ethanol (>99%), benzyl alcohol (BA, >99%) were purchased from Fisher and used as received. Black Pearls 2000® (BP, *ca.* 1400 m^2/g)[48] were purchased from Cabot.

2.2. Catalyst Synthesis

BP was first pre-treated via oxidative purification to eliminate metal impurities and enhance hydrophilicity.[49,50] The material was subjected to a 4 h reflux in concentrated HNO_3 at 90 °C, followed by filtration and washing with distilled water until a neutral pH was achieved. The resulting carbon paste was then dried for two days at 50 °C and subsequently ground in an agate mortar prior to further use.[33,51] Porous carbon-based catalysts were prepared as follows: resorcinol (1.65 g), Pluronic F-127 (2.5 g), and melamine (0.84 g) were first dissolved in a 40 mL solution of water:ethanol (1:1 by vol.) and stirred for 15 min. $Fe(CH_3COO)_2$ (1.5 g) was added to this mixture as a metal precursor, then concentrated HCl (0.2 g), followed by stirring for 1 h. Formaldehyde solution (2.5 g) was added dropwise under stirring, and the mixture was stirred vigorously for another hour, yielding a homogeneous slurry. Purified BP (1.5 g) was added to this dispersion and stirred for an additional 15 min. The mixture was heated in an oven at 50 °C for 2 days in a Teflon-lined autoclave. Samples were dried for two days at 50 °C, ground in a mortar and further dried in a tube furnace (250 °C) under N_2 flow. Finally, the product was annealed (800 °C, 2 h) in a N_2:NH_3 flow (1:1 vol., 200 sccm) followed by cooling under N_2, as show in Figure S1.

2.3. Materials Characterization

Brunauer–Emmett–Teller (BET)[52] specific surface area was determined from nitrogen adsorption at 77 K with a Nova 4200e Surface Area Analyzer (Quantachrome, UK), with the specific surface area calculated from data at relative pressures between 0.10 and 0.30. Pore size distributions were calculated using the Barrett–Joyner–Halenda (BJH) method[53] from the desorption branch of the isotherm. Prior to analysis, the sample was outgassed at 250 °C under vacuum for 2 h. Small angle X-ray scattering (SAXS) was carried out using a custom-built setup with a Cu microfocused generator (GeniX-3D VHF-L, Xenocs) at 50 W, two slit (JJ X-ray) collimation and an image plate detector (Mar345, MarResearch). Thermogravimetric analysis (TGA) was carried out using a Pyris 1 Thermogravimetric Analyzer (PerkinElmer) with a hold time of 10 min at 150 °C, followed by a 10 °C/min ramp in air to 900 °C. Fourier transform infrared spectroscopy (FTIR) was carried out on a FTIR Spectrum 100 spectrometer (PerkinElmer) using an attenuated total internal reflectance (ATR) diamond crystal; 4 scans between the ranges of 4000 cm^{-1} and 400 cm^{-1} were collected for each sample and ratioed against background spectra obtained in air. Powder X-ray diffraction (XRD) was carried out to investigate the crystalline structures before and after annealing using a D2 Phaser diffractometer with LynxEye detector (Bruker) and a Cu Kα source. Scanning electron microscopy (SEM) was performed using a Zeiss Ultra microscope at 5 kV accelerating voltage, and InLens detector. Transmission electron microscopy (TEM) was performed using a Jeol JEM 2100HR with an acceleration voltage of 200 kV, EDS SDD Oxford X–Max 80T detector and Jeol HAADF detector. Inductively coupled plasma-optical emission spectroscopy was performed in a iCAP 7000 ICP-OES Analyser (Thermo Fisher); samples were treated in HNO_3 (≥ 65 %) overnight and diluted in Millipore water to a nominal concentration of 10 mg/L. Raman spectroscopy was carried out using a Witec alpha 300R confocal scanning Raman system using 532 nm excitation; peak areas were analyzed using commercial software (CasaXPS). X-ray photoelectron spectroscopy (XPS) was carried out in a monochromated Omicron XM1000MK II X-ray photoemission spectrometer, with an EA 125 analyzer and an Al Kα (1486.7 eV) source; pass energies of 50 and 15 eV were used for survey and high-resolution spectra, respectively. Spectra were analyzed using CasaXPS; best fits were carried out on spectra after Shirley background correction using mixed Gaussian-Lorentzian functions. Elemental compositions were obtained from peak areas of the high-resolution scans. Product analysis was carried out using an Agilent 8860 Gas Chromatograph coupled to a flame ionization detector (GC-FID), H_2 as carrier gas, split injection (1:10, 2 mL/min flow) and a DB-WAX UI column (30 m×0.250 mm×0.50 μm, Agilent J&W).

2.4. Electrochemical Characterization

Catalyst (0.0100 g ± 0.0003) was used for the preparation of an ink dispersion, adding 135 μL of Millipore water, 270 μL of isopropyl alcohol (IPA) and 50 μL of Nafion solution. The ink was sonicated at room temperature prior to drop casting on carbon working electrodes. Glassy carbon disks (GC, Ø 5 mm, HTW GmbH) were used as working electrodes for cyclic voltammetry experiments. GC disks were polished with decreasing grades of alumina slurry (Ted Pella) according to published procedures;[54,55] disks were thoroughly sonicated and rinsed between polishing steps to remove any residue from the preceding step. GC disks were mounted in a Teflon disc holder (Pine instruments) and modified with the ink dispersion (10 μL), then dried under inert gas, resulting in a loading of 1.10 mg cm^{-2}. A Pt disk electrode (Ø 3 mm, eDAQ) was used for comparison; prior to experiments using Pt as electrode, the disk was polished and then cleaned by cycling into the anodic region until the characteristic response of polycrystalline Pt was obtained.[56–58] Flags of carbon cloth (CC, 1 cm^2 geometric area, FuelCellStore) with microporous layer were used as working electrodes for electrolysis experiments. The CC was used as received after covering the back side with insulating polyimide tape. 50 μL of the ink were drop cast in two equal aliquots, drying the ink after each step in a hot plate (80 °C) followed by compression of the CC in a hydraulic press (Specac) at room temperature; this resulted in loadings of 1.09 mg cm^{-2} for all experiments.

Cyclic voltammetry experiments (CV) were carried out using a standard 3-electrode cell controlled by a potentiostat (Metrohm Autolab), using graphite rods (Morgan Advanced Materials) as counter electrodes (CE) and Ag/AgCl (1 M KCl) as reference electrode (RE, 0.235 V vs SHE). All potentials are reported vs the relative hydrogen electrode (RHE) based on the experimentally determined pH of the electrolyte. The cell was cleaned with piranha and Millipore water prior to each experiment, then filled with 250 mL volume of supporting electrolyte (0.100 M H_2SO_4); the electrolyte was purged with N_2 for at least 15 min prior to characterization. Estimates of electrochemically active surface area (ECSA) were obtained from capacitive CV curves in Na_2SO_4 0.100 M over a no-Faradaic potential window; the double layer capacitance was normalized by an average value of 40 μF cm^{-2} to yield estimates of ECSA.[56,59] Electrolysis was performed in an H-cell, with compartments separated by an ion-conducting membrane (FKE-50 Fumasep) to minimize cross contamination (Figure S2). WE and RE were inserted in 34 mL of catholyte (BZH in 0.1 M H_2SO_4), and the CE was inserted in 34 mL of anolyte (0.1 M H_2SO_4). Before starting the electrolysis both compartments were purged with N_2 for at least 15 min; 2 mL of catholyte were aliquoted for quantitative analysis at $t_0 = 0$ s. CVs at 100 mV/s and 10 mV/s were first collected to condition the electrode surface, followed by measurement of the iR drop via the i-interrupt method (NOVA). Potentiostatic electrolysis was carried out for 2 h, followed by analysis via GC-FID of a 2 mL aliquot of the catholyte; the catholyte was extracted in ethyl acetate (2 mL, 99.1 % and 89.9 % efficiency for BZH and BA, respectively) adding ACP as internal standard.

3. Results and Discussion

Electrode materials for HER and ECH studies were synthesized using a protocol reported by our group,[33] but adapted via modification of the annealing process to include a pre-annealing step at high temperature under N_2 flow. Briefly, the synthesis was based on hydrothermal reactions of a resorcinol resin[60] in the presence of metal precursors, a soft template and a conductive carbon black, as schematically shown in Figure 2a. Resorcinol resins are synthesized via polycondensation of resorcinol and formaldehyde in a mixture of alcohol and water containing BP as conductive carbon support. The presence of melamine and Pluronic F-127 leads to nitrogen incorporation in the carbon network and increases the surface area of the material,[61,62] yielding a BP-supported resin here onwards referred to as FeRPM. The FeRPM resin was then pyrolyzed at high temperature under N_2/NH_3 flow using a new thermal annealing protocol in Figure S1, to graphitize the carbon matrix surrounding the N-functionalities and Fe-rich clusters, thus yielding the material under investigation referred to as Fe@C:N.

The Fe@C:N materials were found to have a porous structure with specific surface area of 430 m^2/g determined from N_2 adsorption isotherms (Figure S3). The BJH pore distribution shows that the material is mesoporous, as expected when using Pluronic-F127 as a soft template[63,64] and in agreement with our previous results on similar materials.[33] SAXS characterization, however, did not show evidence of an ordered mesostructure (Figure S4) as reported using other resorcinol-pluronic resin protocols;[65–67] this is likely due to the incorporation of iron precursors and/or the conductive BP scaffold during the first hydrothermal pyrolysis step.

Bulk composition of Fe@C:N material was investigated via ICP-OES yielding an Fe-content of 10.7 % by wt. Figure 2b shows TGA curves in air for FeRPM and Fe@C:N samples, i.e. before and after the annealing process; data for the BP scaffold materials is also shown for comparison. Pure BP particles undergo a single combustion process at high temperature yielding a negligible residual mass of 3.7 %. The FeRPM solid obtained from the hydrothermal reaction yielded two broad weight loss processes, a first one at *ca.* 230 °C and a second one at *ca.* 430 °C, with a final residual mass of 9.47 %. After graphitization, Fe@C:N materials show a single well defined mass loss at *ca.* 360 °C with a final residue of 20.6 %. This observation is consistent with the sample undergoing graphitization, yielding a more crystalline and stable carbon structure that is oxidized at higher temperatures than the partially graphitized FeRPM. Assuming that the inorganic residue from Fe@C:N consists of Fe_2O_3 exclusively, the observed 20.6 %

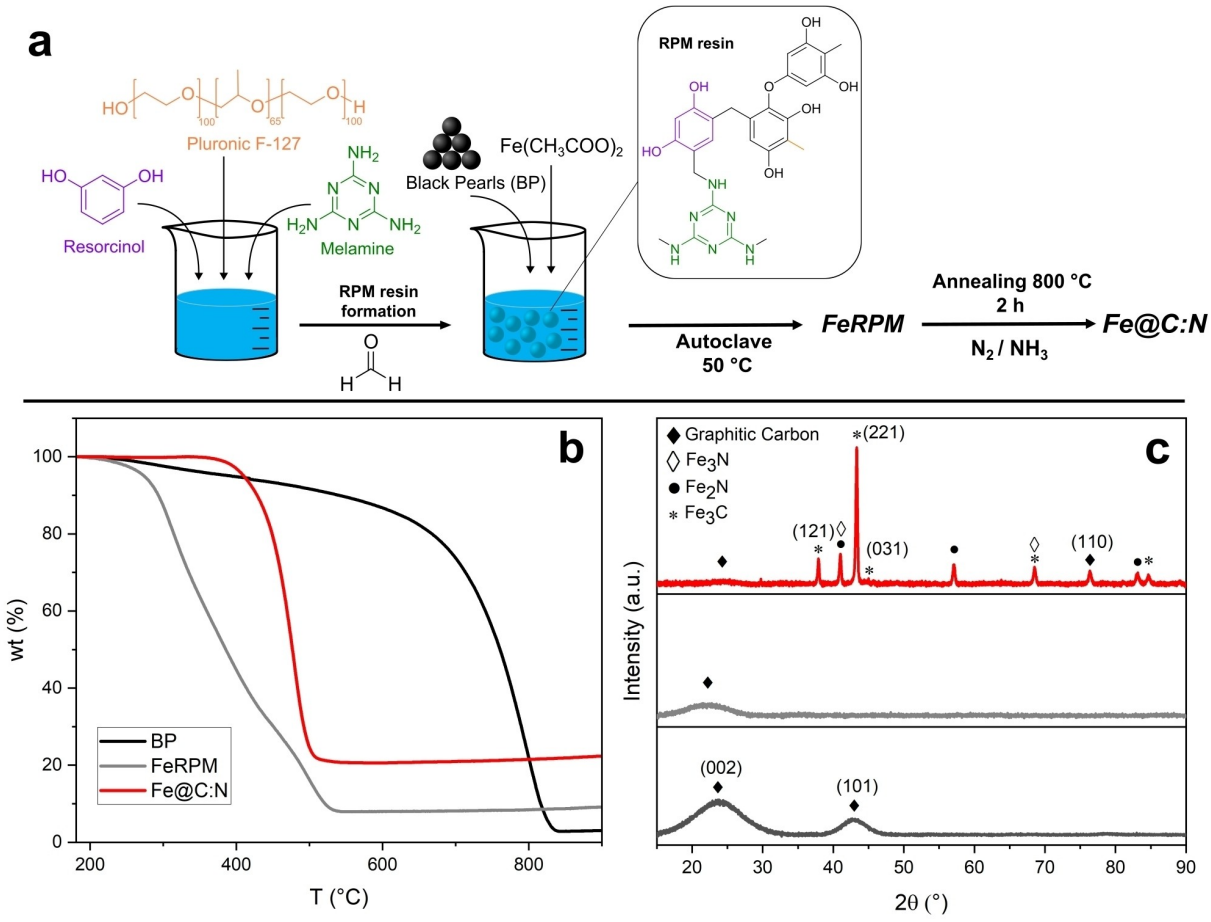

Figure 2. (a) Scheme showing the main steps in the materials synthesis protocol used in this work. (b) TGA curves obtained in air at 10 °C/min for materials FeRPM, Fe@C:N and the carbon black support BP. (c) XRD patterns of the same carbon-based materials; characteristic peaks are indicated with assignments.

corresponds to an estimated Fe-content of 14.4% by wt. which is in excellent agreement with values determined using ICP-OES, after accounting for the BP solid residue. Notably, a lower decomposition temperature was observed for Fe@C:N compared to BP; this is likely due to the presence of iron oxides which are known to catalyze the oxidation of carbons.[68] FTIR transmittance spectra for FeRPM and Fe@C:N further supported TGA results indicating that the material undergoes significant graphitization (see Figure S5). The FeRPM spectrum shows broad peaks consistent with the presence of an RPM resin,[62,69] while the absence of peaks in the spectrum of Fe@C:N is supportive of decomposition of the organic precursors and concomitant graphitization. Finally, Raman spectra also support graphitization as evidenced by an increase after annealing of the D-band contribution that is associated with the breathing mode of six-membered rings in graphitic carbons (Figure S6), and in agreement with graphitization trends in amorphous carbon materials.[70]

Figure 2c shows XRD data for BP, FeRPM and Fe@C:N materials. The only prominent peaks in the patterns of BP and FeRPM can be indexed as (002) (at 23.7°, d = 3.75 Å) and (101) (at 42.9°, d = 2.10 Å) reflections of the graphite structure, in agreement with literature values.[65,71] The large fwhm observed is indicative of structural disorder in the carbon phase. In the case of Fe@C:N the pattern is instead dominated by relatively narrow and intense peaks; reflections at 2θ = 37.8°, 43.3° and 44.5° are in good agreement with (121), (211) and (031) reflections, respectively, of Fe_3C;[33] peaks at 2θ = 41.0°, 57.1°, 68.5°, 83.0° and 84.7° are assigned to contributions from nitrides and carbides in agreement with reference patterns for Fe_2N (PDF#73-2102), Fe_3N (PDF#01-1236) and Fe_3C (PDF#89-2005). The formation of nitrides and carbides is consistent with a process involving carbonization of the organic resin under the ammonia-rich atmosphere while in the presence of iron salts. XRD does not show evidence of crystalline Fe^0, given the absence of any of the characteristic peaks at 65.2° and 85.2°, or at 63.4° and 80.1° of metallic iron patterns PDF#87-0722 and PDF#89-4186, respectively (Figure S7). Therefore, the XRD pattern indicates that the annealing process results in the decomposition of the iron salt and its reduction to carbide-nitride solids.

Surface composition of annealed Fe@C:N samples was characterized using XPS. Figure 3a shows the survey spectrum displaying characteristic Fe $2p_{3/2}$ (710 eV), N 1s (398 eV), C 1s

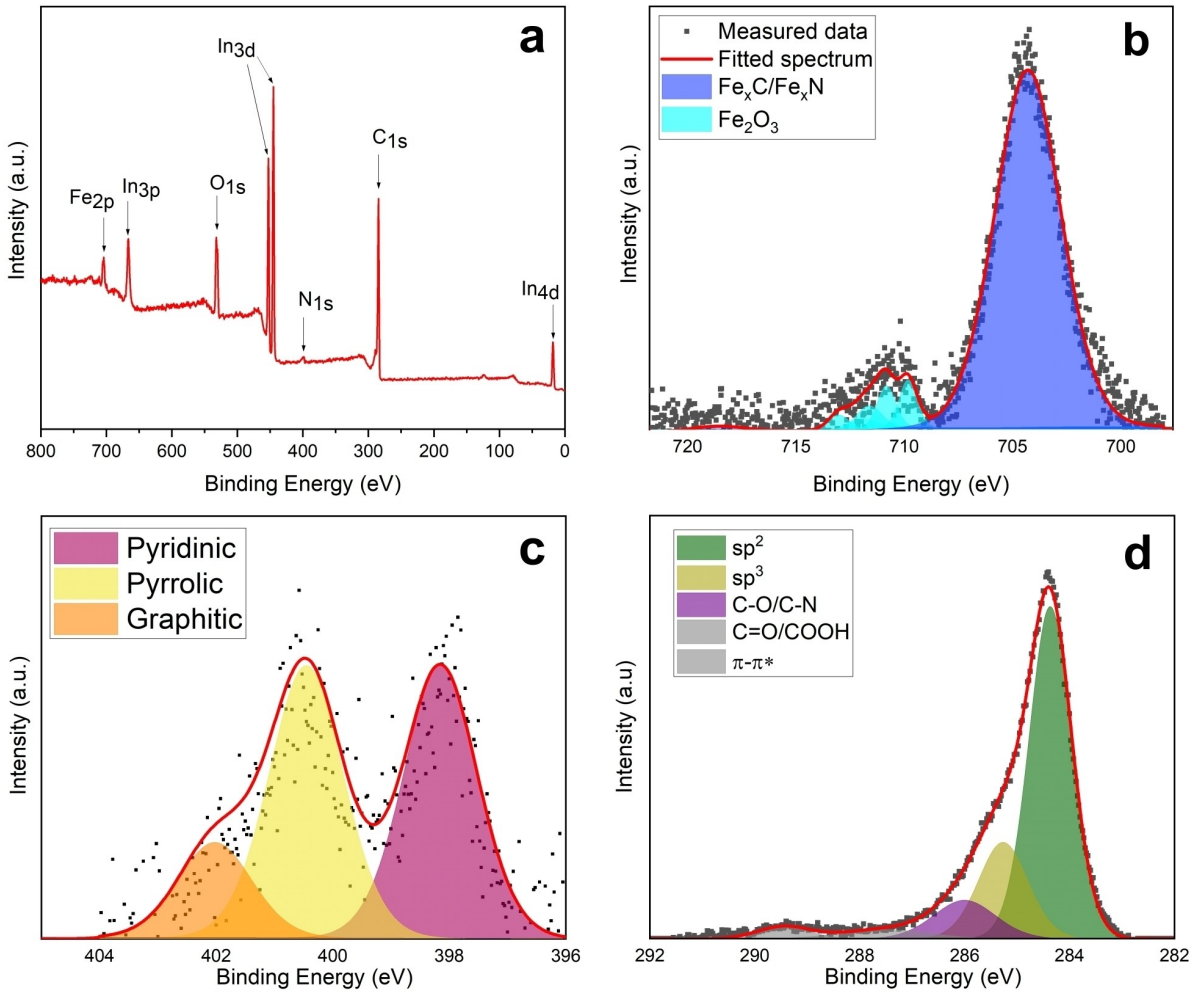

Figure 3. XPS (a) survey, (b) Fe $2p_{3/2}$, (c) N 1s and (d) C 1s spectra of Fe@C:N; best-fit components and simulated spectral envelope are also shown where relevant.

(284 eV) and O 1s (531 eV) peaks; additional peaks are due to contributions from the In foil used as support.[72] The elemental composition is reported in Table 1; values were obtained from the area ratios of the high-resolution scans of the core level excitations, shown in Figures 3b–3d, after correction by relative sensitivity factors. The oxygen content of Fe@C:N was estimated by subtracting the oxide contribution arising from the indium foil (In_2O_3), from the total area of the O 1s peak (see Figure S8). Figure 3b shows the best-fit of the Fe $2p_{3/2}$ spectrum, which displays two maxima at 704 and 710 eV. The peak at 704 eV was best-fit using a single component that can be assigned to Fe, Fe_xC or Fe_xN species based on its binding energy.[73–75] Iron carbides, its nitrides and metallic iron all have similar binding energies and cannot be fully resolved via XPS,[73–75] however, based on the XRD results the contribution at 704 eV likely arises from carbides and/or nitrides. The envelope with maximum at 710 eV is consistent with the presence of Fe(III) oxides/oxy-hydroxides, which typically give rise to multiple peaks and an overall asymmetric lineshape;[76] accordingly, the best-fit was obtained using multiple peaks (709.8, 710.8, 711.6, 711.9 and 713.0 eV) all assigned to Fe(III) oxide species. The 704 eV peak has significantly higher intensity than the oxide components, thus indicating that most of the iron present at the surface/sub-surface is in a low oxidation state. Importantly, metallic iron and its carbides/nitrides are known to be easily oxidized in air;[77,78] therefore, the absence of significant FeO_x contributions in the Fe 2p spectrum strongly suggests that iron-rich phases are encapsulated and thus protected from oxidation by a carbon shell.

Figure 3c shows the best-fit of the N 1s spectrum which was obtained using three components attributed to graphitic-N (400.9 eV), pyrrolic-N (400.0 eV) and pyridinic-N (398.0 eV).[79,80] The relative contributions of these three functionalities are reported in Table 1 and indicate that the majority of the nitrogen is present in the form of pyrrolic/pyridinic groups. It was not possible to resolve any contributions at 397 eV expected for Fe–N species;[75] this is likely due to their relative contributions being much smaller than those arising from N-functionalities in the carbon scaffold. Figure 3 d shows the best-fit of the C 1s spectrum obtained using five components, attributed to sp^2 (284.4 eV) and sp^3 (285.3 eV) carbon, C–O/C–N (286.0 eV), C=O/COOH (287.5 eV) groups, and π–π^* transitions (289.5 eV).[72,79,81,82] The absence of a carbide peak indicates that most of the C 1s intensity arises from the graphitized scaffold; this is consistent with a surface Fe content of ca. 1.8% (Table 1), that indicates that the contribution arising from carbide should account for <0.7% of the total C 1s peak, based on the Fe_3C stoichiometry. The sp^2-C component is larger than the sp^3-C one, also supporting that the majority of carbon observed is part of a graphitized network as the result of the annealing process. As shown in Figure S9, the C_{sp^2}/C_{tot}content increases from 23.7% to 60.9% when the FeRPM material is annealed to Fe@C:N, thus supporting the conclusion that the annealing process increases the degree of graphitization in agreement with FTIR and Raman results.

The morphology of the material was investigated via electron microscopies. Figure S10 shows SEM images of the Fe@C:N solid, which indicate that the sample consists of a complex matrix containing dispersed/embedded nanoparticles characterized by a rough and irregular surface. Further investigation via TEM reveals that the solid consists of nanoparticles with size similar to those of the primary BP particles, as shown in Figures 4a–4c, and additional larger and denser particles with diameter of 150 ± 57 nm. Figures 4d, 4e and 4f show TEM-EDX images of the Fe, C and O signals, respectively, that show that the larger particles are rich in Fe and are dispersed over a graphitized carbon scaffold support.

To evaluate the electrochemical response in both HER and ECH reactions, voltammetry experiments were carried out in aqueous electrolytes using BZH as a diagnostic organic compound. Figure 5 shows linear sweep voltammograms (LSV) in the cathodic region obtained for polished GC and Fe@C:N disk electrodes in 0.1 M H_2SO_4 at 5 mV s^{-1}, in the absence and presence of 10 mM BZH. In background electrolyte, GC displays poor HER activity ($\eta \cong -0.99$ V at 1 mA cm^{-2}) in agreement with previous findings.[56] Fe@C:N yields a lower overpotential ($\eta \cong -0.30$ V at 1 mA cm^{-2}), which indicates improved HER currents relative to GC albeit below values observed at a Pt disk under the same conditions (see Figure S11).[56] HER activity in the -0.3 to -0.5 V region is attributable to the incorporation of iron carbide/nitride nanoparticles at the surface/subsurface of the electrode material. Indeed, the overpotential at 10 mA cm^{-2}, Tafel slope and exchange current density values estimated at Fe@C:N disk electrodes (see Figure S12, Table S1) are in good agreement with those reported in literature for mild steel and cast iron in acid,[83–86] suggesting that HER currents are dominated by Fe/Fe_xC sites.

In the presence of 10 mM of BZH, bare GC and Fe@C:N show a change in cathodic current densities, with η of -0.89 and -0.57 V (at 1 mA cm^{-2}), respectively, observed in the HER region. This indicates that benzaldehyde adsorbs and blocks surface sites involved in proton reduction, quenching the HER activity at Fe@C:N as previously observed in the case of precious metal electrocatalysts[20,87] and of base metal electrodes in acid aldehyde solutions.[23] Interestingly, cathodic peaks are observed at *ca.* -0.92 and -0.64 V for GC and Fe@C:N, respectively, associated with BZH reduction.[13] The Pt disk electrode tested under the same conditions does not display an

Table 1. Elemental composition in atomic-%, obtained from XPS high-resolution spectra of Fe@C:N.

Material	C (%)	O[a] (%)	N (%)	Fe (%)	$N_{Graphitic}$ (%)	$N_{Pyridinic}$ (%)	$N_{Pyrrolic}$ (%)	C_{sp^2}/C_{tot} [b]
Fe@C:N	88.5	7.39	2.25	1.82	14.9	42.5	42.6	60.9

[a] atomic-% content calculated from the contribution to the O 1s area that does not arise from I_2O_3. [b] Calculated as area ratio of the best-fit component at 284.4 eV over the total C 1s peak.

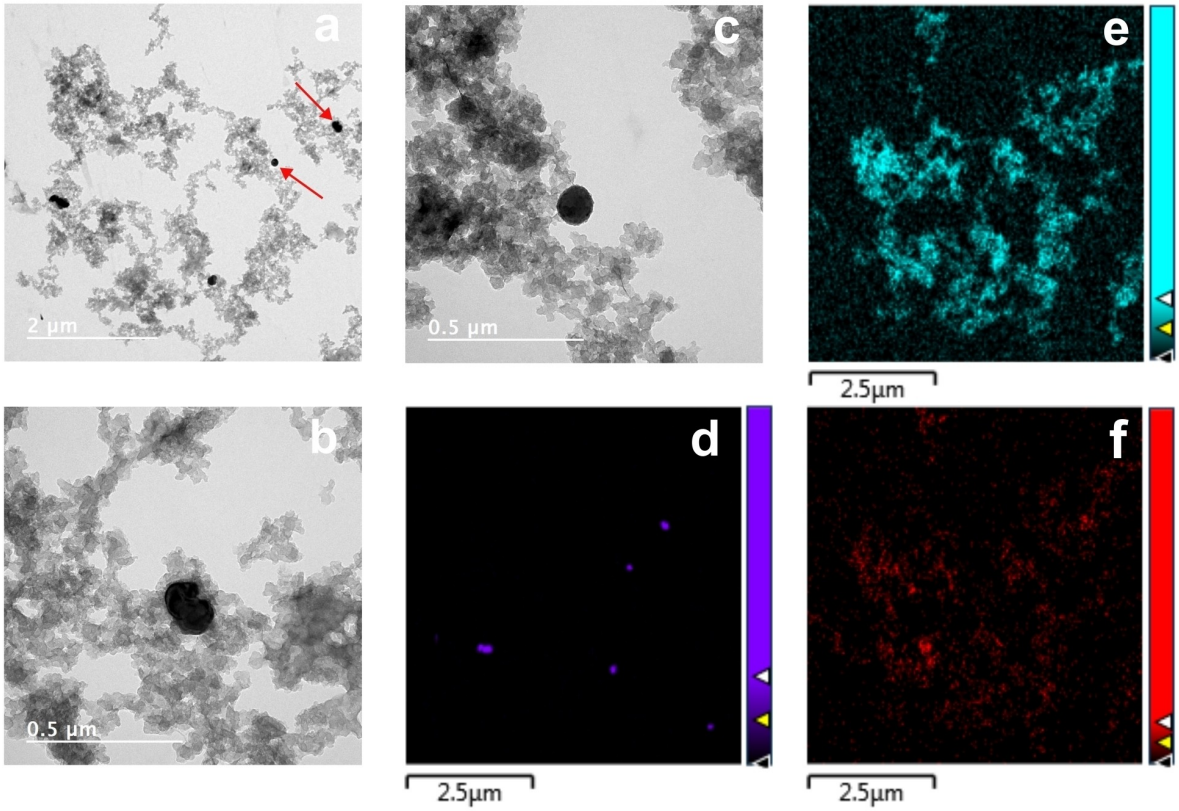

Figure 4. TEM images of (a) Fe@C:N and (b,c) expanded images with details of metal-rich nanoparticles (indicated with arrows in (a)) resulting from the annealing process. TEM-EDX chemical mapping of the image in (a) in the (d) Fe, (e) C and (f) O spectral regions.

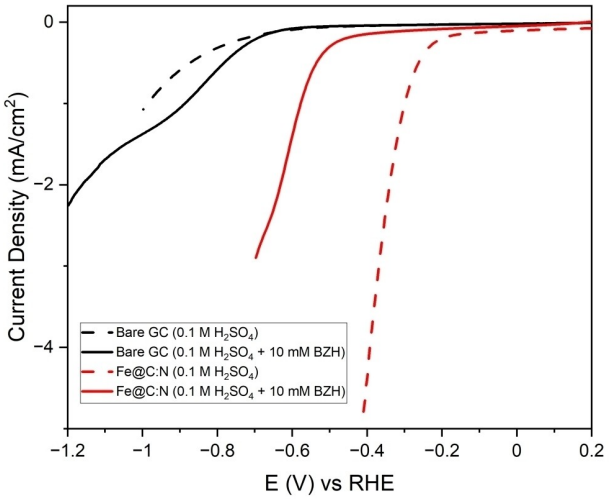

Figure 5. CVs collected for bare CC (black) and Fe@C:N (red) in 0.1 M H_2SO_4 (dash line) and H_2SO_4 with 10 mM BZH (solid line), at 5 mV/s scan rate in 3 cycles. Only the cathodic region of the last cycle is plotted.

evident reduction peak (Figure S11), however the high HER current background dominates the cathodic response at these surfaces below −0.4 V.

The same catalyst ink was then used to investigate BZH reductions via electrolysis experiments. Figure 6a shows an SEM image of a 1 cm^2 CC electrode decorated with a uniform drop-cast layer of the electrocatalyst ink. SEM-EDX mapping of the Fe@C:N/CC electrode in Figures 6b–6d indicates a uniform distribution of the ink content over the CC area, with a low Fe intensity arising from metal centers and F signal arising from the Nafion binder. Figure 7a shows uncompensated linear sweep voltammograms (LSV) of bare CC and of Fe@C:N/CC (1 cm^2) obtained in an H-cell (Figure S2) at 10 $mV\,s^{-1}$ in 0.1 M H_2SO_4. In the presence of 30 mM of BZH a clear cathodic peak at *ca.* −0.7 V is observed in good agreement with results obtained at drop-cast disk electrodes. An additional cathodic peak is observed at −0.26 V for Fe@C:N/CC that is absent in the case of bare CC. Figure 7b shows LSV collected for Fe@C:N/CC at varying BZH concentrations of 1.0, 10.0 and 30.0 mM, at 10 $mV\,s^{-1}$; results show that the cathodic peak at −0.26 V does not change current density as a function of concentration thus suggesting that this peak is likely dominated by surface redox processes. On the other hand, the peak at −0.8 V increases with BZH concentration and can be clearly ascribed to an organic reduction.

The LSV in Figure 7a show an increased background current density for Fe@C:N/CC electrodes relative to bare CC. This was further investigated by measuring CV at varying scan rates in a non-faradaic potential window, as shown in Figure S13. The double-layer capacitance (C_{dl}) was estimated from a linear fit of the capacitive currents and found to be 1.32 and 5.57 $mF\,cm^{-2}$ for bare CC and Fe@C:N/CC, respectively. Therefore, drop-casting of the catalyst ink increases the electrochemical specific surface area (ECSA); assuming the specific double-layer capaci-

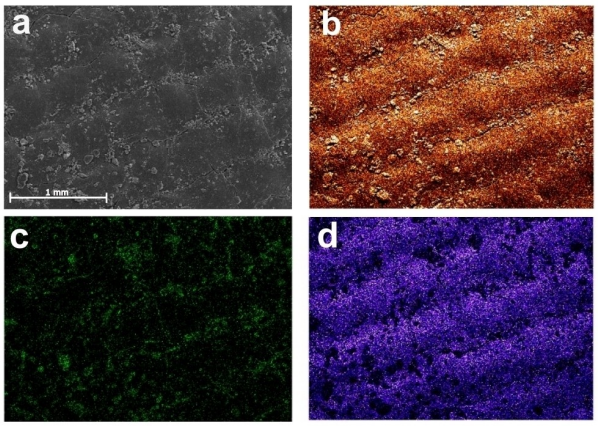

Figure 6. (a) SEM image of a CC electrode decorated with the Fe@C:N electrocatalyst ink, showing the structure of woven fibers in the CC underlying support. SEM-EDX mapping for C (b), Fe (c) and F (d) atomic species of the electrode surface in (a) indicating uniform distribution of the ink material.

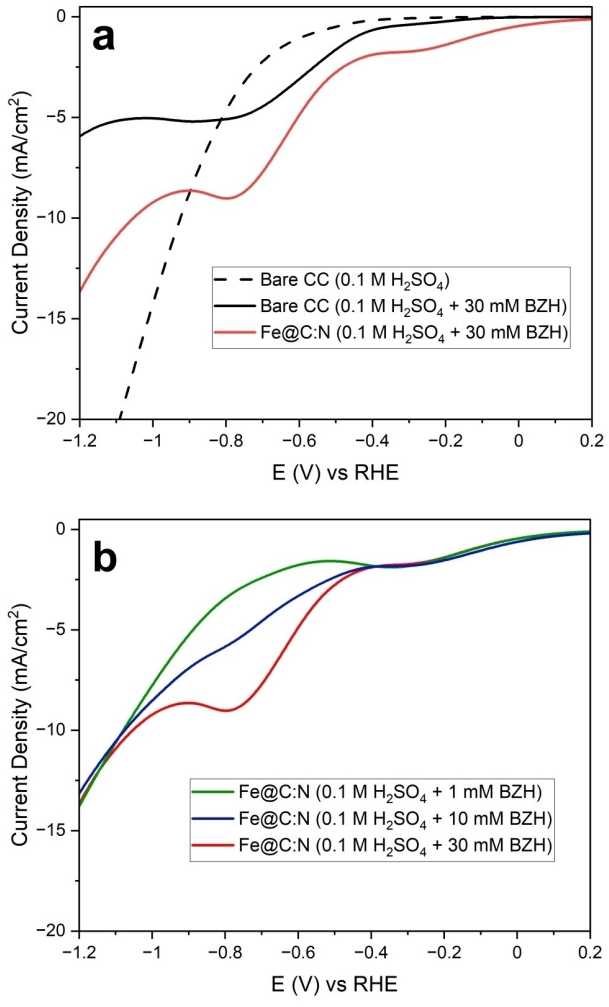

Figure 7. (a) CVs collected for bare CC (black) and Fe@C:N (red) in 0.1 M H_2SO_4 (dashed line) and H_2SO_4 + 30 mM BZH (solid line), at 10 mV/s scan rate in 3 cycles. (b) CVs collected for Fe@C:N in 0.1 M H_2SO_4 + 1, 10, 30 mM BZH, at 10 mV/s scan rate in 3 cycles. Only cathodic region of last cycle is plotted.

tance to remain constant,[56,59] the microscopic area can be estimated to increase approximately four-fold after deposition of Fe@C:N/C on the CC support. This higher value is consistent with high porosity developing during the synthesis of the catalyst material.

To further evaluate reactions taking place at cathodic potentials, electrolysis experiments with product analysis were carried out using the H-cell setup described above. In a first set of experiments, chronoamperometry experiments were carried out at the peak potential of −0.8 V in 0.1 M H_2SO_4 solutions containing three concentrations of BZH for 2 h under static conditions. The current density remained stable over the entire duration of the experiment, thus confirming that the electrodes prepared as in Figure 6 display high stability even when subject to the mechanical stresses associated with evolution of hydrogen bubbles in the HER region (see Figure S14). Two products were identified from the chromatogram at t_{2h}: benzyl alcohol (BA) and hydrobenzoin (HBZ), thus confirming that hydrogenation of the organic substrate takes place at the peak potential (Figure S15). For all the experiments the carbon balance was ca. 90% (Figure S16), which supports that the majority of the products are being detected in the liquid phase of the catholyte compartment. Figure 8a shows the total faradaic efficiency (FE) associated with BZH reductions obtained as a function of BZH concentration. FE values were found to increase up to 70.1% at 30.0 mM concentrations; higher concentrations were not tested to remain well below the solubility limit of the reactant (65 mM).[36] It is important to note that although a cathodic peak can be observed at bare CC electrodes, the hydrogenation performance summarized in Figure 8 can be largely attributed to the presence of Fe@C:N; in fact, a control experiment (Figure S17) shows that the bare support yields less than half of the FE at Fe@C:N. Yield, selectivity and conversion values were also calculated and are shown in Supporting Information (Figure S18). The total yield for the reduction ($Yield_{ECH}$%) decreases from 16.3% to 7.2% when the BZH concentration is increased from 1 to 30 mM. Similarly, BZH conversion decreases from 33.6% to 24.3% as the concentration of the benzaldehyde increases. These values are higher than estimates for a diffusion-controlled reaction at a smooth 1 cm^2 electrode with a similar cell and electrode geometry as in our experiments (Figure S19), thus suggesting that the reduction rates are facilitated by convection due to the generation of H_2 bubbles, as previously reported.[88] Further, under these electrolysis conditions the selectivity towards BA is highest at the lowest BZH concentrations, whereas the dimer becomes the preferred product at the highest concentration investigated. This suggests that when the BZH concentration increases from 1 to 30 mM the cathodic process results in increased ketyl radical concentrations leading to higher probability of dimerization via pinacolic coupling.[89] On the other hand, at 1 mM the ketyl radicals should have a higher probability of reacting with protons or H_{ads} species at the electrode surface thus enhancing the selectivity towards BA.

To better understand the interplay among product selectivity, FE and potential, we then carried out a more detailed investigation of hydrogenation performance indicators using

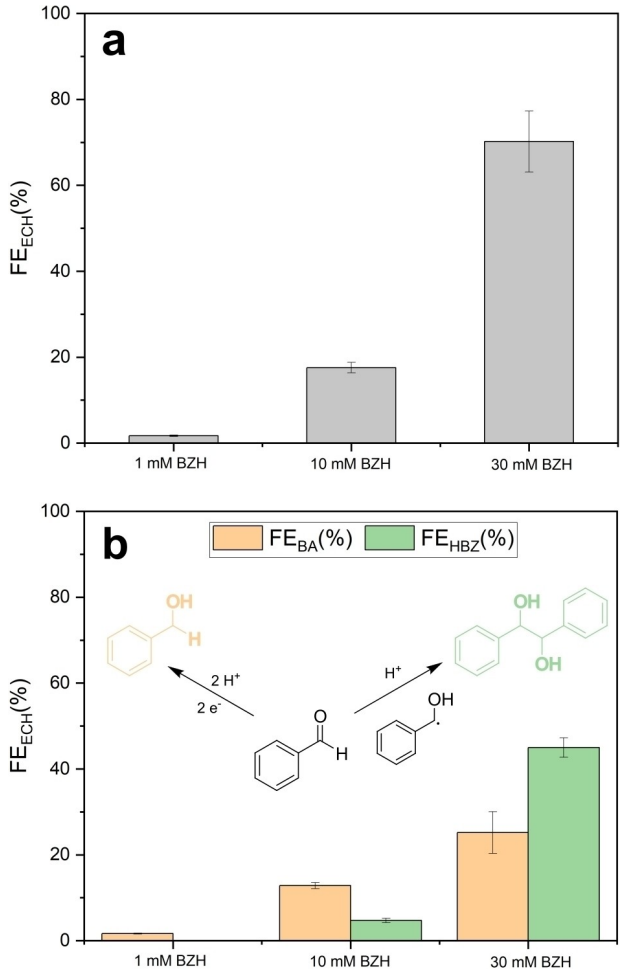

Figure 8. (a) Total faradaic efficiency (FE) for organic reductions at −0.8 V. (b) Contributions of benzyl alcohol (BA) and hydrobenzoin (HBZ) to the total faradaic efficiency of BZH reductions.

the electrolyte composition that yielded the highest FE performance in Figure 7, i.e. 30 mM BZH in 0.1 M H_2SO_4. Figure 9a shows the uncompensated CV of a Fe@C:N/CC electrode in the above electrolyte, obtained in the H-cell, with potentials marked at −0.26, −0.50, −0.80 and −1.00 V to indicate values chosen for further chronoamperometry experiments. The corresponding chronoamperograms are shown in Figure 9b; all plots display nearly constant currents, which is diagnostic of a highly stable electrode performance over the entire duration of the experiments. Figure 9c shows the change in total FE of the organic hydrogenations as a function of potential. First, it is interesting to note that there is detectable organic hydrogenation activity at potentials as high as −0.26 V vs RHE. A control experiment run under identical conditions but at open circuit confirmed that the products observed are indeed the result of an electrochemical hydrogenation process (see Figure S20). As the potential is lowered, the FE first increases and then decreases significantly at −1.00 V; in contrast, the average rate and TOF values for the production of hydrogenated organics remain approximately constant, as shown in Figure 9 d. These results are consistent with improvements in hydrogenation efficiency at −0.50 and −0.80 V, and the drop at −1.00 V being attributable to competition from increased rates of HER.[90] Therefore, for potentials below −0.80 V, any further increases in cathodic current are almost exclusively due to increased rates of HER rather than to enhanced rates of organic hydrogenation. Finally, a control experiment using a bare CC in 30 mM BZH/0.1 M H_2SO_4 (Figure S21) further confirms that the faradaic efficiency at −0.50 V results from an improvement of more than a factor of two in the intrinsic efficiency of Fe@C:N surfaces towards ECH relative to that of a graphitic carbon support.

The trends in FE vs potential for the two products, BA and HBZ, are particularly interesting and are shown in Figure 9e. It is clear that under the conditions of our experiments, BA is the preferred product at more anodic potentials whereas HBZ is instead favored at the more cathodic potentials. This is also evident by examining the rates of production for the two compounds, shown in Figure 9f; the corresponding TOF values are reported in Supporting Information (Table S2). Notably, at −0.56 V the selectivity towards BA is very high, while also achieving a close to maximum average rate of production of hydrogenated organics and high total FE. This suggests that it is possible to tailor the electrolysis conditions to achieve electrochemical hydrogenations with high selectivity and high efficiency. Optimal conditions are likely to be found at intermediate potentials that are sufficiently cathodic to result in H_{ads} coverage,[5,91] but also sufficiently anodic to inhibit uncontrolled/too fast reduction rates of BZH to α-hydroxybenzyl radicals and, consequently, fast dimerization. In fact, greater selectivity for BA in Figure 9 is achieved at the lowest overpotentials relative to the thermodynamic value for the conversion of BZH to BA ($E^\circ = 0.14–0.19$ V).[6,92] A similar mechanism for increased selectivity towards dimerization at base metals was proposed by Andrews et al.[15] based on product trends in continuous flow cell experiments. Our data therefore suggests that using metal-encapsulated Fe@C:N heterostructured materials it is possible to achieve hydrogenation via an electrocatalytic mechanism, as opposed to a direct electronation-protonation pathway. This can take place over a selected potential range that enables fast rates of hydrogenation via surface-activated proton transfer. It is important to note that the specific influence of nitrides and carbides on the ECH performances cannot be easily discriminated/resolved and fundamental studies on pure carbides and nitrides would be desirable in order to clarify this aspect.

Prior work on the reduction of BZH indicates that achieving high FE values while controlling selectivity for BA and/or HBZ remains a challenge in the literature, particularly when balanced against the choice of metal in terms of their cost and abundance.[11,12,15,19,20,87] Electrode materials with high HER activity, such as Pt/C, catalyze hydrogenation selectively to BA at low overpotentials; however, as the potential is shifted to more cathodic values, competition from the HER lowers the FE of hydrogenations.[20] This is similar to our observed trends in Figure 9e, further supporting the idea that BA production at Fe@C:N surfaces and low overpotentials takes place via H_{ads} transfers. It is interesting to note that FE values for Fe@C:N in

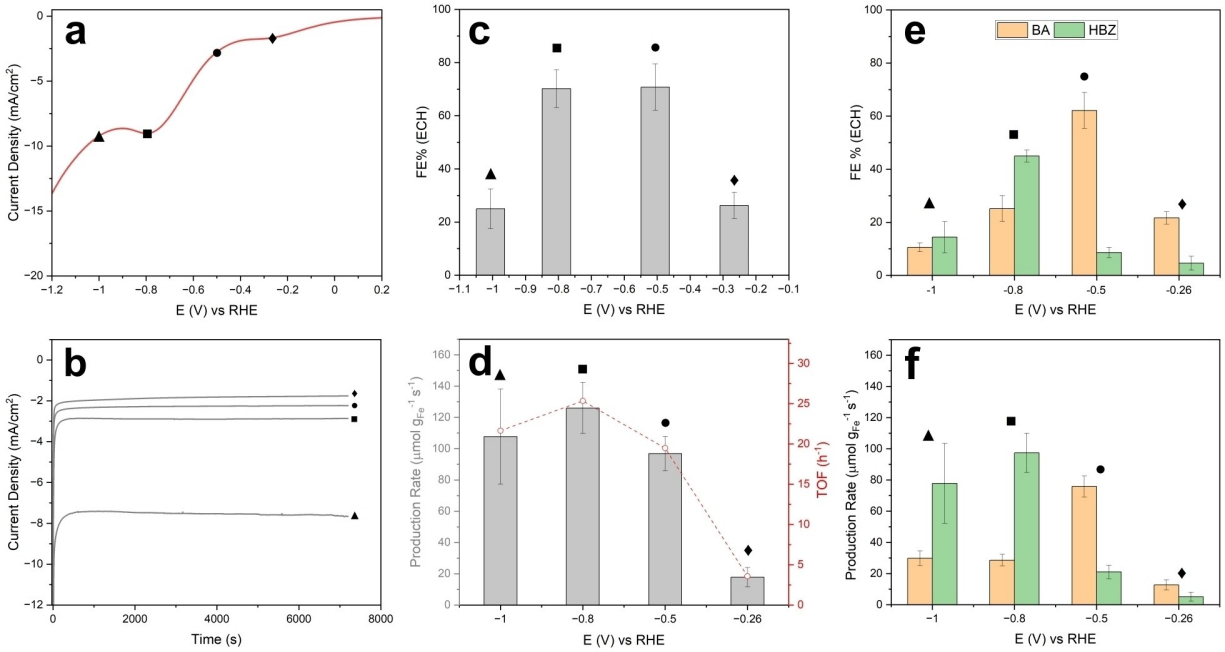

Figure 9. (a) CV collected for Fe@C:N on CC–MPL in 0.1 M H_2SO_4/30 mM BZH at 10 mV/s. (b) Chronoamperometries collected for each potential for 2 h. Total ECH FE% (c) and total product rate with TOF values (d) for −0.26, 0.5, −0.8, −1 V vs RHE. Contribution of BA and HBZ to ECH FE% (e) and to product rate (f) for each potential.

this work at −0.26 V are only slightly inferior to those for Rh/C and Pt/C in pH 5 batch cells at similar potentials (vs. RHE) reported by Song et al., while the performance appears comparable or better at −0.50 V.[20] TOF values at Fe@C:N are approximately two orders of magnitude lower than those reported for Rh/C and Pt/C in the same work, as expected from the much higher HER activity at these Pt-group metals compared to Fe.[83] However, using a continuous flow cell configuration with carbon felt electrodes, Lopez-Ruiz et al.[93] reported TOF_{ECH} values at pH 2 and 5 mA cm^{-2} using Pd/C, one of the best metal electrodes for ECH of BZH, that are only ~12 times larger than those observed with Fe@C:N/CC at similar current density. Anibal et al.[14] also investigated BZH reduction studies on metal foils in pH 4.6 electrolyte at −0.5 V vs RHE; interestingly, rates of production at −0.56 V with Fe@C:N in this work are intermediate between those reported in the study for Pd and Pt, and are similar to those measured at Au foils. Given the well-known difference in cost and criticality between Fe and Pt-group metals, the performances observed at Fe@C:N appear promising to further develop novel Fe-based composite electrocatalysts with selectivity towards the alcohol.

ECH of BZH using base metal electrodes has been previously investigated and the performance of Fe@C:N compares very well to those of e.g. Ni[20] and Cu[14] in terms of TOF values and production rates in aqueous electrolytes. To the best of our knowledge there are no reports of ECH of BZH at Fe or Fe@C electrodes, however there have been several studies using iron electrodes for the reduction of other aldehydes. In such previous work, high selectivity towards the simple alcohol product is not usually observed.[23,25,29,30] For instance, in acid electrolyte the ECH of furfural using iron electrodes has been shown to lead almost exclusively to the pinacolic dimer[29] or to the highly hydrogenated methylfuran product.[30] Hydrogenation of glucose to sorbitol is somewhat of an exception, as it was observed to take place with high selectivity using Fe at neutral pH, but no hydrogenated products were detected in sulfuric acid solutions, as the hydrogenation was proposed to require a local alkaline pH to proceed.[25] Mixed product streams with different degree of hydrogenation were detected at Fe electrodes using HMF as a substrate in acid electrolyte.[23] Under our experimental conditions, we observed BA with good selectivity at intermediate potentials and neither hydrogenation of the aromatic ring or hydrogenolysis to toluene were detected. The BA-selectivity is likely due to a combination of higher stability of phenyl vs. furanyl rings and differences in the organic-surface adsorption strengths. Although this argument is consistent with descriptors and reactivity trends observed in the literature,[90,94] further studies aimed at modulating the partitioning of BZH onto the surface are needed to support this hypothesis. An interesting aspect of the Fe@C:N electrocatalyst architecture is that the rich library of surface functionalization strategies applicable to carbon nanomaterials is available to fine tune the binding strengths of substrate and intermediates, as previously demonstrated in our group for other organic and inorganic redox processes.[55,80,95]

4. Conclusions

In this work we prepared and studied a porous Fe@C:N heterostructured material via hydrothermal synthesis. We introduced a new annealing protocol that includes a pre-

annealing step and that yields predominantly Fe/Fe_xC metal sites at the carbon surface with only small FeO_x content, in contrast with previously reported methods.[33] To evaluate the performance of the material as electrocatalyst in organic hydrogenations we used benzaldehyde as a diagnostic substrate. Chronoamperometry coupled with product analysis using gas chromatography demonstrate that it is possible to achieve hydrogenation of benzaldehyde to the alcohol and the pinacolic coupling products.

Interestingly, results show that the applied potential can influence the contribution to the total faradaic efficiency for hydrogenations of the two products, thus indicating that electrolysis conditions can be tailored to achieve both high product selectivity and high efficiency. Optimal conditions were identified at intermediate potentials that enable control over the competition between ECH and HER, with BA and HBZ being the preferred products at low and high overpotentials, respectively. Estimates of TOF and production rates compare extremely well to those reported using base metal electrodes such Ni and Cu for the ECH of BZH in aqueous electrolytes.[14,20] Notably, TOF values for Fe@C:N are only an order of magnitude smaller than those observed for a carbon supported precious metal electrocatalysts such as Pd/C (pH 2) in previous reports.[20] Given that our experiments are not carried out under conditions that necessarily maximize mass transport, the calculated TOF values for Fe@C:N are likely to represent a lower boundary value.

To the best of our knowledge, there are no reports of comparable or better performances in the ECH of benzaldehyde using iron-carbon composites. Considering the wide possibility of implementing these architectures with different functionalizations, we believe that our results could open the door to improved M@C:N architectures for hydrogenation of organics using low-cost and abundant metals not yet explored in this configuration and tested as catalysts for different organic substrates.

Acknowledgements

This publication has emanated from research conducted with the financial support of Science Foundation Ireland under Grant No. 19/FFP/6761. MCDO gratefully acknowledges support by the Irish Research Council under grant number GOIPD/2021/530. PEC, FB and JAB thank the France-Ireland PHC ULYSSES 2021 programme for supporting part of the work. SEM imaging was carried out at the Advanced Microscopy Laboratory (AML) at the AMBER Research Centre, Trinity College Dublin, Ireland. We acknowledge Dr. Ludivine Rault of the SCANMAT platform at the Université de Rennes for access to TEM. Use of the XPS of I. V. Shvets and C. McGuinness provided under SFI Equipment Infrastructure funds. Open Access funding provided by IReL.

Conflict of Interests

The authors declare no conflict of interest.

Data Availability Statement

The data that support the findings of this study are available from the corresponding author upon reasonable request.

Keywords: electrocatalysis · electrocatalytic hydrogenation · benzaldehyde · biomass · sustainable chemistry

[1] L. Gustavsson, J. Holmberg, V. Dornburg, R. Sathre, T. Eggers, K. Mahapatra, G. Marland, *Energy Policy* **2007**, *35*, 5671–5691.
[2] E. Union, *Off. J. Eur. Union* **2009**, *5*, 2009.
[3] E. T. Commission, Energy Transition Commission, London, UK **2022**.
[4] L. Zhang, T. U. Rao, J. Wang, D. Ren, S. Sirisommboonchai, C. Choi, H. Machida, Z. Huo, K. Norinaga, *Fuel Process. Technol.* **2022**, *226*, 107097.
[5] J. Lessard, *Encyclopedia of Applied Electrochemistry* (Eds: G. Kreysa, K.-I. Ota, R. F. Savinell), Springer New York, New York, NY **2014**, pp. 443–448.
[6] S. A. Akhade, N. Singh, O. Y. Gutiérrez, J. Lopez-Ruiz, H. Wang, J. D. Holladay, Y. Liu, A. Karkamkar, R. S. Weber, A. B. Padmaperuma, M.-S. Lee, G. A. Whyatt, M. Elliott, J. E. Holladay, J. L. Male, J. A. Lercher, R. Rousseau, V.-A. Glezakou, *Chem. Rev.* **2020**, *120*, 11370–11419.
[7] P. Zhou, J. Zhang, *Sci. China Chem.* **2023**, *66*, 1011–1031.
[8] M. Ďurovič, J. Hnát, K. Bouzek, *J. Power Sources* **2021**, *493*, 229708.
[9] S. Wang, A. Lu, C.-J. Zhong, *Nano Converg.* **2021**, *8*, 4.
[10] B. Zhao, M. Chen, Q. Guo, Y. Fu, *Electrochim. Acta* **2014**, *135*, 139–146.
[11] Y. Zeng, M. Zhao, H. Zeng, Q. Jiang, F. Ming, K. Xi, Z. Wang, H. Liang, *eScience* **2023**, *3*, 100156.
[12] C. Catizane, Y. Jiang, J. Sumner, *Energy Adv.* **2024**, *3*, 366–388.
[13] D. C. Cantu, A. B. Padmaperuma, M.-T. Nguyen, S. A. Akhade, Y. Yoon, Y.-G. Wang, M.-S. Lee, V.-A. Glezakou, R. Rousseau, M. A. Lilga, *ACS Catal.* **2018**, *8*, 7645–7658.
[14] J. Anibal, A. Malkani, B. Xu, *Catal. Sci. Technol.* **2020**, *10*, 3181–3194.
[15] E. Andrews, J. A. Lopez-Ruiz, J. D. Egbert, K. Koh, U. Sanyal, M. Song, D. Li, A. J. Karkamkar, M. A. Derewinski, J. Holladay, O. Y. Gutiérrez, J. D. Holladay, *ACS Sustain. Chem. Eng.* **2020**, *8*, 4407–4418.
[16] K. Amouzegar, O. Savadogo, *Electrochim. Acta* **1998**, *43*, 503–508.
[17] S. J. C. Cleghorn, D. Pletcher, *Electrochim. Acta* **1993**, *38*, 425–430.
[18] Z. Li, S. Kelkar, L. Raycraft, M. Garedew, J. E. Jackson, D. J. Miller, C. M. Saffron, *Green Chem.* **2014**, *16*, 844–852.
[19] J. Yu, P. Zhang, L. Li, K. Li, G. Zhang, J. Liu, T. Wang, Z.-J. Zhao, J. Gong, *Nat. Commun.* **2022**, *13*, 7909.
[20] Y. Song, U. Sanyal, D. Pangotra, J. D. Holladay, D. M. Camaioni, O. Y. Gutiérrez, J. A. Lercher, *J. Catal.* **2018**, *359*, 68–75.
[21] J. Valverde Carbonell, M. Menéndez de Medina, C. Pietrobelli, *An Estimate Through Economic Complexity Techniques*, UNU-MERIT **2023**.
[22] C. European, I. E. Directorate-General for Internal Market Smes, M. Grohol, C. Veeh, *Study on the Critical Raw Materials for the EU 2023 – Final Report*, Publications Office of the European Union **2023**.
[23] Y. Kwon, Y. Y. Birdja, S. Raoufmoghaddam, M. T. M. Koper, *ChemSusChem* **2015**, *8*, 1745–1751.
[24] Y. Kwon, E. de Jong, S. Raoufmoghaddam, M. T. M. Koper, *ChemSusChem* **2013**, *6*, 1659–1667.
[25] Y. Kwon, M. T. M. Koper, *ChemSusChem* **2013**, *6*, 455–462.
[26] L. R. L. Ting, Y. Peng, B. S. Yeo, *ChemSusChem* **2021**, *14*, 2963–2971.
[27] W. Sauter, O. L. Bergmann, U. Schröder, *ChemSusChem* **2017**, *10*, 3105–3110.
[28] S. Calado Galvão de Melo, M. E. P. da Silva, M. E. B. da Silva, J. A. da Paz, C. M. B. de Menezes Barbosa, F. D. de Menezes, R. N. A. Loureiro, M. Navarro, J. Â. P. da Costa, G. F. da Silva, A. A. O. Villa, M. Vilar, *Int. J. Hydrogen Energy* **2020**, *45*, 22855–22872.
[29] P. Nilges, U. Schröder, *Energy Environ. Sci.* **2013**, *6*, 2925–2931.
[30] Z. Li, S. Kelkar, C. H. Lam, K. Luczek, J. E. Jackson, D. J. Miller, C. M. Saffron, *Electrochim. Acta* **2012**, *64*, 87–93.
[31] G. Yang, Y. Jiao, H. Yan, Y. Xie, C. Tian, A. Wu, Y. Wang, H. Fu, *Nat. Commun.* **2022**, *13*, 3125.
[32] A. Li, S. A. Nicolae, M. Qiao, K. Preuss, P. A. Szilágyi, A. Moores, M.-M. Titirici, *ChemCatChem* **2019**, *11*, 3602–3625.
[33] A. Iannaci, S. Ingle, C. Domínguez, M. Longhi, O. Merdrignac-Conanec, S. Ababou-Girard, F. Barrière, P. E. Colavita, *Bioelectrochemistry* **2021**, *142*, 107937.
[34] M. Tavakkoli, T. Kallio, O. Reynaud, A. G. Nasibulin, C. Johans, J. Sainio, H. Jiang, E. I. Kauppinen, K. Laasonen, *Angew. Chem. Int. Ed.* **2015**, *54*, 4535–4538.

[35] O. Hammerich, B. Speiser, *Organic Electrochemistry: Revised and Expanded*, CRC Press **2015**.
[36] A. G. Mitchell, L. S. C. Wan, S. G. Bjaastad, *J. Pharm. Pharmacol.* **2011**, *16*, 632–633.
[37] L. Wang, R. Tang, A. Kheradmand, Y. Jiang, H. Wang, W. Yang, Z. Chen, X. Zhong, S. P. Ringer, X. Liao, W. Liang, J. Huang, *Appl. Catal. B* **2021**, *284*, 119759.
[38] A. K. Vasiliou, J. H. Kim, T. K. Ormond, K. M. Piech, K. N. Urness, A. M. Scheer, D. J. Robichaud, C. Mukarakate, M. R. Nimlos, J. W. Daily, Q. Guan, H.-H. Carstensen, G. B. Ellison, *J. Chem. Phys.* **2013**, *139*, 104310.
[39] R. J. Evans, T. A. Milne, *Energy Fuels* **1987**, *1*, 123–137.
[40] D. J. Nowakowski, A. V. Bridgwater, D. C. Elliott, D. Meier, P. de Wild, *J. Anal. Appl. Pyrolysis* **2010**, *88*, 53–72.
[41] C. Bährle, V. Custodis, G. Jeschke, J. A. van Bokhoven, F. Vogel, *ChemSusChem* **2014**, *7*, 2022–2029.
[42] Y. Ran, J. Li, J. Sun, B. Yu, F. Tan, G. Cheng, Z. Zhang, *Appl. Catal. A* **2024**, *678*, 119725.
[43] L. Gong, C. Y. Zhang, J. Li, G. Montaña-Mora, M. Botifoll, T. Guo, J. Arbiol, J. Y. Zhou, T. Kallio, P. R. Martínez-Alanis, A. Cabot, *ACS Appl. Mater. Interfaces* **2024**, *16*, 6948–6957.
[44] G. Cheng, J. Sun, Y. Ran, F. Tan, W. Ma, Z. Zhang, *Chem. Eng. J.* **2024**, *481*, 148735.
[45] Benzyl Alcohol Price Outlook | Q4 2022, https://medium.com/intratec-products-blog/benzyl-alcohol-prices-latest-historical-data-in-several-countries-6203daaecd3b.
[46] Benzyl Alcohol Price | Current and Forecast, https://www.intratec.us/chemical-markets/benzyl-alcohol-price.
[47] K. Okano, *Tetrahedron* **2011**, *67*, 2483–2512.
[48] V. Gómez-Serrano, C. M. González-García, M. L. González-Martín, *Powder Technol.* **2001**, *116*, 103–108.
[49] W.-C. Chang, M. T. Nguyen, *J. Power Sources* **2011**, *196*, 5811–5816.
[50] M.-T. Nguyen, B. Mecheri, A. D'Epifanio, T. P. Sciarria, F. Adani, S. Licoccia, *Int. J. Hydrogen Energy* **2014**, *39*, 6462–6469.
[51] A. Iannaci, B. Mecheri, A. D'Epifanio, M. J. Lázaro Elorri, S. Licoccia, *Int. J. Hydrogen Energy* **2016**, *41*, 19637–19644.
[52] S. Brunauer, P. H. Emmett, E. Teller, *J. Am. Chem. Soc.* **1938**, *60*, 309–319.
[53] E. P. Barrett, L. G. Joyner, P. P. Halenda, *J. Am. Chem. Soc.* **1951**, *73*, 373–380.
[54] J. A. Behan, A. Iannaci, C. Domìnguez, S. N. Stamatin, M. K. Hoque, J. M. Vasconcelos, T. Perova, P. E. Colavita, *Carbon* **2019**, *148*, 224–230.
[55] J. A. Behan, E. Mates-Torres, S. N. Stamatin, C. Domínguez, A. Iannaci, K. Fleischer, M. K. Hoque, T. S. Perova, M. García-Melchor, P. E. Colavita, *Small* **2019**, *15*, 1902081.
[56] H. Nolan, C. Schröder, M. Brunet-Cabré, F. Pota, N. McEvoy, K. McKelvey, T. S. Perova, P. E. Colavita, *Carbon* **2023**, *202*, 70–80.
[57] P. Daubinger, J. Kieninger, T. Unmüssig, G. A. Urban, *Phys. Chem. Chem. Phys.* **2014**, *16*, 8392–8399.
[58] S. H. Glarum, J. H. Marshall, *J. Electrochem. Soc.* **1979**, *126*, 424.
[59] C. C. L. McCrory, S. Jung, J. C. Peters, T. F. Jaramillo, *J. Am. Chem. Soc.* **2013**, *135*, 16977–16987.
[60] J. Liu, S. Z. Qiao, H. Liu, J. Chen, A. Orpe, D. Zhao, G. Q. Lu, *Angew. Chem., Int. Ed.* **2011**, *50*, 5947–5951.
[61] J. Heydaripour, M. Gazi, A. A. Oladipo, H. O. Gulcan, *J. Porous Mater.* **2019**, *26*, 1249–1258.
[62] Y. Shao, H. Chen, Y. Li, S. Xie, B. Li, *RSC Adv.* **2017**, *7*, 37604–37611.
[63] N. Brun, S. R. S. Prabaharan, C. Surcin, M. Morcrette, H. Deleuze, M. Birot, O. Babot, M.-F. Achard, R. Backov, *J. Phys. Chem. C* **2012**, *116*, 1408–1421.
[64] Y. Zhai, Y. Dou, X. Liu, S. S. Park, C.-S. Ha, D. Zhao, *Carbon* **2011**, *49*, 545–555.
[65] M. Karthik, A. Faik, S. Doppiu, V. Roddatis, B. D'Aguanno, *Carbon* **2015**, *87*, 434–443.
[66] J. Yu, M. Guo, F. Muhammad, A. Wang, G. Yu, H. Ma, G. Zhu, *Microporous Mesoporous Mater.* **2014**, *190*, 117–127.
[67] J. Xu, A. Wang, T. Zhang, *Carbon* **2012**, *50*, 1807–1816.
[68] J. P. A. Neeft, M. Makkee, J. A. Moulijn, *Fuel* **1998**, *77*, 111–119.
[69] G. Socrates, *Infrared and Raman Characteristic Group Frequencies. Tables and Charts*, 3rd ed., John Wiley & Sons, Ltd, Chichester **2001**.
[70] A. C. Ferrari, J. Robertson, *Phys. Rev. B* **2000**, *61*, 14095–14107.
[71] M. Zhao, H. Song, X. Chen, W. Lian, *Acta Mater.* **2007**, *55*, 6144–6150.
[72] J. F. Moulder, W. F. Stickle, P. E. Sobol, K. D. Bomben, *Handbook of X-Ray Photoelectron Spectroscopy: A Reference Book of Standard Spectra for Identification and Interpretation of XPS Data*, Physical Electronics Division, Perkin-Elmer Corporation, Eden Prairie, MN (USA) **1995**.
[73] J. Zhu, P. Wang, X. Zhang, G. Zhang, R. Li, W. Li, T. P. Senftle, W. Liu, J. Wang, Y. Wang, A. Zhang, Q. Fu, C. Song, X. Guo, *Sci. Adv.* **2022**, *8*, eabm3629.
[74] F. Lu, X. Chen, Z. Lei, L. Wen, Y. Zhang, *Appl. Catal. B* **2021**, *281*, 119521.
[75] B. M. Biwer, S. L. Bernasek, *J. Electron Spectrosc. Relat. Phenom.* **1986**, *40*, 339–351.
[76] N. S. McIntyre, D. G. Zetaruk, *Anal. Chem.* **1977**, *49*, 1521–1529.
[77] H. Libenská, J. Hanuš, T. Košutová, M. Dopita, O. Kylián, M. Cieslar, A. Choukourov, H. Biederman, *Plasma Processes Polym.* **2020**, *17*, 2000105.
[78] Y. Dong, B. Wang, K. Zhao, Y. Yu, X. Wang, L. Mai, S. Jin, *Nano Lett.* **2017**, *17*, 5740–5746.
[79] N. Hellgren, R. T. Haasch, S. Schmidt, L. Hultman, I. Petrov, *Carbon* **2016**, *108*, 242–252.
[80] M. A. Costa de Oliveira, C. Schröder, M. Brunet-Cabré, H. Nolan, A. Forner-Cuenca, T. S. Perova, K. McKelvey, P. E. Colavita, *Electrochim. Acta* **2024**, *475*, 143640.
[81] L. Qu, Y. Liu, J.-B. Baek, L. Dai, *ACS Nano* **2010**, *4*, 1321–1326.
[82] J. T. Titantah, D. Lamoen, *Diamond Relat. Mater.* **2007**, *16*, 581–588.
[83] S. Trasatti, *J. Electroanal. Chem. Interfacial Electrochem.* **1972**, *39*, 163–184.
[84] A. R. Zeradjanin, P. Narangoda, J. Masa, R. Schlögl, *ACS Catal.* **2022**, *12*, 11597–11605.
[85] Y. Miyata, Y. Kuwahara, S. Asakura, T. Shinohara, T. Yakou, K. Shiimoto, *Electrochemistry* **2014**, *82*, 104–108.
[86] E. J. Kelly, *J. Electrochem. Soc.* **1965**, *112*, 124.
[87] U. Sanyal, S. F. Yuk, K. Koh, M.-S. Lee, K. Stoerzinger, D. Zhang, L. C. Meyer, J. A. Lopez-Ruiz, A. Karkamkar, J. D. Holladay, D. M. Camaioni, M.-T. Nguyen, V.-A. Glezakou, R. Rousseau, O. Y. Gutiérrez, J. A. Lercher, *Angew. Chem. Int. Ed.* **2021**, *60*, 290–296.
[88] R. Hreiz, L. Abdelouahed, D. Fünfschilling, F. Lapicque, *Chem. Eng. Res. Des.* **2015**, *100*, 268–281.
[89] S. G. Mairanovskii, T. Y. Rubinskaya, V. P. Gul'tyai, I. V. Proskurovskaya, *Bull. Acad. Sci. USSR Div. Chem. Sci.* **1976**, *25*, 2203–2205.
[90] J. A. Lopez-Ruiz, E. Andrews, S. A. Akhade, M.-S. Lee, K. Koh, U. Sanyal, S. F. Yuk, A. J. Karkamkar, M. A. Derewinski, J. Holladay, V.-A. Glezakou, R. Rousseau, O. Y. Gutiérrez, J. D. Holladay, *ACS Catal.* **2019**, *9*, 9964–9972.
[91] A. K. Cheong, Y. Bolduc, J. Lessard, *Can. J. Chem.* **1993**, *71*, 1850–1856.
[92] J. E. Nutting, J. B. Gerken, A. G. Stamoulis, D. L. Bruns, S. S. Stahl, *J. Org. Chem.* **2021**, *86*, 15875–15885.
[93] J. A. Lopez-Ruiz, U. Sanyal, J. Egbert, O. Y. Gutiérrez, J. Holladay, *ACS Sustain. Chem. Eng.* **2018**, *6*, 16073–16085.
[94] N. Singh, U. Sanyal, G. Ruehl, K. A. Stoerzinger, O. Y. Gutiérrez, D. M. Camaioni, J. L. Fulton, J. A. Lercher, C. T. Campbell, *J. Catal.* **2020**, *382*, 372–384.
[95] J. A. Behan, M. K. Hoque, S. N. Stamatin, T. S. Perova, L. Vilella-Arribas, M. García-Melchor, P. E. Colavita, *J. Phys. Chem. C* **2018**, *122*, 20763–20773.

Manuscript received: March 12, 2024
Revised manuscript received: June 13, 2024
Accepted manuscript online: July 22, 2024
Version of record online: October 17, 2024

Journal of Materials Chemistry A

ROYAL SOCIETY OF CHEMISTRY

PAPER

View Article Online
View Journal

Cite this: DOI: 10.1039/d4ta08953g

Electrocatalytic hydrogenation of unsaturated organics using Mo and W porous carbon-encapsulated nanostructures: impact of metal type on properties and performances†

Filippo Pota, [a] Maida Aysla Costa de Oliveira, [a] Christian Schröder,[a] Aran Rafferty, [a] Clara De Castro,[b] Ludivine Rault,[c] James A. Behan,[d] Frédéric Barrière[d] and Paula E. Colavita *[a]

Electrocatalytic hydrogenation (ECH) of organics of biomass origin represents a promising strategy to enable integration of renewables and circular economy practices. However, most electrocatalysts investigated for ECH remain largely based on precious metals. Nanostructured materials based on transition metals encapsulated in a nitrogenated carbon matrix (M@C:N) offer a promising alternative. Herein, we report on the synthesis of Mo@C:N and W@C:N composites that display the same metal atomic concentrations and thus allow for a comparative study of the effect of the metal centre identity on the properties of such heterostructured materials and their performance in the ECH of benzaldehyde, a diagnostic organic substrate. A combination of structural characterisation methods indicates that the type of metal impacts carbon porosity and metal surface concentration in the synthesised structures. W displays a higher tendency to yield encapsulated nanoparticles compared to Mo, which is instead present with surface excess but at predominantly high oxidation states. Electrolysis studies at varying potentials demonstrate high product rates of benzaldehyde hydrogenation, with good selectivity for the production of the corresponding alcohol *vs.* the dimerization side product. Turnover frequency (TOF) estimates under the operational conditions tested suggest that replacing Mo-centres with W-centres in M@C:N architectures improves overall performance. A comparison of performance indicators with those for Pt-group metals suggests that W@C:N could be a competitive material for practical implementations of ECH.

Received 17th December 2024
Accepted 21st March 2025

DOI: 10.1039/d4ta08953g

rsc.li/materials-a

1. Introduction

The development of efficient and high-performing catalysts for electrochemical processes is essential for the advancement of energy technologies and biomass-valorisation strategies.[1,2] Electrocatalytic hydrogenation (ECH) is a sustainable and versatile approach for the reduction of various organic compounds, including those of biomass origin, using renewables as an energy source.[2,3] ECH is appealing due to its potential for fine-tuning reaction conditions, reducing carbon emissions, and enabling reactions under mild conditions compared to conventional hydrogenation processes that often require high pressures and temperatures.[4] Moreover, ECH offers opportunities for carrying out selective hydrogenations, which are highly desirable for the production of pharmaceuticals, agrochemicals, and fine chemicals.

Electrocatalysts for ECH processes are generally still based on precious metals such as Pd, Pt, Au[5–7] and their alloys, or on carbon-supported precious metals (M/C) such as Pt/C, Pd/C, and Ru/C.[8–11] Since the above elements can command market prices ranging from 15 to 90 USD per g,[12] there is an ongoing research effort to develop abundant and low-cost electrocatalysts as viable alternatives. Recently, the use of metal nanostructures encapsulated within N-doped carbon architectures (M@C:N) has emerged as a promising strategy for the preparation of materials with ECH activity.[13] M@C:N materials have received significant attention as electrocatalysts for a range of cathodic processes of high importance in energy technologies, including the hydrogen evolution reaction (HER), and the reduction of O_2 and CO_2.[14–20] M@C:N heterostructures can display unique properties such as high surface area and tuneable surface electronic structure and chemical reactivity.[18] Moreover, the presence of a carbon shell that protects the metal

[a]School of Chemistry, Trinity College Dublin, College Green, Dublin 2, Ireland. E-mail: colavitp@tcd.ie

[b]Earth Surface Research Laboratory, Geology Department, Trinity College Dublin, College Green, Dublin 2, Ireland

[c]Univ Rennes, CNRS, ScanMAT – UAR 2025, Rennes, F-35000, France

[d]Univ Rennes, CNRS, Institut des Sciences Chimiques de Rennes – UMR 6226, Rennes, F-35000, France

† Electronic supplementary information (ESI) available. See DOI: https://doi.org/10.1039/d4ta08953g

from oxidation due to air exposure or from corrosion in aqueous solutions can expand the range of metals used for electrocatalysis to encompass low-cost and earth abundant transition metals, enhancing the versatility and stability advantages of M@C:N architectures.[18,21] However, development of M@C:N architectures for ECH still presents significant challenges and little is known about how to optimize both the metal core and the graphitised scaffold to improve ECH performances. Organic hydrogenations must progress with efficiency under electrochemical conditions at which the HER is typically a competing reaction. The Volmer reaction step leading to H_{ads} activation at the electrocatalyst surface is a requirement for both the HER and the ECH to take place.[22] However, these two reactions compete for this intermediate to yield final products: indeed the Tafel and Heyrovsky steps in the HER consume H_{ads} species and may drastically suppress the faradaic efficiency (FE) of organic hydrogenations.[11]

Previous work from our group demonstrated for the first time that M@C:N electrocatalyst materials synthesised using a low cost transition metal such as iron are active in the ECH of carbonyl compounds. In this work, we show that this material design strategy can be expanded to incorporate alternative transition metals into the electrocatalyst, namely W and Mo, enabling the optimisation of ECH performance indicators in M@C:N architectures. Mo and W are highly desirable as metal cores due to their significantly lower costs compared to precious metals, with market prices of *ca.* 0.07 USD per g and 0.05 USD per g, respectively.[12] Further, these metals and several of their compounds also possess the ability to activate chemisorbed hydrogen through the Volmer step while displaying differences in their activity towards hydrogen evolution,[18,23,24] thus offering a potential route to regulating the degree of competition between the HER and the ECH. Benzaldehyde (BZH) was used as a model organic compound due to its solubility in water[25,26] and because it enables quantitative benchmarking of performance indicators relative to other results in the ECH literature.[27–29] Our results demonstrate that the identity of the metal core can have a profound influence on the properties of the graphitised carbon matrix and on the surface chemical composition in M@C:N materials with identical atomic metal loadings. This translates into important changes in product rates, faradaic efficiencies and turnover frequencies thus providing new insights on how to optimise transition metal-based heterostructured electrocatalysts for the ECH of organics.

2. Material and methods

2.1 Materials

Nafion® 117 solution (5%), resorcinol (99%), Pluronic F-127, melamine (99%), hydrochloric acid (37%), sulfuric acid (95–98%), nitric acid (≥65%), formaldehyde solution (37 wt%), hydrogen peroxide (30%), sodium sulfate (>99%); benzaldehyde (BZH, >99%); hydrobenzoin (HBZ, 99%); acetophenone (>99%); ethyl acetate (>99%); ammonium heptamolybdate tetrahydrate ($(NH_4)_6Mo_7O_{24}\cdot 4H_2O$, 99%) were all purchased from Sigma Aldrich and used as received. Methanol (>99%), benzyl alcohol (BA, >99%) and ammonium metatungstate hydrate ($(NH_4)_6W_{12}O_{39}\cdot H_2O$, 99%) were purchased from Fisher and used as received. Black Pearls 2000® (BP, >1400 $m^2\ g^{-1}$)[30,31] were purchased from Cabot.

2.2 Methods

BP were purified under reflux in concentrated HNO_3 at 90 °C for 4 h, then filtered and washed until reaching a neutral pH.[13] Porous carbon-based catalysts were synthesised by first dissolving resorcinol (0.83 g), Pluronic F-127 (1.25 g), and melamine (0.42 g) in 20 mL of a 1 : 1 water : methanol solution and stirring for 15 min. Ammonium heptamolybdate tetrahydrate $(NH_4)_6Mo_7O_{24}\cdot 4H_2O$, or ammonium metatungstate hydrate $(NH_4)_6W_{12}O_{39}\cdot H_2O$, were then added as metal precursors in amounts summarised in Table 1, followed by the addition of concentrated HCl (0.2 g) and stirring for 1 h. Formaldehyde (1.25 g) was introduced dropwise, resulting in a homogeneous slurry after vigorous stirring for another hour. Purified BP (0.75 g) was added to the mixture and stirred for an additional 15 min. The mixture was heated in a Teflon-lined autoclave at 50 °C for 2 days, then the vessel was opened and the solid was thoroughly dried at the same temperature. The sample was ground in a mortar, inserted in a tube furnace at 250 °C under N_2 flow and, finally, annealed at 800 °C for 2 h in a N_2 : NH_3 flow (1 : 1 vol., 200 sccm total) following the procedure reported previously.[13]

2.3 Materials characterisation

Brunauer–Emmett–Teller (BET)[32] specific surface area was determined from N_2 adsorption at 77 K with a Nova 2200e surface area analyzer (Quantachrome, UK). The specific surface area was calculated from data in an optimal relative pressure range according to the method proposed by Rouquerol *et al.*,[33] by way of the micropore BET assistant feature of the NovaWin software. Pore size distributions were determined using the density functional theory (DFT) method[34,35] based on the calculation model: N_2 at 77 K on carbon (slit pore, NLDFT equilibrium model). Prior to analysis, the samples were outgassed at 250 °C under vacuum for 2 h. Thermogravimetric analysis (TGA) was carried out using a Pyris 1 thermogravimetric analyser (PerkinElmer) with a hold time of 10 min at 150 °C, followed by a 10 °C min^{-1} ramp in air to 900 °C. Powder X-ray diffraction (XRD) was carried out using a D2 Phaser diffractometer with LynxEye detector (Bruker) and a Cu Kα source. Scanning electron microscopy (SEM) was performed using a Zeiss Ultra microscope at 5 kV accelerating voltage with an SE2 detector. High resolution transmission electron microscopy (HR-TEM) was performed using a Jeol JEM 2100HR at 200 kV using EDS SDD Oxford X-Max 80T detector. Inductively coupled plasma-optical emission spectroscopy was performed in a iCAP 7000 ICP-OES analyser (Thermo Fisher); samples were treated in HNO_3 (≥65%) overnight and diluted in deionised water to a nominal concentration of 10 mg L^{-1}. Energy-dispersive X-ray fluorescence analysis (XRF) was performed using a Rigaku ED-XRF in He atmosphere on bulk solid samples. X-ray photoelectron spectroscopy (XPS) was carried out in a monochromated Omicron XM1000MK II X-ray

Table 1 Summary of samples, details of the metal precursors used, metal content after the final graphitisation step by weight-% and by atomic-%, and BET specific surface area

Material	Metal precursor	Initial metal precursor (g)	wt. (%)	at. (%)	BET ($m^2\ g^{-1}$)
Mo@C:N	$(NH_4)_6Mo_7O_{24}\cdot 4H_2O$	1.78	10.8[a]	1.51	229
W@C:N	$(NH_4)_6W_{12}O_{39}\cdot H_2O$	0.61	17.7[b]	1.41	450
RPM/BP	N/A	N/A	N/A	N/A	600

[a] Data obtained by ICP-OES on the graphitised material. [b] Data obtained by ED-XRF on the graphitised material.

photoemission spectrometer, with an EA 125 analyser and an Al Kα (1486.7 eV) source; pass energies of 50 and 15 eV were used for survey and high-resolution spectra, respectively. Spectra were analysed using CasaXPS; best fits were carried out on spectra after Shirley background correction using mixed Gaussian–Lorentzian functions. Elemental compositions were obtained from peak areas of the high-resolution scans after correction for relative sensitivity factors. Product analysis was carried out using an Agilent 8860 gas chromatograph coupled to a flame ionisation detector (GC-FID), H_2 as carrier gas, split injection (1 : 10, 2 mL min^{-1} flow) and a DB-WAX UI column (30 m × 0.250 mm × 0.50 μm, Agilent J&W).

2.4 Electrochemical characterisation

Synthesised materials were mortared and sieved (20 μm) prior to the preparation of catalyst inks. Ink dispersions contained catalyst (0.0100 g ± 0.0003), 270 μL of deionised water, 160 μL of methanol (MeOH) and 53 μL of Nafion solution. Each addition was followed by 10 min of sonication in a cooling bath; the resulting dispersion was drop-cast on carbon working electrodes for further analysis. Glassy carbon disks (GC, Ø 5 mm, HTW GmbH) were used as working electrodes for cyclic voltammetry experiments. GC disks were polished with decreasing grades of alumina slurry (Ted Pella) according to published procedures;[36] disks were thoroughly sonicated and rinsed between polishing steps to remove any residue from the preceding step. GC disks were mounted in a Teflon disc holder (Pine instruments) and modified with the ink dispersion (10 μL), then dried under inert gas, resulting in a loading of 1.06 mg cm^{-2}. Flags of carbon cloth (CC, 1 cm^2 geometric area, FuelCellStore) with microporous layer were used as current collectors for electrolysis experiments. The CC was used as received after covering the back side with insulating polyimide tape. 52 μL of the ink were drop-cast in two equal aliquots, drying the ink after each step in a hot plate (80 °C), followed by compression of the CC in a hydraulic press (Specac) at room temperature; this resulted in loadings of 1.07 mg cm^{-2} for all samples. Voltammetry experiments were carried out using a standard 3-electrode cell controlled by a potentiostat (Metrohm Autolab), using graphite rods (Morgan advanced materials) as counter electrodes and Ag/AgCl (1 M KCl) as reference electrode (0.235 V *vs.* SHE). All potentials are reported *vs.* the relative hydrogen electrode (RHE) based on the experimentally determined pH of the electrolyte. The cell was cleaned with piranha and deionised water prior to each experiment, then filled with 250 mL volume of supporting electrolyte (0.100 M H_2SO_4); the electrolyte was purged with N_2 for at least 15 min prior to characterisation. Electrolysis was performed in a customised H-cell thermostated at 25 °C as previously reported.[13] Quantitative analysis was conducted *via* GC-FID after extraction with ethyl acetate, using acetophenone as internal standard.

3. Results and discussion

Carbon-based materials were synthesised using a procedure described in our previous study[13] and schematically illustrated in Fig. 1a. Briefly, materials were synthesised *via* polycondensation of resorcinol and formaldehyde with the addition of BP carbon black as a conductive scaffold, Pluronic F-127 as a soft template and melamine as a nitrogen source. Annealing at 800 °C under N_2/NH_4 atmosphere resulted in graphitisation, yielding a material from here onwards referred to as RPM/BP. Metal precursors can also be added to this procedure to achieve metal encapsulation in a M@C:N architecture.[13,37] In this work, we integrated Mo and W metal precursors into the established protocol; Table 1 shows the precursor quantities used for the synthesis of each sample, as well as the metal content obtained after the final graphitisation step in the synthesis, by weight and by atomic percent. The bulk composition of Mo-based materials was investigated *via* ICP-OES, while for W-based electrodes ED-XRF analysis was performed. The atomic-% content in the bulk was calculated assuming carbon and metal to be the main components. The two M@C:N materials exhibit similar metal atomic content of *ca.* 1.5% and can therefore be used to compare the effects of a change of metal on the nanocomposite structure and its electrochemical performance.

The bulk structure of the materials was first investigated *via* XRD; Fig. 1b reports patterns collected for metal-free RPM/BP, Mo@C:N and W@C:N. RPM/BP materials yielded two peaks at 24.3° and 43.2°, indexed as (002) and (101) reflections of the graphitic carbon,[38] respectively. The Mo@C:N pattern indicates the presence of crystalline phases consisting of mostly Mo_2C, with contributions from MoO_2 oxide. Peaks at 34.4°, 37.8°, 39.3°, 51.9°, 61.5°, 69.3°, 74.4°, 75.6°, match well those Mo_2C reference (PDF#35-0787) and are assigned to reflections (100), (002), (101), (102), (110), (103), (112) and (201), respectively. The broad peak at 25.3° is assigned to (002) reflection of graphitic carbon and matches the main reflection in the pattern of metal-free RPM/BP. The small broad peak at 36.9° indicates the presence of MoO_2 (PDF#65-5787) as well. The XRD pattern for

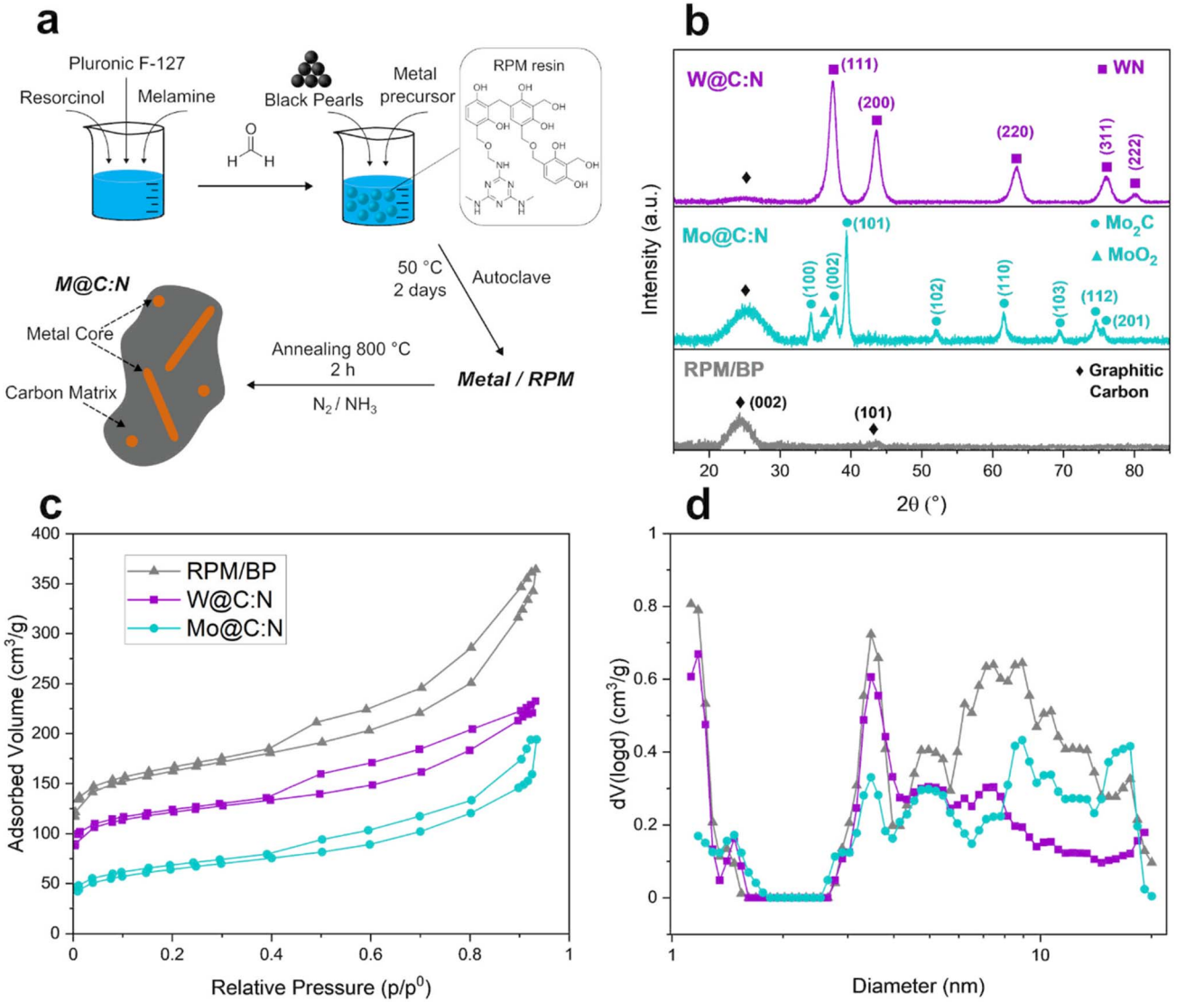

Fig. 1 (a) Scheme illustrating main steps of the materials synthesis protocol. (b) XRD patterns for metal-free RPM/BP, Mo@C:N and W@C:N. (c) Nitrogen adsorption–desorption isotherms and (d) pore size distributions for RPM/BP, W@C:N and Mo@C:N materials.

W@C:N shows peaks at 37.4°, 43.6°, 63.3°, 76.1° and 80.1°, that match those of the WN reference pattern (PDF#65-2898) and are assigned to reflections (111), (200), (220), (311), and (222), respectively.[39,40] The (002) reflection of graphitic carbon is also detectable at 24.6°.

Synthesised materials were found to be porous; Fig. 1c shows the N_2 adsorption/desorption isotherms collected for Mo@C:N, W@C:N and the metal-free RPM/BP. Samples display similar hysteresis loops characteristic of type IV isotherms, associated with capillary condensation, and type H4 loops reported for narrow slit-like micro-/mesopores.[41,42] The BET specific surface area values calculated from the isotherms are summarised in Table 1. The incorporation of Mo or W into the structure results in a decrease in BET surface areas by 15% to 67% compared to metal-free RPM/BP. Assuming that contributions to the surface area from metal-containing phases are negligible relative to those from the carbon phases, and accounting for the metal wt% in Table 1, it is possible to note that for W@C:N the BET area is only slightly lower than expected from a replacement of 1.4% of C atoms in RPM/BP with W (494 $m^2 g^{-1}$). This suggests that the development of the carbon microscopic area during graphitisation is not significantly affected by the presence of the W centres at these concentrations. On the other hand, for Mo@C:N the BET area is less than half the value expected based on replacement of 1.5% of C atoms alone (535 $m^2 g^{-1}$). This suggests that Mo centres impact the development of pores in the carbon phase to a much greater extent than W. Metal centres can have a catalytic effect on carbon gasification and graphitisation,[37,43–47] and such processes can enhance pore opening and lead to reductions in BET areas.

To better understand the impact on pore size, the DFT method was used to generate pore size distributions (PSD), shown in Fig. 1d. The three materials are similar insofar as they exhibit distinct occurrences of porosity in the micro (<2 nm)

and meso (2–50 nm) ranges, with broadly similar distributions, *i.e.* peaks at 1.5, 3.5 and 5 nm, characteristic of the parent carbon phase. W@C:N and RPM/BP share the most obvious similarities, with a significant volume of micro-pores, which are key contributors to the surface area. A closer inspection of the micropore region shows differences, in that the second peak (*ca.* 1.5 nm) grows according to Mo@C:N > W@C:N > RPM/BP, while the peak at 1.1 nm decreases accordingly. In other words, larger micropores are generated at the expense of smaller ones. Notably, Mo@C:N displays limited contributions from micro-pores relative to both RPM/BP and W@C:N. This likely explains the lower surface area observed for this sample, as well as its low pore volume (Table S1†). Further, it highlights a key difference between Mo@C:N and W@C:N: for Mo@C:N the smallest tranche of micropores have either been rendered inaccessible or have undergone enlargement. DFT pore width values (mode), in Table S1,† show that pore size increases with a decrease in surface area, as expected. Of note is the fact that the values for RPM/BP and W@C:N occur in the micropore range, where that of Mo@C:N falls in the mesopore range thus confirming that pore evolution in the N-doped carbon matrix is significantly affected by the incorporation of Mo centres.

TGA analysis in air was carried out and results are reported in Fig. S1.† Briefly, in the case of the metal-free RPM/BP a single combustion process with zero residual mass is observed over 650–750 °C, associated with oxidation of graphitised carbon. In the presence of metals, carbon oxidation occurs at significantly lower temperatures, with the effect on onset temperature being more pronounced in the case of Mo-containing materials. This is consistent with oxidation being catalysed by metal centres, in agreement with prior literature;[48,49] while the enhanced effect of Mo *vs.* W in these reactions is also consistent with observations from BET and DFT analysis that suggest a greater effect of Mo centres on pore opening processes.

Morphology was investigated *via* electron microscopy. Fig. 2a shows an SEM image of Mo@C:N, revealing particles with rough and irregular surfaces. SEM-EDX analysis confirms that Mo is uniformly distributed over the carbon matrix (see also Fig. S2†). HR-TEM, in Fig. 2b, indicates that the sample consists of opaque nanoparticles (~5 nm diameter), embedded within

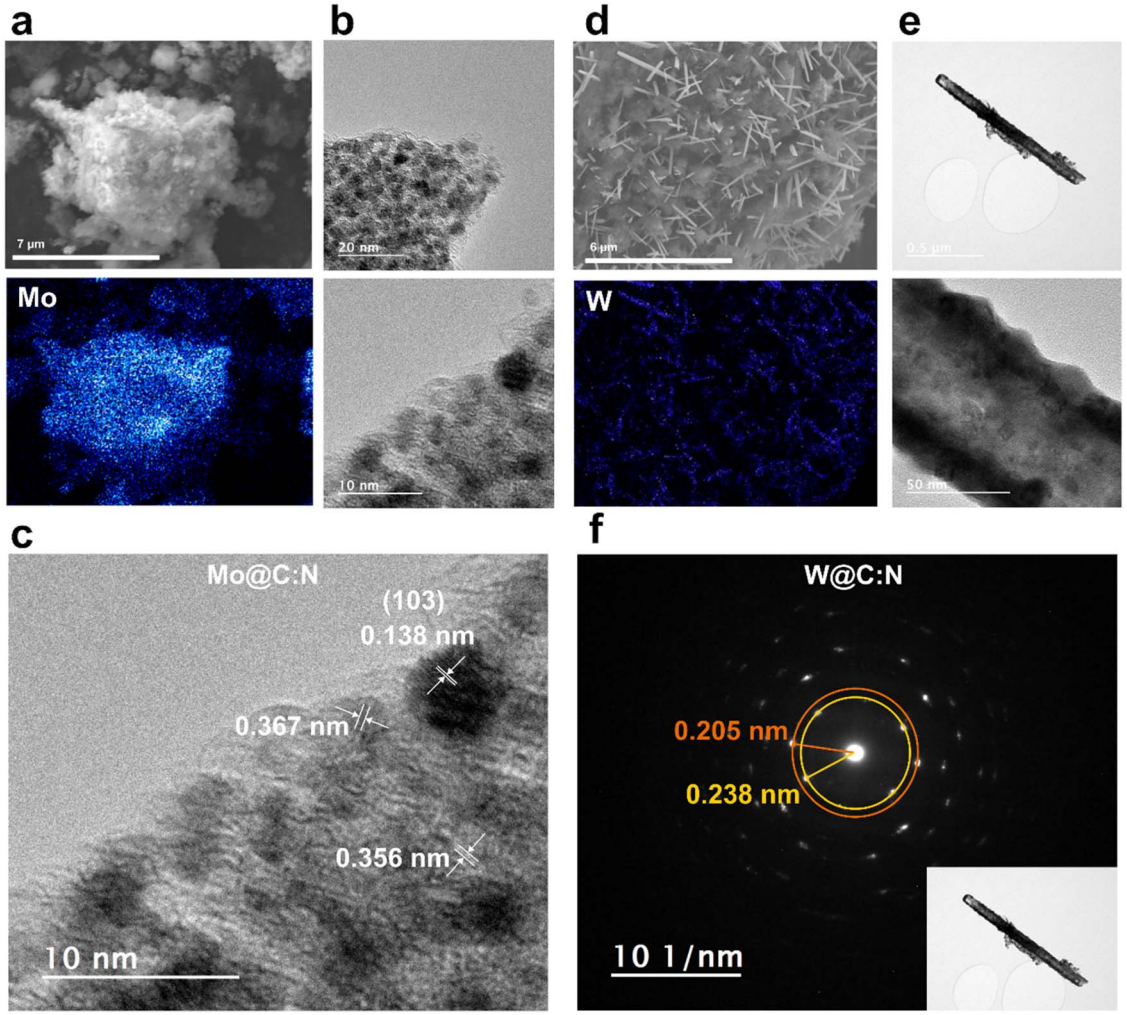

Fig. 2 SEM and EDX mapping (a) and HR-TEM (b) of Mo@C:N; (c) HR-TEM for Mo@C:N with measured *d*-spacings (white arrow). SEM and EDX mapping (d) and HR-TEM (e) of W@C:N; (f) SAED pattern of WN nanorods with estimated *d*-spacing.

a graphitised carbon matrix: nanoparticles exhibit lattice *d*-spacing of 0.138 nm, in Fig. 2c, closely matching (103) reflections of Mo_2C at 0.135 nm (PDF#35-0787). SEM of W@C:N, in Fig. 2d, displays a porous solid matrix with well-defined rod-like nanostructures with diameters in the 50–200 nm range. SEM-EDX indicates that these nanorods are rich in W (see also Fig. S2†). HR-TEM of such features, in Fig. 2e, reveals that they display well defined crystal facets and are encapsulated within a graphitised shell 10–20 nm in thickness. The selected area electron diffraction (SAED) pattern of nanorods, in Fig. 2f, confirms *d*-spacings of 0.238 nm and 0.205 nm, consistent with the (111) and (200) reflections of WN at 0.238 nm and 0.206 nm, respectively (PDF#65-2898).

Surface composition was studied using XPS and Table 2 summarises results obtained from best fits of high-resolution spectra for all materials. Survey spectra, Fig. S3,† display peaks associated with C 1s, N 1s and O 1s ionisations, as well as those associated with characteristic Mo and W ionisations for the respective M@C:N materials. Both the nitrogen and metal %-contents are much lower for W@C:N than for Mo@C:N, despite the two metals being present at similar atomic bulk concentrations. Indeed, a comparison between metal/carbon atomic %-ratios obtained by XPS and those from bulk determinations (Table 1) indicates that while W remains preferentially in the bulk, or below sub-surface, Mo is found predominantly at the air interface.

C 1s spectra of Mo@C:N and W@C:N are shown in Fig. 3a. The C 1s peak was deconvoluted using five components attributed to sp^2 (*ca.* 284.4 eV) and sp^3 (*ca.* 285.4 eV) carbon, C–O/C–N (*ca.* 287 eV) and C=O/COOH (*ca.* 289 eV) groups, and π–π^* excitations (*ca.* 292 eV).[50–53] For all materials, the sp^2 peak constitutes the largest contribution to the total intensity, as shown in Table 2 suggesting that materials undergo graphitisation to a similar extent during the annealing step. N 1s spectra are shown in Fig. S3;† the low N-content in W@C:N results in low overall intensity, nonetheless, peak binding energies at *ca.* 498 eV for both spectra suggest that pyridinic-N accounts for the majority of contributions, as was also observed for metal-free RPM/BP (Fig. S4†). Best-fits obtained using three components assigned to graphitic-N, pyrrolic-N and pyridinic-N,[51,54] with details summarised in Table S2,† support this conclusion. An additional peak at 394.6 eV is also observed for Mo@C:N and is characteristic of Mo $3p_{3/2}$ ionisations.[55–57] Finally, we note that differences in N/C surface content observed *via* XPS spectra are consistent with results from XRD characterization. XRD showed that annealing yields MoC_x/MoO_x and WN phases in Mo@C:N and W@C:N, respectively. This indicates that N-precursors react readily with W and are sequestered to the subsurface, as is the case for the W atoms, whereas for Mo@C:N they remain available to react with the carbon matrix.

The Mo 3d spectrum of Mo@C:N, Fig. 3b, was fitted using three doublets with an energy splitting of 3.1 eV, assigned to Mo^{2+} (228.5 eV), Mo^{4+} (229.8 eV), and Mo^{6+} (232.2 eV) species. Mo^{2+} components indicate the presence of molybdenum carbides in the form of Mo_2C and/or MoC, whereas Mo^{4+} and Mo^{6+} arise from oxide species due to surface oxidation in air, in agreement with previous reports for Mo carbides.[55,58,59] Peak area ratios indicate that the majority of surface Mo (>80%) is indeed oxidised after air exposure, in contrast with the predominance of carbide phases in the bulk, evidenced by XRD studies.

The W 4f spectrum of W@C:N, Fig. 3c, was fitted using two doublets with energy splitting of *ca.* 3 eV.[50,60–62] The $4f_{7/2}$ peak at low binding energy (32.2 eV) is characteristic of either W_2C or WN,[63–65] and therefore consistent with XRD results. The $4f_{7/2}$ peak at high binding energy (35.2 eV) is assigned to oxidised tungsten in the form of WO_3.[61,65] Notably, the oxide component accounts for a minority of surface W species, while carbides/nitrides constitute 64–68% of the contributions from metal centres. These compounds have been reported to oxidise in air as demonstrated by multiple studies,[58,66–69] therefore the absence of significant contributions from oxide species suggests that the majority of the carbide/nitride phases are encapsulated within a protective carbon shell that prevents/minimises oxidation.[13] This further supports findings from HR-TEM, while being consistent with the surface W-content being lower than the bulk value.

The electrochemical response was investigated *via* voltammetry experiments in 0.1 M H_2SO_4 using glassy carbon disks modified with the M@C:N materials *via* drop casting. Fig. 4 shows linear sweep voltammograms (LSV) for Mo@C:N and W@C:N at 2 mV s^{-1} in the presence and absence of 30.0 mM benzaldehyde in the electrolyte. In the absence of benzaldehyde, Mo@C:N displays HER activity ($\eta = -0.16$ V at 1.5 mA cm^{-2}) comparable to that observed at a range of Mo_2C electrodes under similar conditions.[59,70–72] The presence of a cathodic peak at −0.078 V, characteristic of proton-coupled reductions of MoO_3 at low pH,[72–74] is consistent with a significant concentration of Mo^{6+} at the electroactive surface of Mo@C:N and with evidence from XPS characterisation. Mo_2C is reported to be activated under cathodic polarisation,[72] while MoO_2/MoO_3 are sluggish in the HER;[72] therefore the observed

Table 2 Summary of atomic elemental compositions and selected best-fit results obtained from high resolution XPS spectra of synthesised materials

Material	C_{sp^2}/C_{tot}[a] (%)	N/C (at%)	M/C (at%)	MC_x or MN_x/M_{tot} (%)	$M-O/M_{tot}$ (at%)
Mo@C:N	63.4	19.5	5.7	16.3	83.7
W@C:N	57.4	1.7	0.45	64.3	35.7
RPM/BP	51.6	4.69	NA	NA	NA

[a] Calculated as area ratio of the best-fit component at 284.4 eV over the total C 1s peak.

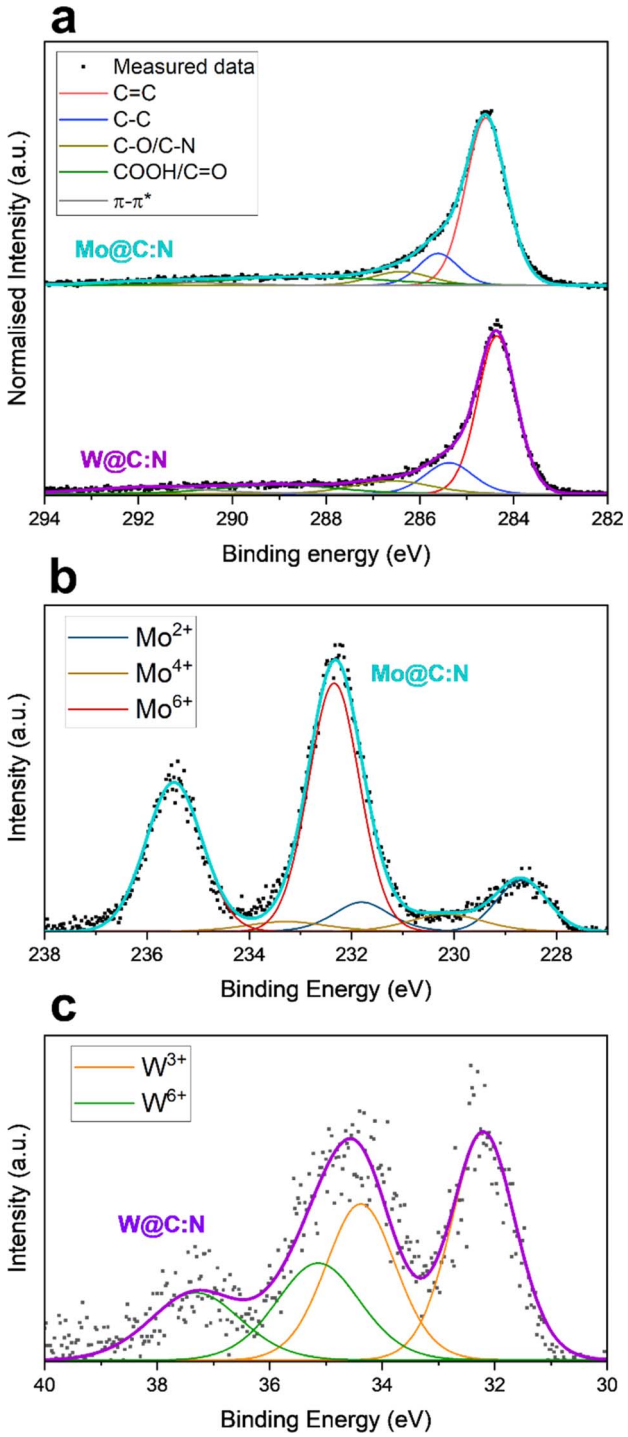

Fig. 3 (a) High resolution spectra and best-fits in the C 1s region for Mo@C:N (top) and W@C:N (bottom). High resolution spectra and best-fits in the (b) Mo 3d and (c) W 4f regions of Mo@C:N and W@C:N, respectively.

activity of Mo@C:N in acid electrolytes is likely to be dominated by Mo^{2+} centres at the electrolyte interface.

W@C:N also shows activity in the HER ($\eta = -0.50$ V at 1.5 mA cm^{-2}) but with lower current densities relative to Mo@C:N. Similar overpotentials have been reported for either WN[75] or carbon-encapsuled WC electrodes.[76] Interestingly, the LSV is

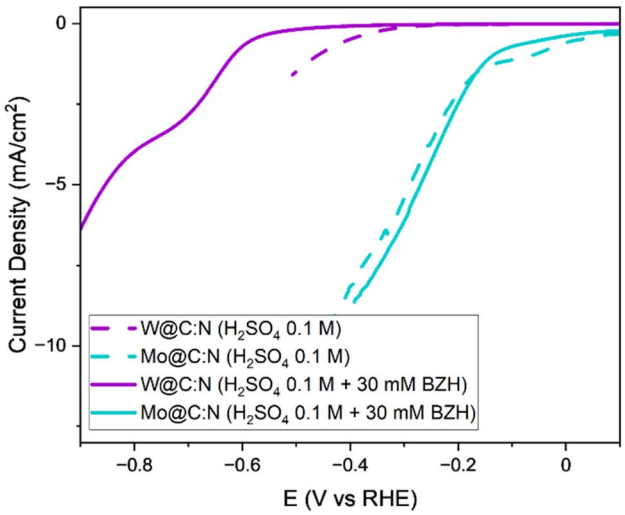

Fig. 4 LSV collected on GC disk for W@C:N and Mo@C:N in 0.1 M H_2SO_4 (dashed line) and 0.1 M H_2SO_4 with 30 mM BZH (solid line), at 2 mV s^{-1} scan rate.

devoid of peaks characteristic of proton-coupled reductions of WO_3 species,[77] thus supporting the conclusion from XPS that the majority of W surface sites are in a low oxidation state. Given that drop-cast films are porous, a comparison of the LSV curves was also carried out after normalisation by capacitive contributions to account for differences in microscopic area (Fig. S5†).[78–80] Mo@C:N was found to still display higher HER currents than W@C:N in agreement with prior reports of better HER performance in general for MoC_x *vs.* WC_x electrodes in acid electrolytes.[81] Finally, control LSV experiments with polished glassy carbon and metal-free RPM/BP electrodes, Fig. S5,† yielded higher HER overpotentials than either Mo@C:N or W@C:N after correction for microscopic area. Results, therefore, strongly suggest that M@C:N materials have improved intrinsic HER activity relative to metal-free graphitic carbons and that this can be attributed to the incorporation of Mo/W centres in the form of carbides/nitrides.

LSV in 0.1 M H_2SO_4 with 30 mM benzaldehyde at 2 mV s^{-1}, in Fig. 4, show a cathodic peak associated with the reduction of the organic at W@C:N (*ca.* −0.7 V), while the overall cathodic current density is decreased relative to the LSV in supporting electrolyte. This indicates a general quenching of HER faradaic currents due to adsorption of the organic species.[13,82,83] On the other hand, Mo@C:N displays only slight changes in current density while only a broad, ill-defined peak is discernible over the cathodic background current (*ca.* −0.3 V). This suggests that there is minimal competition by organic species for the HER-active sites at the Mo@C:N surface. Nonetheless, the peak at −0.078 V, visible in supporting electrolyte, is suppressed thus suggesting that benzaldehyde interacts with Mo^{6+} surface sites.

Benzaldehyde reactions were then studied using electrolysis experiments coupled to product detection. Carbon cloth (CC) current collectors were drop-coated using the same ink dispersions as for disk voltammetry studies. Fig. 5a and b show SEM and SEM-EDX images of CC coated with Mo@C:N and W@C:N,

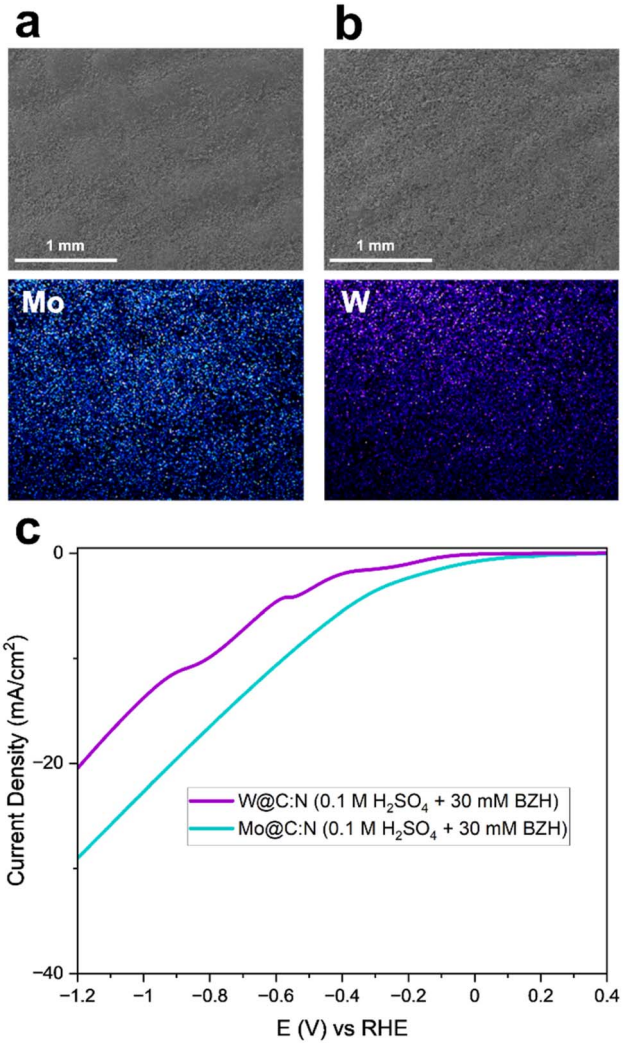

Fig. 5 SEM images and EDX mapping of CC electrodes coated with (a) Mo@C:N and (b)W@C:N electrocatalyst inks. (c) LSV collected for W@C:N and Mo@C:N on CC support in 0.1 M H_2SO_4 + 30 mM BZH. An expanded view over 0 to −0.9 V is shown in Fig. S8.†

respectively, indicating uniform metal distribution over the CC surface. The LSV in supporting electrolyte (Fig. S6†) shows that the presence of the carbon materials increases the capacitance of CC significantly, as expected after coating with a porous particle film. Capacitance values were found to be comparable for Mo@C:N and W@C:N (Fig. S7 and Table S3†), suggesting that the two materials do not differ significantly in ECSA despite their differences in BET area. Fig. 5c shows LSVs recorded for Mo@C:N and W@C:N on CC in 30 mM BZH in 0.1 M H_2SO_4. W@C:N displays multiple broad cathodic peaks between −0.8 and −0.26 V whereas Mo@C:N yields a featureless response, likely due to HER being the dominant contribution to the LSV, as observed for disk electrodes. The presence of multiple peaks associated with benzaldehyde in the LSV could arise from either mixed mass transport regimes in the porous CC electrode,[84,85] or from reduction at different functional sites, as observed by some even at carbon disk electrodes of well-defined geometry.[86]

An H-cell was used for electrolysis studies, as previously described.[13] Chronoamperometry experiments were carried out in a 30 mM BZH in 0.1 M H_2SO_4 solution at three selected potentials: −0.26, −0.5 and −0.8 V *vs.* RHE, as shown in Fig. 6a. Catalyst layers displayed high mechanical stability over the duration of the experiments thus yielding stable chronoamperogram curves (Fig. S9†). Repeat potential step experiments also yielded comparable chronoamperograms (Fig. S9†), thus confirming the robustness and stability of the fabricated electrodes. Log–log plots of current *vs.* time (Fig. S9†) show that after *ca.* 100–150 s, the slope of these plots transitions from a value of *ca.* −0.5 to a value close to zero, indicative of convective control. Evidence of convection is in agreement with prior work on similar electrode materials and is attributed to gas evolution during HER.[13]

Both benzyl alcohol (BA) and hydrobenzoin (HBZ) were identified as reduction products *via* gas chromatography, confirming the hydrogenation of benzaldehyde. Carbon balance was found to be *ca.* 90% (Fig. S10†) for all materials, indicating negligible mass losses due to diffusion through the membrane, loss to the headspace and/or to surface adsorption. Yields and conversion values were calculated for all materials and are shown in Fig. S11.† As the potential is shifted to more cathodic values, both conversion and yield show an increase, while the preferred product remains BA (Fig. S12†). At any given potential, better yields and conversions were observed for W@C:N *vs.* Mo@C:N over 2 h, thus suggesting that given, the same metal atomic concentrations, W-containing catalyst layers result in better operational performances in organic hydrogenations.

The faradaic efficiency, FE_{ECH} were calculated and are summarised in Fig. 6b. Mo@C:N shows good FE_{ECH} at the lowest overpotential, but the efficiency of reductions decreases significantly at −0.5 V before increasing slightly at −0.8 V again. The greater HER activity of Mo@C:N *vs.* W@C:N and RPM/BP, enables facile H_{ads} activation even at −0.26 V which increases rates of ECH *via* H_{ads} addition or concerted e-H^+ additions;[5,82] however, as the potential is shifted to more cathodic values, the HER becomes the dominant faradaic process decreasing the overall efficiency of ECH. At higher cathodic overpotentials proton coupled reductions of BZH can become an additional and energetically favourable pathway for the production of BA/HBZ particularly at carbon surfaces, as discussed in detail in computational studies by Cantu *et al.*[5] We believe this is likely to explain the increase in FE_{ECH} at −0.8 V for Mo@C:N. In the case of both W@C:N and RPM/BP, the efficiencies are low at −0.26 V but superior to that of Mo@C:N at −0.5 V, which is consistent with these materials being less effective at evolving hydrogen and with the HER being suppressed as a competing reaction at −0.5 V.

Product rates normalised by geometric area and by capacitance are shown in Fig. 6c and d, respectively. Normalisation by capacitance puts in clear evidence the significant differences in specific electroactive area between the metal-free material and M@C:N catalysts, as well as the superior performance in organic hydrogenations obtained with the latter. W@C:N materials offer significant advantages at −0.5 and −0.8 V. Interestingly, while the Volmer step is facile and H_2 desorption

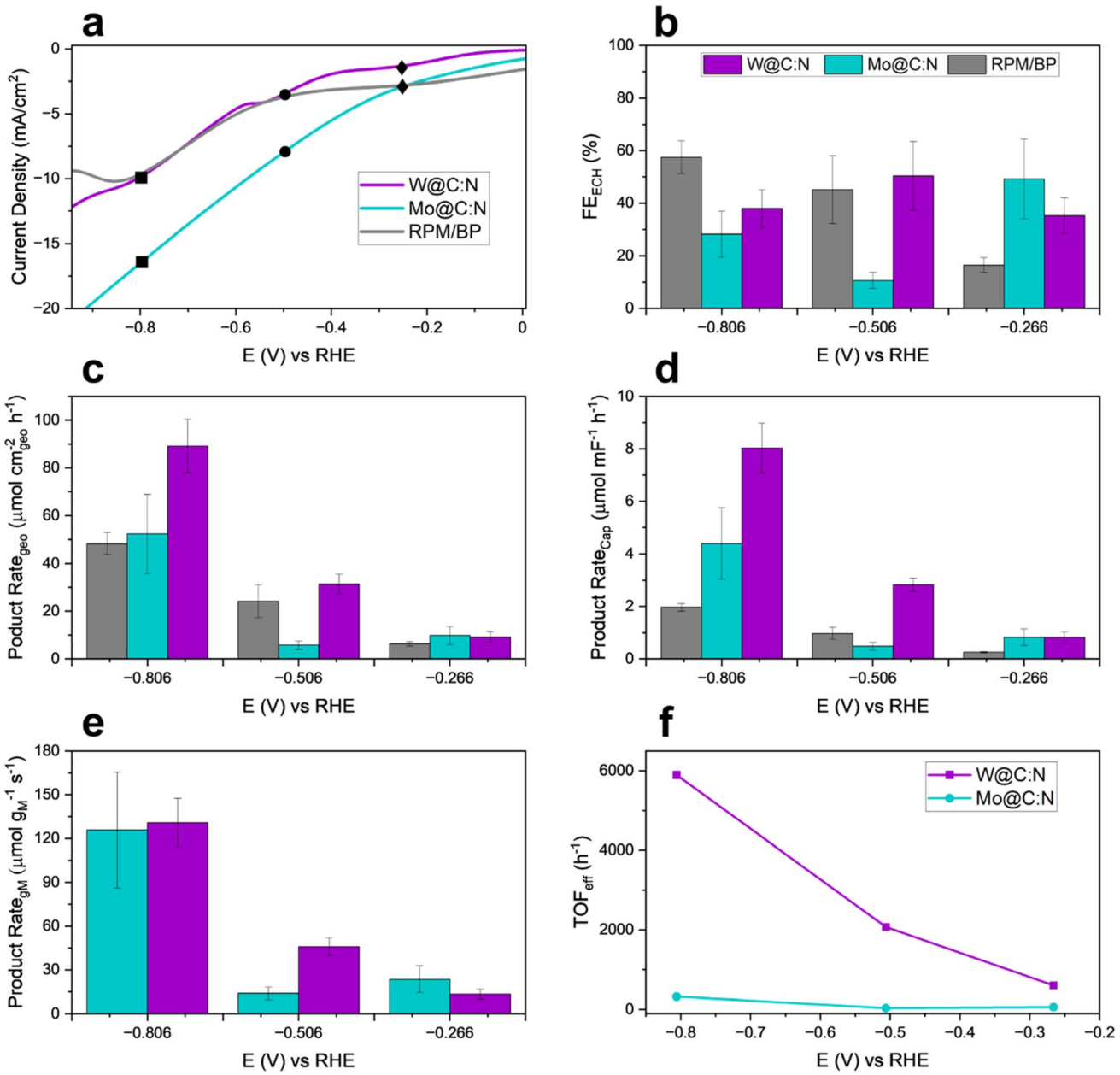

Fig. 6 (a) LSV collected for W@C:N and Mo@C:N on CC support in 0.1 M H_2SO_4 + 30 mM BZH with highlighted potential at −0.26 V (◆), −0.5 V (●) and −0.8 V (■) *vs.* RHE. (b) Total ECH FE %. Product rate normalised by geometric area (c), by capacitance (d), and by amount of metal in the bulk for both M@C:N (e). TOF calculated values for both M@C:N samples normalised for surface atomic concentrations (f).

limiting at WC/WN,[24,87] it is H_{ads} activation that is rate determining at carbons. Therefore, H_{ads} coverages should remain low at RPM/BP but increase readily with cathodic overpotential at WN, which likely explains why the product rate normalised by specific area is markedly superior for W@C:N at both −0.5 V and −0.8 V.

Fig. 6e shows product rates for Mo@C:N and W@C:N after normalisation by bulk metal contents. These results align with trends in FE_{ECH}, showing higher performance for Mo@C:N at −0.26 V and for W@C:N at −0.5 V; while at −0.8 V the two material shows similar product rates. However, their performances diverge when considering differences in surface segregation between Mo and W centres observed for the two M@C:N. This can be taken into account by estimating an effective turnover frequency (TOF_{eff}) for W and Mo metal centres at the electrolyte interface. Assuming that the double-layer capacitance arises from the carbon matrix alone (20 μF cm^{-2})[88,89] and accounting for the areal carbon density of graphite of 3.82×10^{15} atoms per cm^2,[90] TOF_{eff} values can be calculated using the atomic %-contents of 0.43% and 4.3% for W and Mo, respectively, obtained from XPS. TOF_{eff} values thus calculated are shown in Fig. 6f and suggest that encapsulated W centers yield significant advantages in terms of intrinsic activity.

The above results indicate that both Mo@C:N and W@C:N show activity in the hydrogenation of benzaldehyde and that W@C:N appears to be particularly promising, achieving satisfactory FE_{ECH} and good product rates at moderate potentials. At low overpotentials, FE_{ECH} values for Mo@C:N samples are comparable to those reported for Pt/C (~60%) and exceed those of similar M@C:N architectures synthesised using Fe as a metal core.[13,82] Further, W@C:N shows good FE_{ECH} at −0.5 V compared to Pt/C, as determined by Song *et al.* at pH 5 and similar potentials.[82] Interestingly, TOF_{eff} values estimated for W@C:N under our operational conditions are comparable to those reported for Pt/C and Rh/C catalysts at −0.5 V *vs.* RHE in the same work. Additionally, both M@C:N materials show high TOF values relative to our previous report using Fe@C:N.[13] Our findings therefore suggest that compositional changes can be successfully leveraged to modulate and improve ECH performance at M@C architectures based on transition metals.

It is important however to highlight that, when interpreting differences in performance between Mo and W-containing electrodes it remains challenging to disentangle the effects of a change in metal identity (W *vs.* Mo), from those arising from morphological and compositional differences that result from metal-catalysed graphitisation. In the case of W@C:N materials, metal centres are encapsulated and protected from oxidation; the majority of them are present in the form of WN nanorods that can improve, simultaneously, H_{ads} stabilisation[24,87] and metallic character/conductivity of the porous carbon matrix. For Mo@C:N it is also possible to argue that H_{ads} coverages are stabilised relative to RPM/BP; however, the presence of surface MoO_x indicates that only a fraction of metal sites should facilitate H_{ads} activation, while charge transfer impedances are likely to be negatively affected by surface oxidised phases.[91]

Finally, the calculation of TOF_{eff} values assumes implicitly that the metal sites are responsible for BZH reduction rates. This is likely an oversimplification that neglects possible activation of multiple N-/C-sites due to *e.g.* proximity effects of metal in the sub-surface,[18,20] as well as the fact that hydrogenation pathways are potential-dependent.[5] First, several proposed hypotheses have been put forward to explain the nature of the active site at M@C:N electrodes in the HER. Both M-sites in contact with the electrolyte but with their reactivity modulated by the surrounding carbon matrix, or C/N-sites with their reactivity modulated by metals in the subsurface are considered as possible and experimentally consistent explanations for H_{ads} activation at carbon-encapsulated architectures. However, unequivocal identification of these active sites remains a topic of ongoing debate, as highlighted recently by Yoo *et al.*,[92] despite the HER being a considerably simpler reaction than the ECH of benzaldehyde. Nonetheless, and regardless of whether the active sites are C- or M-centers, the activity remains dependent on the degree to which the metal is in proximity to, or at, the surface. Therefore, XPS atomic coverages, which reflect metal content within the first 1–3 nm from the surface, are a relevant quantity when attempting to account for metal effects on surface reactivity. A more in-depth analysis of the active site in the ECH is likely to require further experimental work, including *e.g.* use of poisoning/capping agents.[92] Second, potential-dependence of the active site must also be contemplated; at increasing cathodic overpotentials it is reasonable to assume that the total product rate stems at least in part from proton coupled reductions, as noted when discussing FE_{ECH} values at −0.8 V. Indeed, contributions from M-site mediated H-addition and from proton coupled reduction of BZH_{ads} must both be considered, particularly at high overpotentials and based on the current mechanistic understanding of ECH.[5,93–95] Therefore, the validity of assumptions underpinning TOF_{eff} calculations might be limited at the most negative potentials tested and comparisons between metal TOF values are best restricted to the low overpotential range where metal catalysed pathways are expected to dominate hydrogenation rates. Finally, although electrolysis experiments are performed in this work under natural convection and in an H-cell, well-defined convective conditions *e.g.* flow through electrolyser devices, would be desirable to fully account for mass transport effects, support comparative performance studies and investigate stability under conditions closer to those encountered in electrolyser applications.[20]

4. Conclusions

In this work we have investigated M@C:N architectures as a promising approach for developing materials that are active in the electrocatalytic hydrogenation of benzaldehyde. Building on encouraging results that demonstrated activity with low-cost metals such as Fe,[13] we show that the type of metal centre in M@C:N structures can be leveraged to regulate ECH performances, as observed by the significant enhancements in effective TOF resulting from a replacement of Mo with W centres.

The synthesis and properties of materials Mo@C:N and W@C:N, with nearly identical atomic metal contents of *ca.* 1.5%, were investigated. Structural characterisation revealed that Mo@C:N has a bulk composition primarily consisting of Mo_2C, but its surface is rich in oxides. In contrast, W@C:N has a bulk structure consisting of WN with minimal oxide present at its surface; W is localised in rod-like nanostructures protected from oxidation and likely corrosion by a graphitised shell. Both materials were found to be porous: the presence of W centres introduces only small changes in carbon porosity relative to the metal-free analogue material, whereas Mo centres catalyse pore opening.

Incorporation of Mo and W centres improves the HER activity for both materials compared to the metal free analogue RPM/BP, with Mo@C:N displaying higher HER cathodic currents. Electrolysis experiments coupled with gas chromatography analysis of products demonstrated that this translates into increased ECH activity at low overpotentials in the hydrogenation of benzaldehyde, the unsaturated compound used as a diagnostic substrate. Selectivity for the benzyl alcohol product was observed at all tested potentials; this is a promising result as achieving selectivity remains a challenge for most studied electrocatalysts, particularly at cathodic potentials.[13,82,83] Mo@C:N shows high FE at anodic potentials, while W@C:N is more efficient at cathodic potentials due to suppressed competition between HER and ECH pathways. Product rates

and TOF_{eff} values were used as a basis for comparison, with W@C:N showing higher ECH performances at the investigated atomic loading, especially when considering the differences in surface excess between the two metals. Estimated TOF_{eff} are comparable to those for Rh/C and Pt/C catalysts;[82] given the four orders of magnitude difference in material cost, results suggests that W@C:N architectures are likely to be cost-competitive for ECH applications and could reduce pressure on precious and critical raw materials for ECH implementation at scale.

Data availability

Data for this article, including X-ray diffraction (XRD), isotherms and pore size distributions, X-ray photoelectron spectroscopy (XPS), Scanning electron microscopy (SEM), cyclic and linear sweep voltammetry (CV and LSV), electrolysis raw data at different conditions of organic concentration and potential, Faradic efficiency (FE), product rates, turn over frequency (TOF), and transmission electron microscopy (TEM), are available at Trinity's Access to Research Archive (TARA) at **https://hdl.handle.net/2262/110448**.

Conflicts of interest

There are no conflicts of interest to declare.

Acknowledgements

This publication has emanated from research conducted with the financial support of Taighde Éireann – Research Ireland under Grant number 19/FFP/6761 and GOIPD/2021/530. PEC, FB and JAB thank the France-Ireland PHC ULYSSES 2021 programme for supporting part of the work. SEM imaging was carried out at the Advanced Microscopy Laboratory (AML) at the AMBER Research Centre, Trinity College Dublin, Ireland. We acknowledge kind support from the Earth Surface Research Laboratory for access to ED-XRF. We are grateful to the THEMIS platform (ScanMAT) at the Université de Rennes for support with HR-TEM. Use of the XPS of I. V. Shvets and C. McGuinness provided under SFI Equipment Infrastructure funds.

References

1 G. Zhao, K. Rui, S. X. Dou and W. Sun, Heterostructures for Electrochemical Hydrogen Evolution Reaction: A Review, *Adv. Funct. Mater.*, 2018, **28**, 1803291.
2 S. A. Akhade, N. Singh, O. Y. Gutiérrez, J. Lopez-Ruiz, H. Wang, J. D. Holladay, Y. Liu, A. Karkamkar, R. S. Weber, A. B. Padmaperuma, M.-S. Lee, G. A. Whyatt, M. Elliott, J. E. Holladay, J. L. Male, J. A. Lercher, R. Rousseau and V.-A. Glezakou, Electrocatalytic hydrogenation of biomass-derived organics: a review, *Chem. Rev.*, 2020, **120**, 11370–11419.
3 Y. Zeng, M. Zhao, H. Zeng, Q. Jiang, F. Ming, K. Xi, Z. Wang and H. Liang, Recent progress in advanced catalysts for electrocatalytic hydrogenation of organics in aqueous conditions, *eScience*, 2023, **3**, 100156.
4 L. Zhang, T. U. Rao, J. Wang, D. Ren, S. Sirisommboonchai, C. Choi, H. Machida, Z. Huo and K. Norinaga, A review of thermal catalytic and electrochemical hydrogenation approaches for converting biomass-derived compounds to high-value chemicals and fuels, *Fuel Process. Technol.*, 2022, **226**, 107097.
5 D. C. Cantu, A. B. Padmaperuma, M.-T. Nguyen, S. A. Akhade, Y. Yoon, Y.-G. Wang, M.-S. Lee, V.-A. Glezakou, R. Rousseau and M. A. Lilga, A combined experimental and theoretical study on the activity and selectivity of the electrocatalytic hydrogenation of aldehydes, *ACS Catal.*, 2018, **8**, 7645–7658.
6 J. Anibal, A. Malkani and B. Xu, Stability of the ketyl radical as a descriptor in the electrochemical coupling of benzaldehyde, *Catal. Sci. Technol.*, 2020, **10**, 3181–3194.
7 E. Andrews, J. A. Lopez-Ruiz, J. D. Egbert, K. Koh, U. Sanyal, M. Song, D. Li, A. J. Karkamkar, M. A. Derewinski, J. Holladay, O. Y. Gutiérrez and J. D. Holladay, Performance of base and noble metals for electrocatalytic hydrogenation of bio-oil-derived oxygenated compounds, *ACS Sustainable Chem. Eng.*, 2020, **8**, 4407–4418.
8 K. Amouzegar and O. Savadogo, Electrocatalytic hydrogenation of phenol on dispersed Pt: reaction mechanism and support effect, *Electrochim. Acta*, 1998, **43**, 503–508.
9 S. J. C. Cleghorn and D. Pletcher, The mechanism of electrocatalytic hydrogenation of organic molecules at palladium black cathodes, *Electrochim. Acta*, 1993, **38**, 425–430.
10 Z. Li, S. Kelkar, L. Raycraft, M. Garedew, J. E. Jackson, D. J. Miller and C. M. Saffron, A mild approach for bio-oil stabilization and upgrading: electrocatalytic hydrogenation using ruthenium supported on activated carbon cloth, *Green Chem.*, 2014, **16**, 844–852.
11 B. zhao, M. Chen, Q. Guo and Y. Fu, Electrocatalytic hydrogenation of furfural to furfuryl alcohol using platinum supported on activated carbon fibers, *Electrochim. Acta*, 2014, **135**, 139–146.
12 **https://www.dailymetalprice.com**and **https://www.metal.com/**, accessed 10, December, 2024.
13 F. Pota, M. Costa de Oliveira, C. Schröder, M. Brunet Cabré, H. Nolan, A. Rafferty, O. Jeannin, F. Camerel, J. Behan, F. Barrière and P. E. Colavita, Porous N-doped carbon-encapsulated iron as a novel catalyst architecture for the electrocatalytic hydrogenation of benzaldehyde, *ChemSusChem*, 2025, **18**, e202400546.
14 M. Tavakkoli, T. Kallio, O. Reynaud, A. G. Nasibulin, C. Johans, J. Sainio, H. Jiang, E. I. Kauppinen and K. Laasonen, Single-shell carbon-encapsulated iron nanoparticles: synthesis and high electrocatalytic activity for hydrogen evolution reaction, *Angew. Chem., Int. Ed.*, 2015, **54**, 4535–4538.
15 J. Deng, P. Ren, D. Deng and X. Bao, Enhanced electron penetration through an ultrathin graphene layer for highly efficient catalysis of the hydrogen evolution reaction, *Angew. Chem., Int. Ed.*, 2015, **54**, 2100–2104.

16 H. Wei, J. Wang, Q. Lin, Y. Zou, X. a. Chen, H. Zhao, J. Li, H. Jin, Y. Lei and S. Wang, Incorporating ultra-small N-doped Mo2C nanoparticles onto 3D N-doped flower-like carbon nanospheres for robust electrocatalytic hydrogen evolution, *Nano Energy*, 2021, **86**, 106047.
17 N. Han, K. R. Yang, Z. Lu, Y. Li, W. Xu, T. Gao, Z. Cai, Y. Zhang, V. S. Batista, W. Liu and X. Sun, Nitrogen-doped tungsten carbide nanoarray as an efficient bifunctional electrocatalyst for water splitting in acid, *Nat. Commun.*, 2018, **9**, 924.
18 Y. Peng and S. Chen, Electrocatalysts based on metal@carbon core@shell nanocomposites: an overview, *Green Energy Environ.*, 2018, **3**, 335–351.
19 C. Gao, F. Lyu and Y. Yin, Encapsulated metal nanoparticles for catalysis, *Chem. Rev.*, 2021, **121**, 834–881.
20 L. Zhang, J. Xiao, H. Wang and M. Shao, Carbon-based electrocatalysts for hydrogen and oxygen evolution reactions, *ACS Catal.*, 2017, **7**, 7855–7865.
21 W. Wan, S. Wei, J. Li, C. A. Triana, Y. Zhou and G. R. Patzke, Transition metal electrocatalysts encapsulated into N-doped carbon nanotubes on reduced graphene oxide nanosheets: efficient water splitting through synergistic effects, *J. Mater. Chem. A*, 2019, **7**, 15145–15155.
22 J. Lessard, Electrocatalytic hydrogenation, in *Encyclopedia of Applied Electrochemistry*, 2014, pp. 443–448.
23 S. Trasatti, Work function, electronegativity, and electrochemical behaviour of metals: III. Electrolytic hydrogen evolution in acid solutions, *J. Electroanal. Chem. Interfacial Electrochem.*, 1972, **39**, 163–184.
24 R. Michalsky, Y.-J. Zhang and A. A. Peterson, Trends in the hydrogen evolution activity of metal carbide catalysts, *ACS Catal.*, 2014, **4**, 1274–1278.
25 A. G. Mitchell and L. S. C. Wan, Oxidation of aldehydes solubilized in nonionic surfactants I: solubility of benzaldehyde and methylbenzaldehyde in aqueous solutions of polyoxyethylene glycol ethers, *J. Pharm. Sci.*, 1964, **53**, 1467–1470.
26 O. Hammerich and B. Speiser, *Organic Electrochemistry*, CRC press, Boca Raton, 2016.
27 Y. Ran, J. Li, J. Sun, B. Yu, F. Tan, G. Cheng and Z. Zhang, Impact of alloying on electrocatalytic hydrogenation of benzaldehyde over sputtered NiCu film catalysts, *Appl. Catal., A*, 2024, **678**, 119725.
28 G. Cheng, J. Sun, Y. Ran, F. Tan, W. Ma and Z. Zhang, Effective free-standing electrodes with refined structure *via* sputtering Ti sublayer and altering working pressure for electrocatalytic benzaldehyde hydrogenation, *Chem. Eng. J.*, 2024, **481**, 148735.
29 L. Gong, C. Y. Zhang, J. Li, G. Montaña-Mora, M. Botifoll, T. Guo, J. Arbiol, J. Y. Zhou, T. Kallio, P. R. Martínez-Alanis and A. Cabot, Enhanced electrochemical hydrogenation of benzaldehyde to benzyl alcohol on Pd@Ni-MOF by modifying the adsorption configuration, *ACS Appl. Mater. Interfaces*, 2024, **16**, 6948–6957.
30 C.-C. Liu, A. B. Walters and M. A. Vannice, Measurement of electrical properties of a carbon black, *Carbon*, 1995, **33**, 1699–1708.
31 M. Carmo, A. R. dos Santos, J. G. R. Poco and M. Linardi, Physical and electrochemical evaluation of commercial carbon black as electrocatalysts supports for DMFC applications, *J. Power Sources*, 2007, **173**, 860–866.
32 S. Brunauer, P. H. Emmett and E. Teller, Adsorption of gases in multimolecular layers, *J. Am. Chem. Soc.*, 1938, **60**, 309–319.
33 J. Rouquerol, P. Llewellyn and F. Rouquerol, Is the BET equation applicable to microporous adsorbents?, in *Studies in Surface Science and Catalysis*, Elsevier, 2007, vol. 160, pp. 49–56.
34 V. Fierro, G. Bosch and F. R. Siperstein, Pore size distribution in microporous carbons obtained from molecular modeling and density functional theory, in *Studies in Surface Science and Catalysis*, ed. P. L. Llewellyn, F. Rodriquez-Reinoso, J. Rouqerol and N. Seaton, Elsevier, 2007, vol. 160, pp. 519–526.
35 G. Kupgan, T. P. Liyana-Arachchi and C. M. Colina, NLDFT pore size distribution in amorphous microporous materials, *Langmuir*, 2017, **33**, 11138–11145.
36 J. A. Behan, A. Iannaci, C. Domínguez, S. N. Stamatin, M. K. Hoque, J. M. Vasconcelos, T. S. Perova and P. E. Colavita, Electrocatalysis of N-doped carbons in the oxygen reduction reaction as a function of pH: N-sites and scaffold effects, *Carbon*, 2019, **148**, 224–230.
37 A. Iannaci, S. Ingle, C. Domínguez, M. Longhi, O. Merdrignac-Conanec, S. Ababou-Girard, F. Barrière and P. E. Colavita, Nanoscaffold effects on the performance of air-cathodes for microbial fuel cells: sustainable Fe/N-carbon electrocatalysts for the oxygen reduction reaction under neutral pH conditions, *Bioelectrochemistry*, 2021, **142**, 107937.
38 M. Karthik, A. Faik, S. Doppiu, V. Roddatis and B. D'Aguanno, A simple approach for fabrication of interconnected graphitized macroporous carbon foam with uniform mesopore walls by using hydrothermal method, *Carbon*, 2015, **87**, 434–443.
39 M. Zhang, Y. Qiu, Y. Han, Y. Guo and F. Cheng, Three-dimensional tungsten nitride nanowires as high performance anode material for lithium ion batteries, *J. Power Sources*, 2016, **322**, 163–168.
40 L. Shen and N. Wang, Effect of nitrogen pressure on the structure of Cr-N, Ta-N, Mo-N, and W-N nanocrystals synthesized by Arc discharge, *J. Nanomater.*, 2011, **2011**, 781935.
41 K. S. W. Sing, Reporting physisorption data for gas/solid systems with special reference to the determination of surface area and porosity (Recommendations 1984), *Pure Appl. Chem.*, 1985, **57**, 603–619.
42 M. Thommes, K. Kaneko, A. V. Neimark, J. P. Olivier, F. Rodriguez-Reinoso, J. Rouquerol and K. S. W. Sing, Physisorption of gases, with special reference to the evaluation of surface area and pore size distribution (IUPAC Technical Report), *Pure Appl. Chem.*, 2015, **87**, 1051–1069.
43 R. T. K. Baker, J. J. Chludzinski, N. C. Dispenziere and L. L. Murrell, Catalytic gasification of graphite by:

tungsten, rhenium, and tungsten-rhenium, *Carbon*, 1983, **21**, 579–588.
44 T. Wang, J. Tang, X. Fan, J. Zhou, H. Xue, H. Guo and J. He, The oriented growth of tungsten oxide in ordered mesoporous carbon and their electrochemical performance, *Nanoscale*, 2014, **6**, 5359–5371.
45 J. Li, Z. Zhang, Z. Wang, Q. Cao, F. Guo and Q. Cao, Low temperature graphitization and electrochemical properties of porous carbon catalyzed with bimetal Ni-Mo, *Diamond Relat. Mater.*, 2022, **123**, 108862.
46 H. Guo, Y. Song, P. Chen, H. Lou and X. Zheng, Effects of graphitization of carbon nanospheres on hydrodeoxygenation activity of molybdenum carbide, *Catal. Sci. Technol.*, 2018, **8**, 4199–4208.
47 A. Ōya and S. Ōtani, Catalytic graphitization of carbons by various metals, *Carbon*, 1979, **17**, 131–137.
48 S. Braun, L. G. Appel and M. Schmal, Molybdenum species on alumina and silica supports for soot combustion, *Catal. Commun.*, 2005, **6**, 7–12.
49 J. P. A. Neeft, M. Makkee and J. A. Moulijn, Catalysts for the oxidation of soot from diesel exhaust gases. I. An exploratory study, *Appl. Catal., B*, 1996, **8**, 57–78.
50 J. Chastain and R. C. King Jr, *Handbook of X-Ray Photoelectron Spectroscopy*, Perkin-Elmer Corporation, 1992, 40, p. 221.
51 N. Hellgren, R. T. Haasch, S. Schmidt, L. Hultman and I. Petrov, Interpretation of X-ray photoelectron spectra of carbon-nitride thin films: new insights from *in situ* XPS, *Carbon*, 2016, **108**, 242–252.
52 L. Qu, Y. Liu, J.-B. Baek and L. Dai, Nitrogen-doped graphene as efficient metal-free electrocatalyst for oxygen reduction in fuel cells, *ACS Nano*, 2010, **4**, 1321–1326.
53 J. T. Titantah and D. Lamoen, Carbon and nitrogen 1s energy levels in amorphous carbon nitride systems: XPS interpretation using first-principles, *Diamond Relat. Mater.*, 2007, **16**, 581–588.
54 M. A. Costa de Oliveira, C. Schröder, M. Brunet Cabré, H. Nolan, A. Forner-Cuenca, T. S. Perova, K. McKelvey and P. E. Colavita, Effects of N-functional groups on the electron transfer kinetics of VO^{2+}/VO_2^+ at carbon: decoupling morphology from chemical effects using model systems, *Electrochim. Acta*, 2024, **475**, 143640.
55 Y.-Y. Chen, Y. Zhang, W.-J. Jiang, X. Zhang, Z. Dai, L.-J. Wan and J.-S. Hu, Pomegranate-like N,P-doped Mo_2C@C nanospheres as highly active electrocatalysts for alkaline hydrogen evolution, *ACS Nano*, 2016, **10**, 8851–8860.
56 H. Wei, Q. Xi, X. a. Chen, D. Guo, F. Ding, Z. Yang, S. Wang, J. Li and S. Huang, Molybdenum carbide nanoparticles coated into the graphene wrapping N-doped porous carbon microspheres for highly efficient electrocatalytic hydrogen evolution both in acidic and alkaline media, *Adv. Sci.*, 2018, **5**, 1700733.
57 X. Yang, X. Feng, H. Tan, H. Zang, X. Wang, Y. Wang, E. Wang and Y. Li, N-doped graphene-coated molybdenum carbide nanoparticles as highly efficient electrocatalysts for the hydrogen evolution reaction, *J. Mater. Chem. A*, 2016, **4**, 3947–3954.
58 H. Preiss, B. Meyer and C. Olschewski, Preparation of molybdenum and tungsten carbides from solution derived precursors, *J. Mater. Sci.*, 1998, **33**, 713–722.
59 N. Malone, H. Fiedler, D. R. G. Mitchell, J. V. Kennedy, G. I. N. Waterhouse and P. Gupta, High turnover frequency for the hydrogen evolution reaction on molybdenum carbide thin films synthesized by ion implantation, *ACS Appl. Eng. Mater.*, 2023, **1**, 2377–2385.
60 C. C. Baker and S. I. Shah, Reactive sputter deposition of tungsten nitride thin films, *J. Vac. Sci. Technol. A*, 2002, **20**, 1699–1703.
61 Z. Wang, Z. Liu, Z. Yang and S. Shingubara, Characterization of sputtered tungsten nitride film and its application to Cu electroless plating, *Microelectron. Eng.*, 2008, **85**, 395–400.
62 Y. G. Shen, Y. W. Mai, D. R. McKenzie, Q. C. Zhang, W. D. McFall and W. E. McBride, Composition, residual stress, and structural properties of thin tungsten nitride films deposited by reactive magnetron sputtering, *J. Appl. Phys.*, 2000, **88**, 1380–1388.
63 S. Ouendi, K. Robert, D. Stievenard, T. Brousse, P. Roussel and C. Lethien, Sputtered tungsten nitride films as pseudocapacitive electrode for on chip micro-supercapacitors, *Energy Storage Mater.*, 2019, **20**, 243–252.
64 P. V. Krasovskii, O. S. Malinovskaya, A. V. Samokhin, Y. V. Blagoveshchenskiy, V. A. Kazakov and A. A. Ashmarin, XPS study of surface chemistry of tungsten carbides nanopowders produced through DC thermal plasma/hydrogen annealing process, *Appl. Surf. Sci.*, 2015, **339**, 46–54.
65 C. B. Rodella, D. H. Barrett, S. F. Moya, S. J. A. Figueroa, M. T. B. Pimenta, A. A. S. Curvelo and V. Teixeira da Silva, Physical and chemical studies of tungsten carbide catalysts: effects of Ni promotion and sulphonated carbon, *RSC Adv.*, 2015, **5**, 23874–23885.
66 A. S. Kurlov and A. I. Gusev, Oxidation of tungsten carbide powders in air, *Int. J. Refract. Met. Hard Mater.*, 2013, **41**, 300–307.
67 R. F. Voitovich and É. A. Pugach, High-temperature oxidation characteristics of the carbides of the Group VI transition metals, *Powder Metall. Met. Ceram.*, 1973, **12**, 314–318.
68 X. Huang, J. Wang, H. Bing Tao, H. Tian, Z. Zhang and H. Xu, Unraveling the oxide layer on Mo2C as the active center for hydrogen evolution reaction, *J. Catal.*, 2020, **389**, 461–467.
69 D. V. Esposito and J. G. Chen, Monolayer platinum supported on tungsten carbides as low-cost electrocatalysts: opportunities and limitations, *Energy Environ. Sci.*, 2011, **4**, 3900–3912.
70 B. Deng, Z. Wang, W. Chen, J. T. Li, D. X. Luong, R. A. Carter, G. Gao, B. I. Yakobson, Y. Zhao and J. M. Tour, Phase controlled synthesis of transition metal carbide nanocrystals by ultrafast flash Joule heating, *Nat. Commun.*, 2022, **13**, 262.
71 C. Wan, Y. N. Regmi and B. M. Leonard, Multiple phases of molybdenum carbide as electrocatalysts for the hydrogen evolution reaction, *Angew. Chem., Int. Ed.*, 2014, **53**, 6407–6410.

72 H. Vrubel and X. Hu, Molybdenum boride and carbide catalyze hydrogen evolution in both acidic and basic solutions, *Angew. Chem., Int. Ed.*, 2012, **51**, 12703–12706.
73 V. S. Saji and C.-W. Lee, Molybdenum, molybdenum oxides, and their electrochemistry, *ChemSusChem*, 2012, **5**, 1146–1161.
74 X. Wang, Y. Xie, K. Tang, C. Wang and C. Yan, Redox chemistry of molybdenum trioxide for ultrafast hydrogen-ion storage, *Angew. Chem., Int. Ed.*, 2018, **57**, 11569–11573.
75 S. R. Denny, B. M. Tackett, D. Tian, K. Sasaki and J. G. Chen, Exploring electrocatalytic stability and activity of unmodified and platinum-modified tungsten and niobium nitrides, *Int. J. Hydrogen Energy*, 2020, **45**, 22883–22892.
76 Y. C. Kimmel, D. V. Esposito, R. W. Birkmire and J. G. Chen, Effect of surface carbon on the hydrogen evolution reactivity of tungsten carbide (WC) and Pt-modified WC electrocatalysts, *Int. J. Hydrogen Energy*, 2012, **37**, 3019–3024.
77 M. A. Spencer, N. P. Holzapfel, K.-E. You, G. Mpourmpakis and V. Augustyn, Participation of electrochemically inserted protons in the hydrogen evolution reaction on tungsten oxides, *Chem. Sci.*, 2024, **15**, 5385–5402.
78 H. Nolan, C. Schröder, M. Brunet-Cabré, F. Pota, N. McEvoy, K. McKelvey, T. S. Perova and P. E. Colavita, MoS_2/carbon heterostructured catalysts for the hydrogen evolution reaction: N-doping modulation of substrate effects in acid and alkaline electrolytes, *Carbon*, 2023, **202**, 70–80.
79 S. I. Perez Bakovic, P. Acharya, M. Watkins, H. Thornton, S. Hou and L. F. Greenlee, Electrochemically active surface area controls HER activity for Fe_xNi_{100-x} films in alkaline electrolyte, *J. Catal.*, 2021, **394**, 104–112.
80 J. Kibsgaard, Z. Chen, B. N. Reinecke and T. F. Jaramillo, Engineering the surface structure of MoS_2 to preferentially expose active edge sites for electrocatalysis, *Nat. Mater.*, 2012, **11**, 963–969.
81 S. Hussain, D. Vikraman, A. Feroze, W. Song, K.-S. An, H.-S. Kim, S.-H. Chun and J. Jung, Synthesis of Mo_2C and W_2C nanoparticle electrocatalysts for the efficient hydrogen evolution reaction in alkali and acid electrolytes, *Front. Chem.*, 2019, **7**, 716.
82 Y. Song, U. Sanyal, D. Pangotra, J. D. Holladay, D. M. Camaioni, O. Y. Gutiérrez and J. A. Lercher, Hydrogenation of benzaldehyde *via* electrocatalysis and thermal catalysis on carbon-supported metals, *J. Catal.*, 2018, **359**, 68–75.
83 U. Sanyal, S. F. Yuk, K. Koh, M. S. Lee, K. Stoerzinger, D. Zhang, L. C. Meyer, J. A. Lopez-Ruiz, A. Karkamkar and J. D. Holladay, Hydrogen bonding enhances the electrochemical hydrogenation of benzaldehyde in the aqueous phase, *Angew. Chem., Int. Ed.*, 2021, **133**, 294–300.
84 M. J. Sims, N. V. Rees, E. J. F. Dickinson and R. G. Compton, Effects of thin-layer diffusion in the electrochemical detection of nicotine on basal plane pyrolytic graphite (BPPG) electrodes modified with layers of multi-walled carbon nanotubes (MWCNT-BPPG), *Sens. Actuators, B*, 2010, **144**, 153–158.
85 G. P. Keeley and M. E. G. Lyons, The effects of thin layer diffusion at glassy carbon electrodes modified with porous films of single-walled carbon nanotubes, *Int. J. Electrochem. Sci.*, 2009, **4**, 794–809.
86 M. Chandrasekaran, M. Noel and V. Krishnan, Glassy carbon surface effects on the electroreduction of aromatic carbonyl compounds: part 1. Benzaldehyde, *J. Electroanal. Chem. Interfacial Electrochem.*, 1991, **303**, 185–197.
87 H. Jin, H. Zhang, J. Chen, S. Mao, Z. Jiang and Y. Wang, A general synthetic approach for hexagonal phase tungsten nitride composites and their application in the hydrogen evolution reaction, *J. Mater. Chem. A*, 2018, **6**, 10967–10975.
88 D. T. Fagan, I. F. Hu and T. Kuwana, Vacuum heat-treatment for activation of glassy carbon electrodes, *Anal. Chem.*, 1985, **57**, 2759–2763.
89 M. K. Hoque, J. A. Behan, S. N. Stamatin, F. Zen, T. S. Perova and P. E. Colavita, Capacitive storage at nitrogen doped amorphous carbon electrodes: structural and chemical effects of nitrogen incorporation, *RSC Adv.*, 2019, **9**, 4063–4071.
90 E. Pop, V. Varshney and A. K. Roy, Thermal properties of graphene: fundamentals and applications, *MRS Bull.*, 2012, **37**, 1273–1281.
91 W. Zheng, iR compensation for electrocatalysis studies: considerations and recommendations, *ACS Energy Lett.*, 2023, **8**, 1952–1958.
92 J. M. Yoo, H. Shin, D. Y. Chung and Y.-E. Sung, Carbon shell on active nanocatalyst for stable electrocatalysis, *Acc. Chem. Res.*, 2022, **55**, 1278–1289.
93 E. S. Chan-Shing, D. Boucher and J. Lessard, The electrochemical reduction of α-nitrocumene in a protic and basic medium on large surface area (porous) electrodes: electronation-protonation or electrocatalytic hydrogenation?, *Can. J. Chem.*, 1999, **77**, 687–694.
94 H. Chen, J. Iyer, Y. Liu, S. Krebs, F. Deng, A. Jentys, D. J. Searles, M. A. Haider, R. Khare and J. A. Lercher, Mechanism of electrocatalytic H_2 evolution, carbonyl hydrogenation, and carbon–carbon coupling on Cu, *J. Am. Chem. Soc.*, 2024, **146**, 13949–13961.
95 J. A. Lopez-Ruiz, E. Andrews, S. A. Akhade, M.-S. Lee, K. Koh, U. Sanyal, S. F. Yuk, A. J. Karkamkar, M. A. Derewinski, J. Holladay, V.-A. Glezakou, R. Rousseau, O. Y. Gutiérrez and J. D. Holladay, Understanding the role of metal and molecular structure on the electrocatalytic hydrogenation of oxygenated organic compounds, *ACS Catal.*, 2019, **9**, 9964–9972.

